

AD-A186 120

AFOSR-TR- 87-1202

DTIC FILE COPY

(2)

R87-956939-3

Unsteady Stall Penetration Experiments  
at High Reynolds Number

Peter F. Lorber and Franklin O. Carta

United Technologies Research Center  
East Hartford, CT 06108

April 14, 1987

Prepared For

U. S. Air Force Office of Scientific Research  
Bolling AFB, DC 20332  
under  
Contract F49620-84-C-0082

DTIC  
ELECTE  
OCT 02 1987  
S D  
CD

(The views and conclusions contained in this document are those of the authors and should not be interpreted as necessarily representing the official policies or endorsements, either expressed or implied, of the Air Force Office of Scientific Research or the U.S. Government)

DISTRIBUTION STATEMENT A  
Approved for public release  
Distribution Unlimited

97 9 24 097

AD-A186120

## REPORT DOCUMENTATION PAGE

1a. REPORT SECURITY CLASSIFICATION UNCLASSIFIED			1b. RESTRICTIVE MARKINGS		
2a. SECURITY CLASSIFICATION AUTHORITY			3. DISTRIBUTION/AVAILABILITY OF REPORT Approved for public release, distribution unlimited		
2b. DECLASSIFICATION/DOWNGRADING SCHEDULE			5. MONITORING ORGANIZATION REPORT NUMBER(S) AFOSR-TR-87-1202		
4. PERFORMING ORGANIZATION REPORT NUMBER(S) R87-956939-3			7a. NAME OF MONITORING ORGANIZATION Air Force Office of Scientific Research		
6a. NAME OF PERFORMING ORGANIZATION United Technologies Research Center		6b. OFFICE SYMBOL (if applicable) AFOSR/NA		7b. ADDRESS (City, State, and ZIP Code) Bldg. 410 Bolling AFB, DC 20332	
6c. ADDRESS (City, State, and ZIP Code) 400 Main St. East Hartford, CT 06108		9. PROCUREMENT INSTRUMENT IDENTIFICATION NUMBER F49620-84-C-0082			
8a. NAME OF FUNDING/SPONSORING ORGANIZATION Air Force Office of Scientific Research		10. SOURCE OF FUNDING NUMBERS PROGRAM ELEMENT NO. 61102F PROJECT NO. 2307 TASK NO. A2 WORK UNIT ACCESSION NO.			
8b. ADDRESS (City, State, and ZIP Code) Building 410 Bolling, AFB, DC 20332		11. TITLE (Include Security Classification) Unsteady Stall Penetration Experiments at High Reynolds Number			
12. PERSONAL AUTHOR(S) Peter F. Lorber and Franklin O. Carta					
13a. TYPE OF REPORT Final		13b. TIME COVERED FROM 8/14/84 TO 2/14/87		14. DATE OF REPORT (Year, Month, Day) 1987, April, 14	
15. PAGE COUNT 202					
16. SUPPLEMENTARY NOTATION Monitored for AFOSR by Drs. M. Francis, J. Wilson, and H. Helin					
17. COSATI CODES FIELD GROUP SUB-GROUP			18. SUBJECT TERMS (Continue on reverse if necessary and identify by block number) Dynamic Stall Vortex Propagation Unsteady Flow Supermaneuverability Separated Flow Aerodynamic Testing		
19. ABSTRACT (Continue on reverse if necessary and identify by block number) An experiment has been performed to study the aerodynamics of dynamic stall penetration at constant pitch rate and high Reynolds number, in an attempt to more accurately model conditions during aircraft post-stall maneuvers and during helicopter high speed forward flight. An airfoil was oscillated at non-dimensional pitch rates between 0.001 and 0.020, Mach numbers between 0.2 and 0.4, and Reynolds numbers between $2 \times 10^5$ and $4 \times 10^5$ . Surface pressures were measured using 72 miniature transducers, and the locations of transition and separation were determined using 8 surface hot film gages. The results demonstrate the influence of the leading edge stall vortex on the unsteady aerodynamic response during and after stall. The vortex is strengthened by increasing the pitch rate, and is weakened by increasing the Mach number and by starting the motion close to the steady-state stall angle. A periodic pressure oscillation occurred after stall at high pitch angle and moderate Reynolds number; the oscillation frequency was close to that predicted for a von Karman					
20. DISTRIBUTION/AVAILABILITY OF ABSTRACT <input checked="" type="checkbox"/> UNCLASSIFIED/UNLIMITED <input type="checkbox"/> SAME AS RPT. <input type="checkbox"/> DTIC USERS			21. ABSTRACT SECURITY CLASSIFICATION UNCLASSIFIED		
22a. NAME OF RESPONSIBLE INDIVIDUAL DR JAMES McMICHAEL			22b. TELEPHONE (Include Area Code) 202-767-4935		
22c. OFFICE SYMBOL AFOSR/NA					

DD FORM 1473, 84 MAR

83 APR edition may be used until exhausted.  
All other editions are obsolete.

SECURITY CLASSIFICATION OF THIS PAGE

UNCLASSIFIED

UNCLASSIFIED

UNCLASSIFIED

SECURITY CLASSIFICATION OF THIS PAGE

Block 19. (Cont'd) vortex street. A small supersonic zone near the leading edge at  $M = 0.4$  was found to significantly reduce the peak suction pressures and the unsteady increments to the airloads. These results provide the first known data base of constant pitch rate data at realistic combinations of Reynolds and Mach number.

UNCLASSIFIED

SECURITY CLASSIFICATION OF THIS PAGE

R87-956939-3

Unsteady Stall Penetration Experiments  
at High Reynolds Number

Peter F. Lorber and Franklin O. Carta

United Technologies Research Center  
East Hartford, CT 06108

April 14, 1987

Prepared For

U. S. Air Force Office of Scientific Research  
Bolling AFB, DC 20332  
under  
Contract F49620-84-C-0082



(The views and conclusions contained in this document are those of the authors and should not be interpreted as necessarily representing the official policies or endorsements, either expressed or implied, of the Air Force Office of Scientific Research or the U.S. Government)

Accession For	
NTIS CRA&I	<input checked="" type="checkbox"/>
DTIC TAB	<input type="checkbox"/>
Unannounced	<input type="checkbox"/>
Justification	
By	
Distribution /	
Availability Codes	
Dist	Avail and/or Special
A-1	

# CONTENTS

	<u>Page</u>
SUMMARY	iii
FOREWORD	iv
NOMENCLATURE	v
LIST OF TABLES	vi
LIST OF ILLUSTRATIONS	vii
INTRODUCTION	1
DESCRIPTION OF EXPERIMENT	3
Model and Instrumentation	3
Data Acquisition	5
Airfoil Motions	5
Data Processing and Calibration	6
Test Conditions	7
STEADY STATE CHARACTERISTICS	9
CHARACTERISTICS OF A 0 TO 30 DEG RAMP AT $M = 0.2$	11
Pressure Time Histories	11
Forces and Moment	12
Individual Cycle Results	13
Root-mean-square Pressures	14
Hot Film Gage Results	15
THE EFFECT OF PITCH RATE AT $M = 0.2$	18
Forces and Moment	18
Upper Surface Pressures	19
Transition and Separation	21
RESULTS AT HIGHER MACH NUMBERS	23
Pressure Time Histories at $M = 0.4$	23
Hot Film Gage Results	24
Pitch Rate Effects	24
Forces and Moment	25
Results at $M = 0.3$	26

## CONTENTS (Concluded)

	<u>Page</u>
RESULTS FOR SINUSOIDAL OSCILLATIONS	28
Upper Surface Pressures	28
Forces and Moment	29
Lower Surface Pressures	29
Root-mean-square Pressures	30
THE EFFECT OF STARTING AND ENDING ANGLE	31
Final Pitch Angle	31
Initial Pitch Angle	32
RESULTS FOR NEGATIVE PITCH RATE	34
CONCLUSIONS	36
APPENDIX A - THREE-DIMENSIONAL EFFECTS WITH A TWO-DIMENSIONAL GEOMETRY	37
APPENDIX B - PITCHING MOMENT OFFSETS IN ATTACHED FLOW	38
APPENDIX C - DETERMINING TRANSITION FROM R.M.S. PRESSURE RESULTS	39
APPENDIX D - VORTEX PROPAGATION SPEED IN WIND AND MODEL AXES	40
REFERENCES	42
TABLES	
ILLUSTRATIONS	

## SUMMARY

An experiment has been performed to examine the unsteady aerodynamics of stall penetration at constant pitch rate and high Reynolds number, in an attempt to more accurately model conditions during aircraft post-stall maneuvers and during helicopter high speed forward flight. The model spanned the 8 ft (2.4 m) wind tunnel and consisted of a 17.3 in. (43.9 cm) chord wing with a Sikorsky SSC-A09 airfoil section. Two forms of pitching motion were used: constant pitch rate ramps and sinusoidal oscillations. Ramp data were obtained for 36 test points at pitch rates,  $A = \dot{\alpha} c / 2U$ , between 0.001 and 0.020, Mach numbers between 0.2 and 0.4, and Reynolds numbers between  $2 \times 10^6$  and  $4 \times 10^6$ . Sinusoidal data were obtained for an additional 9 conditions. The wing instrumentation consisted of 72 miniature transducers to measure surface pressure and 8 surface hot film gages to determine the locations of transition and separation.

The results demonstrate the influence of the leading edge stall vortex on the unsteady aerodynamic response during and after stall. The vortex-related unsteady increments to the lift, drag, and pitching moment increase with pitch rate; the maximum  $\Delta C_L$  is 1.2 at  $A = 0.02$ . The angular delays in the stall events also increase with pitch rate; the angle of maximum  $C_L$  is delayed by 10 deg at  $A = 0.02$ . The vortex strength and propagation velocity were determined from the pressures induced on the airfoil surface. The vortex is strengthened by increasing the pitch rate, and is weakened both by increasing the Mach number and by starting the motion close to the steady-state stall angle. The propagation velocity increases linearly with pitch rate. A periodic pressure oscillation occurs after stall at high pitch angle and moderate Reynolds number; the oscillation frequency of 62 to 64 Hz is close to that predicted for a von Karman vortex street. A small supersonic zone is formed near the leading edge at  $M = 0.3$  and  $M = 0.4$ . The effects of compressibility significantly reduce the peak suction pressures and the unsteady increments to the airloads.

This experiment has produced an extensive and detailed data base for unsteady airfoil motions at realistic values of Reynolds and Mach number. In addition to providing insight into the physics of such motions, the data will also serve as a basis for validating computational results. These results constitute the first known compendium of constant pitch rate data at these values of Reynolds and Mach number.

## FOREWORD

This experiment was supported by the U.S. Air Force Office of Scientific Research (AFSC) under Contract F49620-84-C-0082, initiated by Dr. M. S. Francis and monitored by Drs. J. D. Wilson and H. E. Helin. This support was used to construct the instrumented model, conduct the experiment, analyze the results, and write this report.

The model support and drive system was developed under funding supplied by the Sikorsky Aircraft Division of United Technologies Corporation. The hydraulic drive system is believed to provide unique capabilities for this type of testing. Mr. Thomas Saviano of Sikorsky was responsible for its design and operation. Messrs. Richard Ross and John Ayer of UTRC made major contributions to the design and installation of the support system.

The signal conditioning and data acquisition system is the product of several years of development at the United Technologies Research Center (UTRC). The primary modifications made for this experiment were to the signal conditioning and switching electronics. Messrs. Joseph Haley and Conrad Eckstrom were primarily responsible for the success of these improvements.

Mr. Alfred Covino was responsible for instrumenting the model, modifying the data acquisition software for this experiment, and for operating the data acquisition system during the test program. The authors are grateful to all of these individuals for their efforts, which were essential for the successful completion of this project.



# NOMENCLATURE

A	pitch rate, $\dot{\alpha}c/2U$
c	airfoil chord, m
C	chordwise force (parallel to airfoil chord), N
$C_C$	section chord force coefficient, $C/qc$
$C_D$	section pressure drag coefficient, $D/qc$
$C_L$	section lift coefficient, $L/qc$
$C_M$	section pitching moment coefficient, $M/qc^2$
$C_N$	section normal force coefficient, $N/qc$
$C_p$	pressure coefficient, $(P-P_{static})/q$
$C_{p^*}$	pressure coefficient for local sonic velocity
D	pressure drag (force parallel to wind axis), N
D	diameter of equivalent circular cylinder, m
h	height of vortex path above airfoil pivot point, m
k	reduced frequency of sinusoid, $\omega c/2U$
L	lift (force normal to wind axis), N
M	pitching moment about $x = 0.25 c$ , N-m
M	Mach number
N	normal force (normal to airfoil chord), N
q	freestream dynamic pressure, $0.5 \rho U^2$ , Pa
P	local pressure, Pa
$P_{static}$	static pressure at test section centerline, Pa
Re	Reynolds number, $cU/\nu$
t	time from start of data acquisition, sec
T	data acquisition period, sec
U	freestream velocity, m/sec
V	stall vortex propagation velocity along airfoil chord, m/sec
$V_w$	stall vortex propagation velocity in wind axes, m/sec
x	distance from airfoil leading angle, m
$\alpha$	geometric pitch angle, radians
$\tau$	nondimensional time, $t/T$
$\nu$	kinematic viscosity, $m^2/sec$
$\rho$	air density, $kg/m^3$
$\omega$	frequency of sinusoidal oscillation, rad/sec

## TABLES

### Table

- |   |   |
|---|---|
| 1 | Surface Coordinates for the Sikorsky SSC-A09 Airfoil. |
| 2 | Surface Derivatives for the Sikorsky SSC-A09 Airfoil. |
| 3 | Model Instrumentation Stations.                       |
| 4 | Test Conditions Studied.                              |

## ILLUSTRATIONS

### Figure

- 1 Oscillating wing model in the 8 ft section of the UTRC wind tunnel.
- 2 Model support and hydraulic drive system mounted on the east wall of the test section.
- 3 The Sikorsky SSC-A09 airfoil section.
- 4 Section of the wing model containing unsteady instrumentation.
- 5 Inside view of the upper panel of the instrumented section.
- 6 Planform view of the wing model in the test section, showing the instrumentation stations.
- 7 Comparison of steady pressures measured with pressure taps and miniature transducers at  $M = 0.2$ . a) Attached flow at  $\alpha = 14$  deg. b) Separated flow at  $\alpha = 25$  deg.
- 8 Block diagram of the model instrumentation and control system.
- 9 Model motion during constant pitch rate ramps, showing data acquisition period.
- 10 Time histories of the pitch angle for 0 to 30 deg ramps at  $M = 0.2$ .
- 11 Sample pressure transducer calibration curves at several temperatures.
- 12 Steady-state airloads at  $M = 0.2$  and  $M = 0.4$ . a) Lift. b) Drag. c) Pitching Moment.
- 13 Steady-state pressure distributions at  $M = 0.2$  and  $M = 0.4$ . (a-p).

ILLUSTRATIONS (Continued)

Figure

Results For an  $A = 0.005$ , 0 to 30 Ramp at  $M = 0.4$

- 14 Upper surface pressures. a) forward region.  
b) aft region.
- 15 Lower surface pressures. a) forward region.  
b) aft region.
- 16 Difference pressures. a) forward region.  
b) aft region.
- 17 Airloads. a) lift vs. time. b) lift vs. pitch angle.  
c) drag vs. time. d) drag vs pitch angle. e) moment  
vs. time. f) moment vs pitch angle.
- 18 Individual upper surface pressure records.  
a)  $x/c = 0.005$ . b)  $x/c = 0.262$ . c)  $x/c = 0.950$ .
- 19 Individual lower surface pressure records.  
a)  $x/c = 0.060$ . b)  $x/c = 0.464$ . c)  $x/c = 0.950$ .
- 20 RMS upper surface pressures. a) forward region.  
b) aft region.
- 21 RMS lower surface pressures. a) forward region.  
b) aft region.
- 22 Hot film gage output.
- 23 RMS hot film gage output.
- 24 Individual hot film gage records. a)  $x/c = 0.026$ .  
b)  $x/c = 0.302$ . c)  $x/c = 0.880$ .

## ILLUSTRATIONS (Continued)

### Figure

#### Effect of Pitch Rate at $M = 0.2$

- 25      Airloads. a) lift vs pitch angle. b) lift vs time. c) drag vs pitch angle. d) drag vs time. e) moment vs pitch angle. f) moment vs time.
- 26      Unsteady increments to lift, drag, and moment.
- 27      Sequence of stall events vs pitch rate.
- 28      Sequence of stall events vs square root of pitch rate.
- 29      Delay between moment stall and past moment vs square root of pitch rate.
- 30      Upper surface pressure. a)  $A = 0.0010$ . b)  $A = 0.0025$ . c)  $A = 0.0050$ . d)  $A = 0.0100$ . e)  $A = 0.0200$ .
- 31      Times of minimum pressure at each pitch rate.
- 32      Vortex travel speed vs pitch rate.
- 33      Hot film gage output. a)  $A = 0.0010$ . b)  $A = 0.020$ .

## ILLUSTRATIONS (Continued)

### Figure

#### Results at $M = 0.4$

- 34 Upper surface pressures at  $A = 0.005$ .
- 35 Lower surface (a) and difference (b) pressures at  $A = 0.005$ .
- 36 Hot film gage output at  $A = 0.0010$ . a) ensemble average. b) RMS
- 37 Upper surface pressures. a)  $A = 0.0010$ . b)  $A = 0.0025$ . c)  $A = 0.0050$ . d)  $A = 0.0100$ .
- 38 Times of minimum pressure at each pitch rate.
- 39 Airloads at  $A = 0.0010$ ,  $0.0050$ , and  $0.0100$ . a) lift vs pitch angle. b) lift vs. time. c) moment vs. pitch angle. d) moment vs. time. e) drag vs pitch angle. f) drag vs time.
- 40 Sequence of stall events vs pitch rate.

#### Results at $M = 0.3$

- 41 Upper surface pressures. a) 0 to 20 deg ramp at  $A = 0.0050$ . b) 0 to 30 deg ramp at  $A = 0.0100$ .
- 42 Airloads for a 0 to 20 deg ramp at  $A = 0.0050$  at  $M = 0.2$ ,  $0.3$ , and  $0.4$ . a) lift. b) moment. c) drag.

# ILLUSTRATIONS (Continued)

## Figure

### Sinusoidal Motion at $M = 0.2$

- 43 Upper surface pressures.
- |             |                                  |                                  |
|-------------|----------------------------------|----------------------------------|
|             | $\alpha = 10 - 10 \cos \omega t$ | $\alpha = 20 - 10 \cos \omega t$ |
| $k = 0.025$ | (a)                              | (d)                              |
| $k = 0.050$ | (b)                              | (e)                              |
| $k = 0.100$ | (c)                              | (f)                              |
- 44 Times of minimum pressure for each sinusoid.
- 45 Vortex speed vs pitch rate at stall.
- 46 Loops of airloads vs pitch angle.
- |        |                                  |                                  |
|--------|----------------------------------|----------------------------------|
|        | $\alpha = 10 - 10 \cos \omega t$ | $\alpha = 20 - 10 \cos \omega t$ |
| lift   | (a)                              | (b)                              |
| drag   | (c)                              | (d)                              |
| moment | (e)                              | (f)                              |
- 47 Sequence of stall events vs. pitch rate at stall.
- 48 Lower surface pressures for  $\alpha = 20 - 10 \cos \omega t$  at  $k = 0.050$ .
- 49 Lower surface pressures for  $\alpha = 20 - 10 \cos \omega t$  at  $k = 0.100$ .
- 50 RMS pressures for  $\alpha = 20 - 10 \cos \omega t$  at  $k = 0.050$ .  
a) upper surface. b) lower surface.
- 51 Hot film gage output for  $\alpha = 20 - 10 \cos \omega t$  at  $k = 0.050$ . a) ensemble average. b) RMS

ILLUSTRATIONS (Continued)

Figure

**Ramp Results for Varied Pitch Range**

- 52      Airloads for 0 to 20 deg. ramps at  $A = 0.0010, 0.0025, 0.0050,$  and  $0.0100$ . a) lift vs time. b) moment vs time. c) drag vs time
- 53      Upper surface pressures. a)  $A = 0.010$ . b)  $A = 0.0025$
- 54      Airloads for 10 deg. ramps at  $M = 0.2$  and  $A = 0.010$ . a) lift. b) moment. c) drag.
- 55      Upper surface pressures. a) 10 to 20 deg. b) 12 to 22 deg. c) 14 to 24 deg.
- 56      Times of minimum pressure for each range.

**Negative Pitch Rate 0 to 30 Deg. Ramps at  $M = 0.2$**

- 57      Upper surface pressures. a)  $A = 0.001$ . b)  $A = 0.005$ .
- 58      RMS upper surface pressures. a)  $A = 0.001$ . b)  $A = 0.005$ .
- 59      Lower surface pressures. a)  $A = 0.001$ . b)  $A = 0.005$ .
- 60      Hot film gage output at  $A = 0.001$ . a) ensemble average. b) RMS
- 61      Hot film gage output at  $A = 0.005$ . a) ensemble average. b) RMS
- 62      Airloads vs. time at  $A = 0.001$  and  $A = 0.005$ . a) lift. b) moment. c) drag.
- 63      Up and down ramps plotted simultaneously at  $A = 0.005$ . a) lift. b) moment. c) drag.



## ILLUSTRATIONS (Concluded)

### Figure

#### Appendices

- 64 Spanwise variation of airloads. a) normal force. b) moment.
- 65 Upper surface pressures. a) spanwise station 12. b) spanwise station 20.
- 66 Lower surface pressures. a) spanwise station 12. b) spanwise station 20.
- 67 Pressure and skin friction time histories at  $x/c = 0.026$  near transition for a 0 to 30 deg ramp at  $M = 0.2$ .  
a)  $A = 0.020$ . b)  $A = 0.005$ .

## INTRODUCTION

The aerodynamic effect of rapidly pitching an airfoil beyond its steady-state stall angle has been studied by numerous investigators. An extensive period of experimentation occurred between the early 1960's and the mid 1970's. This work emphasized application to the retreating blade stall of a helicopter rotor that occurs in high speed forward flight. Consequently, measurements were typically made of the unsteady airloads during sinusoidal pitch oscillations in the range of 0 to 20 deg, and at Mach and Reynolds numbers characteristic of this application ( $M < 0.4$ ,  $Re < 5 \times 10^6$ ). Representative efforts were reported in Refs. 1-4.

A more recent interest has developed in using the lift and drag augmentations that occur during dynamic stall to improve combat aircraft maneuverability (Refs. 5-6). The motions required for this application include constant rate ramps up to pitch angles substantially above stall. While the Mach numbers of interest remain below  $M = 0.4$ , the Reynolds numbers of a typical combat aircraft wing are quite large, between  $10^6$  and  $10^8$ . Several experiments have been performed to study constant pitch rate dynamic stall. The early work of Ham and Garelick (Ref. 7) measured the surface pressures on a NACA 0012 airfoil that was pitched up to 20 to 30 deg at roughly constant dimensional rates between  $A = 0.005$  and  $0.02$  and at Reynolds numbers of  $3.4 \times 10^5$ . Additional constant pitch rate experiments have been reported in Refs. 8-12. These studies have concentrated on obtaining airload and flow visualization results for large amplitude motions (up to  $\alpha = 90$  deg) at high pitch rates (up to  $A = 1.0$ ). However, this work was conducted at Mach numbers less than  $0.1$  and Reynolds numbers between  $4 \times 10^4$  and  $3 \times 10^5$ , values substantially below those of the desired applications. Steady-state measurements on airfoils at low Reynolds numbers indicate that stall frequently occurs when the laminar upper surface flow separates and then reattaches as a turbulent boundary layer, which may in turn separate again further down the chord (Ref. 13). This process leads to large steady-state stall hysteresis at Reynolds numbers less than about  $5 \times 10^5$ . A turbulent boundary separation is more common at higher Reynolds number. It is likely that the unsteady stall characteristics will also differ.

The current experiment was designed to provide detailed aerodynamic information at a more representative scale. Earlier dynamic stall studies at the United Technologies Research Center (UTRC) used a tunnel-spanning-wing system to oscillate an airfoil in a sinusoidal motion that approximated the pitch range, reduced frequency, Mach number, and Reynolds number of a helicopter rotor (Refs. 14-16). A new version of this apparatus has been built that retains the scale of the original but incorporates a high response hydraulic drive system that permits arbitrary airfoil pitching motions. The present

study measures surface pressures and flow conditions for a series of constant pitch rate ramps and sinusoidal oscillations at Mach numbers of 0.2, 0.3 and 0.4, Reynolds numbers between 2 and  $4 \times 10^6$ , and pitch rates between  $A = 0.001$  and 0.02.

## DESCRIPTION OF EXPERIMENT

The model wing was mounted across the 8 ft (2.44 m) test section of the UTRC Large Subsonic Wind Tunnel (Fig. 1). The primary structural element of the model was a steel spar 5.5 inches (14 cm) in width and 1 in. (2.5 cm) in thickness. The spar was attached at each wind tunnel wall to 4 in. (10 cm) diameter circular shafts supported by pairs of pillow block bearings. As shown in Fig. 1, two quarter-chord supports were attached to the spar from the wind tunnel floor to secure the model during high lift operations and to prevent undesirable bending oscillations. Each side was driven by a hydraulic actuator connected to a hydraulic supply located outside of the wind tunnel. The drive and support system for one side is shown in Fig. 2.

The positions of the hydraulic actuators were set by high response servo valves. The hydraulics were controlled by a dual-channel closed loop system that could be driven either by an internal oscillator or by an external signal of arbitrary waveform. High frequency angular position transducers were mounted at each end of the spar. Safety circuits in the controller were able to shut down the hydraulic system if differences developed between the shaft positions at the two shaft-end actuators or between the desired and actual positions. The external signal to the controller was supplied by a digital waveform synthesizer. The shape of the waveform could be set to one of three independently programmable functions (such as a sinusoid or a periodic ramp). The frequency, mean value, and peak-to-peak amplitude of the waveform could also be selected. The synthesizer had two outputs. One was the analog signal that was used by the hydraulic controller to set the pitch angle of the wing. The second was a pulse train that was used by the data system to synchronize acquisition of data from the instrumentation on the model.

## MODEL AND INSTRUMENTATION

The model was a 17.3 in. (43.9 cm) chord airfoil with a Sikorsky SSC-A09 profile. As shown in Fig. 3, this is a 9% thick supercritical section with a relatively sharp leading edge radius of 0.7% of chord. The surface coordinates and derivatives are given in Tables 1 and 2, respectively. A series of fiberglass panels having this cross-section were mounted along the spar. Figure 4 shows the 22 in. (56 cm) wide panel that contained the primary instrumentation. It was constructed from two sections, a top panel that included the leading and trailing edge regions, and a bottom panel. The interior of the top panel is shown in Fig. 5. This panel contains 53 miniature 15 psi (0.1 MPa) differential pressure transducers (Kulite model XCQ-73U-093-15D), and 8 surface hot film gages (TSI model 1268). The pressure transducers are bonded to the inside of the fiberglass skin and are connected to the airfoil surface by 0.1 in. (2.5 mm) long, .018 in. (.046 mm) ID pipettes.

This method of construction maintains a smooth surface contour and a relatively high frequency response (flat within 5% to at least 5-7 kHz). The reference ports of the transducers are manifolded and connected to the wind tunnel total pressure. The hot films are deposited onto the ends of cylindrical quartz rods, 0.15 in. (.38 mm) in diameter, that penetrate the fiberglass skin and also leave a smooth surface.

Each group of eight pressure transducers is wired to a multilayer printed circuit board that distributes the excitation voltage (8 Volts DC) and contains an electronic multiplexer that selects which of the eight pairs of transducer outputs is being monitored. The use of these circuit boards inside the model reduces the number of wires that must be routed along the spar and transferred from the moving (airfoil) frame to the fixed (data-system) frame. In addition to the six circuit boards shown in Fig. 5, an additional three boards are mounted in the lower panel (not shown). The lower panel also contains 19 pressure transducers, but no hot films.

The layout of the instrumentation on the wing model is shown in Fig. 6. The 72 pressure transducers are arranged in four arrays: a primary array of 18 transducers on each surface located 8 in. (20.3 cm) from the wind tunnel centerline, two secondary arrays of 10 upper surface and 6 lower surface transducers located 16 in. (40.6 cm) and 24 in. (70 cm) from the centerline, and an array of 4 transducers arranged at a 30 deg angle to the chord. The secondary arrays are intended for use in a future part-span experiment, while the 30 deg array is to be used during swept wing testing. During this experiment the additional arrays were used to verify the two-dimensionality of the flow, as described in Appendix A. With the exception of an apparent irregularity in the formation of the leading edge vortex at the stations furthest from the centerline, the data show only a small amount of spanwise variation. The transducers in each array are arranged in a segmented Gaussian distribution to minimize the numerical error introduced in integrating to determine the sectional airloads. The transducer coordinates are given in Table 3. Also given in Table 3 are the locations for the eight hot film gages. The gages are located either 1 or 2 in. (2.5 or 5 cm) to the side of the primary pressure array (the 2 in. spacing was alternated with the 1 in. spacing near the leading edge to reduce thermal wake effects). A series of steady pressure taps are located on the opposite side of the model, 6 in. (15.2 cm) from the wind tunnel centerline. These taps are connected through a scanivalve to a Druck 15 psid (0.1 MPa) transducer, and are used to measure steady-state pressures and verify operation of the miniature transducers. Figure 7 shows a comparison between steady-state pressures measured with the the tap/scanivalve system and with the miniature transducers. Attached flow pressures at a Mach number of 0.2 and a pitch angle of 14 deg are shown in Fig. 7a; separated flow pressures at a pitch angle of 25 deg are shown in Fig. 7b. The results generally compare very well.

## DATA ACQUISITION

A schematic of the instrumentation and data acquisition system is shown in Fig. 8. The analog signals from the model-mounted instrumentation are first conditioned by a set of preamplifiers located immediately outside of the wind tunnel test section (the small chassis shown in Fig. 2). In the wind tunnel control room additional analog signal conditioning is performed by the 26 channel ATLAS (Aeromechanics Transient Logging and Analysis System). Each channel is programmed by the Perkin Elmer 3210 central processor to subtract a predetermined offset voltage, amplify the remainder, and pass the resultant through a low-pass filter (set at a corner frequency of 1 kHz for these tests). Twenty-six simultaneous sample-and-hold analog to digital converters (having a variable sampling frequency between 0.3 and 250 kHz) digitize the signals and store the results in local memories of 1024 samples each. The digital data is then transferred to the central computer memory. The signals sampled by this system include the 9 channels of pressure data (72 individual transducers), the 8 hot film gages, the pitch angles measured at both ends of the shaft, and the spar twist angle and bending strain, as measured by four-element strain gage bridges.

A separate data system is used to measure other parameters. These include the barometric pressure, dewpoint, wind tunnel temperature, total pressure, and the test section static pressure. The dynamic pressure derived from these readings is used to determine the test section centerline Mach number, accounting for compressibility and humidity effects. These readings are also digitized and sent to the central processor. A continuously updated display of the wind tunnel and model conditions is generated on a video terminal. Preset limits are used by the computer to warn the operators of potentially unsafe or out of range conditions.

## AIRFOIL MOTIONS

Two types of airfoil motions were used for this experiment: a sinusoidal oscillation and a constant pitch rate ramp. For the sinusoid, 1024 samples of data were taken over each period of the motion. Data acquisition was triggered by the pulse train generated by the angle synthesizer. For the up- (or down-) ramp motions the airfoil was initially held fixed at the minimum (or maximum) angle to allow conditions to stabilize, pitched up (or down) at a constant rate to the maximum (or minimum) angle, held there for approximately 1-2 seconds, and returned to the minimum (or maximum) angle. As shown in Fig. 9, the 1024 samples of data are acquired only during a portion,  $T$ , of this cycle.  $T$  is a function of the test conditions:

$$T = \Delta\alpha c / U A.$$

For a typical up-ramp, the airfoil remains stationary at its minimum angle until  $\tau = t/T = 0.125$ . The up-ramp occurs between  $\tau = 0.125$  and  $\tau = 0.625$ , and the pitch is then kept at the maximum value through  $\tau = 1.0$ . Therefore

512 samples are acquired during the up-ramp. Figure 10 shows the actual time histories of the wing angle of attack for a 0 to 30 deg ramp at  $M = 0.2$  for pitch rates of 18, 45, 90, 180, and 360 deg/sec (non-dimensional rates of  $A = 0.001, 0.0025, 0.005, 0.010, \text{ and } 0.020$ ). At the lower pitch rates the corners of the ramp are quite sharp, while the damping of the hydraulic system rounds the corners at the higher pitch rates. The most important characteristic of the ramp, the slope over the central portion of the motion, is still uniform for all cases. A second effect of the hydraulic response is to delay the airfoil motion behind the input waveform. A corrective time displacement has been imposed on all ramp time histories (and their associated responses) such that all ramps coincide during the constant slope region and extrapolate to  $\alpha = \alpha_{\min}$  at  $\tau = 0.125$ . Thus, stall events for all runs are directly comparable.

#### DATA PROCESSING AND CALIBRATION

For all cases studied, an ensemble average of the signals was formed from 20 cycles of the motion. The cycles were not consecutive because of the time required to transfer the data to the central processor and add it to the ensemble-averaging arrays. Also, the pressure data at each of the eight multiplexer switch positions must be taken separately (i.e. 20 data cycles are taken with all multiplexers set at position one, the multiplexers are switched to the next position, and the process repeated until data for all eight positions have been recorded). In addition to the ensemble average of each signal,  $\langle p \rangle$ , the ensemble average of the rms variation about  $\langle p \rangle$  is also computed:

$$\langle p \rangle(t) = \frac{1}{N} \sum_{i=1}^N p(t_i)$$

$$P_{\text{rms}}(t) = \sqrt{\frac{1}{N} \sum_{i=1}^N (p(t_i) - \langle p \rangle(t))^2}$$

This information is useful in determining how the degree of randomness in the signals (such as that caused by turbulence or separation) varies during the cycle. Both the ensemble average and the rms are stored on digital magnetic tape. For selected runs the unaveraged signals for all 20 cycles are also stored on tape. After data acquisition is complete for each test condition, the processed results may be displayed on video terminals or drawn on paper.

The data as stored on tape have already been converted to pressure coefficient:

$$C_p = (P - P_{\text{static}})/q$$

The transducers have been calibrated by placing the entire model into a pressure and temperature controlled chamber, connecting each transducer to the same channel of the signal conditioning and digitizing system used for the wind tunnel test, and recording the output voltages over the full range of pressures and temperatures expected. Typical least squares calibration curves for a single transducer at several temperatures are shown in Fig. 11. The primary thermal effect is a change in offset at the higher temperature. Calibration at several temperatures allows thermal shifts in the transducer sensitivity and offset to be automatically accounted for. Accurate mean pressures may therefore be obtained, as was demonstrated in Fig. 7. The estimated accuracy of the results is within  $\pm 1\%$  of the calibration range ( $-5$  to  $+1.5$  psid for this experiment). The hot film gages were not calibrated, and are used solely to determine the qualitative characteristics of the surface flow (laminar, transitional, turbulent, or separated).

#### TEST CONDITIONS

There are four basic parameters that characterize the experimental conditions: (M, Re, pitch rate, and pitch range). The majority of the data was taken at a Mach number of 0.2, with additional data being taken at Mach numbers of 0.3 and 0.4. These Mach numbers cover the range expected both for aircraft maneuvers at high angle of attack (Ref. 5), and helicopter blades on the retreating side of the rotor at high advance ratio (Ref. 14). The corresponding Reynolds numbers based upon airfoil chord were 2, 3 and 4 million, respectively. Since the chord of the model is very close to that of a helicopter main rotor, the Reynolds numbers will be correctly matched for this application at the appropriate Mach numbers. Typical fighter aircraft wings are of course larger, with chords (and therefore Reynolds numbers) between 5 and 20 times the values used here. Nevertheless, the Reynolds numbers of 2 to 4 million obtained are still at least an order of magnitude greater than those used by previous investigators of constant pitch-rate aerodynamics.

The airfoil angle of attack was limited by the part-span supports to values between  $-5$  and  $+30$  deg. This is adequate for modelling helicopter rotors (Ref. 14), but less than the maximum 60-70 deg pitch angle cited in Ref. 10. However, the results described below indicate that at the pitch rates used here, the majority of the aerodynamic changes occur below 30 deg angle of attack, with an aerodynamic response at higher angles similar to that expected for a flat plate at the same angle. Therefore this experiment can provide data at the pitch angles of greatest aerodynamic interest for the pitch rates studied.

Table 4 shows the test conditions studied for the two types of motion: the constant pitch-rate ramp and the sinusoid. Both positive and negative



pitch rate ramps were studied, at nondimensional pitch rates,  $A = \dot{\alpha} c/2U$ , between 0.001 and 0.02. For the maneuvers described in Ref. 5, pitch rates ranged from approximately 0.001 for a 'typical' maneuver to  $A = 0.0044$  for a 'minimum time' maneuver. For the sinusoidal oscillations data were taken at reduced frequencies,  $k = \omega c/2U$ , of 0.025, 0.050, and 0.100. These frequencies are characteristic of helicopter main rotor applications. In summary then, in terms of type of motion, angle of attack range, pitch rate (or reduced frequency), Mach number, and Reynolds number, this experiment provides data at conditions that either accurately model those on aircraft wings or helicopter rotors, or that are a better approximation than has been previously obtained in this type of test.

As indicated in Table 4, data from all sensors were not taken at all test points, in the interest of obtaining the most data possible during a limited test period. Pressure data were obtained along the primary array of transducers in all cases. An 's' in the table means that skin friction gage data and pressure data at the secondary arrays were also obtained. An 'r' indicates that unaveraged (i.e. "raw") data time histories were recorded for each of the 20 cycles of the motion, in addition to the ensemble averages and rms values.

## STEADY-STATE CHARACTERISTICS

Steady pressure distributions were measured at Mach numbers of 0.2 and 0.4. The pressures were integrated over the airfoil chord to determine the lift and drag force coefficients and the pitching moment coefficient about  $x/c = 0.25$  (positive nose up):

$$C_N = \frac{1}{qc} \int (P_{LO} - P_{UP}) dx$$

$$C_C = \frac{1}{qc} \int (P_{LO} - P_{UP}) \frac{dy}{dx} dx$$

$$C_M = \frac{1}{qc^2} \int (P_{LO} - P_{UP})(x - 0.25c) dx$$

$$C_L = C_N \cos \alpha - C_C \sin \alpha$$

$$C_D = C_C \cos \alpha + C_N \sin \alpha$$

No corrections were applied to account for wind tunnel wall effects. The force and moment coefficient curves are shown in Figs. 12a, b, and c. At  $M = 0.2$  the peak  $C_L$  of 1.42 occurs at 14 deg, followed by a steep drop in  $C_L$  and  $C_M$  between 14 and 17 deg. The lift curve then flattens out, before beginning to rise in the fully separated region above 22 deg. The drag curve (Fig. 12b) also increases rapidly during stall (14 to 17 deg), with a more gradual increase after stall. The primary effects of increasing the Mach number to 0.4 are to decrease the angle of maximum lift and of moment stall to 12 deg, and to decrease the maximum  $C_L$  to 1.19. Also, the lift coefficient is greater at  $M = 0.4$  in the fully stalled region.

Many of these integrated load features may be explained by examining the steady pressure coefficient distributions. Figures 13a and b show the pressures at  $\alpha = 0$  deg for  $M = 0.2$  and 0.4, respectively. There are few differences visible at this angle. This similarity is maintained at angles of 6 (Figs. 13c and d) and 9 deg (Figs. 13e and f). One notable feature is the appearance of a supersonic zone in Fig. 13f near the leading edge at  $M = 0.4$ . At this Mach number the critical pressure coefficient,  $C_{p^*}$ , is -3.66. At  $\alpha = 9$  deg, pressures are above  $C_{p^*}$  on the upper surface for the first 0.8% of

the chord. The supersonic zone grows to a maximum length of 2.5% of chord by  $\alpha = 11$  deg (Fig. 13g), and reaches a maximum local Mach number of 1.4. A shock occurs between 2.5 and 4% of chord, followed by a smooth subsonic recompression. The supersonic zone causes large differences between the leading edge characteristics at  $M = 0.4$  and at  $M = 0.2$  (Fig. 13g). At  $M = 0.2$   $C_{p^*}$  is -16.3, so that a very intense leading edge suction peak can develop and produce higher lift coefficients than at  $M = 0.4$  (Fig. 12a). Suction peak pressures at  $M = 0.2$  reach -8.2 at  $\alpha = 13$  deg (Fig. 13i), but remain at -5.2 at  $M = 0.4$  (Fig. 13j). Stall effects become more evident at  $\alpha = 15$  deg for both Mach numbers (Figs. 13k and l). The flow appears to remain attached at the leading edge, but separates over the rear 30% of chord at  $M = 0.2$  and over the rear 60% of chord at  $M = 0.4$ . At  $\alpha = 17$  deg the flow is fully separated at  $M = 0.2$  (Fig. 13m), but remains attached for the first 8% of chord at  $M = 0.4$  (Fig. 13n). The flow remains slightly supersonic in this region. At  $\alpha = 20$  deg the flow is always subsonic at  $M = 0.4$  (Fig. 13o), but still maintains a higher pressure gradient on the upper surface than at  $M = 0.2$  (Fig. 13p). This behavior explains the higher lift coefficients at  $M = 0.4$  than at  $M = 0.2$  for  $\alpha > 17$  deg.

## CHARACTERISTICS OF A 0 TO 30 DEG RAMP AT $M = 0.2$

### PRESSURE TIME HISTORIES

In order to illustrate the general characteristics of constant pitch rate motion at  $M = 0.2$ , the results for a 0 to 30 deg ramp at a pitch rate of  $A = 0.005$  will be discussed in detail. The ensemble averaged upper surface pressure distributions are shown in Fig. 14. The pressures at the nine stations ahead of  $x/c = 0.262$  are presented in Fig. 14a, while the pressures at the nine aft stations are presented in Fig. 14b. The pressures remain constant while the airfoil is held at 0 pitch (for  $0 < \tau < 1.25$ ), and then increase smoothly until the maximum suction is reached at  $\tau = 0.4$ , corresponding to  $\alpha = 15.5$  deg. The minimum pressure of  $C_p = -12.5$  occurs near the leading edge at  $x/c = 0.005$ . This is identified as letter A in Fig. 14a. The local Mach number reaches 0.84, a value well above the upper bound of incompressible aerodynamics. The suction at  $x/c = 0.005$  collapses rapidly when the stall vortex is released; the pressure reaches an approximately constant value of  $C_p = -1.3$  by  $\tau = 0.50$  ( $\alpha = 22$  deg). A similar response occurs at  $x/c = 0.026$  and  $0.060$  (also shown in Fig. 14a), but at lower levels of  $C_p$ . At locations further downstream on the upper surface the response is more complicated. The suction increases smoothly until approximately  $\tau = 0.4$ , when the passage of the stall vortex causes a rapid increase in suction (letter B in Figs. 14a and b). The peak pressure associated with the vortex propagates downstream at an average speed of 16% of the freestream velocity (the computation of this speed is discussed below), and reaches the trailing edge at  $\tau = 0.45$ . There is a rapidly damped secondary oscillation that follows the passage of the vortex (letter C in Fig. 14b), and then the pressures on the entire upper surface become relatively constant in both time and space. Increasing the pitch angle to 30 deg (at  $\tau = 0.625$ ) and holding it at this value does not produce any substantial changes in the upper surface pressures.

The lower surface pressures for this case naturally respond quite differently, as shown in Fig. 15. Near the leading edge at  $x/c = 0.005$ ,  $C_p$  has a value of  $-0.30$  at  $\alpha = 0$ , and increases parabolically as the stagnation point moves past this measurement station (stagnation occurs at  $x/c = 0.005$  at  $\tau = 0.22$ ). Once the stagnation point has passed, this station is effectively on the upper airfoil surface, and the pressure response is similar to that discussed above. The stagnation point moves to a maximum downstream position of  $x/c = 0.060$  at  $\tau = 0.40$ , and then retreats to  $x/c = 0.026$  following stall. Downstream of the stagnation point the lower surface pressures respond smoothly before stall, show a small transition period for  $0.42 < \tau < 0.44$ , and then resume responding to increases in the pitch angle until the motion ceases at  $\tau = 0.625$ . This contrasts with the upper surface pressures, which do not

respond to further pitch changes once stall is complete. A second difference between the upper and lower surface responses is the presence of small oscillations in the lower surface pressures over the rear 70% of chord (Fig. 15b). On the upper surface, such oscillations are significant in the ensemble averaged pressures only very close to the trailing edge (letter D in Fig. 14b). The oscillations at the various chordwise locations appear to be in phase and have a frequency of 62 Hz. For a circular cylinder having a Reynolds number,  $UD/\nu$ , less than about  $1 \times 10^6$ , a periodic von Karman vortex street has been observed at a Strouhal number,  $fD/U$ , equal to 0.21 (Ref. 17). The vortex street frequency for a bluff body with a projected area equivalent to this airfoil would be  $0.21U/(c \sin \alpha)$ . At  $M = 0.2$  and  $\alpha = 30$  deg this frequency is 65 Hz, a value very close to the observed frequency. The airfoil pressures therefore may be responding to the velocity potential field generated by a periodic vortex street downstream of the airfoil. This phenomenon will be discussed at greater length below.

Time histories of the difference pressure coefficient,  $\Delta C_p = C_{p, \text{lower}} - C_{p, \text{upper}}$ , are shown in Fig. 16. Near the leading edge ( $x/c < 0.1$ ) the difference pressures show characteristics similar to those of the upper surface: a nearly linear increase with pitch angle until  $\tau = 0.4$ , followed by a rapid stall with a strongly damped oscillation, and a constant pressure for  $\tau > 0.55$ . Over the rest of the chord, the difference pressures resemble the upper surface pressures before the stall vortex passes, and the lower surface pressures afterwards. The explanation is as follows: before stall the pressure changes on the upper surface are much larger than the variations on the lower surface; after stall the upper surface pressures are uniform in time and space, so that any changes in the difference pressures must originate on the lower surface, which remains unstalled. The difference pressures thus continue to change as pitch increases after stall, allowing the lift of the airfoil to also increase. Oscillations from the vortex street are observed in the difference pressure time histories near the trailing edge, indicating that the oscillations include flow angle changes in addition to pressure disturbances. (A disturbance caused solely by a propagating pressure wave would affect both surfaces in the same manner and therefore would disappear when the surface pressures are subtracted.)

#### FORCES AND MOMENT

The airloads obtained from integrating the pressure distributions are plotted in Fig. 17 versus time and pitch angle. The lift force (the force normal to the freestream velocity vector) shows a linear increase with time (Fig. 17a) and with angle (Fig. 17b) up to  $\tau = 0.30$  ( $\alpha = 12$  deg), with a slope of  $dC_L/d\alpha = 0.11/\text{deg}$ , slightly higher than the value for steady flow. After  $\tau = 0.30$  the lift slope remains positive but decreases slightly until the stall vortex forms at  $\tau = 0.40$ . The lift coefficient at this time is 1.7, 15%

larger than the maximum steady value. The presence of the stall vortex causes a sharp increase in the local lift slope to  $dC_L/d\alpha = 0.20$ . The maximum  $C_L$  of 2.0 is reached at  $\tau = 0.425$  ( $\alpha = 16.8$  deg), and is followed by a drop to a  $C_L$  of 1.0 at  $\tau = 0.5$  ( $\alpha = 22$  deg). The lift then begins to increase again as the lower surface continues to respond to angle of attack changes. The pressure drag force (Fig. 17c and d) increases smoothly before  $\tau = 0.4$ , jumps rapidly from  $C_D = 0.15$  to 0.52 when the stall vortex forms, and then increases again as the airfoil motion rotates the aerodynamic force vector towards the wind axis. Note that Figs. 17c and d do not include the viscous drag component, which will add a positive increment to the drag at all times. The relative importance of the viscous drag will be much greater at the lower pitch angles, and is not likely to significantly change the results after  $\tau = 0.4$ . The pitching moment coefficient (Figs. 17e and f) starts at a constant value near 0 at  $\alpha = 0$  and decreases to -0.008 during the initial unstalled pitching motion. This offset may be predicted by unsteady thin airfoil theory (Appendix B and Ref. 18). The pitching moment begins to increase again as the stall vortex forms near the leading edge, and then drops precipitously to  $C_M = -0.3$  as the vortex travels to the trailing edge. The oscillations from the vortex street are particularly noticeable in the pitching moment after a pitch angle of 30 deg has been reached.

#### INDIVIDUAL CYCLE RESULTS

The results presented so far have been based upon the ensemble average of 20 cycles of the motion. Examination of the time histories for some of the individual unaveraged data records will help explain the separation process and the vortex street-induced oscillations. Figure 18a shows some of these results for the upper surface pressure at  $x/c = 0.005$ . The top curve is the ensemble average (also shown in Fig. 14a); the scale on the left refers to this curve. The lower curves are individual records, each shifted down by a  $C_p$  of 5 for clarity. Prior to flow separation the curves are almost identical. During separation ( $0.40 < \tau < 0.50$ ) the individual pressure time histories vary significantly. For two of the records separation is essentially complete by  $\tau = 0.42$ , while for the others the flow appears to partially reattach at about  $\tau = 0.45$  before separating fully at  $\tau = 0.50$ . In all cases, once separation is complete the pressures are relatively uniform. The oscillation resulting from the vortex street is seen for some of the individual records, but it is relatively small at this scale and is not visible in the ensemble average. The oscillation is more easily seen at  $x/c = 0.262$ , in Fig. 18b. The ensemble average at the top shows a much smaller amplitude oscillation than do the individual records. This implies that at this location these oscillations are not well correlated in time. This contrasts with the sharp peak from the stall vortex, which occurs at about the same time and with the same amplitude during each record. At  $x/c = 0.950$ , the peak-to-peak amplitude of the 62 Hz oscillations has

increased to a maximum of  $C_p = 0.5$  (Fig. 18c), but because there is a phase difference from one record to the next, the oscillations do not appear in the ensemble average. The signature of the stall vortex has also become quite irregular at  $x/c = 0.950$ , indicating that random effects can change the vortex propagation velocity and the rate at which it dissipates. These irregularities are significant only for  $x/c > 0.85$ . Figure 18c also shows that the pressures at  $x/c = 0.950$  have significant random variations even before stall. This implies that there is a thick and energetic turbulent boundary layer on the rear of this airfoil.

Results for individual records on the airfoil lower surface are shown in Fig. 19. At  $x/c = 0.060$  (Fig. 19a) the pressure time histories are quite repeatable with the exception of the post-stall oscillations, which again are only modestly correlated in phase. The step effect seen in the attached flow pressures results from the analog-to-digital converter and indicates that the amplifier gain was not set high enough for this particular transducer. This does not affect the overall character of the results. The time histories at all stations on the lower surface show similar behavior, as illustrated by the additional results at  $x/c = 0.464$  (Fig. 19b) and  $x/c = 0.950$  (Fig. 19c). In all cases there is considerable variation in the phase of the oscillation, but there is sufficient correlation for a portion of the oscillation to appear in the ensemble average, particularly at the rear of the airfoil. This supports the belief that the oscillations are the result of a trailing edge vortex street. If they resulted from periodic shedding at the leading edge separation point, they would be best correlated in phase on the forward upper surface, near their point of origin. (This is in fact what is observed for the pressure pulse resulting from the primary stall vortex.)

#### ROOT-MEAN-SQUARE PRESSURE

A quantitative measure of the degree of randomness in the pressures is provided by the rms variation about the ensemble average. Figure 20 shows the time histories of the rms for the upper surface pressures. The curve for each chordwise position starts at a value of 0, and is scaled in terms of  $C_p$ . For example, the top curve in Fig. 20a is for  $x/c = 0.005$ , and starts at  $C_{p,rms} = 0$  and has a maximum of about  $C_{p,rms} = 2$ . Each successive curve is offset down for clarity. The rms time histories have maximum values for  $0.4 < \tau < 0.5$ , the period when separation is in progress. Downstream of the stall vortex release point ( $x/c = 0.1$ ) the rms has a peak that corresponds to the irregularity in the pressure response to the vortex (letter A in Fig. 20a). For stations closer to the rear of the airfoil (Fig. 20b) this peak is preceded by a gradual increase between the time of initial separation at the leading edge (at  $\tau = 0.40$ ) and the time that the vortex passes each station (letter B in Fig. 20b). This means that pressure disturbances from separation at the leading edge reach the downstream stations well before the

stall vortex itself passes. Near the trailing edge ( $x/c > 0.80$ ) the rms response to the vortex is less highly peaked since the vortex arrival time is somewhat irregular. Also, the phase variations in the 62 Hz vortex street oscillations cause an increase in the rms at these stations for  $t > 0.7$ .

The rms time histories on the lower airfoil surface generally have much lower amplitudes, as shown in Figs. 21a and b. As previously noted with the ensemble average (Fig. 15a), the station at  $x/c = 0.005$  is usually ahead of the stagnation point and therefore responds like an upper surface station. For other lower surface stations ahead of  $x/c = 0.7$  there are only two times of non-zero rms: during separation and during the 62 Hz oscillation. Even during these periods the rms amplitude is quite small, approximately  $C_{p,rms} = 0.03$ . The rms is somewhat larger near the trailing edge, where the vortex street effects are strongest.

#### HOT FILM GAGE RESULTS

Further information on the nature of the flow for this case was obtained using the surface hot film gages. Figure 22 shows the ensemble averaged results. The output of each gage has been self-scaled so that the difference between the maximum and minimum is one unit. For the two stations closest to the leading edge ( $x/c = 0.026$  and  $0.060$ ) the airfoil boundary layer is originally laminar and becomes turbulent as the pitch angle increases. This is shown by the relatively low initial values of heat transfer, the gradual decrease in heat transfer as the laminar boundary layer begins to thicken (which provides more thermal insulation), and the sharp increase in heat transfer when the boundary layer becomes turbulent (letter A in Fig. 22). Transition occurs at  $\tau = 0.241$  ( $\alpha = 7.0$  deg) at  $x/c = 0.060$ , and at  $\tau = 0.254$  ( $\alpha = 7.7$  deg) at  $x/c = 0.026$ . The hot film gage at  $x/c = 0.103$  was not functioning for this run, but for all similar runs it indicated turbulent flow at all times. Therefore the transition point was located between  $x/c = 0.060$  and  $0.103$  for  $\alpha < 7$  deg, moved forward from  $x/c = 0.060$  to  $x/c = 0.026$  as  $\alpha$  increased from 7 to 8 deg, and remained ahead of  $x/c = 0.026$  for the remainder of the cycle. Further downstream at  $x/c = 0.192$  and  $0.302$ , the heat transfer responds to pitch increases by first increasing slightly and then decreasing more rapidly. This may be explained by noting that there are two ways in which the airfoil pitch affects the heat transfer: the velocity outside of the boundary layer increases, and the boundary layer thickness increases. The first effect increases the heat transfer while the second decreases it. Further, movement of the transition point changes the length of turbulent boundary layer that precedes each station on the chord. This also changes the boundary layer thickness. It seems that ahead of  $x/c = 0.10$ , the heat transfer increases with pitch angle when there is an attached turbulent boundary layer ( $0.25 < \tau < 0.35$ ), implying that the increase in velocity outside of the boundary layer dominates. Between  $x/c = 0.10$  and  $0.30$ , the



increase in velocity outside the boundary layer initially dominates, but after  $\tau = 0.25$  the transition point has moved very close to the leading edge and the boundary layer thickness effect dominates. At the rear of the airfoil ( $x/c = 0.682$  and  $0.880$ ) the boundary layer is always turbulent and the heat transfer in attached flow always decreases.

Separation as indicated by the hot film gages (letters B and C in Fig. 22) correlates very well in time with separation as indicated by the adjacent pressure transducers (Fig. 14). In the region upstream of the stall vortex release point ( $x/c = 0.1$ ), separation is marked by a rapid drop in the ensemble averaged heat transfer (letter B in Fig. 22), because the separated flow has a small mean velocity and hence little convection. Downstream of the stall vortex shedding point, separation is marked by an increase in heat transfer as the vortex passes (letter C in Fig. 22), because the vortex temporarily increases the mixing of the flow and therefore increases the heat transfer. Following passage of the stall vortex, the heat transfer drops gradually. In the vicinity of the last hot film gage (at  $x/c = 0.880$ ) the heat transfer following separation remains at a relatively high level. This may be because the periodic vortex shedding introduces a substantial amount of additional mixing into the flow near the trailing edge.

The rms hot film gage results are shown in Fig. 23. They have been normalized by applying the same factors used for the ensemble averages of Fig. 22. Therefore the units of the two figures are the same. The vertical shift of each rms curve is arbitrary. The small variation in the time of transition is shown by the blips in the rms curves for  $x/c = 0.026$  and  $0.060$  (letter A in Fig. 23). As with the pressures, the random variations in the separation process creates a high rms between  $\tau = 0.40$  and  $0.50$ . At the rear of the airfoil the rms remains high, lending support to the idea that the increased ensemble averaged heat transfer is a result of vortex street induced velocities that vary in phase.

Individual records of the hot film gage output are shown in Fig. 24. As before, the top curve is the ensemble average and all curves have been self-scaled so that the maximum minus the minimum is equal to 1.0. The most interesting feature at  $x/c = 0.026$  (Fig. 24a) is the momentary reattachment that occurs near  $\tau = 0.45$ , which raises the heat transfer almost back to the previous levels (letter A in Fig. 24a). At  $x/c = 0.302$  (Fig. 24b) the heat transfer has an initial random component from the turbulence which is not present in the laminar flow of Fig. 24a. The output during and after separation varies considerably from record to record, in agreement with the large observed rms (Fig. 23). Closer to the trailing edge, at  $x/c = 0.880$  (Fig. 24c), the individual records have a very rough appearance after stall, but much of the variation occurs at the vortex street frequency of 62 Hz.

This supports the contention that it is the vortex street that induces mixing and increases the ensemble averaged heat transfer near the trailing edge.

Appendix C describes a new method that has been developed to determine the unsteady motion of the transition point from the rms pressures. This technique may allow this information to be obtained much more easily in complex unsteady or three-dimensional flows, and will be of particular utility when pressure transducers are the primary instrumentation.

## THE EFFECT OF PITCH RATE AT $M = 0.2$

### FORCES AND MOMENT

Pitch rate effects were studied for 0 to 30 deg ramps at  $M = 0.2$  by taking data at  $A = 0.0010, 0.0025, 0.0050, 0.0100, \text{ and } 0.0200$ . The integrated forces and moment will be discussed first. Curves of the lift, pitching moment, and drag coefficients versus time and pitch angle are shown in Fig. 25. Before stall, increasing pitch rate decreases the lift slope, decreases the pitching moment, and increases the drag. The decrease in lift slope with  $A$  is in agreement with trends predicted and observed by Jumper (Ref. 9). During stall, increasing the pitch rate delays the formation of the stall vortex, increases the peak values attained by  $C_L$ ,  $C_D$ , and  $C_M$ , and delays the completion of stall (defined as when  $C_L$ ,  $C_D$ , and  $C_M$  have reached stable values). After stall, increasing the pitch rate increases the amplitude and the relative period (with respect to  $\alpha$  and  $\tau$ ) of the vortex street oscillations. As shown in Fig. 26, the increase in the unsteady increment to  $C_L$ ,  $C_M$ , and  $C_D$  has an approximately linear dependence on  $A$ . This observation agrees with the low pitch rate portion of the data of Francis and Keese (Ref. 11).

Several events that characterize the stall process are identified in the several parts of Fig. 25: 1) the beginning of the rise in  $C_L$  and  $C_D$ , and of the fall in  $C_M$  are related to the formation of the stall vortex; 2) the maximum  $C_L$  occurs when the vortex is at a position over the chord where it induces maximum suction over the entire surface; and 3) the peaks in  $C_M$  and  $C_D$  occur when the vortex is close to the trailing edge. Figure 27 shows how these events vary with pitch rate and how they relate to one another. For constant pitch-rate motion, the  $\alpha$  ordinate is equivalent to time, and a sequence of events emerges at any constant value of  $A$ . First,  $C_L$  and  $C_D$  begin to rise sharply as the stall vortex begins to form. The ' $C_M$  stall' then occurs as the vortex is released and  $C_M$  begins to drop rapidly. The maximum in  $C_L$  occurs next, followed by the maximum in  $C_D$  and the minimum in  $C_M$ . Both the angle of initiation of this sequence and the spread in angle between the various events increase as pitch rate increases. For the values of pitch rate studied here, the angle of moment stall increases linearly with pitch rate. This agrees with the earlier results for sinusoidal oscillations of a NACA 0012 airfoil (Ref. 16), but does not agree with the predictions of Gormont (Ref. 19), or the high pitch rate data of Strickland and Graham (Ref. 20). Gormont's correlation states that the delay in the moment stall is proportional to the square root of the pitch rate. Figure 28 presents the various stall events identified here as functions of  $\sqrt{A}$ , together with Gormont's correlation as modified in Ref. 20. A linear fit to the  $C_M$  stall results is plausible; however the slope is reduced as compared to the correlation, and there is an offset of approximately two degrees at  $\sqrt{A} = 0$ . These

differences with the correlation are similar to those found in Refs. 15 and 16, and suggest that the constants used in the correlation need to be modified for this application and that the square root dependence does not apply for very low pitch rates, below  $A = 0.002$ . The other stall events shown in Fig. 28 do not show any linear dependence on the square root of pitch rate. The difference between the angles of  $C_M$  stall and of minimum  $C_M$  does, however, show an acceptable linear fit to the square root of pitch rate, as shown in Fig. 29. If the peak  $C_M$  is assumed to occur when the stall vortex passes the trailing edge, this implies that the vortex travels along the airfoil chord at a faster speed ( $V$ ) at higher pitch rates. A vortex propagation speed with respect to the freestream velocity that does not change with pitch rate would produce a linear dependence of the angle difference on pitch rate. The increase in vortex speed with  $A$  agrees with the wave speed results of Refs. 15 and 16. Vortex propagation speeds will be discussed further below in connection with the pressure time histories.

#### UPPER SURFACE PRESSURES

The time histories of the ensemble averaged pressures also differ significantly at different pitch rates. Figures 30a through e show the upper surface pressures at 11 of the 18 stations for the five pitch rates. The ordinate scale on the lower left refers absolutely to the curve for  $x/c = 0.005$ . For clarity, each successive curve is offset vertically by  $\Delta C_p = 1.0$ , and each curve is referenced to its own origin, as indicated by the upper left scale. Before stall, there are few qualitative differences in the pressures at different pitch rates. For example, the peak suction pressure coefficient remains between -12.5 and -13.8. The largest differences between the cases at different pitch rates occur while the vortex is forming and travelling along the chord. At all pitch rates the pressure signature of the vortex (letter B in each part of Fig. 30) is not well defined for  $x/c < 0.149$ , implying that the vortex is formed ahead of this position. At low pitch rates the pressures at  $x/c < 0.15$  become very erratic after the vortex has been released. For some of the individual records (not shown here) a pressure gradient is maintained in this region until about  $t = 0.50$ , while for other records the separation is completed rapidly and the pressures become approximately constant in space. This randomness in the individual records is reflected in the ensemble averages of Fig. 30 as pressures with value midway between the two extreme possibilities (letter A in Figs. 30a, b, and c). This behavior occurs over a shorter period of time at higher pitch rates, and disappears completely for  $A = 0.010$  and  $A = 0.020$  (Figs. 30d and e). It is possible that the more energetic stall vortex formed at the higher pitch rates is able to purge any leading edge flow irregularities more effectively.

The unsteady increment to the airloads is directly related to the strength of the stall vortex and to the speed with which it propagates.

Variations in vortex strength may be estimated from the change in pressure induced by the passage of the vortex. At  $x/c = 0.302$  this increment rises from  $\Delta C_p = 1.0$  at  $A = 0.001$  to 1.5 at  $A = 0.005$  and to 2.5 at  $A = 0.020$  (letter B in Figs. 30a-e). The speed with which the vortex travels along the chord may be estimated based on the times of minimum  $C_p$ . Figure 31 shows the times of minimum  $C_p$  at each station for the five pitch rates. The linear region of the data generally begins downstream of the vortex release point near  $x/c = 0.1$  and ends ahead of the trailing edge, where the vortex behavior becomes less well defined. The speed of travel of the vortex ( $V = dx/dt$ ) in the linear region ( $0.15 < x/c < 0.90$ ) increases approximately linearly with pitch rate, from approximately  $0.13U$  at  $A = 0.001$  to  $0.33U$  at  $A = 0.020$ , as shown in Fig. 32. These results agree with the measurements on the aft 85% of the chord reported in Ref. 16. In this experiment different disturbance wave speeds were found for regions ahead of and behind  $x/c = 0.15$ . It is proposed here that the forward region in both experiments is associated with the formation of the vortex, and the aft region associated with the propagation of the vortex along the chord.

The vortex propagation speeds computed here are with respect to the airfoil chord. These speeds may be converted to the fixed wind axis system if the path of the vortex is prescribed. The simplest path would be horizontal convection downstream from the vortex release point. If the increase in pressure on the airfoil chord is assumed to occur when the distance from the vortex to the pressure transducer is a minimum, then, as discussed in Appendix D, the velocities are related by:

$$\frac{V}{U} = \frac{V_W}{U} \cos \alpha - 2A \left( \frac{x}{c} \tan \alpha + \frac{h}{c} \sec \alpha \right)$$

where  $h$  is the height of the vortex path above the airfoil pivot point. The magnitude of the term proportional to pitch rate is very small, and contributes a change of less than  $0.02U$  at any condition tested here. Therefore if the speed and path in the wind axis system do not change with pitch rate, the speed along the chord should change only slightly with pitch rate. This does not agree with the results in Fig. 32, and implies that either the vortex convection speed in the wind axis changes with pitch rate or that the vortex path changes.

A change in the vortex path is likely since the velocity at the vortex position is altered by the presence of the airfoil. One component of the induced velocity is a downwash from the rotation, and is approximately

$$W = 2\pi(x - 0.25) \frac{d\alpha}{dt}$$

Additionally, the velocity at the vortex is affected by the details of the unsteady flow about the airfoil. Flow visualization or accurate computational modelling is required to determine the actual path of the vortex.

Once the vortex has cleared the trailing edge and a stable pressure distribution has become established on the upper surface, there is still a strong pitch rate dependence. At pitch rates of  $A = 0.005$  and higher, the upper surface pressures are quite uniform in space, while at lower pitch rates a pressure gradient is maintained along the surface (Fig. 30). The rapid passage of the more energetic stall vortex found at higher pitch rates may cause the airfoil to experience massive separation at pitch angles of 30 deg or less, while the weaker disturbance found at lower pitch rates may be insufficient. The oscillations induced by the vortex street also change character with pitch rate. For pitch rates of  $A = 0.01$  or less, the oscillations have a frequency between 59 and 62 Hz and do not occur with the same phase at each individual record of the motion (Figs. 18 and 19). Therefore there are only small oscillations in the ensemble averaged pressures shown in Fig. 30a-e. At the highest pitch rate,  $A = 0.020$ , the oscillations have shifted frequency to 51 Hz and appear to have synchronized with the imposed airfoil motion, producing the large response shown as letter C in Fig. 30e. Large oscillations have been observed previously by Jumper, et al. (Ref. 9) at similar nondimensional pitch rates. Their work was performed on a thicker, NACA 0015 airfoil at Reynolds numbers between 150,000 and 280,000 and Mach numbers below 0.05. Other studies performed under similar conditions did not report such large oscillations (Refs. 11 and 12). It is thus unclear what conditions are necessary to produce strong, synchronized oscillations.

#### TRANSITION AND SEPARATION

Ensemble averaged hot film gage results for pitch rates of  $A = 0.001$  and 0.02 are shown in Fig. 33. The equivalent results for  $A = 0.0050$  were given in Fig. 22. The qualitative features of the time histories do not change with pitch rate, with the exception of the large periodic response at  $x/c = 0.682$  and 0.880 for  $A = 0.02$  (Fig. 33b). This response is approximately 180 deg out of phase with the pressures measured at the same stations (Fig. 30e). Bernoulli's equation for quasi-steady incompressible flow states that the pressures and the velocities at the boundary later edge should have such a phase difference; the heat transfer and skin friction are therefore in phase with the periodic velocity induced by the vortex street at these stations.

Increasing pitch rate delays the angle at which the transition point moves forward past stations near the leading edge and delays the start of boundary layer separation, as shown below:

	$\alpha$ at: Transition		Separation
	$x/c = 0.060$	$0.026$	$0.026$
$A = 0.001$	$6.4^\circ$	$7.1^\circ$	$14.3^\circ$
$A = 0.005$	$7.0$	$7.7$	$15.9$
$A = 0.020$	$8.5$	$9.4$	$19.3$

The pressure results discussed earlier show the presence of a interval immediately after stall when the pressures upstream of  $x/c = 0.15$  are erratic and show little correlation between individual records. This region is also observed in the hot film time histories. The relatively high velocities caused by separation and partial reattachment create an irregular response in the hot film gages at an overall level that is higher than that in fully separated flow but less than that with an attached turbulent boundary layer. At  $A = 0.001$  this interval lasts for  $0.15 \tau$ , while at  $A = 0.005$  it lasts for  $0.08 \tau$ , and at  $A = 0.02$  for only  $0.05 \tau$ . This reduction in the interval of irregular flow at higher pitch rates agrees with the pressure results.

## RESULTS AT HIGHER MACH NUMBERS

### PRESSURE TIME HISTORIES AT $M = 0.4$

The effects of Mach number were investigated by obtaining data at  $M = 0.4$  for a series of 0 to 20 deg ramps at pitch rates,  $A$ , equal to 0.001, 0.0025, 0.0050, and 0.010. Reducing the maximum pitch angle to 20 deg lowers the structural loads at the higher Mach number. The motion remains comparable to the 0 to 30 deg ramps at  $M = 0.2$  because the reduction in stall angle at  $M = 0.4$  allows the stall process to be completed at pitch angles less than 20 deg. The most significant change at  $M = 0.4$  is the presence of the supersonic zone ( $C_p < -3.65$ ) at the airfoil leading edge, as shown in Fig. 13 for steady conditions. Time histories of the upper surface pressure coefficient at  $A = 0.005$  (Fig. 34) show that the flow is supersonic ahead of  $x/c = 0.005$  for  $0.34 < \tau < 0.57$  ( $7.6 < \alpha < 16.8$  deg), and that the supersonic zone expands to include  $x/c = 0.026$  for  $0.40 < \tau < 0.46$  ( $9.9 < \alpha < 13.1$  deg). A peak local Mach number of 1.36 is reached at  $x/c = 0.026$  at  $\tau = 0.45$  ( $\alpha = 10.6$  deg). The shock therefore occurs between  $x/c = 0.005$  and  $x/c = 0.026$  for  $0.34 < \tau < 0.40$ , moves to between  $x/c = 0.026$  and  $x/c = 0.060$  for  $0.40 < \tau < 0.46$ , and returns to between  $x/c = 0.005$  and  $x/c = 0.026$  for  $0.46 < \tau < 0.57$ . The flow at  $x/c = 0.005$  separates while still supersonic at  $\tau = 0.48$  ( $\alpha = 13.1$  deg), and after becoming subsonic at  $\tau = 0.57$ , remains at a relatively high Mach number (0.8) for the rest of the cycle. A distinct stall vortex is released at  $x/c = 0.060$  (letter A in Fig. 34), just downstream of the shock, and moves towards the trailing edge at about 14% of the freestream velocity. The vortex release point is forward of that for  $M = 0.2$  ( $x/c = 0.1$ ) and the vortex speed is about 10% less. A reduction in vortex speed with Mach number was also noted in Ref. 16. The effects of the vortex are not seen in the pressure time histories for  $x/c > 0.57$  at  $M = 0.4$ , in contrast to the results for  $M = 0.2$ , where the vortex could be observed back to  $x/c = 0.88$ . In addition, no clearly defined oscillations are present after stall at  $M = 0.4$ . These effects may be related since both involve the behavior of vortices near the airfoil trailing edge. No data for individual cycles was obtained at  $M = 0.4$ , so that it can not be determined whether non-synchronous oscillations are present. Further study is required, but it appears that the differences in the vortex behavior between  $M = 0.2$  and  $M = 0.4$  are significant.

The lower surface and difference pressure time histories for the 0 to 20 deg. ramp at  $M = 0.4$  and  $A = 0.005$  are shown in Fig. 35. The lower surface pressures (Fig. 35a) are qualitatively similar to the results at  $M = 0.2$  (Fig. 15), in terms of the stagnation point position (between  $x/c = 0.005$  and 0.026) and the flow remaining unstalled and continuing to respond to pitch angle changes throughout the cycle. The difference pressure time histories (Fig. 35b) show the influence of the leading edge supersonic zone and the



motion of the stall vortex, but are otherwise unsurprising. Dadone (Ref. 4) measured airfoil difference pressures during moderate amplitude sinusoidal oscillations at Mach numbers between 0.2 and 0.7. Shock effects were not observed until  $M = 0.6$ , and the time histories do not show the rapid variations of Fig. 35. This may be a result of the different type of motion (sinusoid rather than ramp) or, more likely, to the different airfoil (NLR 7223-62 rather than SSC-A09).

#### HOT FILM GAGE RESULTS

Figure 36 shows the ensemble averaged and rms hot film gage results at  $M = 0.4$  and  $A = 0.001$ . The point of transition to turbulence (letter A in Fig. 36a) is advanced slightly on the airfoil at  $M = 0.4$  as compared to the results for  $M = 0.2$ . The transition point is again located between  $x/c = 0.060$  and  $x/c = 0.103$  for low angles of attack. It moves forward past  $x/c = 0.060$  at a pitch angle of  $6.7^\circ$  at  $M = 0.4$  rather than at  $6.4^\circ$  at  $M = 0.2$  for the same pitch rate (Fig. 33). Motion past  $x/c = 0.026$  is also advanced, from  $\alpha = 7.0^\circ$  at  $M = 0.2$  to  $\alpha = 6.8^\circ$  at  $M = 0.4$ . These small changes are encouraging, since they imply that the Reynolds number change that accompanies the change in Mach number is not significantly altering the transition characteristics. The lessened sensitivity to Reynolds number changes is one advantage of operating at Reynolds numbers above 2 million. It is generally more difficult to separate out Mach and Reynolds number effects for Reynolds number of about 500,000 or less because of the large changes in the transition location that occur as the air velocity is changed. The only major qualitative change in the hot film gage time histories between  $M = 0.2$  and  $M = 0.4$  occurs between transition and separation at  $x/c = 0.026$  (letter B in Fig. 36a). This is a consequence of the supersonic zone at  $M = 0.4$ . The measured heat transfer drops rapidly when the flow becomes supersonic at  $\tau = 0.40$  and increases after the shock has moved forward again at  $\tau = 0.46$ . Several factors cause the heat transfer to decrease at higher local Mach numbers (Ref. 21): the temperature in the boundary layer rises, the boundary layer thickens because of a reduction in density near the wall, and the viscosity decreases and causes the skin friction to decrease and the viscous sublayer to thicken. The variation from cycle to cycle in the location of the supersonic zone is indicated by the spikes in the rms hot film output at  $x/c = 0.026$  shown as letter A in Fig. 36b. Similar spikes at letter B indicate transition to turbulence. Aside from the effects of the supersonic zone, the hot film response shows only minor effects of the change in Mach number.

#### PITCH RATE EFFECTS

The effect of changes in pitch rate on the upper surface pressures at  $M = 0.4$  are shown in Fig. 37. Each successive curve in the figure is offset by  $C_p = 0.5$  and referenced to its own origin. The noise that is superimposed

on the pressures in the attached flow regions on some of these curves (particularly Fig. 37b) is a result of several weak electrical connections and is not of aerodynamic origin. The connections were repaired after these runs were made. The primary information contained in the results was not affected by this noise. The trends of the data are similar to those observed at  $M = 0.2$ . The peak suction pressure changes only slightly with pitch rate. The supersonic zone occupies approximately the same region in dimensionless time ( $\tau$ ) and space. The beginning of stall and the release of the stall vortex are delayed at higher pitch rates, from  $\tau = 0.45$  and  $0.46$  at  $A = 0.001$  to  $\tau = 0.48$  and  $0.49$  at  $A = 0.01$ . The speed of vortex propagation increases with pitch rate, from 10% of the freestream velocity at  $A = 0.001$  to 20% at  $A = 0.01$ . Since the vortex is not as well defined at  $M = 0.4$  and since its influence vanishes well before the trailing edge, the uncertainty of the vortex speed measurements is greater than at  $M = 0.2$ . The increased irregularity is apparent when the plot of the times of minimum  $C_p$  at  $M = 0.4$  (Fig. 38) is compared with the similar plot for  $M = 0.2$  (Fig. 31). The only evidence of periodic oscillations after stall is at the highest pitch rate,  $A = 0.01$  (Fig. 37d). Even here the amplitude is not as strong as at the same dimensional pitch rate (360 deg/sec) at  $M = 0.2$  (Fig. 30d).

#### FORCES AND MOMENT

The integrated airfoil force and moment coefficients at  $M = 0.4$  are very different at from those at  $M = 0.2$ . Figure 39 shows  $C_L$ ,  $C_M$ , and  $C_D$  data for three 0 to 20 deg ramps at  $M = 0.4$ , plotted versus time and pitch angle. At the lowest pitch rate,  $A = 0.001$ , the lift (Figs. 39a and b) increases smoothly until a pitch angle of 10 deg, and then levels off at a lift coefficient approximately 0.09 higher than the steady value. The lift then declines slowly and steadily for the remainder of the cycle. At the higher pitch rate of 0.0050 there is a small overshoot of 0.10 in  $C_L$  and a delay in the pitch angle for maximum lift of 1.1 deg. At the highest pitch rate,  $A = 0.01$ , the overshoot and delay are substantially greater:  $\Delta C_L = 0.43$  and  $\Delta \alpha = 3.2$  deg. In all cases the lift approaches a common value before the motion ceases and maintains a steady decline thereafter. The pitching moment (Figs. 39c and d) maintains a constant value during the initial period of pitch-up in attached flow, as was observed at  $M = 0.2$  (Fig. 25e and Appendix B). The moment at  $M = 0.4$  increases immediately before stall, possibly because of the interaction between the supersonic zone and the stall vortex. An increase of  $\Delta C_M = 0.02$  is observed between  $\alpha = 9$  and 12 deg at  $A = 0.001$ , and of  $\Delta C_M = 0.01$  between  $\alpha = 11$  and 14 deg at  $A = 0.01$ . The moment becomes negative when the vortex is released at stall. The drop is neither as sharp or as large as at  $M = 0.2$ . The minimum  $C_M$  at  $A = 0.01$  is  $-0.19$  at  $M = 0.4$  and  $-0.36$  at  $M = 0.2$ . After the stall vortex has passed the trailing edge ( $\tau = 0.47$ ) and the sharp drop in  $C_M$  is complete,  $C_M$  continues to become more negative as long as the airfoil continues to pitch up. When the pitching

motion ceases, the pitch rate settles out at a constant value. This differs from the response at  $M = 0.2$  (Fig. 25e), where  $C_M$  undergoes a damped oscillation and then maintains a relatively constant level. This change is possibly a result of the lack of a strong vortical response near the trailing edge region at the higher Mach number. The drag (Figs. 39e and f) shows behavior similar to that of the lift and moment: a region of rapid increase during stall followed by a region where the response directly tracks the pitching motion. In all cases the force and moment responses become independent of pitch rate once the stall vortex has cleared the airfoil. Figure 40 summarizes the variation of these stall events with pitch rate, and may be compared with Fig. 27 for  $M = 0.2$ .

#### RESULTS AT $M = 0.3$

Additional data on the effect of Mach number was obtained at  $M = 0.3$  for a 0 to 20 deg ramp at  $A = 0.005$  and for a 0 to 30 deg ramp at  $A = 0.010$ . The upper surface pressure time histories are shown in Fig. 41. Each successive curve is shifted down by  $C_p = 1.0$ . The pressures for the  $A = 0.005$ , 0 to 20 deg ramp (Fig. 41a) differ significantly from the results at this pitch rate at  $M = 0.2$  (Fig. 14a and b) and at  $M = 0.4$  (Fig. 37c). There is no significant peak in the curves that can be identified with the stall vortex, but there are very large amplitude periodic oscillations over the entire surface after stall. The frequency of the oscillations is 36 Hz, much lower than the 51 to 61 Hz oscillations at  $M = 0.2$ , and also much lower than the von Karman vortex street frequency of 68 Hz for an equivalent bluff body. There is some uncertainty about what frequency to predict for the vortex street, since Ref. 17 reports that for a circular cylinder a regular vortex street exists with a Strouhal number of 0.21 only if the Reynolds number is 1 million or less. The vortex street is not re-established until a Reynolds number of 3 to 4 million is reached, and has a higher Strouhal number, 0.27. Compressibility effects may change these values. For the present experiment the equivalent bluff body Reynolds number based on the projection of the chord normal to the freestream velocity was 1 million at both  $M = 0.2$ ,  $\alpha = 30$  deg and at  $M = 0.3$ ,  $\alpha = 20$  deg. It was 1.4 million at  $M = 0.3$ ,  $\alpha = 30$  deg and at  $M = 0.4$ ,  $\alpha = 20$  deg. These values are all apparently in the transitional range, so that it is not surprising that large variations exist between cases. This variation is apparent when Figs. 41a and 41b for the two  $M = 0.3$  cases are compared. The upper surface pressures for a 0 to 30 deg ramp at  $A = 0.01$  (Fig. 41b) do not have the persistent oscillation of the 0 to 20 deg ramp (Fig. 41a). Instead there is a well-defined stall vortex followed by a single secondary oscillation. The major difference between the two cases is the 40% increase in the equivalent bluff body Reynolds number to 1.4 million for the case with the 30 deg maximum pitch angle. This implies that for this particular configuration, the vortex street effects are at their peak when the equivalent bluff body Reynolds number reaches one million and nearly disappear when this Reynolds

number has reached 1.4 million. Data for additional cases for several equivalent bluff body Reynolds numbers is required to verify that this parameter and not the Mach number or chord Reynolds number is the determinant for the vortex street oscillations.

One final illustration of the effects of Mach number on the integrated section parameters is given in Fig. 42. This figure shows the lift, drag, and pitching moment curves for a 0 to 20 deg ramp at  $A = 0.005$  for  $M = 0.2$ ,  $0.3$ , and  $0.4$ . Most of the features have been individually discussed previously, including the reduction, with Mach number, of the peak values of the coefficients and in the angle when the stall events occur. The results for  $M = 0.2$  and  $0.3$  are closest; most of the changes occur between  $M = 0.3$  and  $M = 0.4$ . This supports the argument that it is the strong supersonic zone at the leading edge at  $M = 0.4$  which prevents the development of the massive leading edge suction peak and flattens the force and moment coefficient curves at lower pitch angles. The weaker leading edge suction also reduces the strength of the stall vortex, which leads to smaller lift coefficient overshoots and smaller peak pitching moment coefficients.

## RESULTS FOR SINUSOIDAL OSCILLATIONS

Data for sinusoidal pitch oscillations were obtained for  $M = 0.2$  and one amplitude ( $\bar{\alpha} = 10$  deg) at three reduced frequencies ( $k = \omega c/2U = 0.025$ ,  $0.050$ , and  $0.100$ ) and at two mean angles ( $\alpha_0 = 10$  and  $20$  deg). There are two primary differences between ramp and sinusoidal motions: the airfoil does not start the motion from a steady-state condition and the pitch rate is constantly changing. For a pitch angle given by  $\alpha = \alpha_0 - \bar{\alpha} \cos(\omega t)$  the pitch rate is equal to  $A = \bar{\alpha} k \sin(\omega t)$ . The peak pitch rates for the data presented here are reached at a time of  $\tau = 0.25$  and are equal to  $A = 0.0044$ ,  $0.0087$ , and  $0.0175$  at  $k = 0.025$ ,  $0.050$ , and  $0.100$ , respectively. These pitch rates are therefore within the range of the constant pitch rate data obtained in this experiment. Discussion of these results will concentrate on the ensemble averaged upper surface pressures and on the force and moment loops. Additional aspects of the results will be presented only for  $k = 0.050$ ,  $\alpha_0 = 20$  deg.

### UPPER SURFACE PRESSURES

There are many qualitative similarities between the upper surface pressure distributions for ramps and sinusoids. The results for the six sinusoids are shown in Figs. 43a-f. The time axis of each plot has been shifted so that  $\tau = 0$  corresponds to the minimum angle and  $\tau = 0.5$  to the maximum angle. The pressure time histories begin with a decrease in  $C_p$  as the suction peak develops. The stall vortex forms in a somewhat more concentrated region than at constant pitch rate ( $x/c < 0.06$  instead of  $x/c < 0.15$ ) and then is released to travel downstream. Once the vortex has passed the trailing edge, there is a period of fully separated flow, with some periodic oscillations evident at the higher reduced frequencies. One notable change from the constant pitch rate results is the absence of the region of unstable flow near the leading edge immediately after stall that occurs at the lower constant pitch rates (cf. Figs. 30a, b, and c). This may be because the instantaneous pitch rates at stall for the sinusoids are generally higher than the maximum value for unstable flow at constant pitch rate ( $A = 0.005$ ). The values of the pitch rate at stall are given in the following table, with the box identifying those greater than  $A = 0.005$ .

Pitch Rate at Stall

$k$	$\alpha_0 = 10^\circ$	$\alpha_0 = 20^\circ$
0.025	0.0032	0.0042
0.050	0.0057	0.0086
0.100	0.0086	0.0173

The initial stall vortex travels downstream at an approximately constant rate for  $x/c > 0.06$ , as shown in Fig. 44. The vortex speeds at the same reduced frequency vary as a result of the differing pitch rates, both at vortex release and while it is propagating along the chord. There are differences even when the vortex speed is plotted against the pitch rate at stall (Fig. 45). The vortex speed appears to be higher for the sinusoid at the same pitch rate, approximately  $0.25U$  to  $0.35U$  in Fig. 45, rather than  $0.15U$  to  $0.30U$  in Fig. 32 for constant pitch rate. No further conclusions are drawn since it is difficult to sort out the interconnected effects of pitch rate and rate of change of pitch rate in this sinusoidal motion.

#### FORCES AND MOMENT

The loops of lift, drag, and pitching moment coefficient for the SSC-A09 at  $M = 0.2$  are similar to those obtained for other airfoils (Refs. 3, 4, 14-16, 22, 23). As shown in Figs. 46a-f, increasing reduced frequency has the expected effect of delaying stall and reattachment and increasing the peak forces and moment. The unsteady increments to  $C_L$ ,  $C_D$ , and  $C_M$  have similar magnitudes to those at constant pitch rate. The oscillations after stall for  $\alpha_0 = 20$  deg also have amplitude and frequency similar to those observed at constant pitch rate during this experiment (Fig. 25), and qualitatively similar to those observed during sinusoidal oscillations of some of the airfoils studied by McAlister, et al. (Refs. 22 and 23). The pitch angles for the various stall events are shown in Fig. 47, and may be compared with the constant-pitch rate results in Fig. 27. In general the delays resulting from the unsteady motion are larger for sinusoidal motions at the lower reduced frequency than for ramp motions at the same initial pitch rate. At higher reduced frequency the unsteady delays are comparable. Also the sinusoidal results do not appear to be linearly approaching the steady stall angle of 14 deg, as do the ramp results. Again the uncertainty introduced by the constantly changing pitch rates makes firm conclusions hard to establish.

#### LOWER SURFACE PRESSURES

The ensemble averaged lower surface pressures for the representative case of  $\alpha_0 = 20$  deg,  $k = 0.050$  are shown in Fig. 48. There is a rapid change in pressure near the trailing edge when the upper surface stalls. This is required to maintain zero pressure difference at the trailing edge. Following this there are two cycles of a decaying 47 Hz (19 times frequency of the motion) oscillation related to the stall vortices (letter A in Fig. 48), a brief quiescent period, and a persistent oscillation (letter B) related to the vortex street at approximately 62 Hz (50 times the frequency of the motion). The oscillation frequencies are similar to those observed for constant pitch rate ramps at the same Mach number and angle of attack. However, to be present in the ensemble average the oscillation frequencies must be integer

multiples of the frequency of the airfoil motion. The frequencies must therefore shift slightly with  $k$  to produce integer ratios at each airfoil frequency. At  $k = 0.025$  (not shown here) the stall vortex oscillation frequency is 40 Hz (32 times the frequency of the motion) and the vortex street oscillation frequency is 62 Hz (50 times the frequency of the motion). At  $k = 0.100$  (Fig. 49) the oscillations from the stall vortex and the vortex street combine to form a single oscillation at a frequency of 52 Hz (10 times the frequency of the motion). This shift is similar to that observed at constant pitch rate.

#### ROOT-MEAN-SQUARE PRESSURES

The rms pressures for this case are shown in Fig. 50. On the upper surface (Fig. 50a) there are peaks corresponding to both stall (letter A near  $\tau = 0.22$ ) and reattachment (letter B near  $\tau = 0.85$ ). A double peak in the rms develops near  $\tau = 0.25$  to  $0.35$  for  $x/c > 0.5$  (letter C), apparently related to a secondary stall vortex. Both the upper (Fig. 50a) and lower (Fig. 50b) surface rms pressures have increased levels for  $x/c > 0.75$ , a sign of the vortex street oscillations. The same events (stall, vortex street oscillations, and reattachment) are observed in the hot film gage response shown in Fig. 51. For this case the pitch angle is always greater than 10 deg, so no transition effects are present. The ensemble averaged results (Fig. 51a) show the same double peak at  $x/c = 0.682$  and  $0.880$  (letter A centered about  $\tau = 0.3$ ) as seen in the rms pressures. The rms hot film output (Fig. 51b) has a high and erratic value at these same two stations, indicating the effects of the vortices are not completely synchronized in phase.

## THE EFFECT OF STARTING AND ENDING ANGLE

### FINAL PITCH ANGLE

Changes in the final pitch angle obtained during a ramp motion may alter both the stall and post-stall characteristics. This is illustrated by comparing the results for a series of 0 to 20 deg ramps with the results described earlier for 0 to 30 deg ramps. Integrated force and moment time histories are shown in Fig. 52 for four pitch rates,  $A = 0.0010$ ,  $0.0025$ ,  $0.0050$ , and  $0.0100$ . For pitch rates below  $A = 0.01$ , the results before and during stall are similar to the 0 to 30 deg results shown in Fig. 25. This is because the primary stall events have all occurred before the motion stops (at  $\tau = 0.625$  and  $\alpha = 20$  deg). For  $A = 0.01$  the stall vortex has not yet reached the trailing edge when the motion stops. As shown in Fig. 27, the vortex would have reached the trailing edge at approximately  $\alpha = 21$  deg (it is the passage of the vortex close to the trailing edge that causes the minimum pitching moment plotted in Fig. 27) if the motion continued, but in this case the stall process is prematurely terminated. Hence the peak airloads are less than those in Fig. 25;  $C_{L,max}$  is 2.3 instead of 2.4 and  $C_{M,min}$  is  $-0.32$  instead of  $-0.36$ . A distinct stopping vortex is generated near the leading edge, as shown in Fig. 53a by the sharp spikes in the pressure time histories for  $x/c = 0.026$  and  $0.060$  at  $\tau = 0.625$  (letter A). Two characteristics of this vortex are noted but not explained: First, the vortex signature is observed only near the leading edge, a behavior opposite of that of the initial stall vortex, which is not observed ahead of  $x/c = 0.15$ . Second, both the stopping and stall vortices reduce the pressure coefficient, implying that they have the same sense. There is also a sudden change in the character of the stall vortex itself when the motion stops. The pressure signature of this vortex sharpens at  $\tau = 0.625$ , when the vortex is near  $x/c = 0.4$  (letter B in Fig. 53a). Flow visualization or numerical simulation might be useful in interpreting these results.

At lower pitch rates the stall process has been completed before the motion stops at  $\alpha = 20$  deg. No stopping vortex is observed in the pressure time histories at  $A = 0.0025$  (Fig. 53b). However, the post-stall pressure characteristics at both  $A = 0.0025$  and  $A = 0.010$  are changed by the reduction in ending pitch angle. The upper surface still supports a pressure gradient at  $\alpha = 20$  deg, in contrast to the complete upper surface stall observed at  $\alpha = 30$  deg. The chordwise pressure distribution is similar to that observed for a limited time after stall during the 0 to 30 deg ramps (letter A of Fig. 30). This type of pressure distribution persists indefinitely when the motion is held at 20 deg. The periodic oscillation caused by the vortex street is not present with the lower maximum pitch angle, but a more erratic variation is present, especially near the leading edge.



## INITIAL PITCH ANGLE

The effect of changing both the starting and ending pitch angles is discussed next. The changes are largest and most easily observed at  $A = 0.01$ . Figure 54 shows the integrated forces and moment for the 0 to 30 and 0 to 20 deg ramps discussed above, plus three additional 10 deg ramps ending at 20, 22, and 24 deg. Corresponding upper surface pressure time histories for the three 10 deg ramps are shown in Fig. 55. The lift (Fig. 54a) is not greatly affected by changing the initial angle as long as this angle is less than 14 deg. Since static stall starts near  $\alpha = 14$  deg, the initial lift for the 14 to 24 deg ramp is much lower than for the other cases, and does not reach nearly as high a maximum  $C_L$ . The stall vortex strength, as measured from the change in  $C_p$  at  $x/c = 0.302$ , is approximately 30% less for this case than for the base case of a 0 to 30 deg ramp. For the 12 to 22 deg ramps the reduction in stall vortex strength is only 10%. Changing the ending angle terminates the stall process early for the 0 to 20 and the 10 to 20 deg ramps. In each case  $C_L$  reaches a maximum value close to that of the base case, but drops off rapidly when the motion ceases. For ending angles greater than 20 deg the maximum  $C_L$  is delayed slightly (by 1 deg or less) as the starting angle increases.

Many of the same trends are observed in the pitching moment and drag. As shown in Fig. 54b, the pitching moment quickly shifts from its steady-state value (near  $C_M = 0$ ) to the slightly negative value that results from the imposed motion. The initial angle does not affect the angle of pitching moment stall for initial angles less than 12 deg. The start of the pitching moment stall is delayed by 1.5 deg when the initial angle is 12 deg, but the angle of the minimum  $C_M$  is only about 0.5 deg later than that for the base case of a 0 to 30 deg ramp. The pitching moment for a starting angle of 14 deg shows the effects of beginning during the steady-state stall: the initial value is more negative,  $C_M = -0.05$ , and the minimum is less,  $C_M = -0.30$ . The pressure drag rise (Fig. 54c) is also terminated prematurely for ending angle less than 22 deg and reaches a lower peak for starting angles above 14 deg.

Time histories of the upper surface pressure distributions at  $A = 0.010$  for the three 10 deg ramps (10 to 20, 12 to 22, and 14 to 24 deg) illustrate how the behavior of the stall vortex changes. For the 10 to 20 deg ramp (Fig. 55a) a stopping vortex (letter A) is created at  $\tau = 0.625$ , as observed earlier for the 0 to 20 deg ramp (Fig. 53a). The pressure signature of a stopping vortex is not seen for the 12 to 22 deg ramp (Fig. 55b) or for the 14 to 24 deg ramp (Fig. 55c). However, stopping the motion does change the propagation of the vortex along the airfoil chord. Figure 56 shows a discontinuity in the curves of vortex position versus time (as determined from the minimum  $C_p$  on the surface) at the time when the motion is stopped. The discontinuity appears as a pause of  $\Delta\tau = 0.034$  in the vortex motion. At the vortex travel speed of 28% of the freestream velocity the vortex would have

travelled about 20% of the chord. After the pause the vortex resumes travelling at the same speed for the 10 to 20 deg ramp, while for the 12 to 24 deg ramp the vortex is too close to the trailing edge for regular motion to discerned.

## RESULTS FOR NEGATIVE PITCH RATE

Reattachment was studied by examining the results for two 30 to 0 deg ramps at  $M = 0.2$  and pitch rates of 0.001 and 0.005. Selected upper surface pressure time histories for these cases are shown in Fig. 57. Each curve is offset by a  $C_p$  of 1.0; the scale on the left refers to the lowest curve. The down ramps had shapes similar to the up ramps: there was a one to two second delay at 30 deg pitch; the pitch angle decreased at a constant rate beginning at  $\tau = 0.125$ , and reached 0 pitch at  $\tau = 0.625$ ; the pitch was then held at 0 deg for several seconds and the cycle repeated. At 30 deg pitch the vortex street induced oscillations are present, but they are not large in the ensemble averages of Fig. 57 because the long time delay has allowed any phase synchronization to deteriorate. Reattachment (letter A in Figs. 57a and b) begins when the ensemble averaged pressures become more negative at  $\tau = 0.349$  ( $\alpha = 16.6$  deg) for  $A = 0.001$  and at  $\tau = 0.449$  ( $\alpha = 15.5$  deg) for  $A = 0.005$ . The beginning of reattachment is also shown by an increase in the pressure rms (Fig. 58). This indicates that reattachment, like stall, is an erratic process, both during one cycle and from cycle to cycle. Reattachment is completed at about  $\tau = 0.45$  ( $\alpha = 10.5$  deg) for both pitch rates. At this time  $C_p$  reaches a minimum value of -5.1 at  $A = 0.001$  and -4.6 at  $A = 0.005$ , considerably less than the -12 to -14 values reached with positive pitch rate. The lower surface pressure time histories (Fig. 59) begin to respond to the drop in pitch almost immediately: The stagnation point moves forward to  $x/c = 0.005$  at  $\tau = 0.3$ , while the pressures on the rest of the surface show smooth changes with pitch. The vortex street oscillations are present for  $x/c > 0.88$ . When the upper surface reattaches the stagnation point momentarily moves back to  $x/c = 0.026$  and the trailing edge pressures increase sharply to maintain continuity with the pressure on the upper surface. After reattachment is complete the stagnation point moves forward again and the pressure on the rest of the lower surface resumes responding smoothly to the decreasing pitch.

The beginning of reattachment is shown by a slight increase in the ensemble averaged hot film gage time histories (letter A in Figs. 60a and b) and by a large increase in the rms hot film gage results (letter A in Figs. 61a and b). The completion of reattachment is shown by a sharp increase in the ensemble averaged hot film output (letter B in Figs. 60a and b) and a corresponding sharp drop in the rms (letter B in Figs. 61a and b). The high rms hot film output during reattachment verifies that this is an irregular process. The high ensemble averaged hot film output after reattachment indicates that the flow reattaches with a turbulent boundary layer. As the pitch angle continues to drop, the boundary layer relaminarizes near the leading edge (letter C in Figs. 60 and 61). At  $A = 0.001$  the laminar region reaches  $x/c = 0.026$  at  $\tau = 0.487$  ( $\alpha = 8.3$  deg) and  $x/c = 0.060$  at  $\tau = 0.505$  ( $\alpha = 7.2$  deg). These angles are about 1 deg higher than those at which the

boundary layer became turbulent when the pitch was increasing. At  $A = 0.005$  the relaminarization angles are reduced (delayed) to 7.9 deg at  $x/c = 0.026$  and 6.5 deg at  $x/c = 0.060$ . The difference between the transition and relaminarization angles is also reduced to about 0.5 deg at  $A = 0.005$ .

The force and moment curves for these two 30 to 0 deg down-ramps are shown in Fig. 62. The curves may be divided into several regions. The first occurs between 30 deg and about 20 deg, and consists of a nearly linear decrease in  $C_L$  and  $C_D$  and an increase in  $C_M$  as the pressures on the lower surface (attached flow) and, to a lesser extent, on the upper surface (separated flow) respond to the drop in pitch angle. The difference between the initial values at  $\alpha = 30$  deg at the two pitch rates implies that the 1 to 2 second delay at the maximum pitch rate may not have been sufficient to achieve a true steady state for massively stalled flow. Additionally, this tunnel-spanning model is large enough to affect the flow in the wind tunnel when it remains stalled for a long period of time. The wind tunnel is able to recover during the delays before the start of an up-ramp, but may show the effects of the separated flow during these down-ramps. The forces and moment level out between about 20 deg and the beginning of reattachment at 15 to 16 deg. Reattachment is more sudden (in angle) at  $A = 0.001$ , but is completed at about the same point ( $\alpha = 10.5$  deg). Following reattachment the airloads are qualitatively similar to those for positive pitch rate. As at positive pitch rate, the slopes in attached flow differ because of the lag at the higher rate.

The results for positive and negative pitch rate may be combined to produce a 'constant-pitch-rate loop' similar to the loops for sinusoidal oscillations shown in Fig. 46. The constant-pitch-rate results for  $A = 0.0050$ , shown in Fig. 63, exhibit many of the features associated with sinusoidal loops (Refs. 3, 14-16, 22 and 23), including the crossover in  $C_L$  after reattachment (at  $\alpha = 4$  deg in Fig. 63a) and the three subloops of  $C_M$  (Fig. 63b). As discussed in Ref. 24, it is the central subloop of the  $C_M$  vs.  $\alpha$  curve that is essential to the growth of the pitch oscillations of an elastic airfoil that lead to torsional stall flutter. For both the constant-pitch-rate ramps (Fig. 63b) and sinusoidal oscillation with a similar maximum pitch rate (Fig. 46c) this central destabilizing subloop occurs between about 13 and 17 deg and has an amplitude of about  $C_M = 0.1$ . It is gratifying, if not surprising, to observe the same phenomena in both motions, since this implies that it is the pitch range and the pitch rate, and not the angular acceleration or other higher derivatives present during the sinusoid that are of primary importance to the aeroelastic stability problem.

## CONCLUSIONS

The primary results of this experimental investigation of dynamic stall at large Reynolds number and moderate Mach number include:

- 1) For constant pitch rate ramps the unsteady aerodynamic response near stall is strongly dependent on the characteristics of the leading edge stall vortex. The vortex is released from about  $x/c = 0.10$  during stall, and propagates downstream at a velocity that increases with the pitch rate,  $A$ . The vortex strength also increases with  $A$ , causing related increases in the unsteady increments to  $C_L$ ,  $C_M$ , and  $C_D$ .
- 2) A periodic oscillation of the surface pressures occurs at high angle of attack when the equivalent bluff body Reynolds number,  $Uc \sin \alpha / \nu$ , is less than  $10^6$ . At higher pitch rates, above  $A = 0.01$ , the oscillations synchronize with the motion of the airfoil and of the stall vortex, and increase in amplitude.
- 3) The location of boundary layer transition to turbulence moves forward along the airfoil chord as the pitch angle increases. This shift is delayed at higher pitch rate, but is only slightly advanced by increasing the Reynolds number to  $4 \times 10^6$ .
- 4) A supersonic zone is formed near the leading edge at  $M = 0.4$ . This zone reduces the peak suction pressures and airloads and reduces the strength of the stall vortex.
- 5) Stopping the airfoil pitching motion before the stall vortex has passed the trailing edge generates a stopping vortex near the airfoil leading edge. This vortex may combine with the stall vortex and, after a pause, continue propagating downstream at a speed equal to that of the original stall vortex.
- 6) Starting the airfoil pitching motion at an angle above that at which the stall vortex would have begun to form weakens the vortex and reduces the unsteady increments to the airloads.
- 7) Results for sinusoidal oscillations are qualitatively similar during pitch-up and pitch-down to constant pitch rate motions having similar values of  $M$ ,  $Re$ , and  $A$  at the stall angle, but the sinusoids have somewhat longer delays in the unsteady stall process.

## APPENDIX A

### THREE-DIMENSIONAL EFFECTS WITH A TWO-DIMENSIONAL GEOMETRY

The degree to which this experiment can be said to represent a two-dimensional flow may be estimated by comparing the surface pressures measured at the two supplemental transducer arrays with those measured at the primary array. Because the instrumented airfoil section is designed to be used as part of a future finite tip wing experiment, the supplemental transducers are all between the main array and the wind tunnel wall, as shown in Fig. 6. Therefore data from these arrays will not give a picture of the pressures on both sides of the main array; they will only tell how rapidly three-dimensional effects develop as the wall is approached. The case of a 0 to 30 deg ramp at  $M = 0.2$  and  $A = 0.005$ , described in detail previously, will be used here also. Figure 64 shows the normal force and moment results for the primary array (denoted Sta 04) and for the arrays 8 and 16 inches closer to the wall (denoted by Sta 12 and Sta 20). There are very small differences up to the time of vortex formation. At this point there are relatively small differences in the peak  $C_N$  and  $C_M$ , and in the time of stall. After stall the differences are somewhat larger, particularly at station 20. The oscillations induced during deep stall by the vortex street are in phase at all three stations.

The upper surface pressures at the supplementary stations are shown in Fig. 65, and may be compared with the pressures at the primary station shown in Fig. 14. Since the transducer closest to the leading edge on the supplementary stations is only at  $x/c = 0.010$  rather than  $x/c = 0.005$ , the peak  $C_p$  is -10 rather than -12.5. The only major difference is the presence of the bump at  $x/c = 0.010$  just prior to stall, when the vortex is forming. The bump is only observed at this chordwise location, and is not present at the primary spanwise station. The time histories for individual cycles at  $x/c = 0.005$  (not shown here) indicate that this event occurs at about the same time with about the same amplitude during each cycle. Since the bump occurs slightly earlier at the station closest to the wall, it may be a localized three-dimensional effect related to the formation of the vortex at the leading edge that has vanished at the primary transducer station. The lower surface pressures (Fig. 66) show no significant differences between the various spanwise stations. The support that comes up from the wind tunnel floor close to station 12 (Fig. 1) does not seem to have any significant influence on the pressures. The comparisons at other pitch rates show similar characteristics. In summary the surface pressure results presented here seem reasonably two-dimensional, with the exception of some unusual pressure variations at the supplementary stations during formation of the stall vortex. It appears that the primary array of pressure transducers is far enough from the wind tunnel wall to avoid such effects.

## APPENDIX B

### UNSTEADY PITCHING MOMENT OFFSET IN ATTACHED FLOW

In attached flow at moderate angles of attack, the section force and moment coefficients may often be accurately estimated using unsteady thin airfoil theory. For a constant rate pitching motion about the quarter chord of the section, the expression for the pitching moment [Eq. (4-171) in Ref. 18] is reduced to a single term:

$$M = -\frac{1}{8} \pi \rho U c^3 \dot{\alpha}$$

or, in terms of the nondimensional quantities:

$$C_M = -\frac{1}{2} \pi A$$

A comparison of the experimental and thin airfoil theory results for the 0 to 30 deg ramps at  $M = 0.2$  (Fig. 25e) is summarized below.

A	$C_M$ theory	$C_M$ expt.
0.0010	0.0016	0.0020
0.0025	0.0040	0.0045
0.0050	0.0079	0.0080
0.0100	0.0157	0.0160
0.0200	0.0314	0.0300

## APPENDIX C

### DETERMINATION OF TRANSITION FROM THE RMS PRESSURE

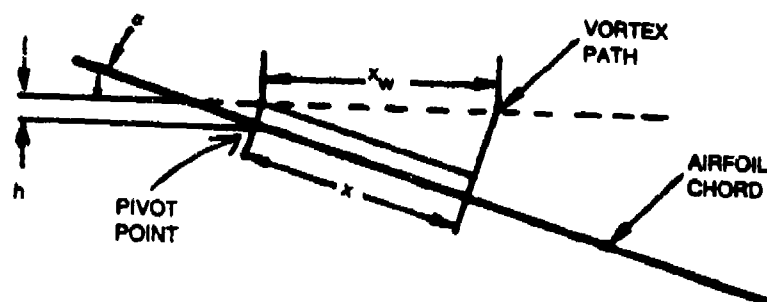
Accurate determination of the point of boundary layer transition is critical to many numerical computations. Surface heat transfer gages are usually required to determine the unsteady motion of the transition point. These gages are frequently cumbersome to install and each requires an individual active anemometer circuit to operate. Examination of the time history results for this experiment has shown that it may be possible to locate the transition point based upon the higher rms pressures measured by an unsteady pressure transducer in a turbulent boundary layer. An example of the correlation between the hot film and pressure transducer results at  $x/c = 0.026$  for a 0 to 30 deg ramp at  $M = 0.20$  is shown in Fig. 67a for  $A = 0.02$  and in Fig. 67b for  $A = 0.005$ . The increase in pressure rms corresponds to the increase in ensemble averaged heat transfer and to the spike in rms heat transfer. No change at transition is apparent in the ensemble averaged pressure. If these promising early results are confirmed, this method may make it much easier to locate transition in complex flows.



## APPENDIX D

### VORTEX PROPAGATION SPEED IN WIND AND MODEL AXES

For a prescribed stall vortex propagation path, the relationship between the propagation path in the wind (fixed) axes and in the model (rotating) can be computed. The simplest path is horizontal, with the height of the vortex above the chord at the pivot point ( $x/c = 0.25$ ) equal to  $h$ . If the vortex is assumed to induce the largest change in pressure when the perpendicular distance to the chord is a minimum, the vortex velocity measured by the airfoil pressure transducers ( $V$ ) may be converted to the velocity in the wind axes ( $V_w$ ) as follows.



The position of the vortex at any time is:

$$x_w = \frac{x}{\cos \alpha} + h \tan \alpha. \quad (D.1)$$

The change in position with time is:

$$\Delta x_w = \frac{x + \Delta x}{\cos(\alpha + \Delta \alpha)} + h \tan(\alpha + \Delta \alpha) - \frac{x}{\cos \alpha} - h \tan \alpha \quad (D.2)$$

For small changes, the trigonometric functions become:

$$\begin{aligned} \cos(\alpha + \Delta \alpha) &= \cos \alpha - \Delta \alpha \sin \alpha \\ \tan(\alpha + \Delta \alpha) &= \tan \alpha + \Delta \alpha (1 + \tan^2 \alpha). \end{aligned} \quad (D.3)$$

Substituting into Eq. (D.2):

$$\Delta x_W = x \Delta \alpha \frac{\tan \alpha}{\cos \alpha} + \frac{\Delta x}{\cos \alpha} + h \Delta \alpha (1 + \tan^2 \alpha) \quad (D.4)$$

The propagation velocity becomes:

$$\frac{V_W}{U} = \frac{\Delta x_W}{U \Delta t} = \frac{\Delta x}{U \Delta t \cos \alpha} + \frac{\Delta \alpha}{U \Delta t} \left( x \frac{\tan \alpha}{\cos \alpha} + h(1 + \tan^2 \alpha) \right) \quad (D.5)$$

Rearranging and non-dimensionalizing:

$$\frac{V}{U} = \frac{\Delta x}{U \Delta t} = \frac{V_W}{U} \cos \alpha - 2A \left( \frac{x}{c} \tan \alpha + \frac{h}{c} \sec \alpha \right) \quad (D.6)$$

If the vortex is released at about  $x/c=0.1$ , a typical value of  $h/c$  is 0.04. At a fixed point of the chord,  $x/c = 0.25$ , the values of  $\alpha$  and  $V/U$  may be obtained from the experimental data for the 0 to 30 deg ramps at  $M = 0.2$  (Figs. 11 and 32), and the velocity in the wind axes computed:

A	0.001	0.005	0.020
$\alpha$	14	18	24
measured $V/U$	0.153	0.241	0.447
computed $V_w/U$	0.158	0.255	0.499

It is apparent that the computed values of  $V_w/U$  are not independent of pitch rate, implying that a more complex representation of the vortex path is required.

## REFERENCES

1. Liiva, J., and F. J. Davenport, "Dynamic Stall of Airfoil Sections for High-Speed Rotors," Journal of the American Helicopter Society, Vol. 13, Apr. 1968, pp. 49-55.
2. Carta, F. O., and C. F. Niebanck, "Prediction of Rotor Instability at High Forward Flight Speeds, Volume III. Stall Flutter," USAAVLABS Tech. Rept. 68-18C, U.S. Army Aviation Material Laboratories, Ft. Eustis, VA, Feb. 1969.
3. McCroskey, W. J., K. W. McAlister, and L. W. Carr, "Dynamic Stall Experiments on Oscillating Airfoils," AIAA Journal, Vol. 14, Jan. 1976, pp. 57-63.
4. Dadone, L. U., "Two-Dimensional Wind Tunnel Test of an Oscillating Rotor Airfoil," NASA CR-2914, Dec. 1977.
5. Herbst, W. B., "Supermaneuverability," Proceedings of the AFOSR-FJSRL-University of Colorado Workshop on Unsteady Separated Flows, U.S. Air Force Academy, Colorado Springs, Aug. 1983.
6. Lang, J. D., "Unsteady Aerodynamics and Dynamic Aircraft Maneuverability," AGARD CP-386, Unsteady Aerodynamics - Fundamentals and Application to Aircraft Dynamics, Goettingen, West Germany, May 1985.
7. Ham, N. D., and M. S. Garelick, "Dynamic Stall Considerations in Helicopter Rotors," Journal of the American Helicopter Society, Vol. 13, Apr. 1968, pp. 49-55.
8. Daley, D. C., and E. J. Jumper, "Experimental Investigation of Dynamic stall for a Pitching Airfoil," Journal of Aircraft, Vol. 21, Oct. 1984, pp. 831-832.
9. Jumper, E. J., S. J. Schreck, and R. L. Dimmick, "Lift-Curve Characteristics for an Airfoil Pitching at Constant Rate," AIAA Paper 86-0117, Jan. 1986.
10. Walker, J. M., H. E. Helin, and J. H. Strickland, "An Experimental Investigation of an Airfoil Undergoing Large Amplitude Pitching Motions," AIAA Journal, Vol. 23, Aug. 1985, pp. 1141-1142.
11. Francis, M. S., and J. E. Keese, "Airfoil Dynamic Stall Performance with Large Amplitude Motions," AIAA Journal, Vol. 23, Nov. 1985, pp. 1653-1659.

# REFERENCES (Concluded)

12. Strickland, J. H., and G. M. Graham, "Force Coefficients for a NACA-0015 Airfoil Undergoing Constant Pitch Rate Motions," AIAA Journal, Vol. 25, April 1987, pp. 622-624.
13. Marchman, J. F., "Aerodynamic Testing at Low Reynolds Numbers," J. Aircraft, Vol. 24, Feb. 1987, pp. 107-114.
14. St. Hilaire, A. O., F. O. Carta, M. R. Fink, and W. D. Jepson, "The Influence of Sweep on the Aerodynamic Loading of an Oscillating NACA 0012 Airfoil," Volume I - Technical Report, NASA CR-3092, 1979.
15. Carta, F. O., "Dynamic Stall of Swept and Unswept Oscillating Wings," Paper 2 in Unsteady Aerodynamics-Fundamentals and Applications to Aircraft Dynamics, AGARD CP-386, Nov. 1985.
16. St. Hilaire, A. O., and F. O. Carta, "Analysis of Unswept and Swept Wing Pressure Data from an Oscillating NACA 0012 Airfoil Experiment. Volume I - Technical Report," NASA CR-3567, March 1983.
17. Schlichting, H., "Boundary Layer Theory," McGraw-Hill, New York, 1979, pp. 31-32.
18. Bisplinghoff, R. L., and H. Ashley, "Principles of Aeroelasticity," John Wiley and Sons, New York, 1962, pg. 120.
19. Gormont, R. E., "A Mathematical Model of Unsteady Aerodynamics and Radial Flow for Application to Helicopter Rotors," USAAMRDL Technical Report 72-67, May 1973.
20. Strickland, J. H., and G. M. Graham, "A Dynamic Stall Inception Correlation for Airfoils Undergoing Constant Pitch Rate Motion," AIAA Journal, Vol. 24, April 1986, pp. 678-679.
21. Schlichting, "Boundary Layer Theory," pp. 719-720.
22. McCroskey, W. J., K. W. McAlister, L. W. Carr, and S. L. Pucci, "An Experimental Study of Dynamic Stall on Advanced Airfoil Sections, Volume 1. Summary of the Experiment," NASA TM-84245, July 1982.
23. McAlister, K. W., S. L. Pucci, W. J. McCroskey, and L. W. Carr, "An Experimental Study of Dynamic Stall of Advanced Airfoil Sections, Volume 2. Pressure and Force Data," NASA TM-84245, Sept. 1982.
24. Carta, F. O., and P. F. Lorber, "Experimental Study of the Aerodynamics of Incipient Torsional Stall Flutter," Journal of Propulsion and Power, Vol. 3, Mar.-Apr. 1987, pp. 164-170.

TABLE 1. SURFACE COORDINATES FOR SIKORSKY SSC-409

X/C	W/C Upper	W/C Lower	X/C	W/C Upper	W/C Lower
0.000000	0.000000	0.000000	0.376873	0.055494	-0.034506
0.000199	0.002000	-0.001454	0.416754	0.055039	-0.034637
0.000798	0.003946	-0.002869	0.436694	0.054663	-0.034558
0.001994	0.006482	-0.004573	0.456635	0.054182	-0.034376
0.002991	0.008029	-0.005446	0.476575	0.053595	-0.034087
0.004487	0.009868	-0.006445	0.496515	0.052899	-0.033683
0.006979	0.012392	-0.007703	0.516456	0.052093	-0.033165
0.009970	0.014921	-0.008877	0.536396	0.051176	-0.032532
0.015952	0.019076	-0.010704	0.556336	0.050149	-0.031790
0.021934	0.022500	-0.012175	0.576277	0.049009	-0.030949
0.027916	0.025445	-0.013447	0.596217	0.047755	-0.030018
0.033898	0.028039	-0.014588	0.616157	0.046381	-0.029002
0.039881	0.030369	-0.015631	0.636097	0.044875	-0.027904
0.045863	0.032494	-0.016594	0.656039	0.043220	-0.026720
0.051845	0.034449	-0.017487	0.675979	0.041391	-0.025448
0.057827	0.036249	-0.018314	0.695919	0.039368	-0.024088
0.067797	0.038903	-0.019568	0.715860	0.037140	-0.022642
0.077767	0.041143	-0.020691	0.735800	0.034719	-0.021121
0.087737	0.043016	-0.021706	0.755740	0.032138	-0.019540
0.097707	0.044583	-0.022638	0.775680	0.029445	-0.017918
0.112663	0.046504	-0.023910	0.795621	0.026681	-0.016272
0.127618	0.048054	-0.025064	0.815561	0.023871	-0.014617
0.142573	0.049345	-0.026124	0.835501	0.021012	-0.012957
0.157529	0.050444	-0.027104	0.855442	0.018089	-0.011289
0.172485	0.051385	-0.028013	0.875382	0.015093	-0.009598
0.187440	0.052184	-0.028853	0.895323	0.012051	-0.007863
0.202395	0.052860	-0.029628	0.915264	0.009046	-0.006081
0.217350	0.053427	-0.030339	0.935204	0.006229	-0.004290
0.232305	0.053911	-0.030988	0.955144	0.003849	-0.002610
0.247261	0.054322	-0.031579	0.975084	0.002288	-0.001325
0.277171	0.054958	-0.032594	0.985055	0.001987	-0.000992
0.307082	0.055369	-0.033402	0.995025	0.002135	-0.000863
0.336992	0.055564	-0.034007	1.000000	0.002408	-0.000803

TABLE 2. SURFACE DERIVATIVES FOR THE SIKORSKY SSC-A09

x/c	dw/dx upper	dw/dx lower	x/c	dw/dx upper	dw/dx lower
0.000000	0.000000	0.000000	0.356932	-0.001800	-0.012500
0.000100	10.051900	-7.304500	0.396813	-0.011400	-0.003300
0.000499	3.247399	-2.363099	0.426724	-0.018900	0.004000
0.001396	2.120399	-1.424199	0.446665	-0.024100	0.009200
0.002493	1.551600	-0.876400	0.466605	-0.029400	0.014500
0.003739	1.230300	-0.667400	0.486545	-0.034900	0.020200
0.005733	1.012199	-0.504700	0.506485	-0.040400	0.026000
0.008475	0.845500	-0.392800	0.526426	-0.046000	0.031700
0.012961	0.694600	-0.305400	0.546366	-0.051300	0.037200
0.018943	0.572400	-0.245800	0.566306	-0.057200	0.042200
0.024925	0.492400	-0.212600	0.586247	-0.062900	0.046700
0.030907	0.433700	-0.190700	0.606187	-0.068900	0.050900
0.036890	0.389400	-0.174400	0.626127	-0.075500	0.055100
0.042872	0.355200	-0.161000	0.646068	-0.083000	0.059400
0.048854	0.326800	-0.149300	0.666009	-0.091700	0.063800
0.054836	0.300900	-0.138400	0.685949	-0.101500	0.068200
0.062812	0.266200	-0.125800	0.705889	-0.111700	0.072500
0.072782	0.224700	-0.112600	0.725830	-0.121400	0.076300
0.082752	0.187900	-0.101800	0.745770	-0.129400	0.079300
0.092722	0.157200	-0.093500	0.765710	-0.135100	0.081400
0.105185	0.128500	-0.085100	0.785651	-0.138600	0.082600
0.120140	0.103600	-0.077100	0.805591	-0.140900	0.083000
0.135095	0.086300	-0.070900	0.825531	-0.143400	0.083200
0.150051	0.073400	-0.065500	0.845472	-0.146600	0.083700
0.165007	0.062900	-0.060800	0.865412	-0.150200	0.084800
0.179962	0.053500	-0.056100	0.885353	-0.152500	0.087000
0.194917	0.045100	-0.051900	0.905293	-0.150700	0.089400
0.209873	0.038000	-0.047500	0.925234	-0.141300	0.089900
0.224828	0.032300	-0.043400	0.945174	-0.119300	0.084200
0.239783	0.027500	-0.039500	0.965114	-0.078300	0.064400
0.262216	0.021300	-0.033900	0.985069	-0.030200	0.033400
0.292126	0.013700	-0.027000	0.990040	-0.014800	0.013000
0.322037	0.006500	-0.020300	0.997512	-0.054800	0.012100

TABLE 3. WING INSTRUMENTATION STATIONS

Primary Pressure Array  
Upper and Lower Surfaces

#	x/c	#	x/c
1	0.0050	10	0.3023
2	0.0256	11	0.3718
3	0.0597	12	0.4638
4	0.1028	13	0.5702
5	0.1490	14	0.6816
6	0.1921	15	0.7880
7	0.2262	16	0.8801
8	0.2468	17	0.9495
9	0.2616	18	0.9902

Secondary Pressure Arrays - 2 stations

Upper Surface		Lower Surface	
#	x/c	#	x/c
1	0.0100	1	0.0200
2	0.0492	2	0.0746
3	0.1066	3	0.1575
4	0.1640	4	0.3934
5	0.2031	5	0.7012
6	0.2501	6	0.9371
7	0.3947		
8	0.6066		
9	0.8184		
10	0.9631		

Swept Pressure Array

#	x/c	z/c
1	0.0050	0.1716
2	0.0597	0.1322
3	0.1490	0.0885
4	0.2262	0.0439

Hot Film Gage Locations

#	x/c
1	0.0256
2	0.0597
3	0.1028
4	0.1921
5	0.3023
6	0.4638
7	0.6816
8	0.8801

TABLE 4. TEST CONDITIONS STUDIED

## a) Ramps

M	$\alpha$ range	Pitch Rate, A				
		0.0010	0.0025	0.0050	0.0100	0.0200
0.2	0-10 deg	x	r	rs	x	
	0-20	r	x	x	x	
	0-30	rs	x	rs	r	rs
	10-20	x	r	r	x	
	12-22	x		s	x	
	14-24				x	
	20-30	x	x			
	20-10	s			s	
	30-0	s		s		
0.3	0-20			x		
	0-30				x	
0.4	0-10	x		x		
	0-20	rs	x	x	x	
	20-0				x	

## b) Sinusoids

M	$\alpha$	Reduced Frequency, k		
		0.025	0.050	0.100
0.2	6- 6cos $\omega t$	x		
	10-10cos $\omega t$	x	s	x
	20-20cos $\omega t$	x	x	x
0.3	9- 8cos $\omega t$		x	
	12- 8cos $\omega t$			x

Key: x- ensemble averaged and rms pressure data acquired.

s- skin friction gage data also acquired.

r- unaveraged data records stored in addition to ensemble average.



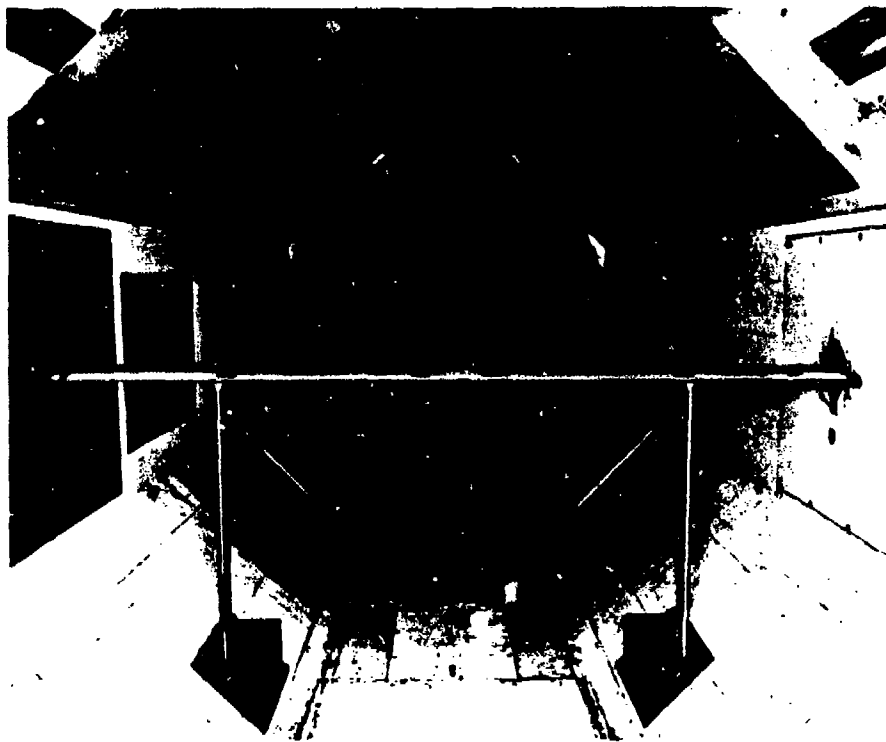


Figure 1. Oscillating wind model in the 8 ft section of the UTRC wind tunnel.

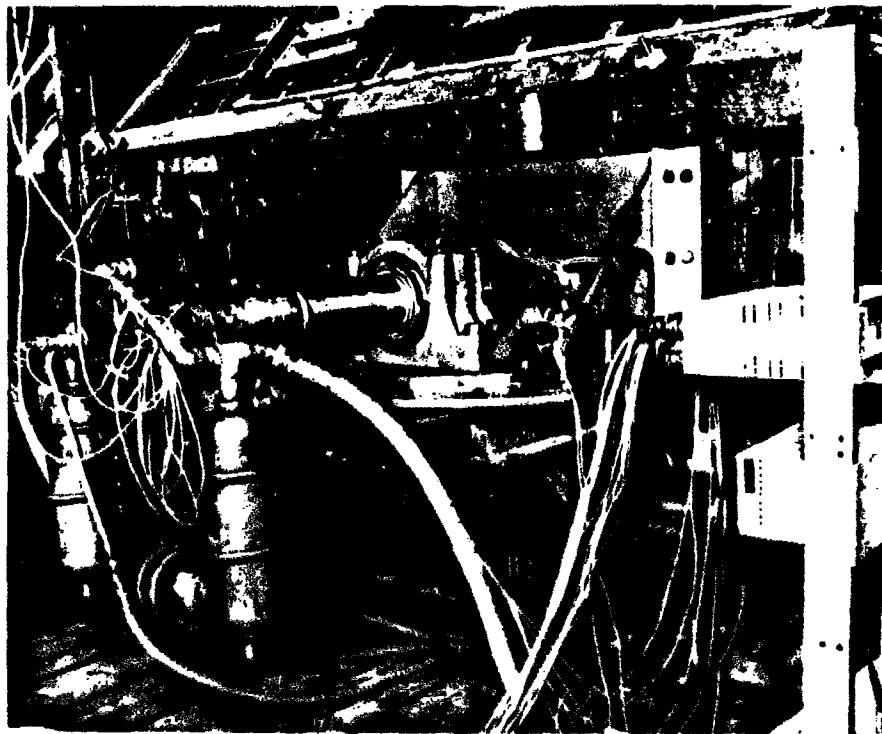


Figure 2. Model support and hydraulic drive system mounted on the east wall of the test section.



Figure 3. The Sikorsky SSC-A09 airfoil section.

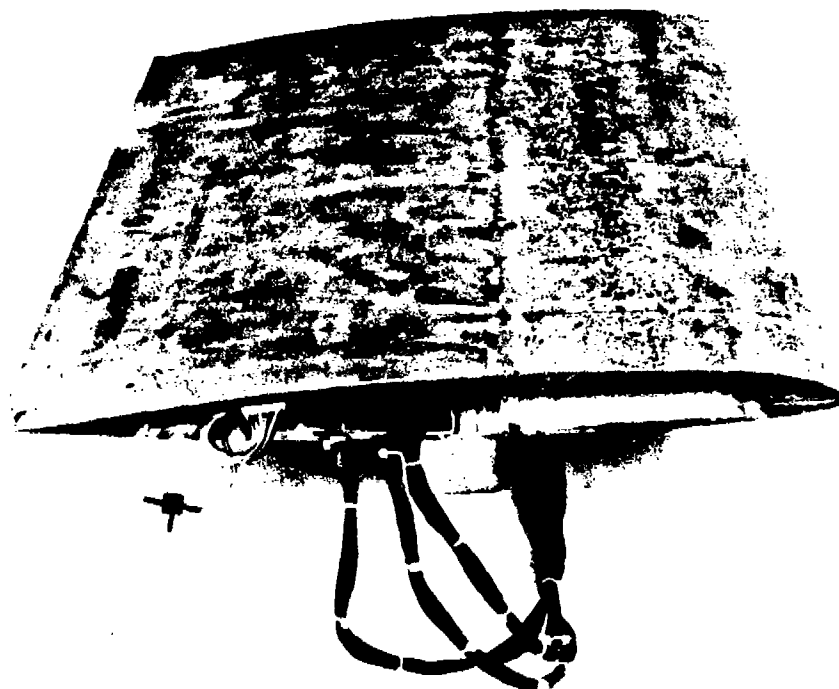


Figure 4. Section of the wing model containing unsteady instrumentation.

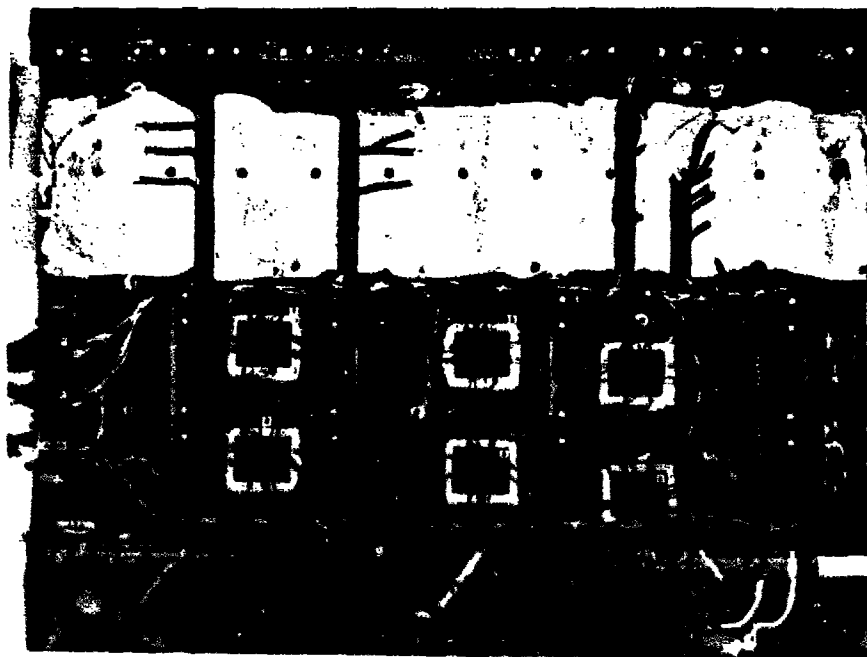


Figure 5. Inside view of the upper panel of the instrumented section.

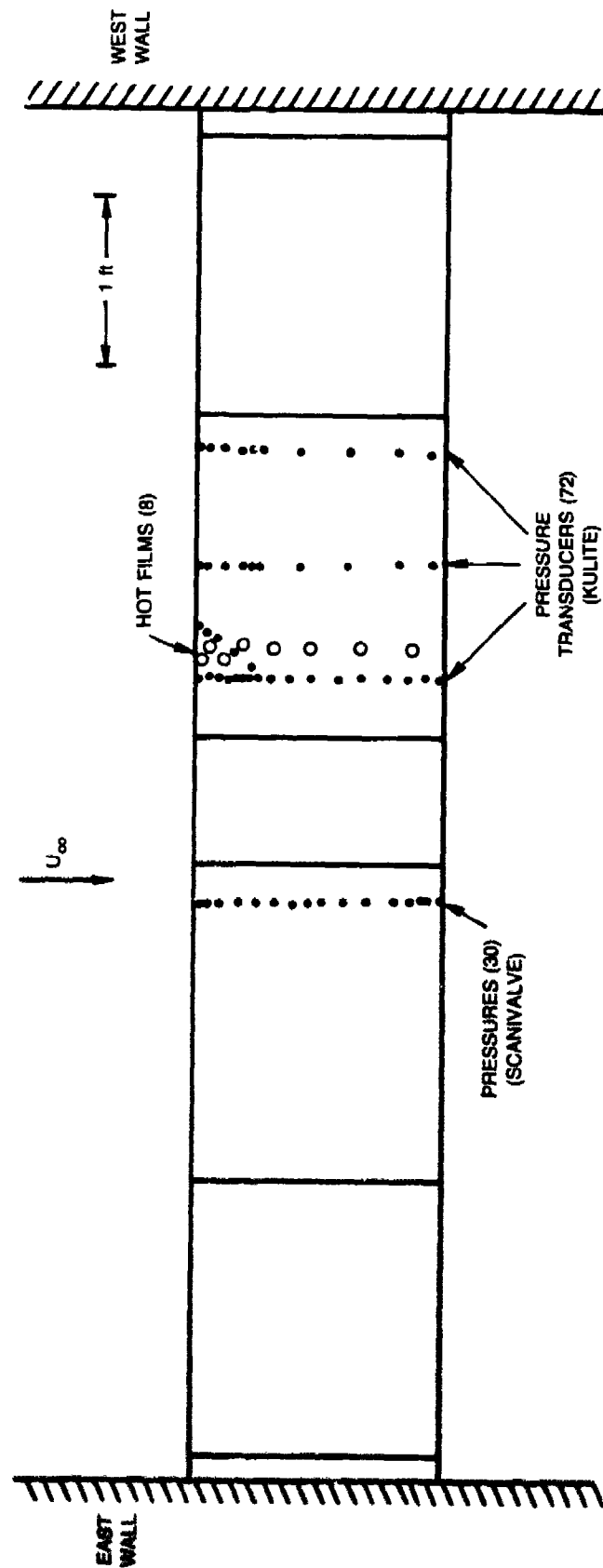


Figure 6. Planform view of the wing model in the test section, showing the instrumentation stations.

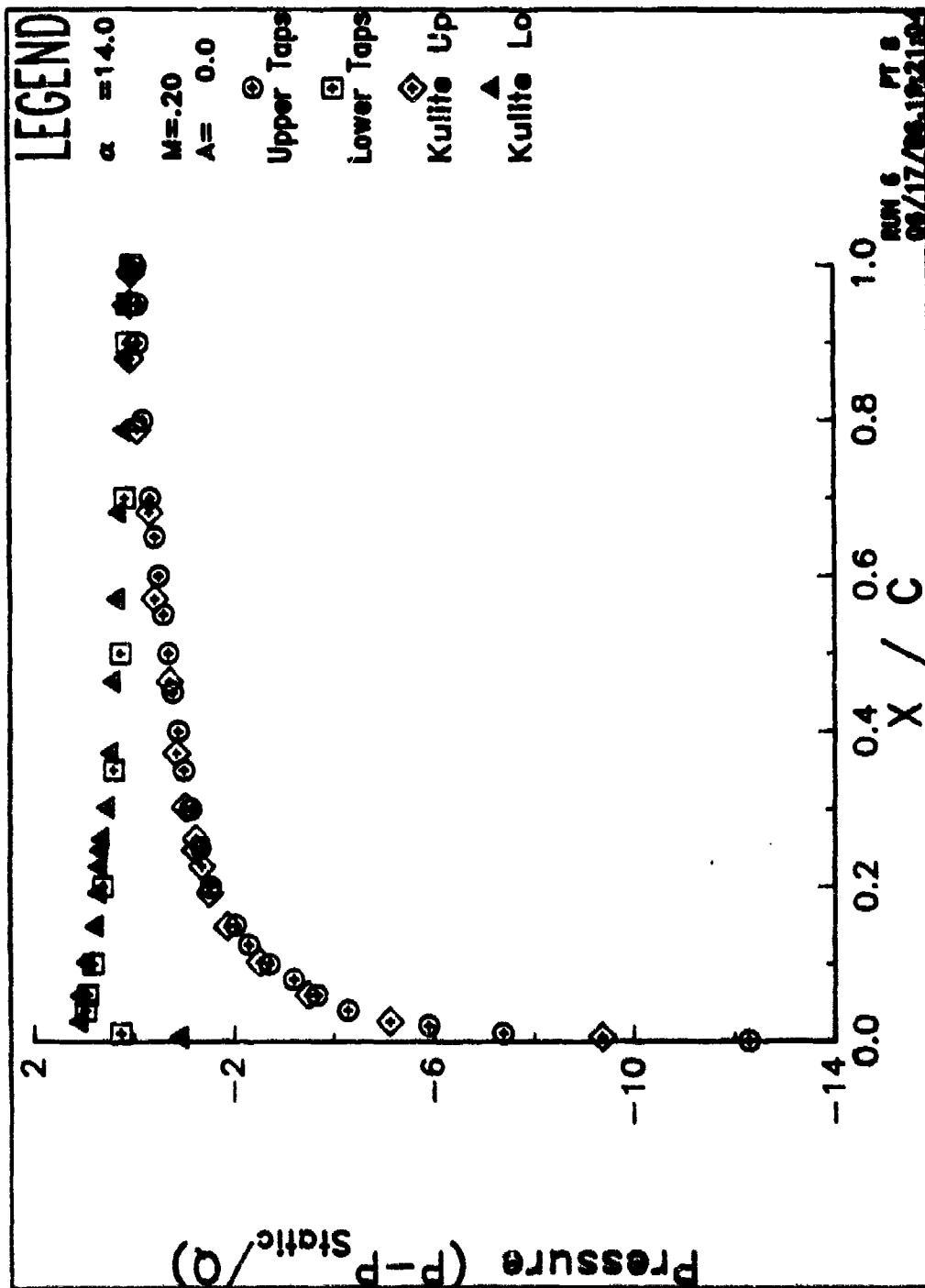


Figure 7. Comparison of steady pressures measured with pressure taps and miniature transducers at  $M = 0.2$ . a) Attached flow at  $\alpha = 14$  deg.

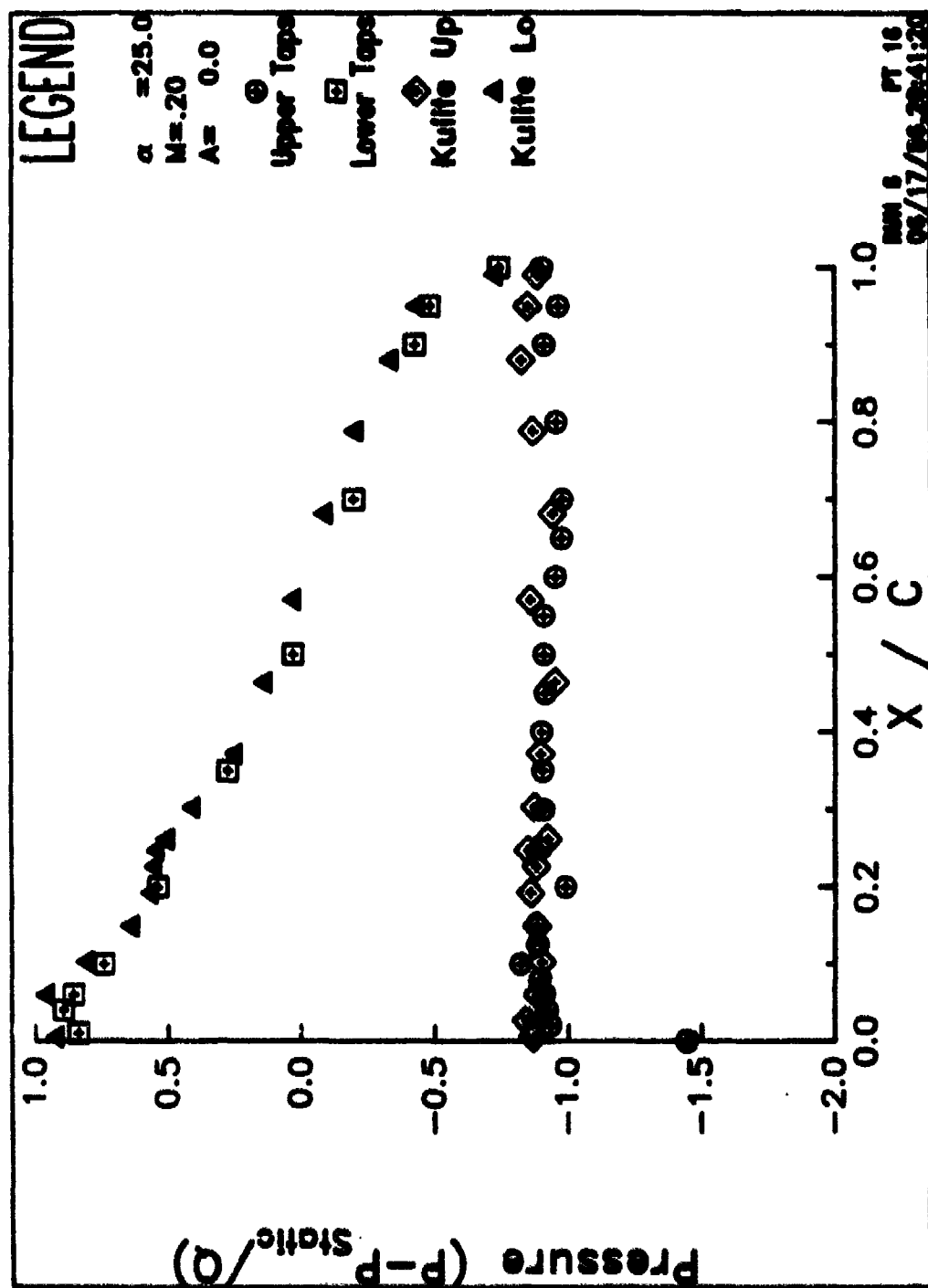


Figure 7. Comparison of steady pressures measured with pressure taps and miniature transducers at  $M = 0.2$ . b) Separated flow at  $\alpha = 25$  deg.

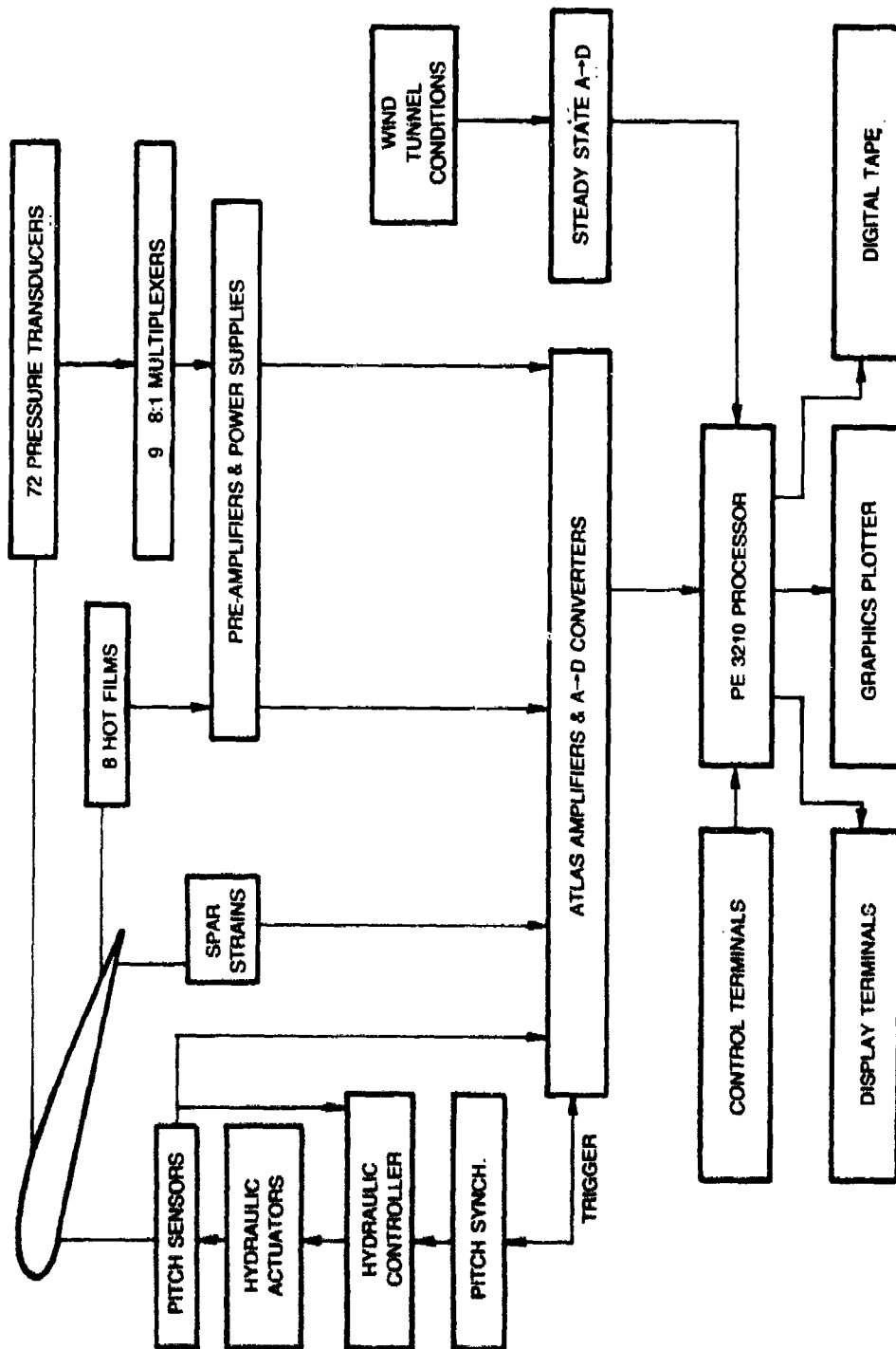


Figure 8. Block diagram of the model instrumentation and control system.

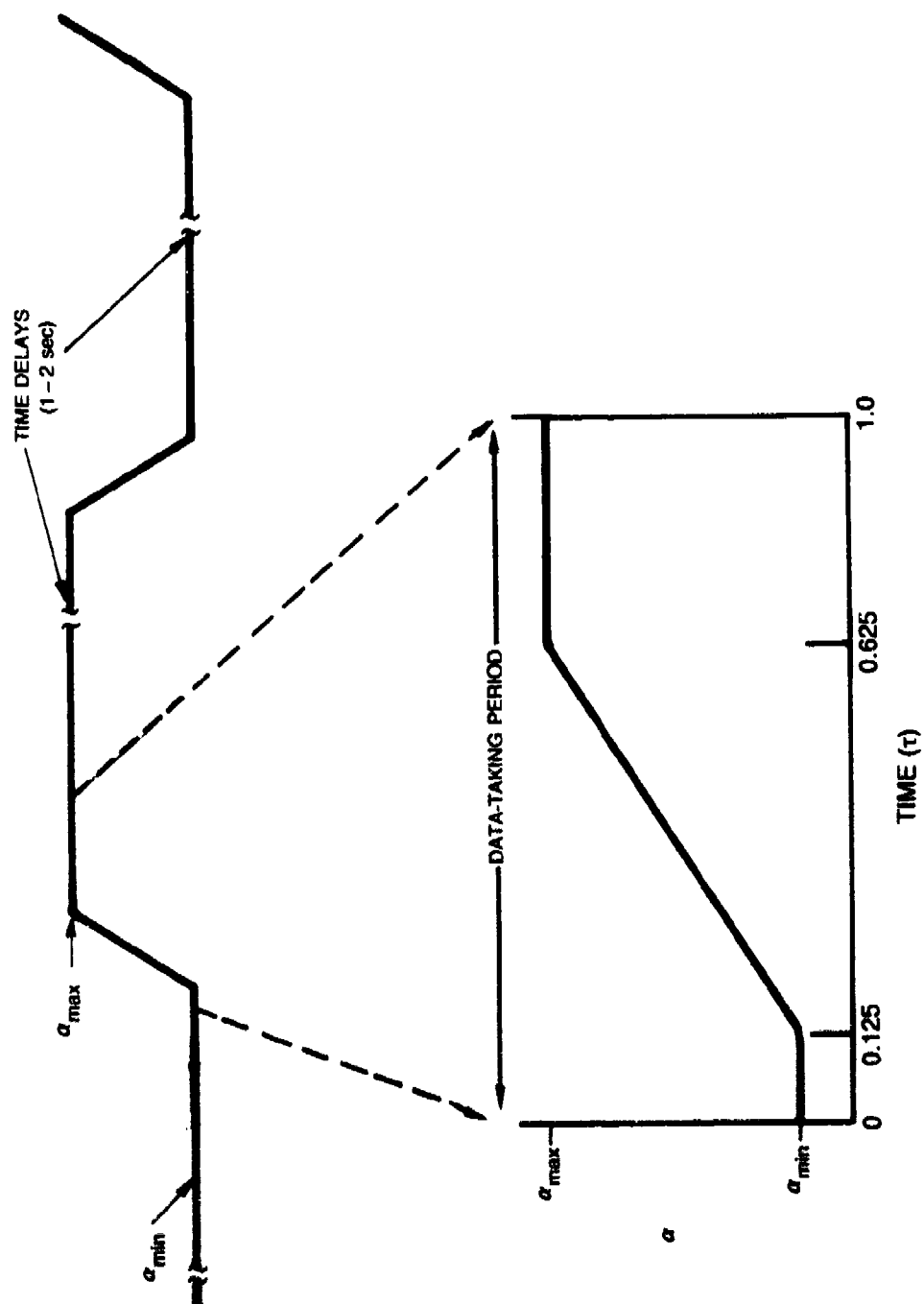


Figure 9. Model motion during constant pitch rate ramps, showing data acquisition period.



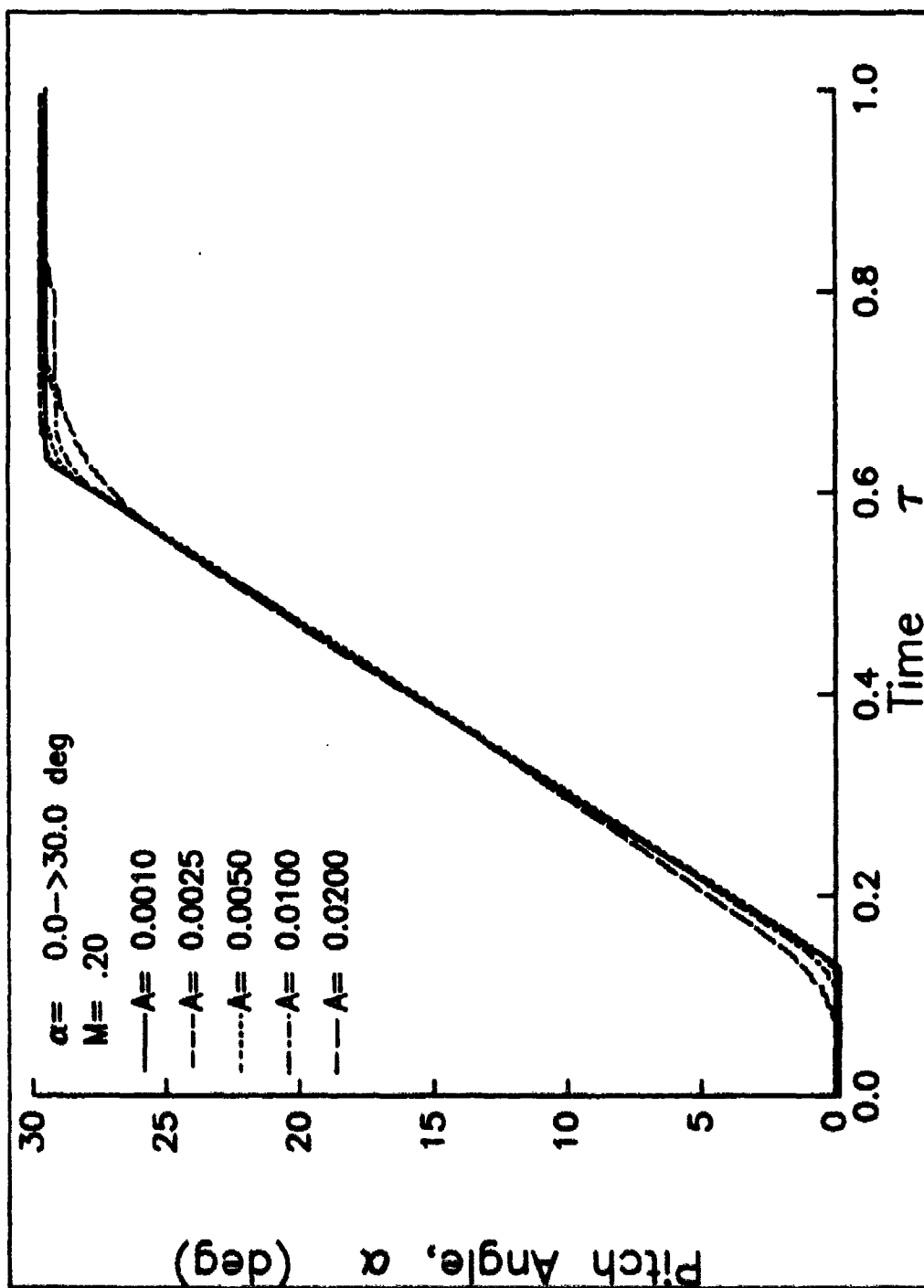


Figure 10. Time histories of the pitch angle for 0 to 30 deg ramps at  $M = 0.2$ .

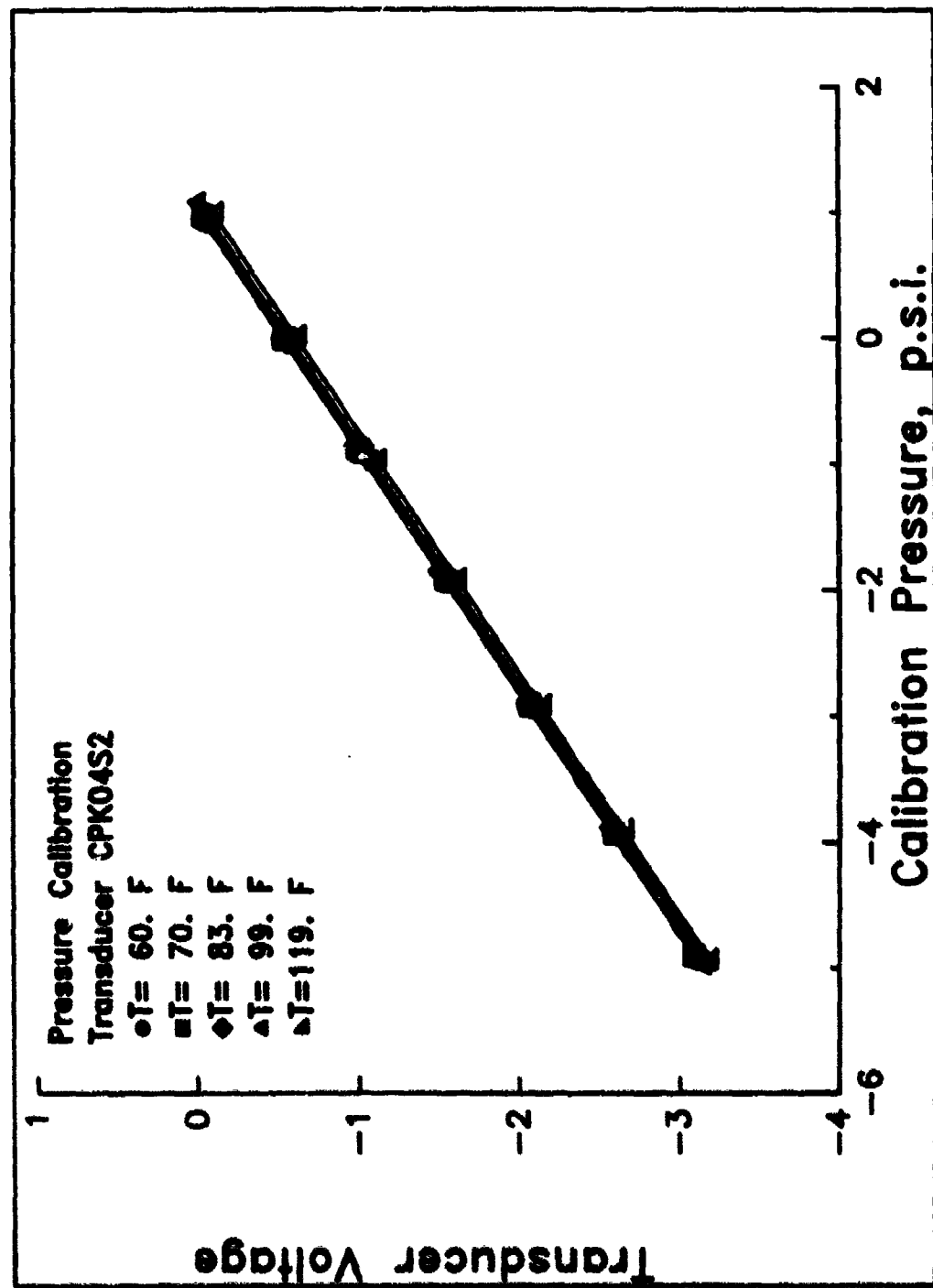


Figure 11. Sample pressure transducer calibration curves at several temperatures.

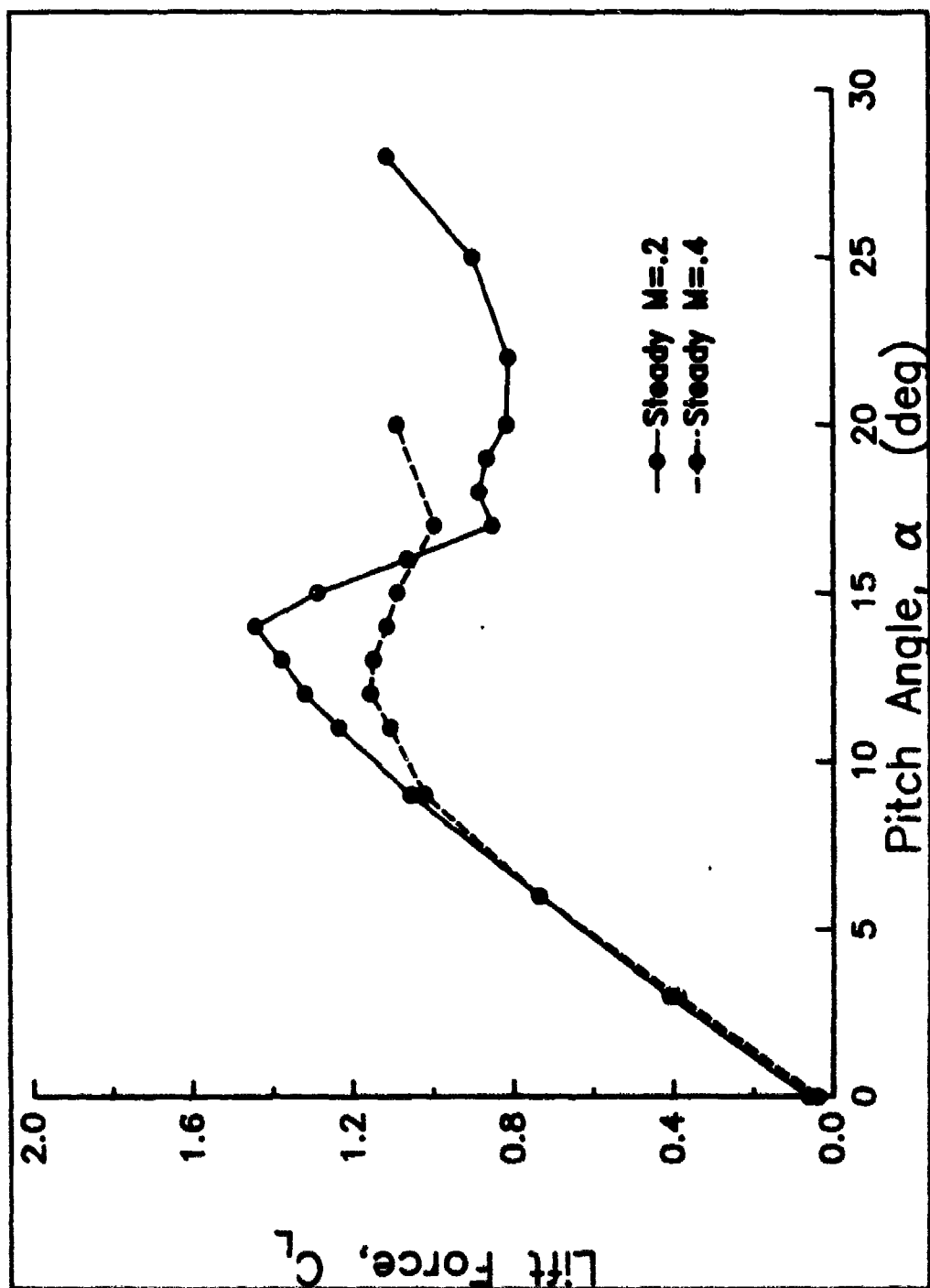


Figure 12. Steady-state airloads at  $M = 0.2$  and  $M = 0.4$ . a) Lift.

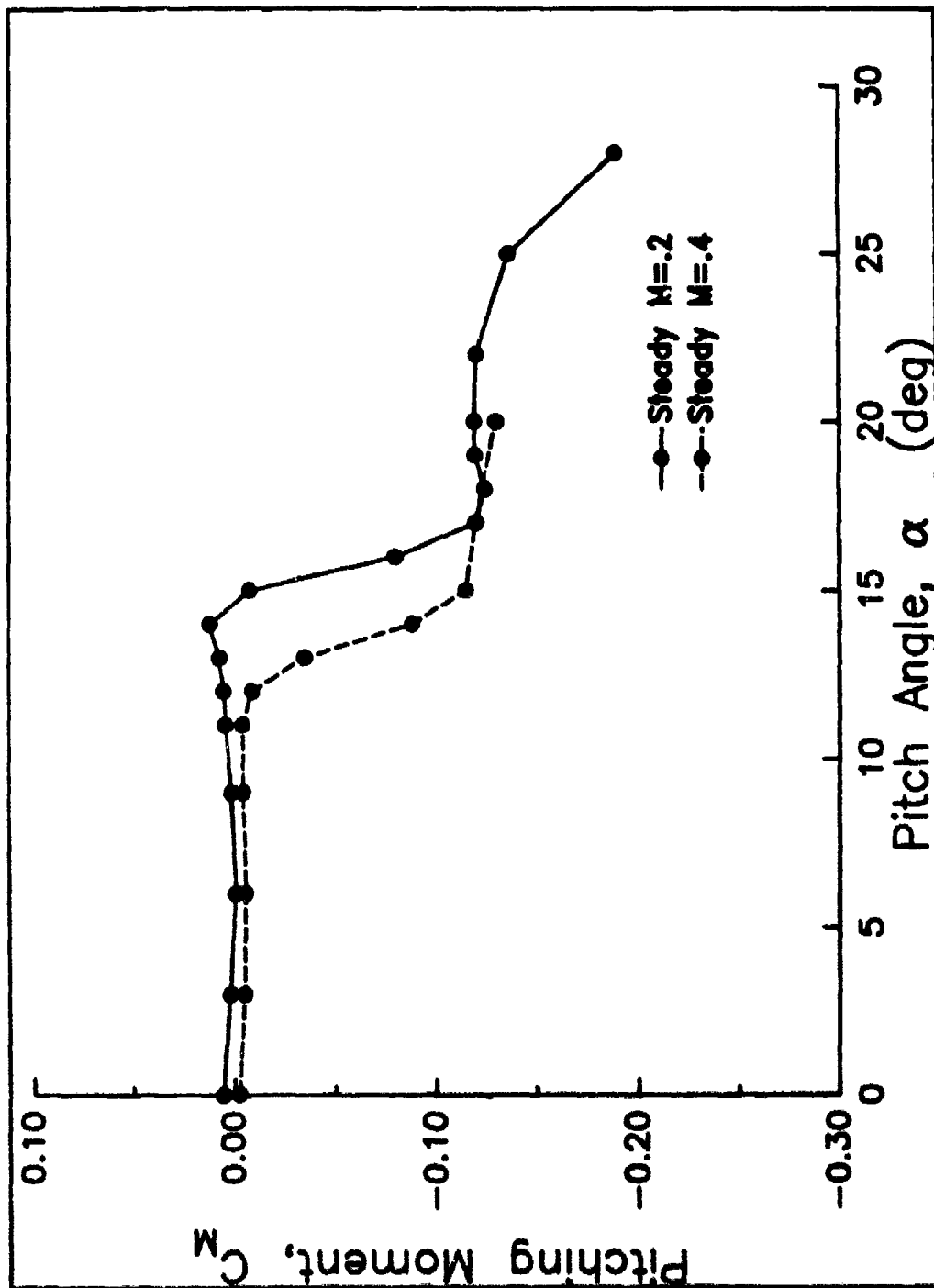


Figure 12. Steady-state airloads at  $M = 0.2$  and  $M = 0.4$ . b) Drag.

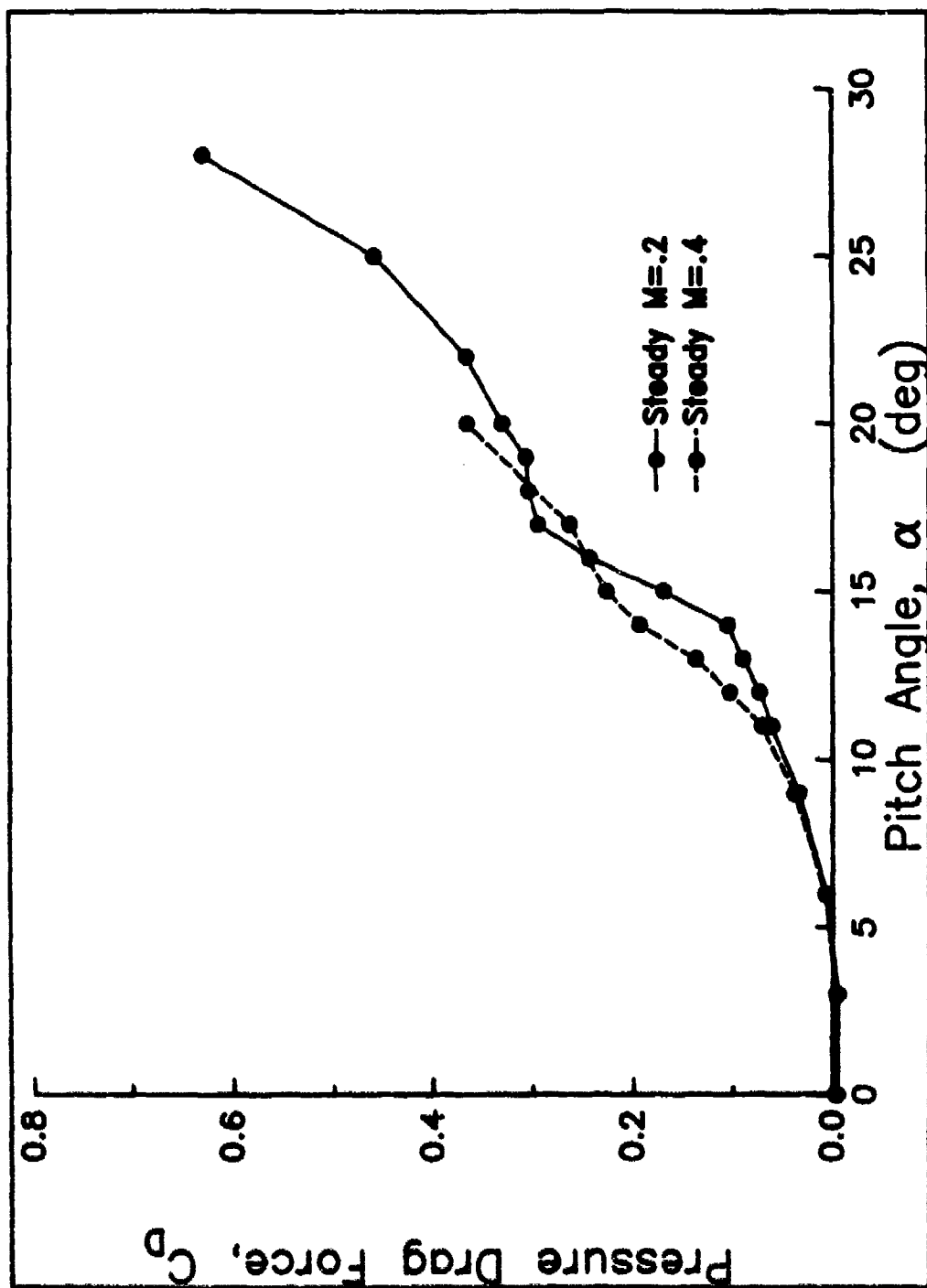


Figure 12. Steady-state airloads at  $M = 0.2$  and  $M = 0.4$ . c) Pitching moment.

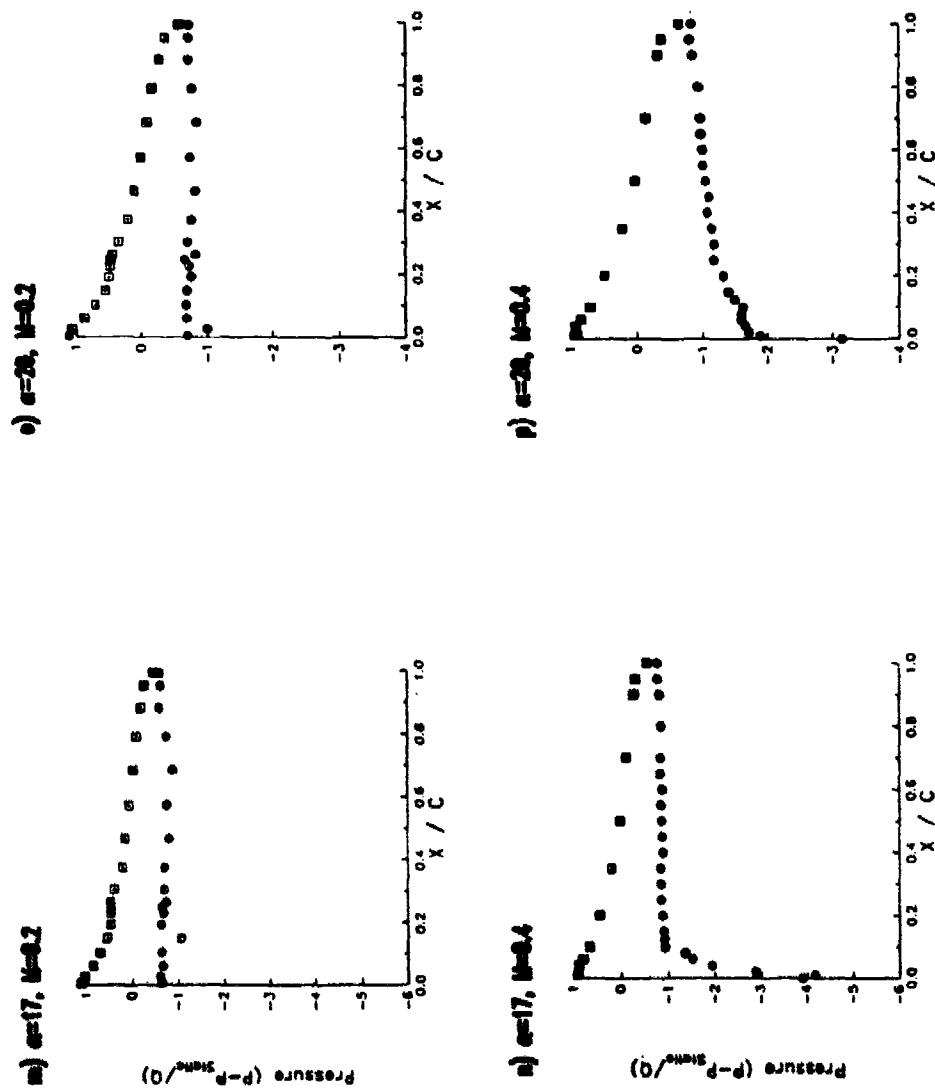


Figure 13. Steady-state pressure distributions at  $M = 0.2$  and  $M = 0.4$ .

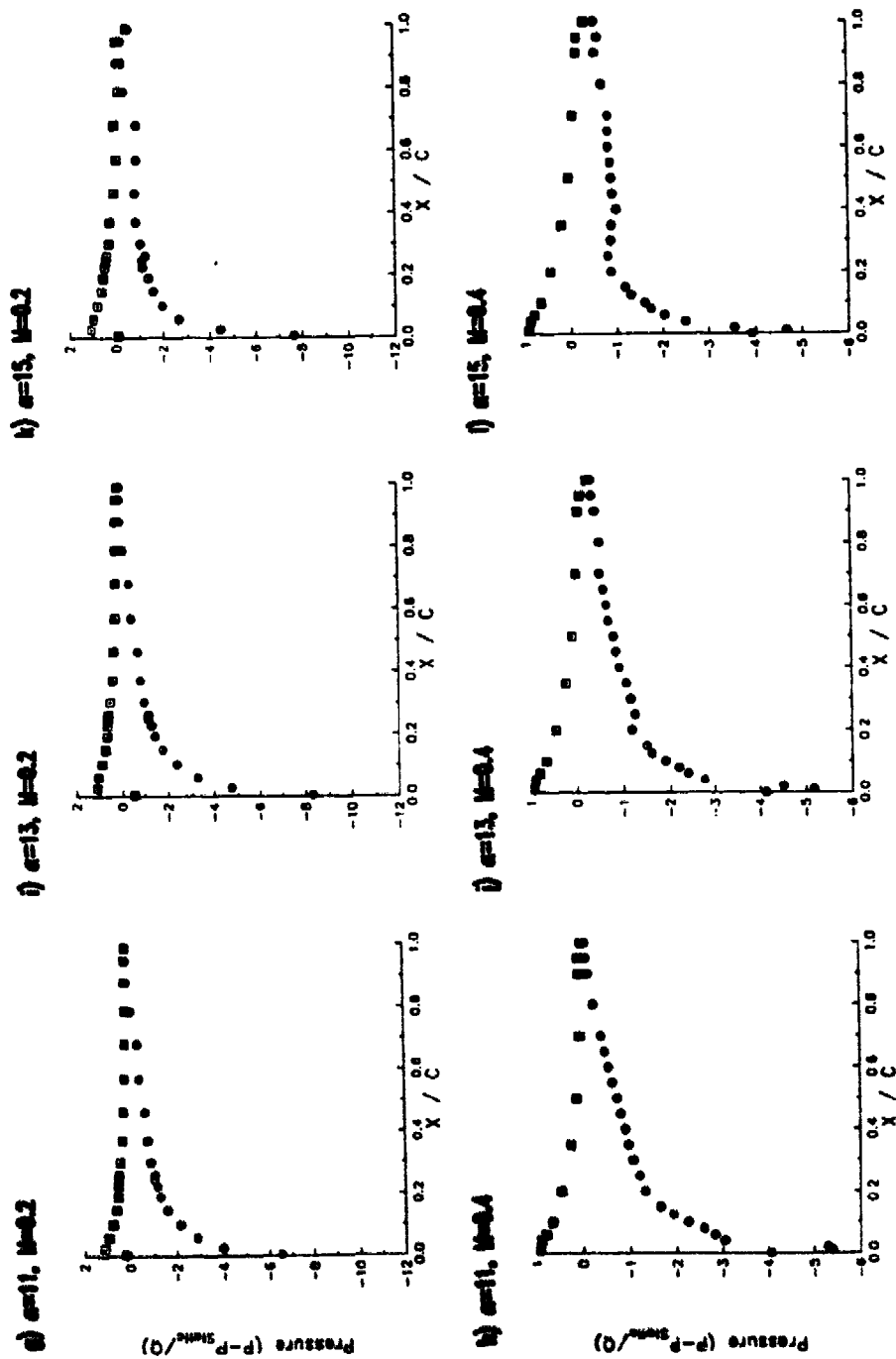


Figure 13. Steady-state pressure distributions at  $M = 0.2$  and  $M = 0.4$ .

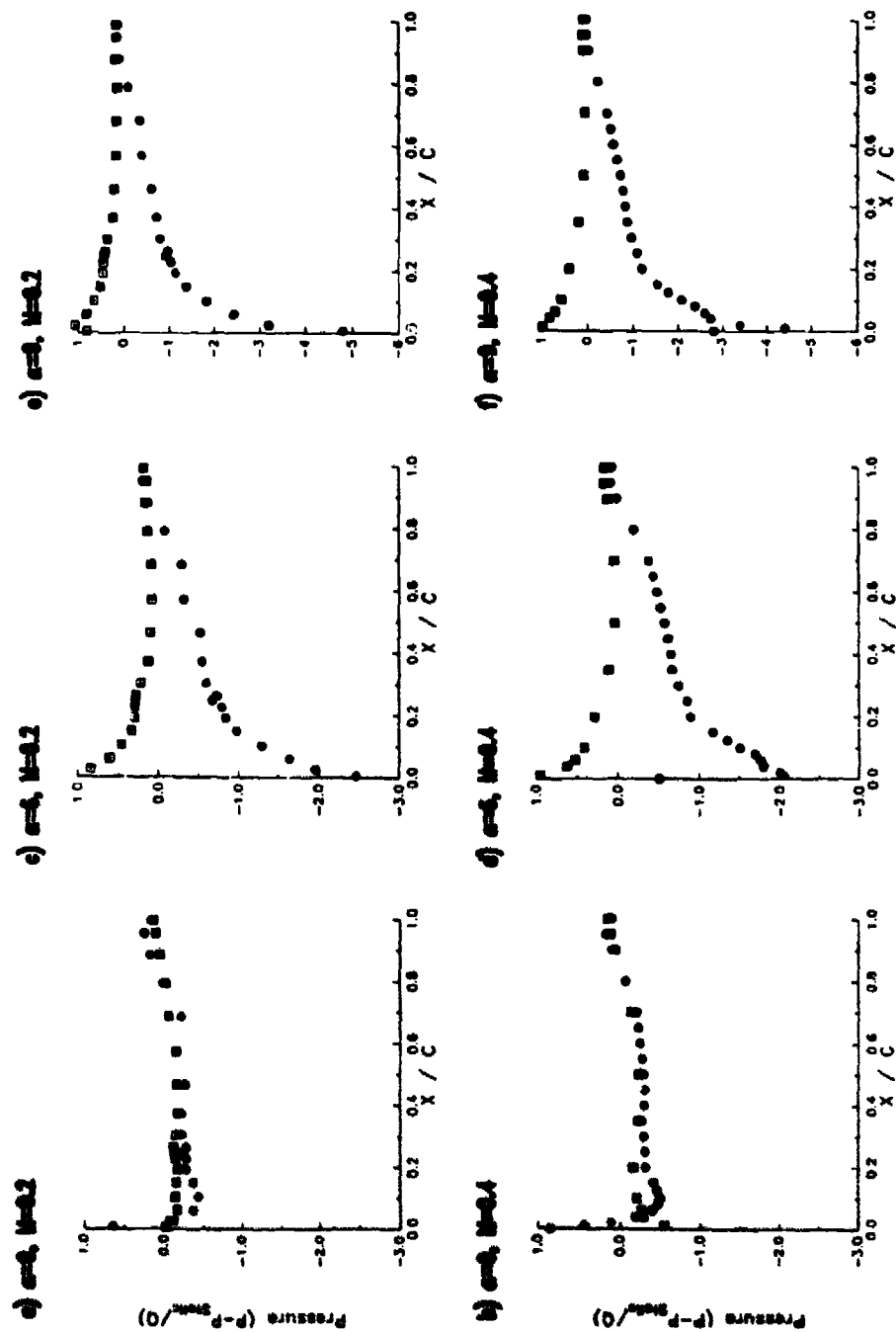


Figure 13. Steady-state pressure distributions at  $M = 0.2$  and  $M = 0.4$ .



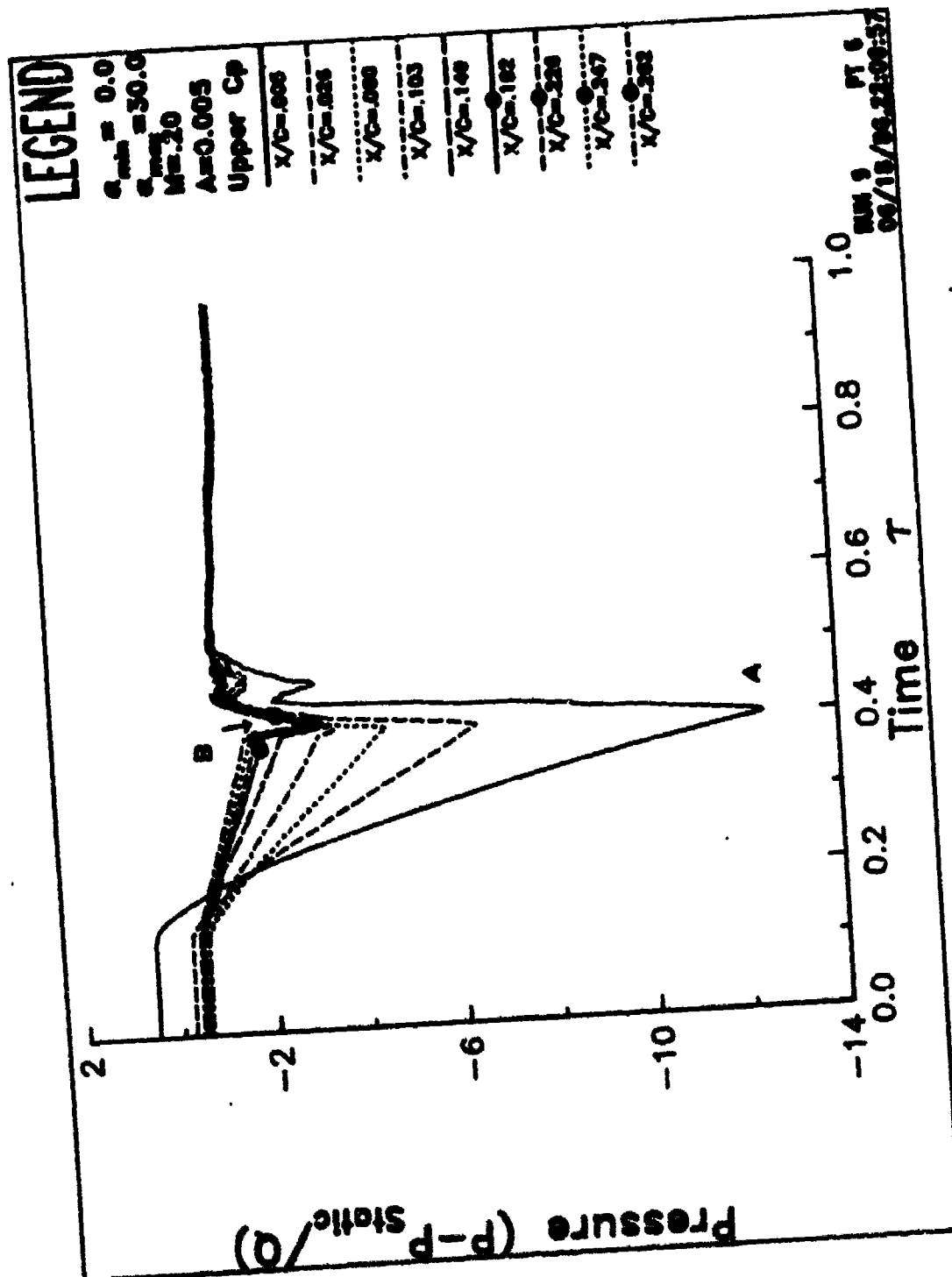


Figure 14. Upper surface pressures. a) forward region.

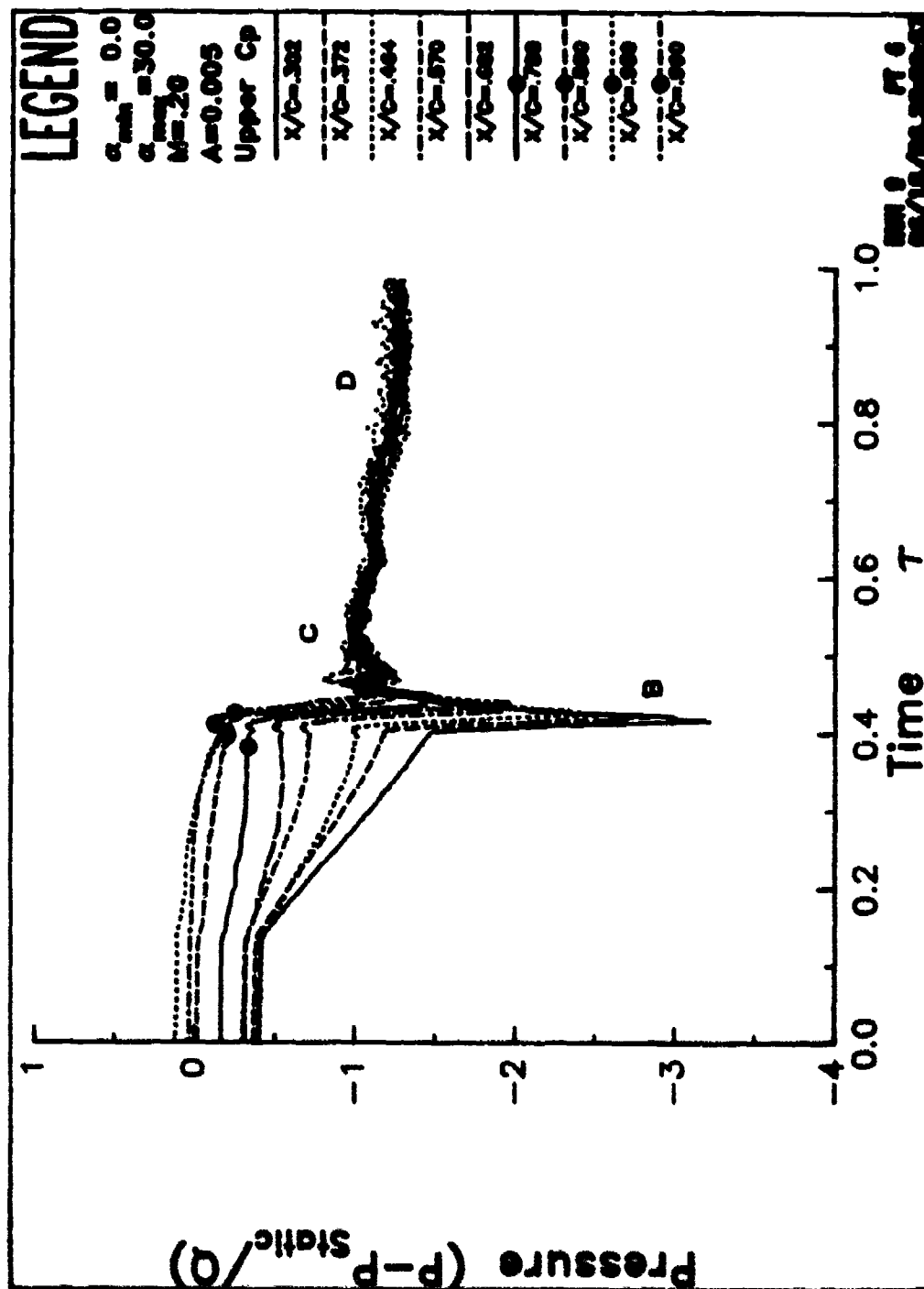


Figure 14. Upper surface pressures. b) Aft region.

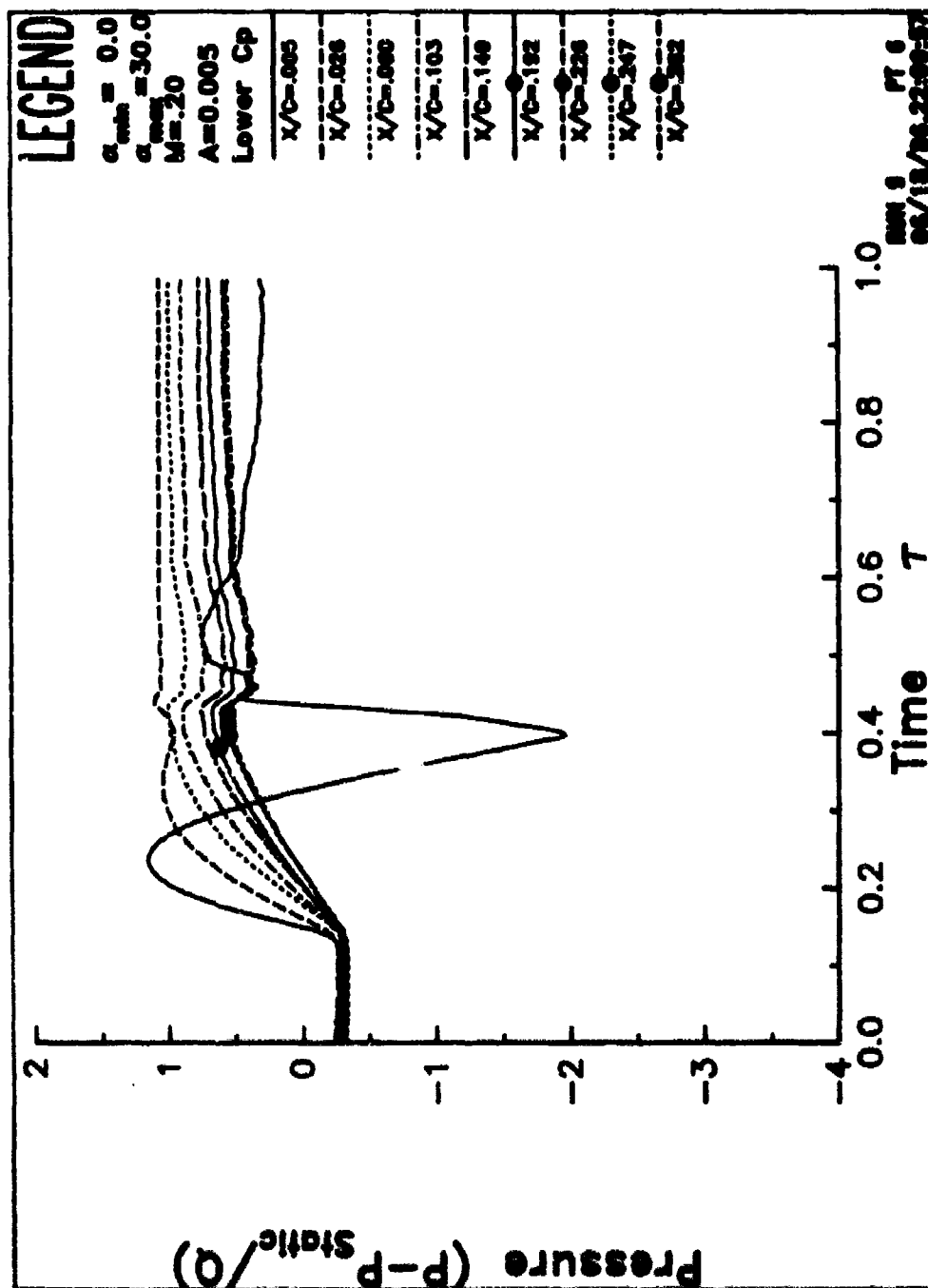


Figure 15. Lower surface pressures. a) forward region.

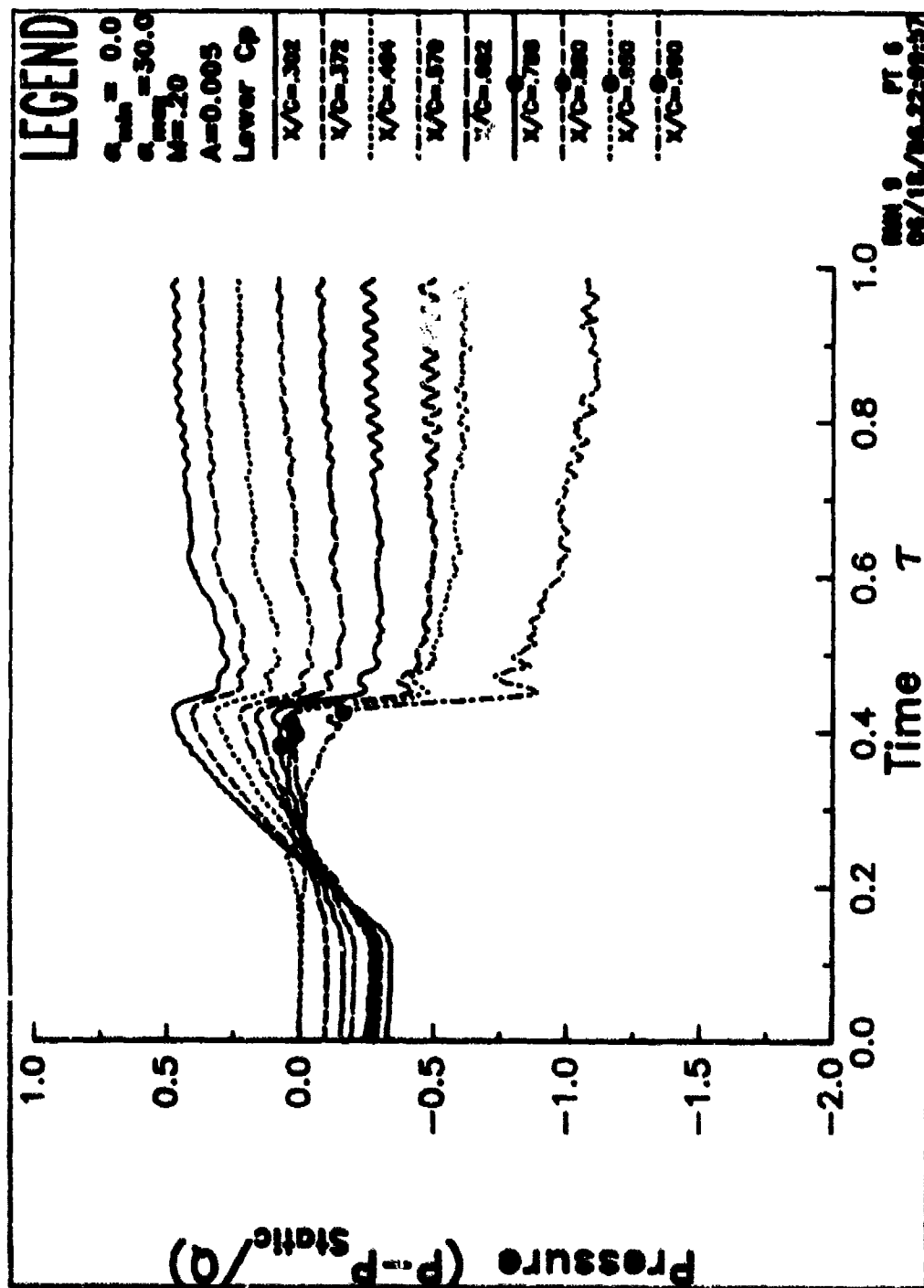


Figure 15. Lower surface pressure. b) Aft region.

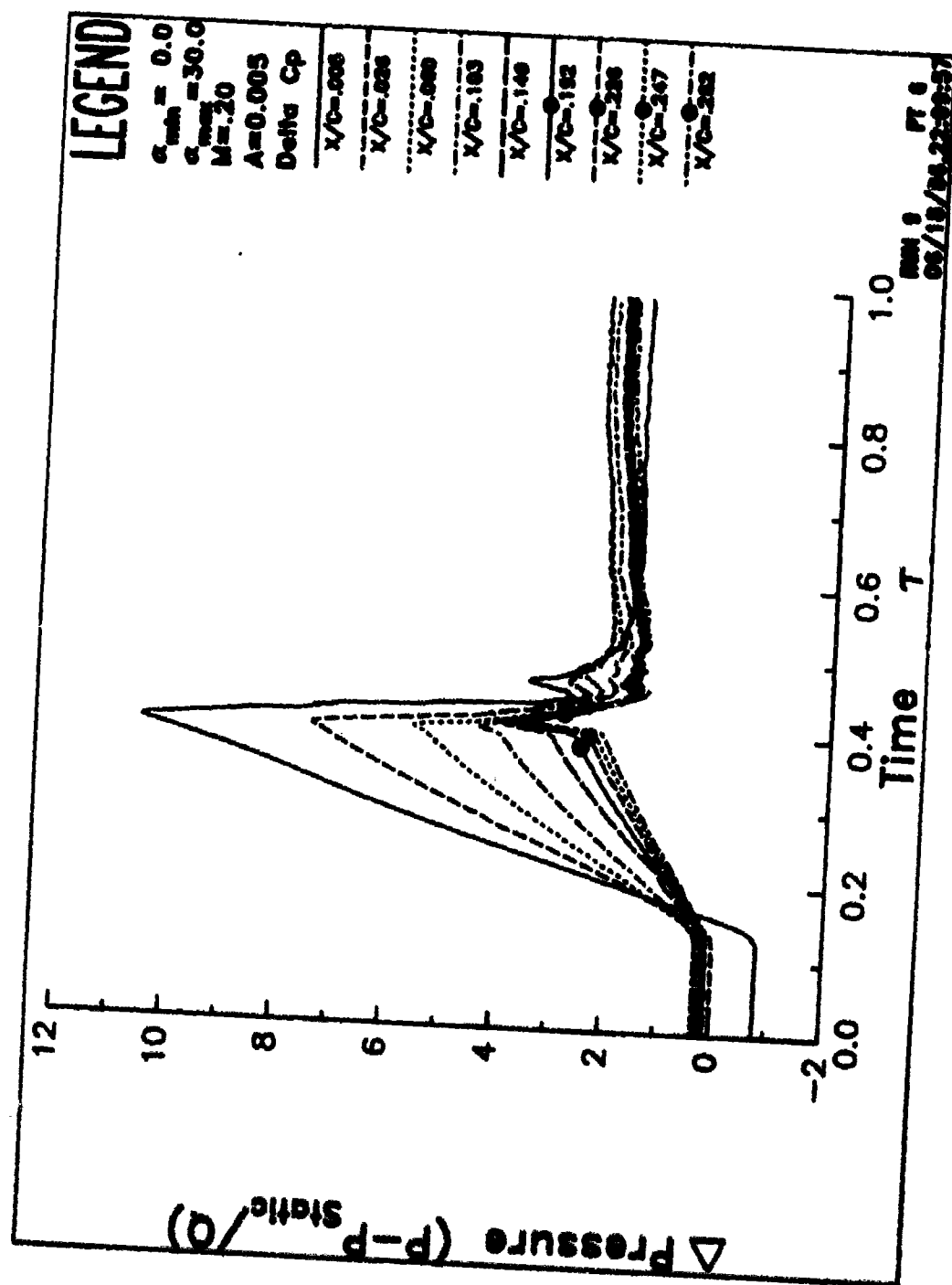


Figure 16. Difference pressures. a) forward region.

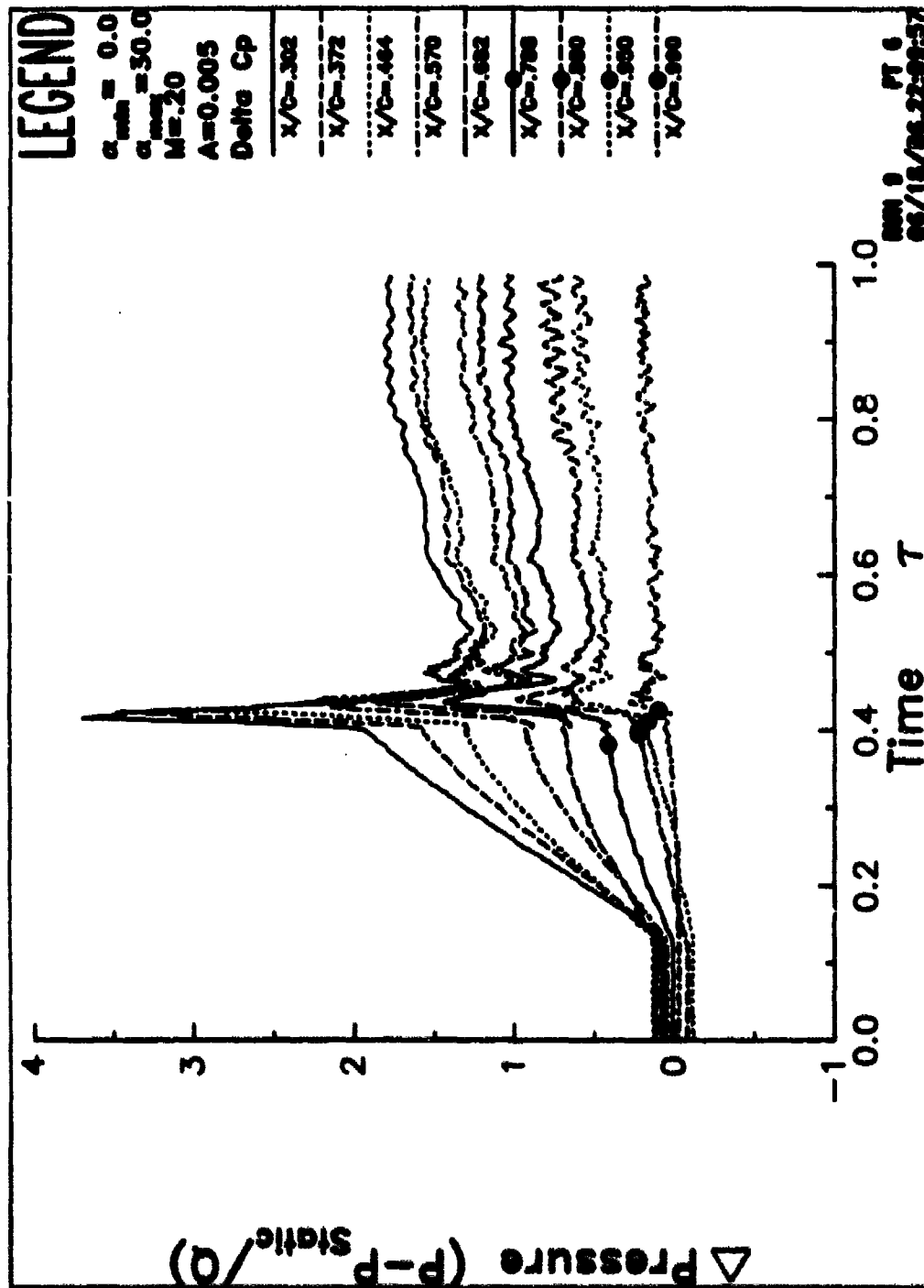


Figure 16. Difference pressures. b) Aft region.

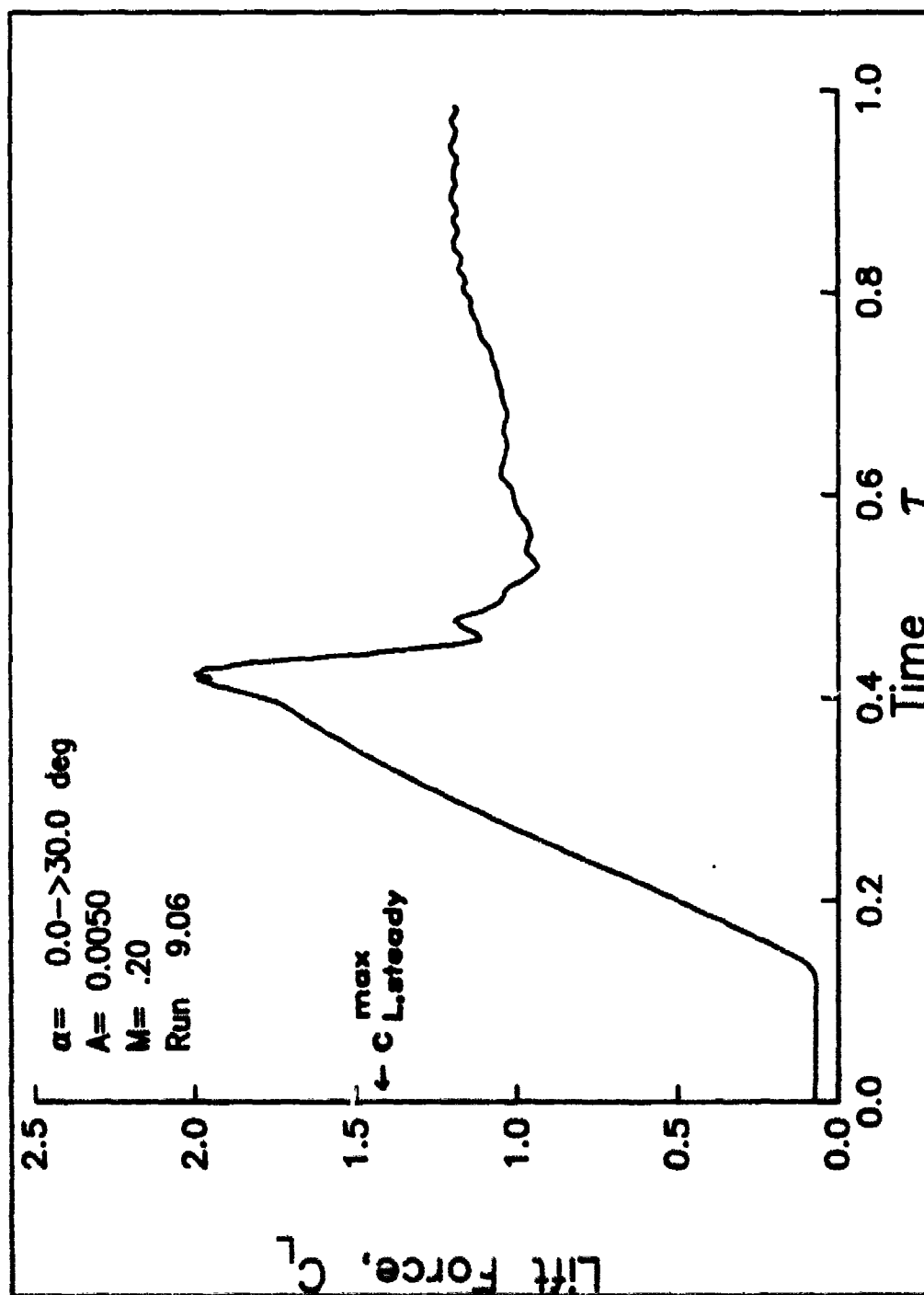


Figure 17. Air loads. a) Lift vs. time.

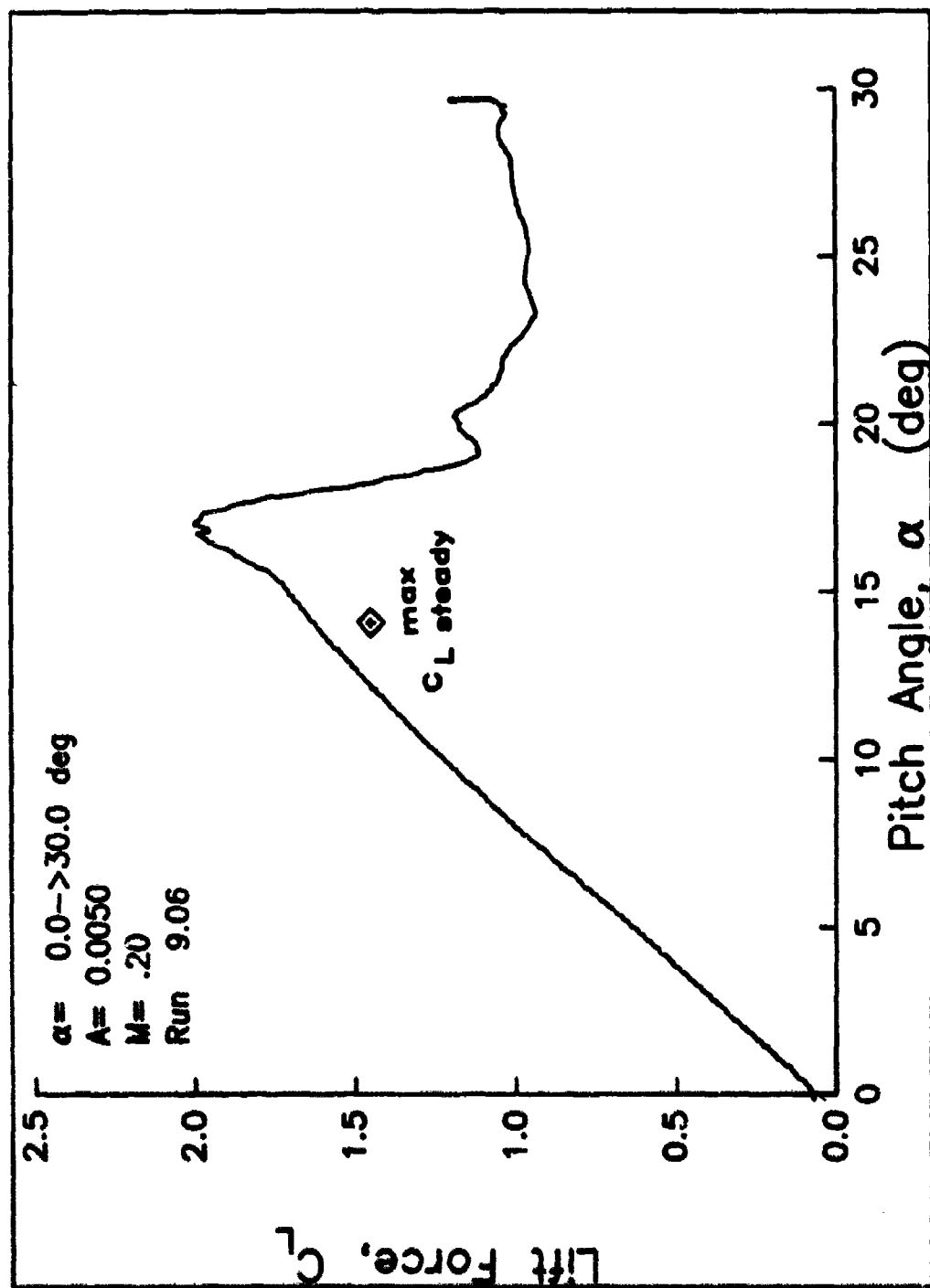


Figure 17. Airloads. b) Lift vs. pitch angle.



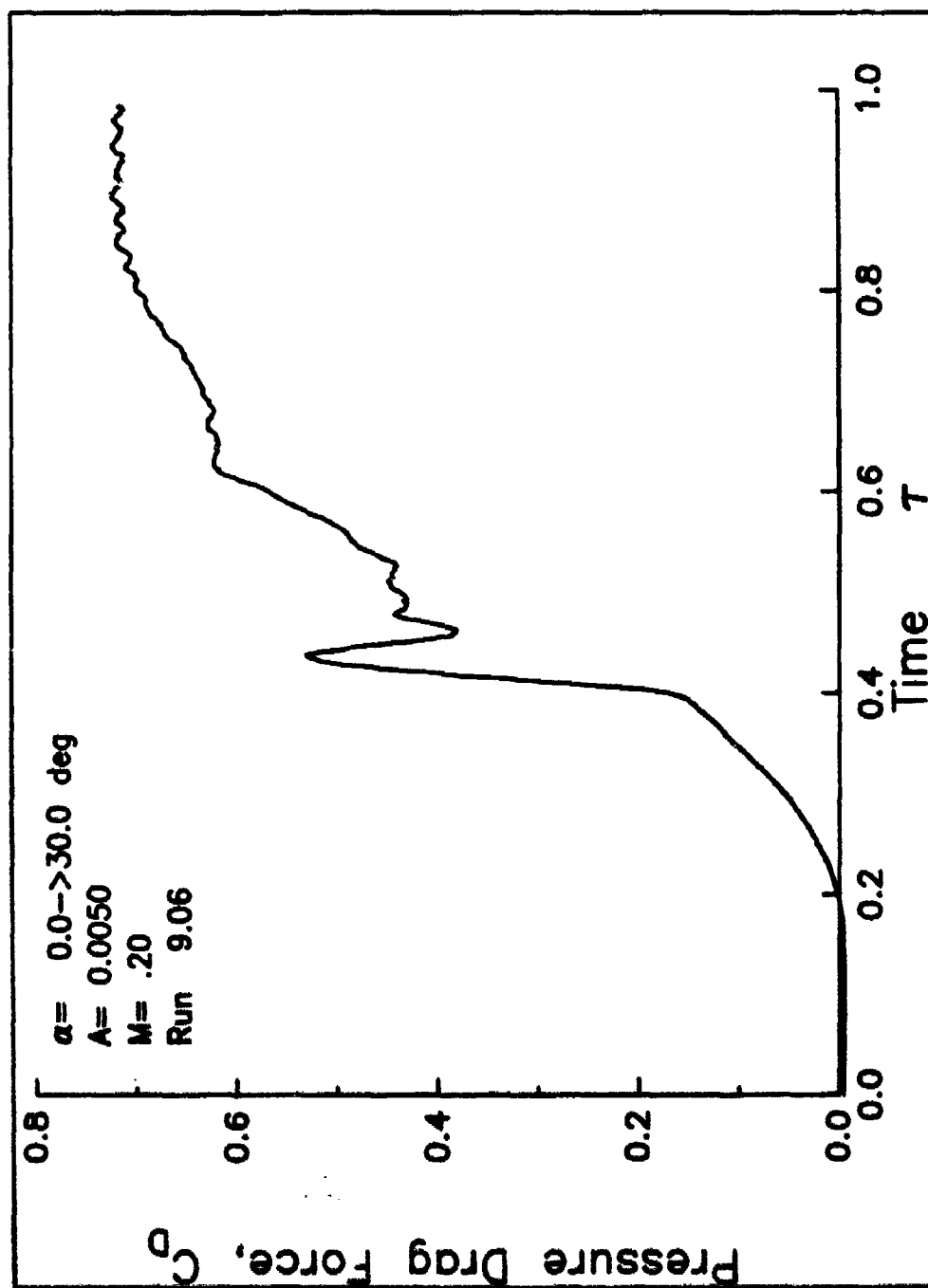


Figure 17. Airloads. c) Drag vs. time.

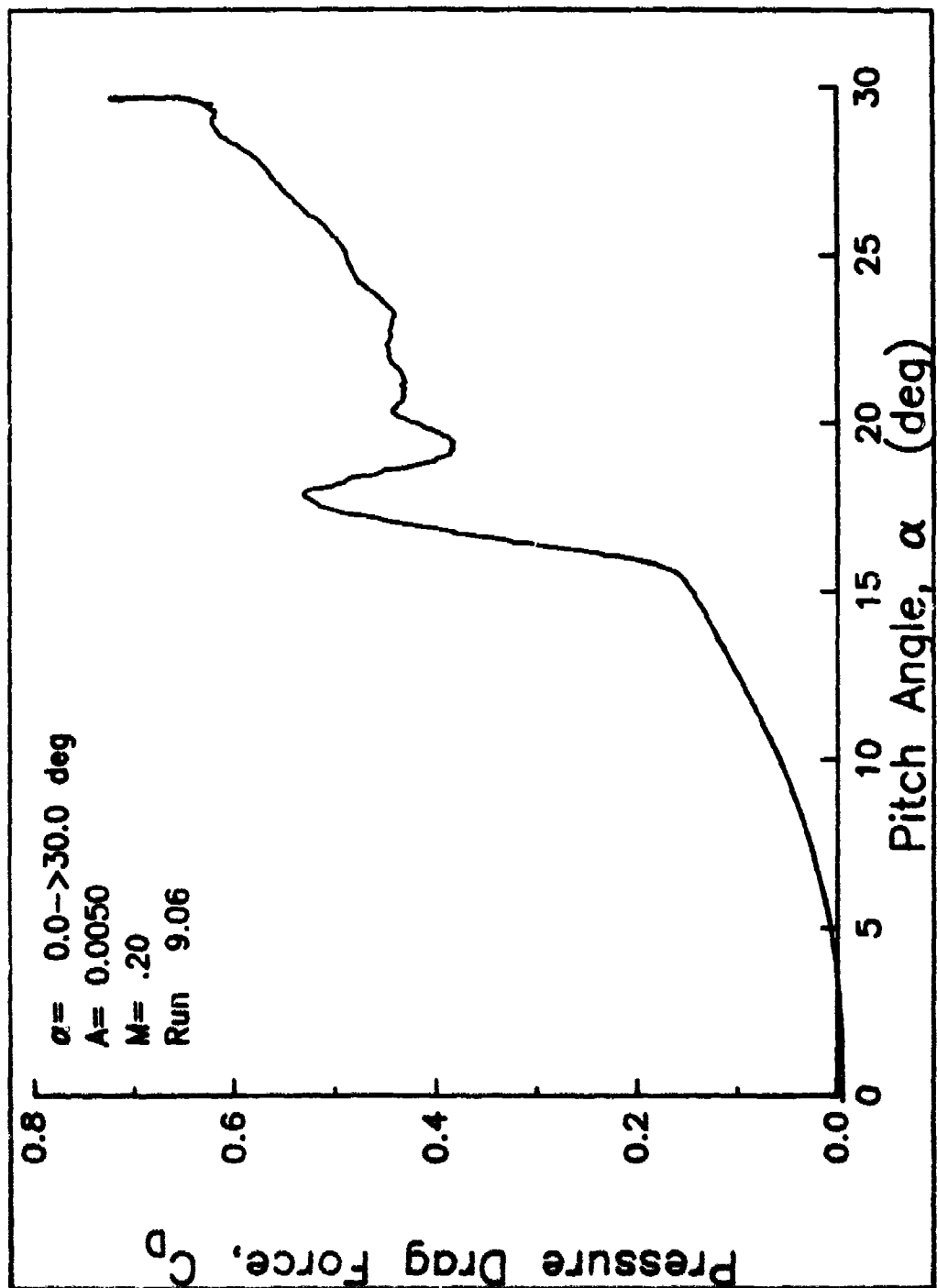


Figure 17. Airloads. d) Drag vs. pitch angle.

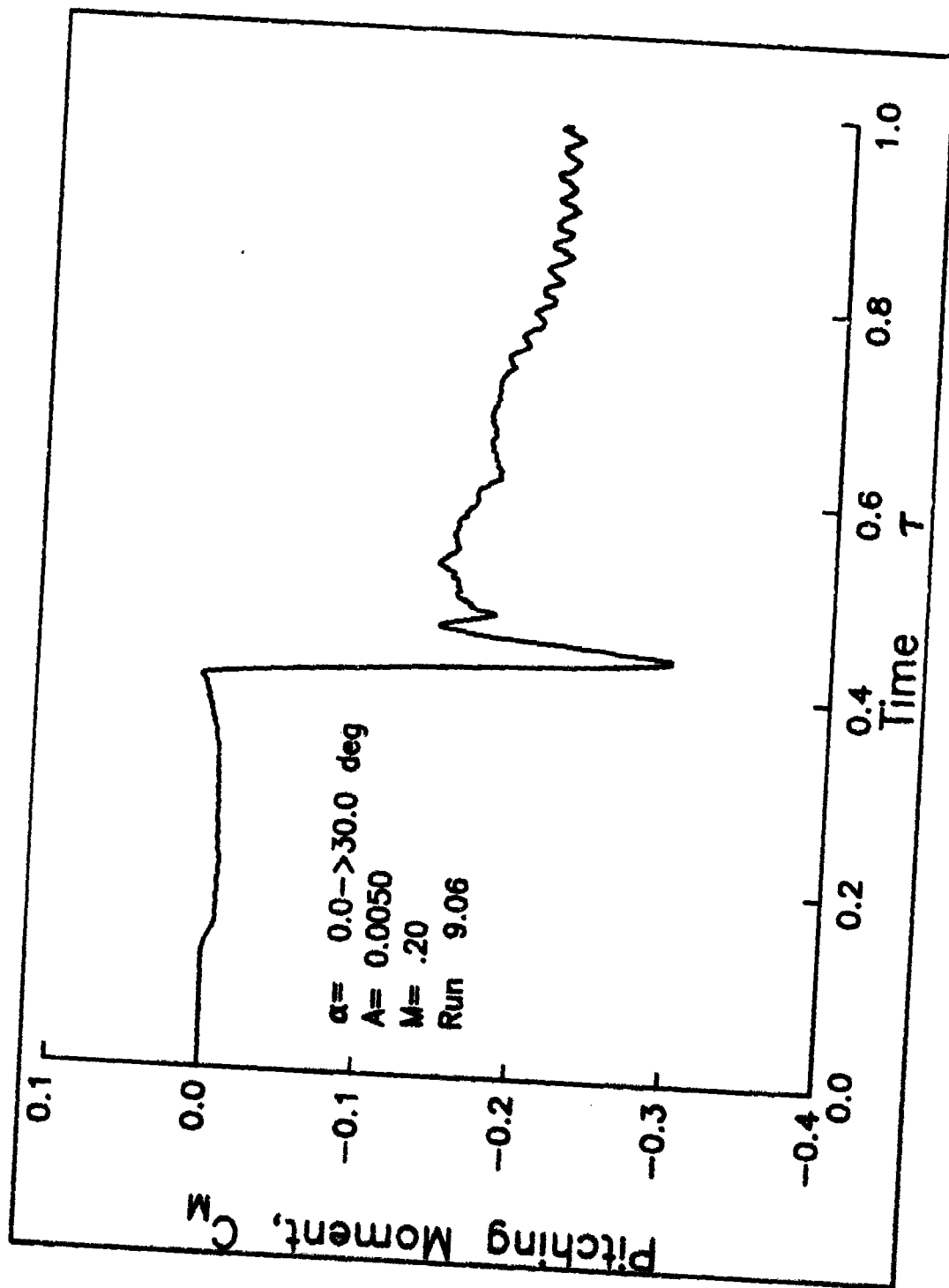


Figure 17. Airloads. e) Moment vs. time.

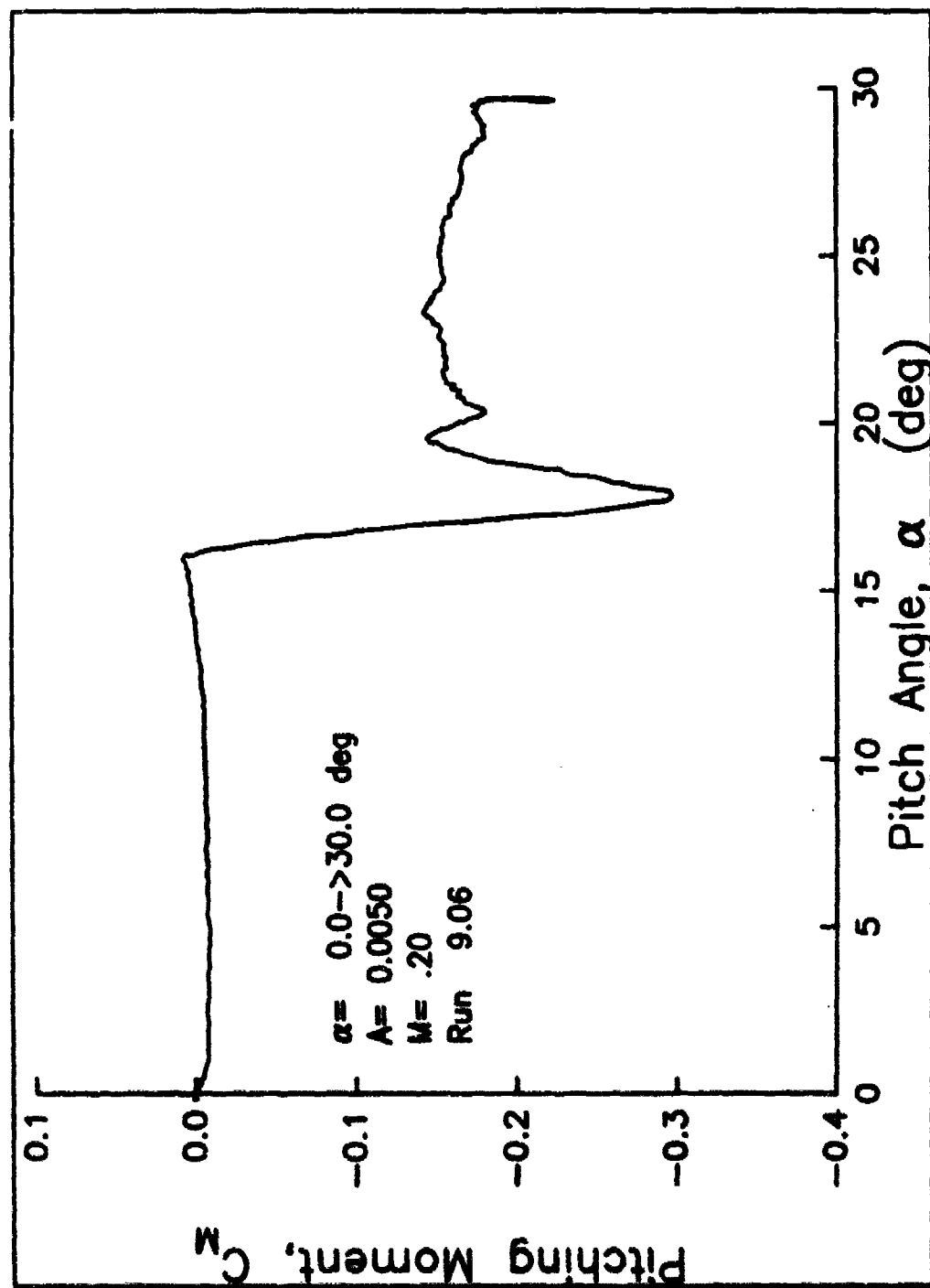


Figure 17. Airloads. f) Moment vs. pitch angle.

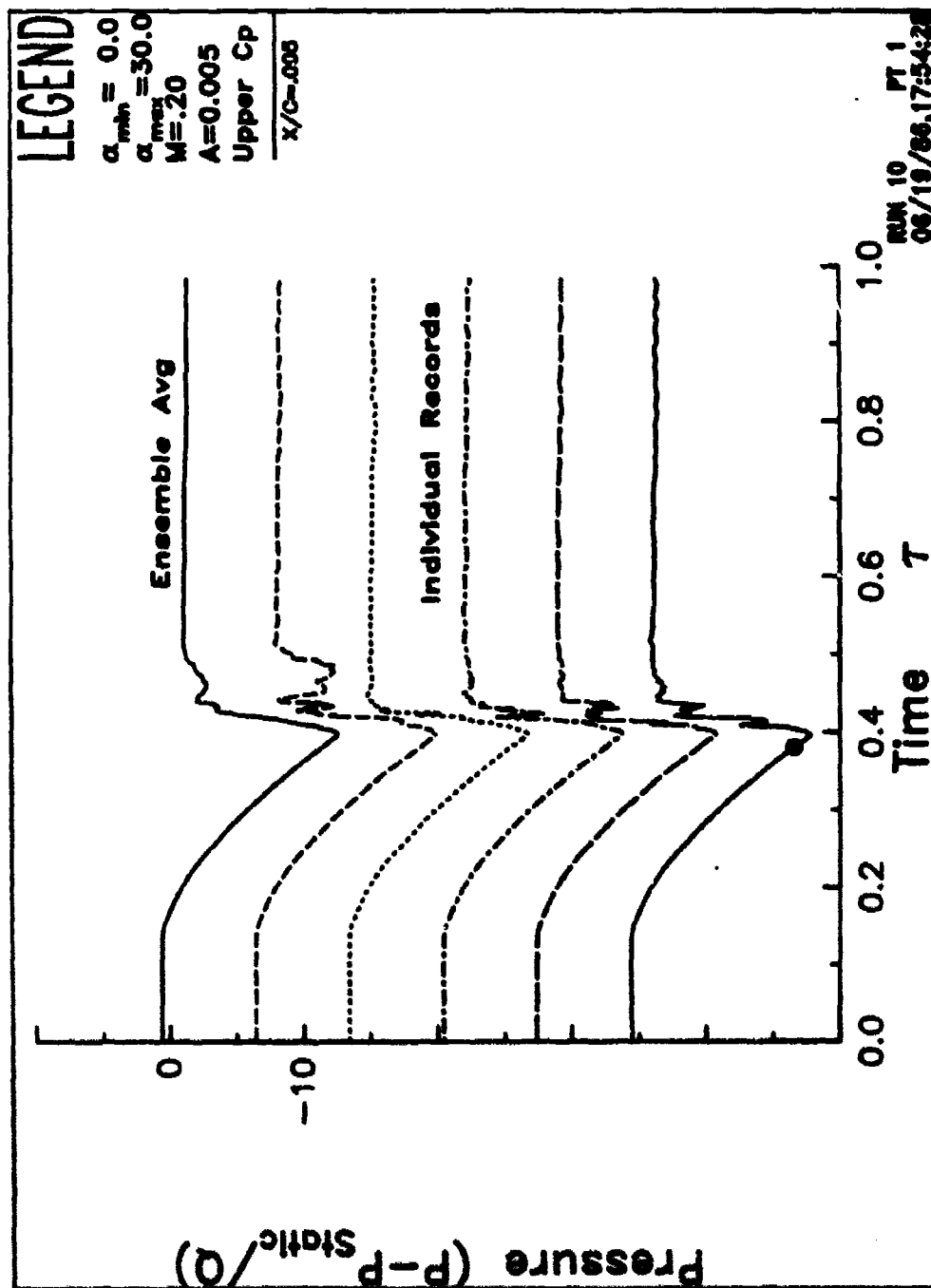


Figure 18. Individual upper surface pressure records. a)  $x/c = 0.005$ .

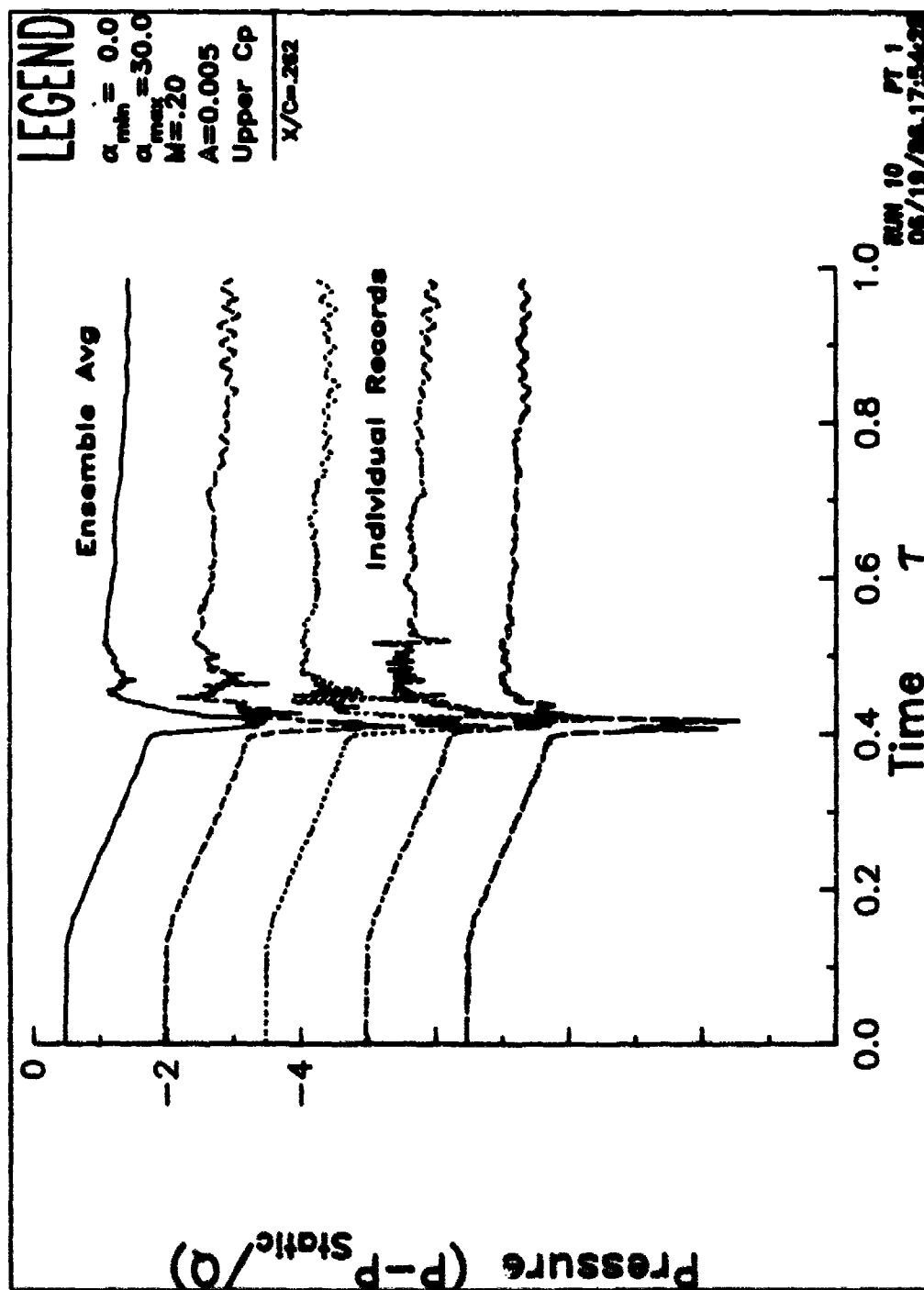


Figure 18. Individual upper surface pressure records. b)  $x/c = 0.262$

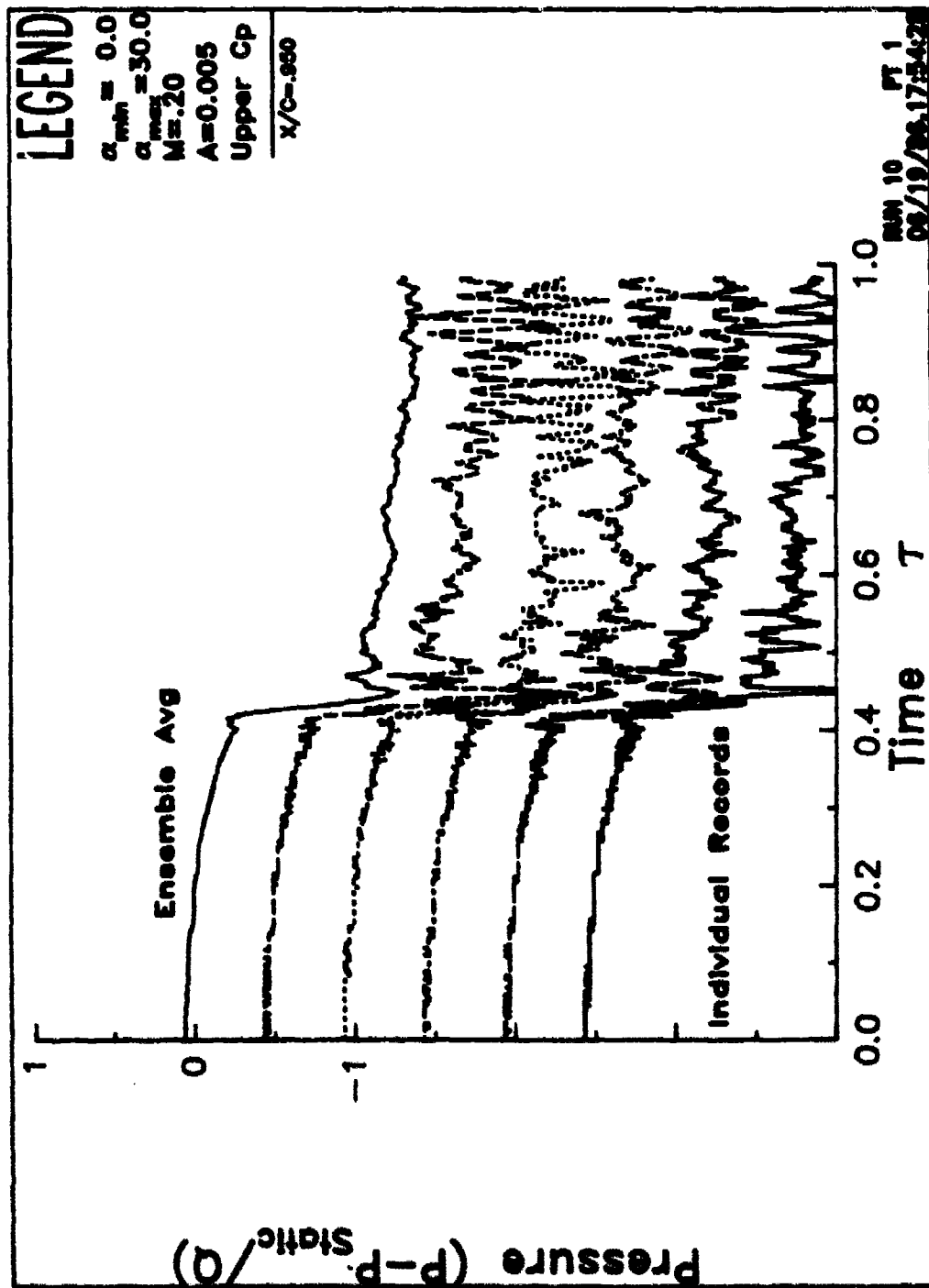


Figure 18. Individual upper surface pressure records. c)  $x/c = 0.950$ .

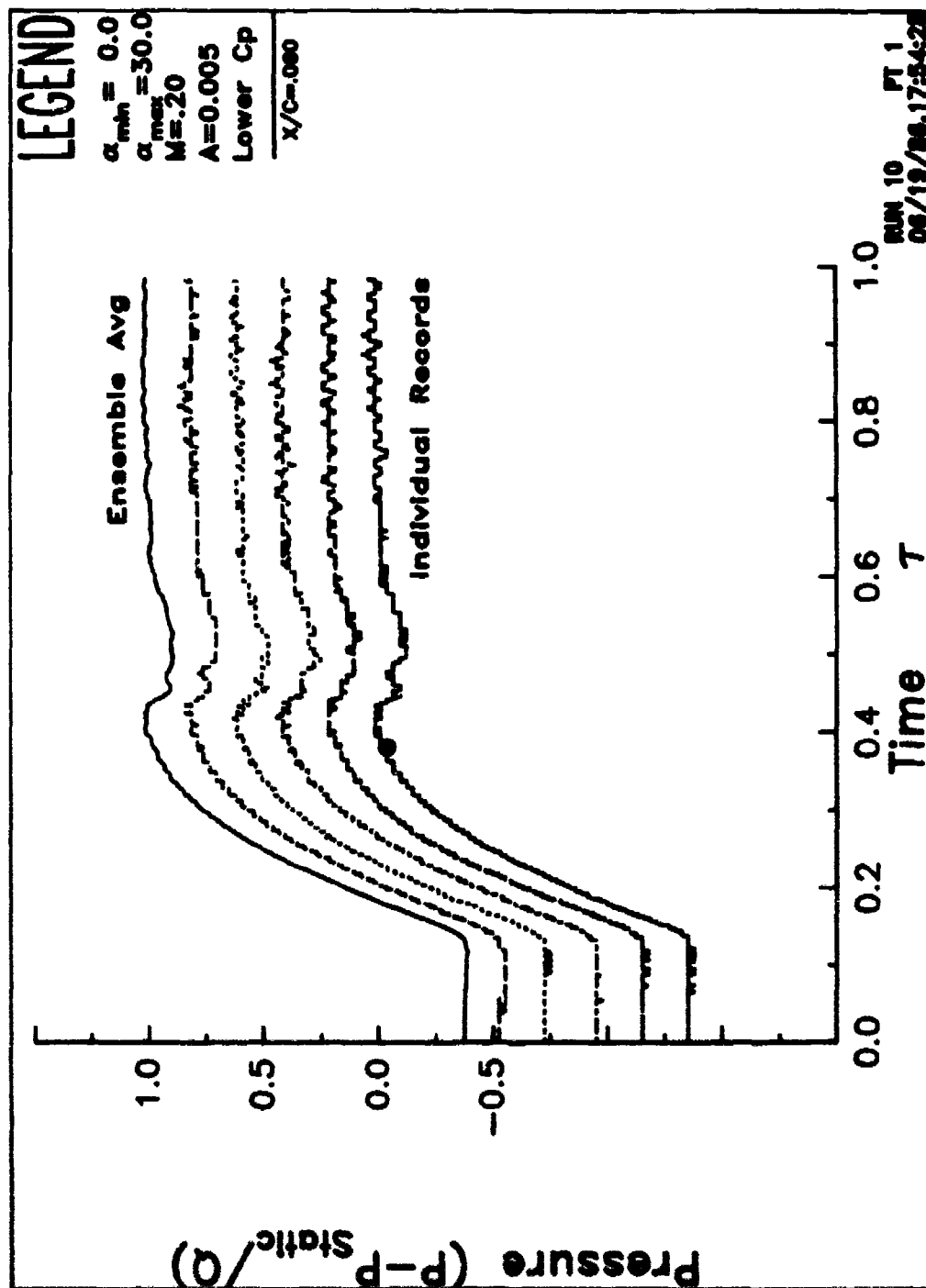


Figure 19. Individual lower surface pressure records. a)  $x/c = 0.060$



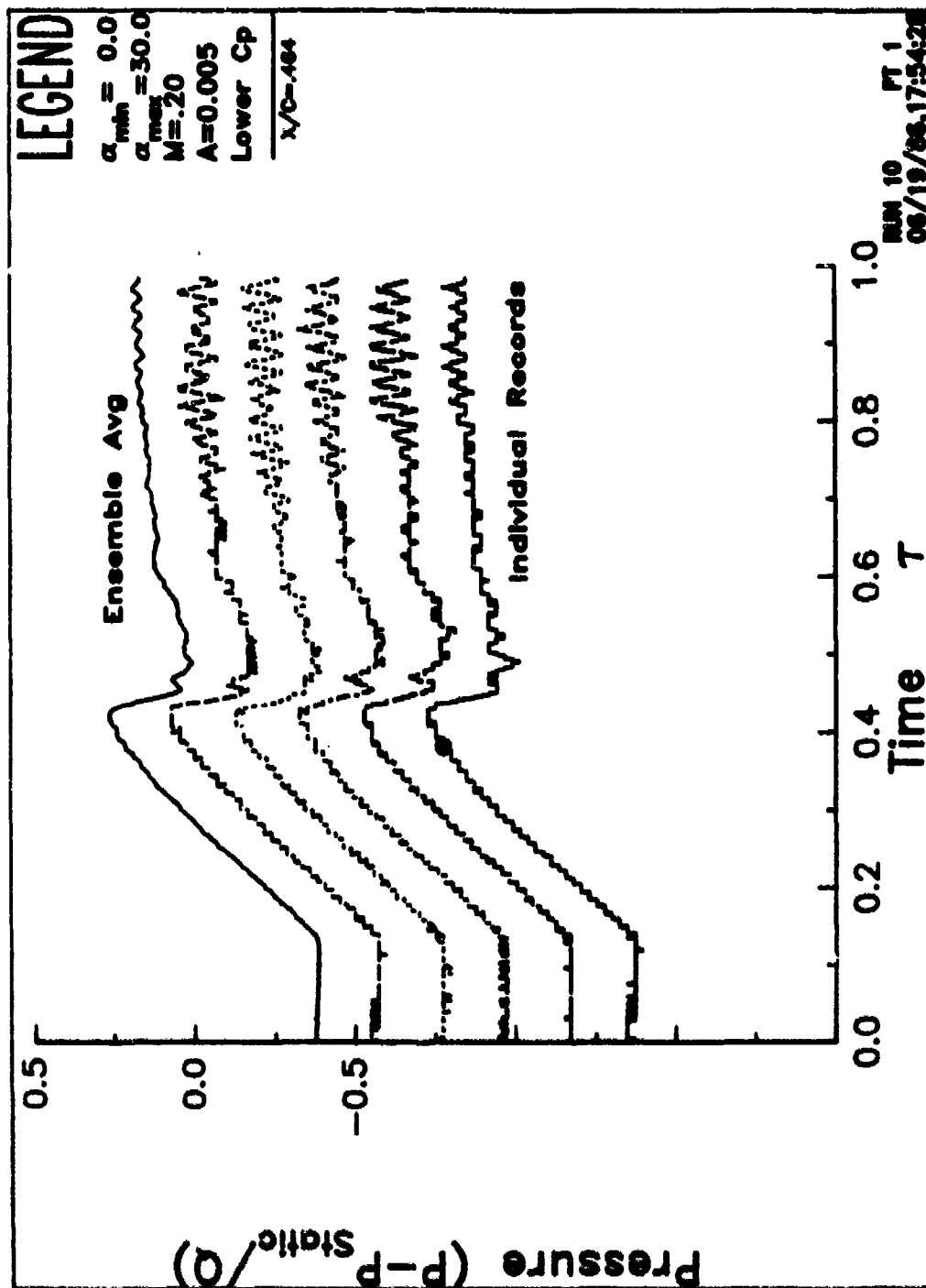


Figure 19. Individual lower surface pressure records. b)  $x/c = 0.464$ .

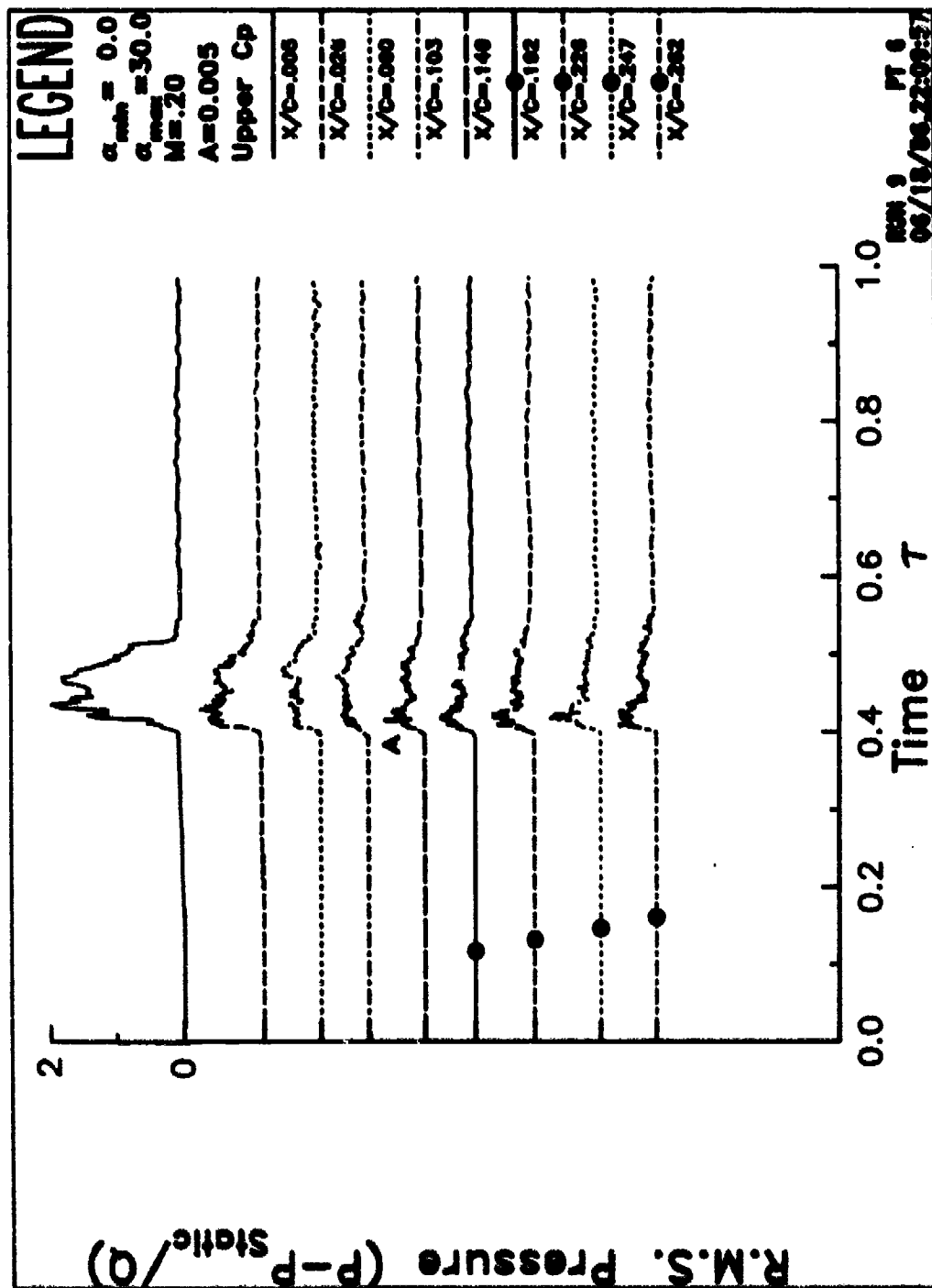


Figure 20. RMS upper surface pressures. a) forward region.

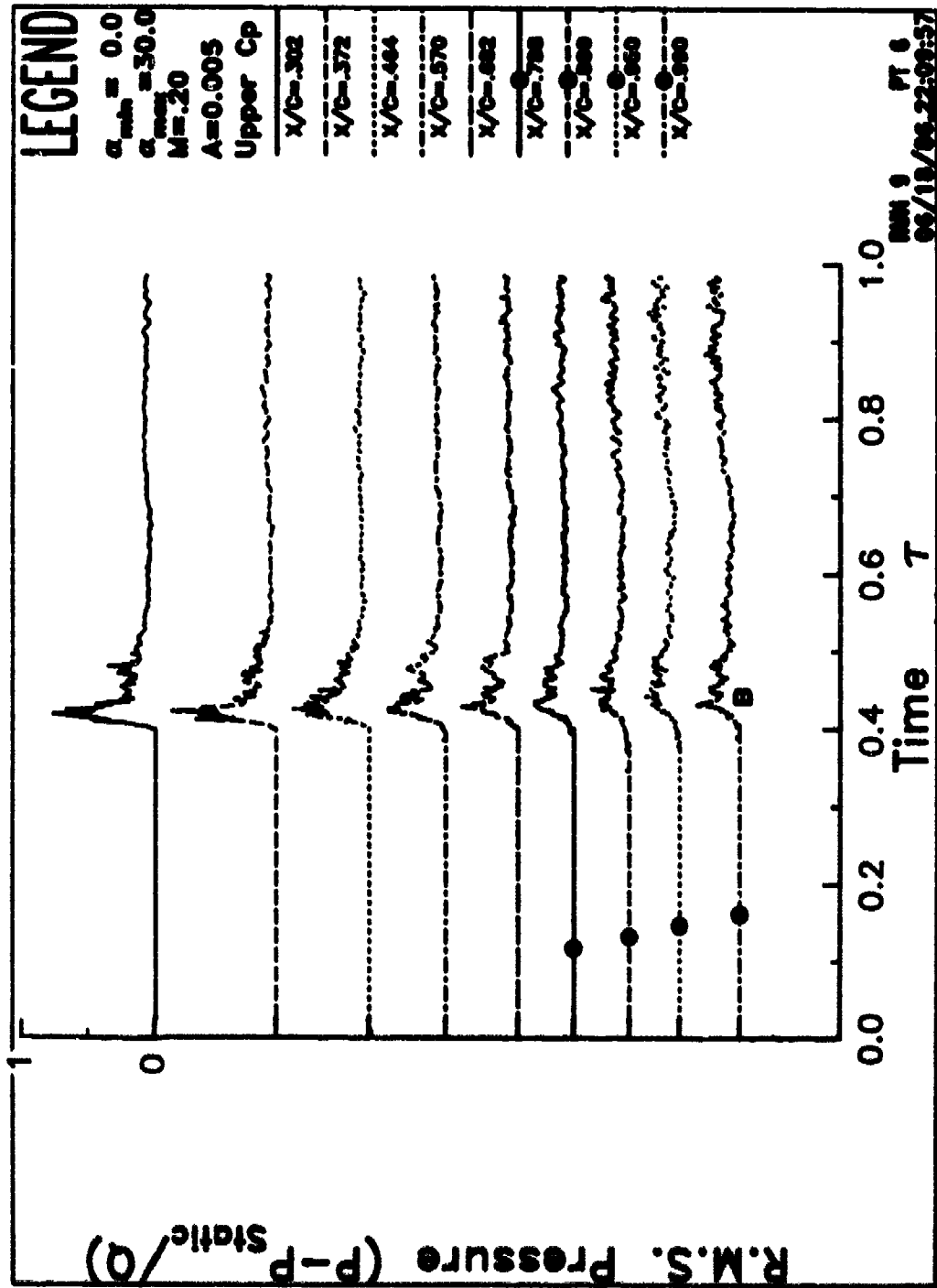


Figure 20. RMS upper surface pressures. b) Aft region.

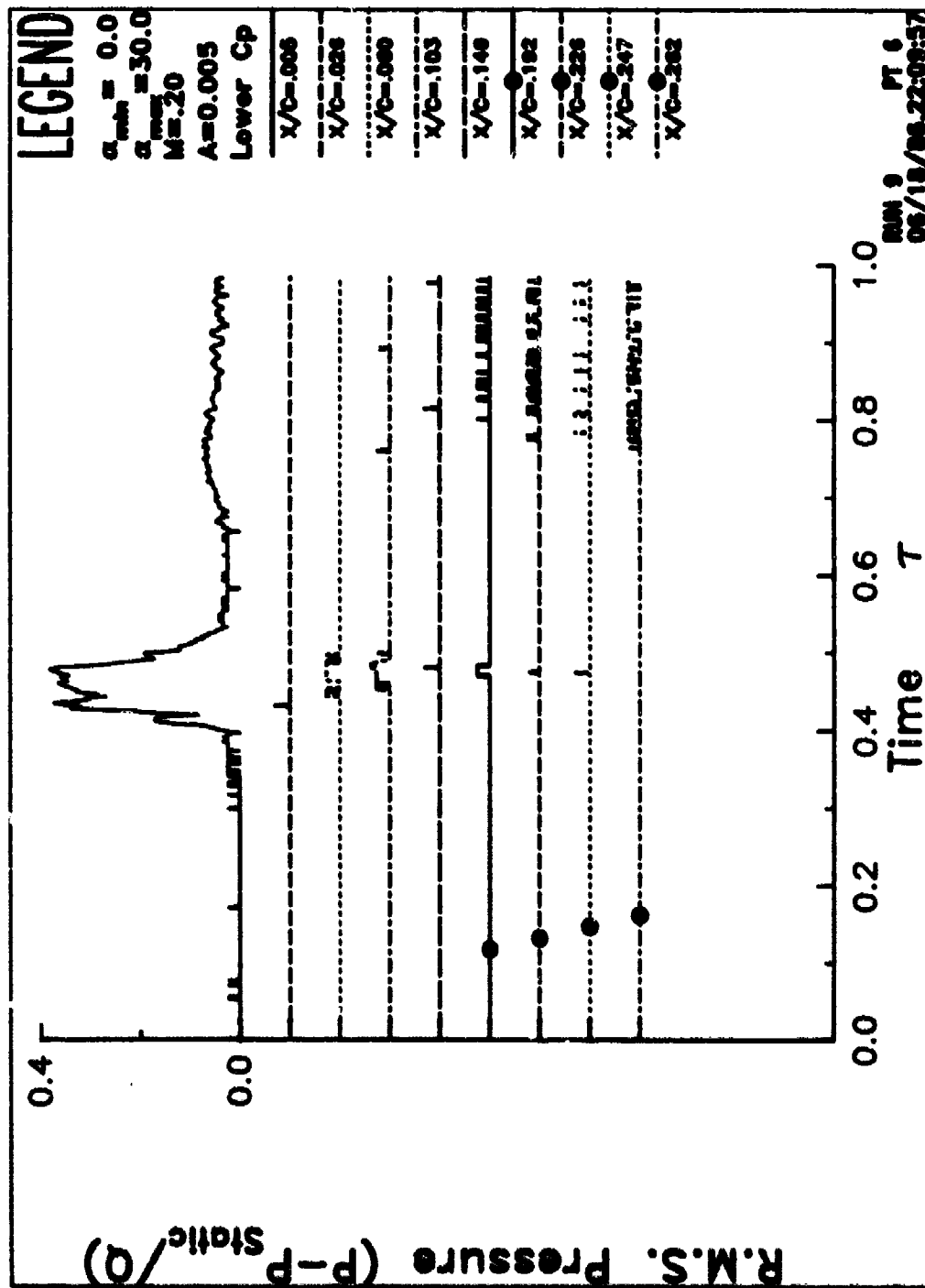


Figure 21. RMS lower surface pressures. a) Forward region.

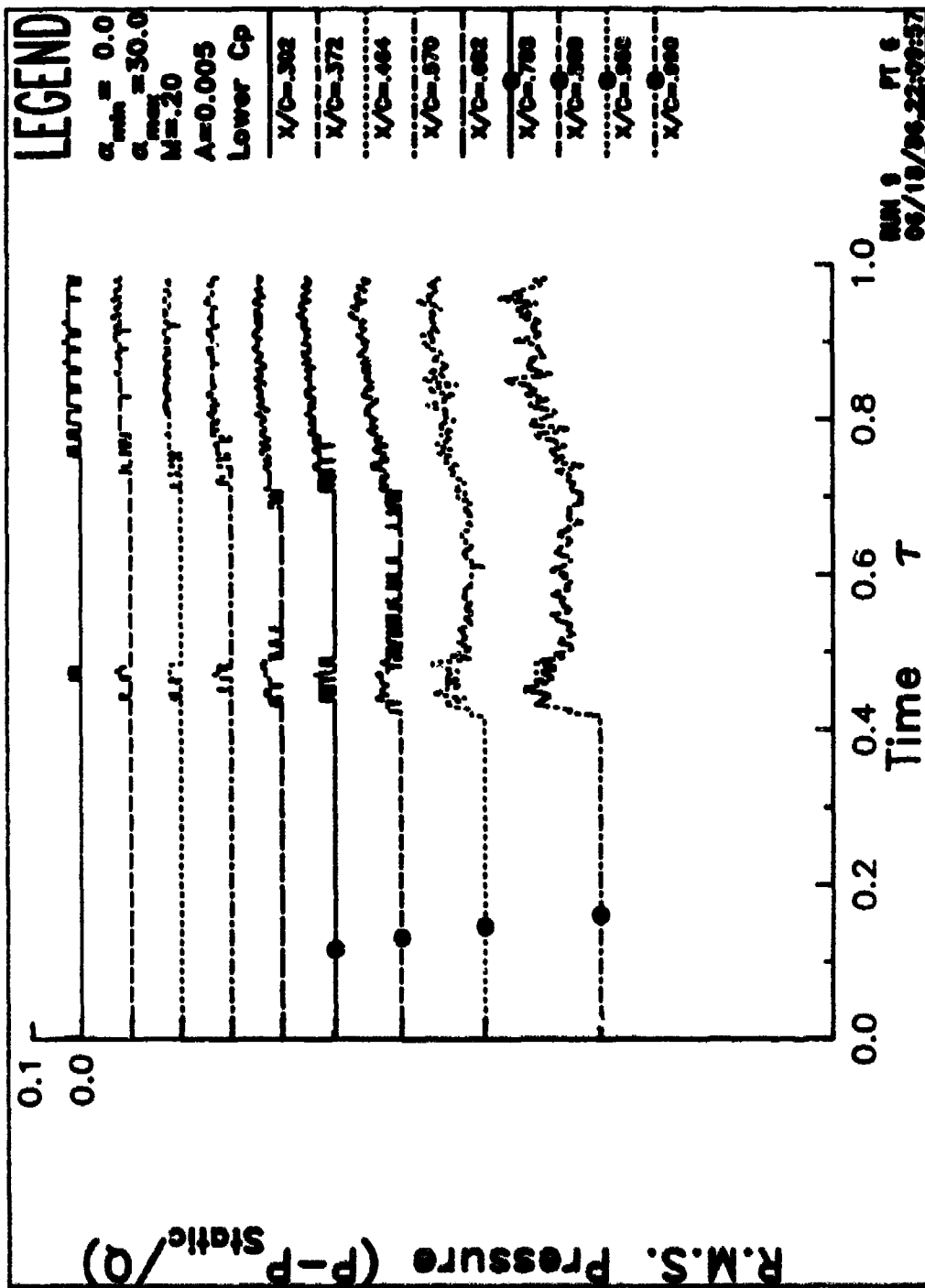


Figure 21. RMS lower surface pressures. b) Aft region.

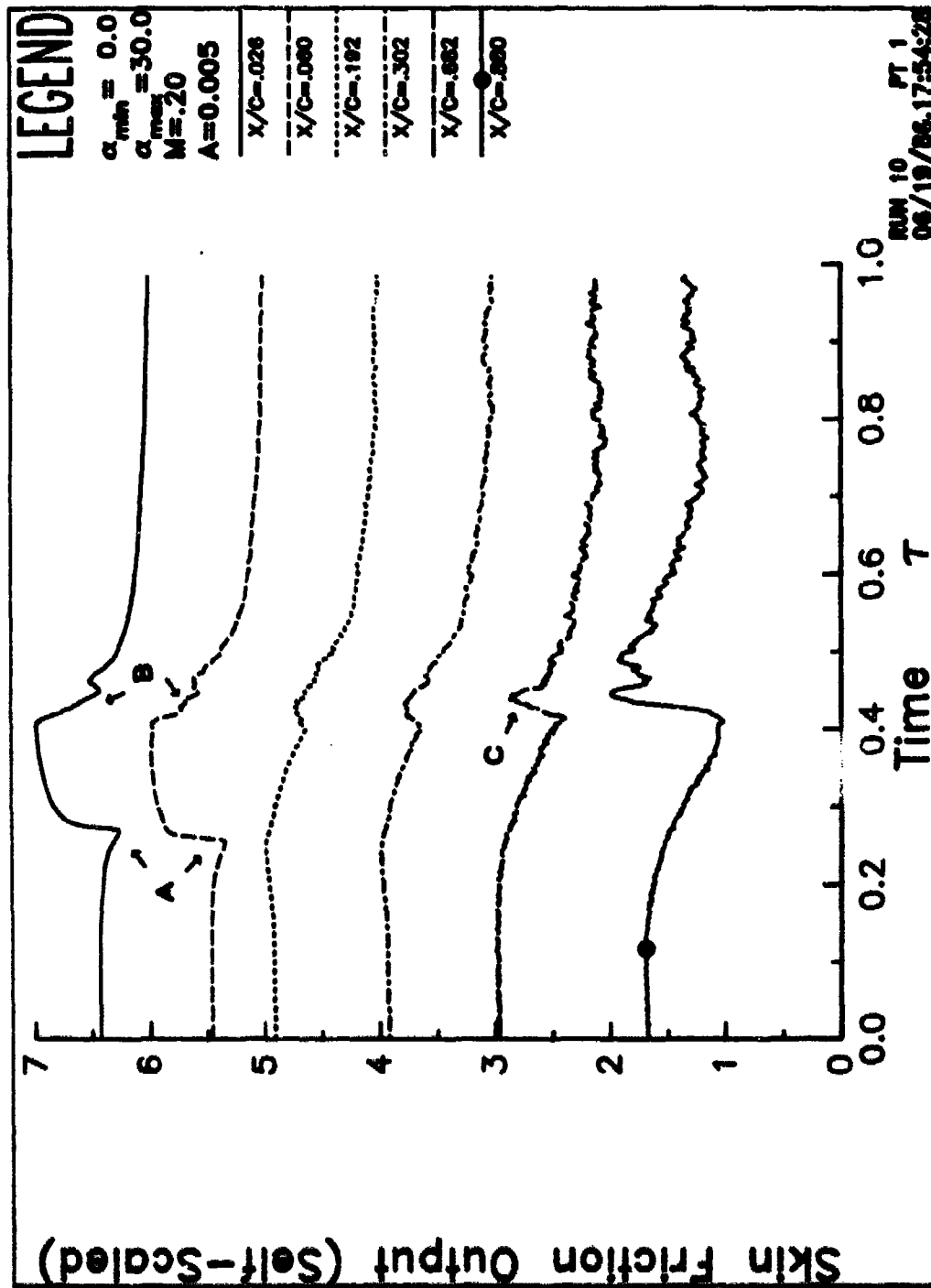


Figure 22. Hot film gage output.

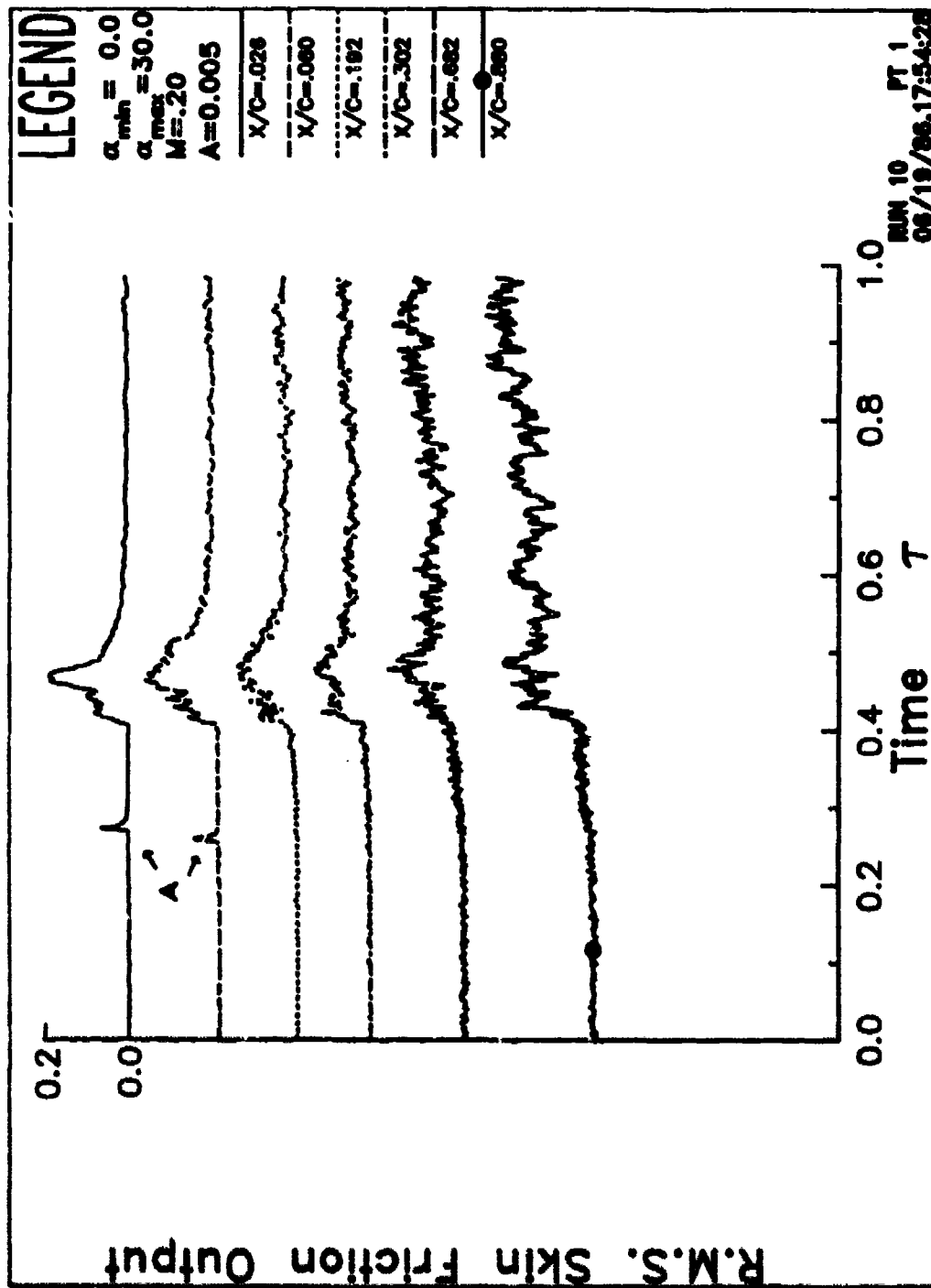


Figure 23. RMS hot film gage output.

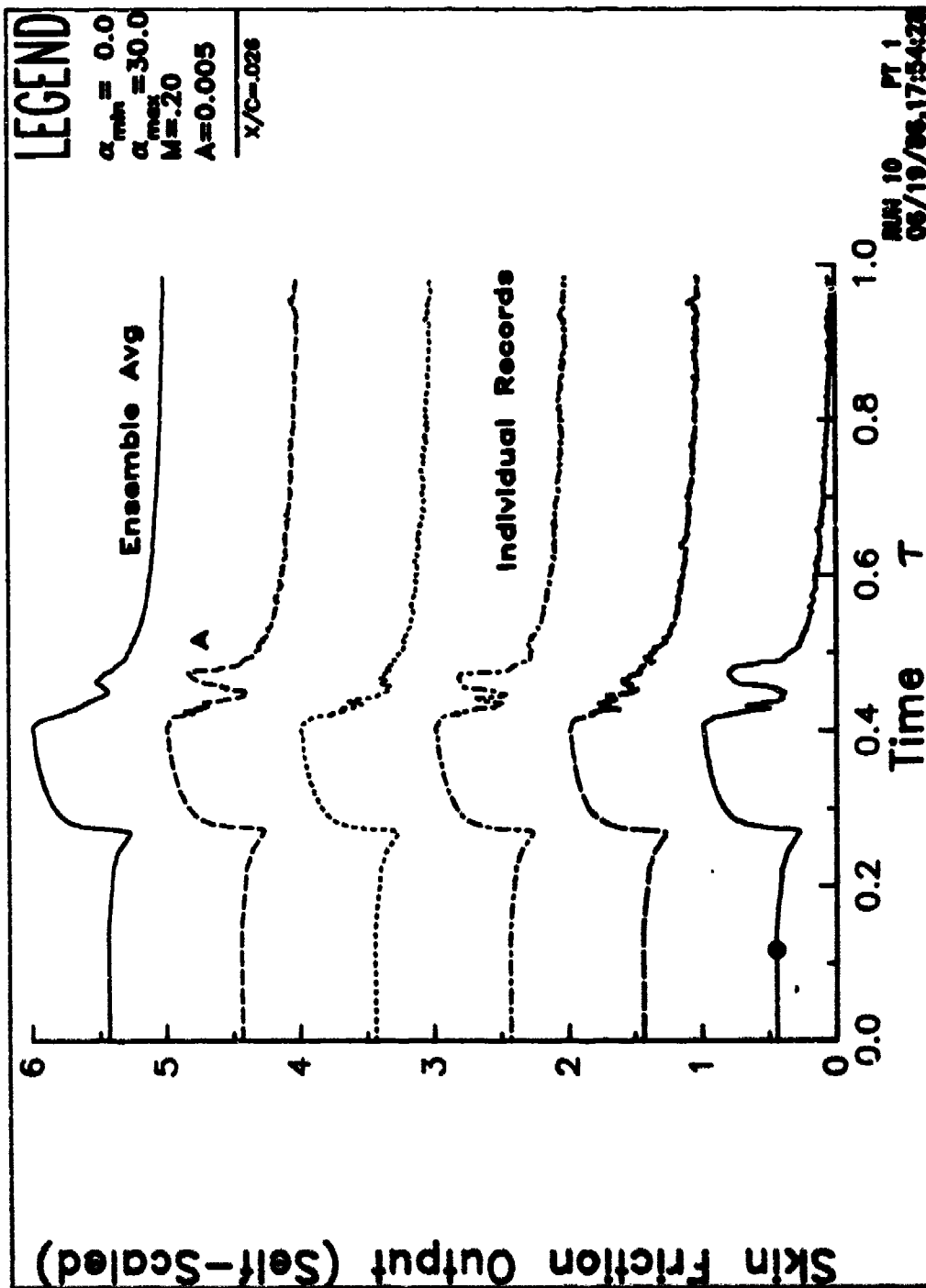


Figure 24. Individual hot film gage records. a)  $x/c = 0.026$ .



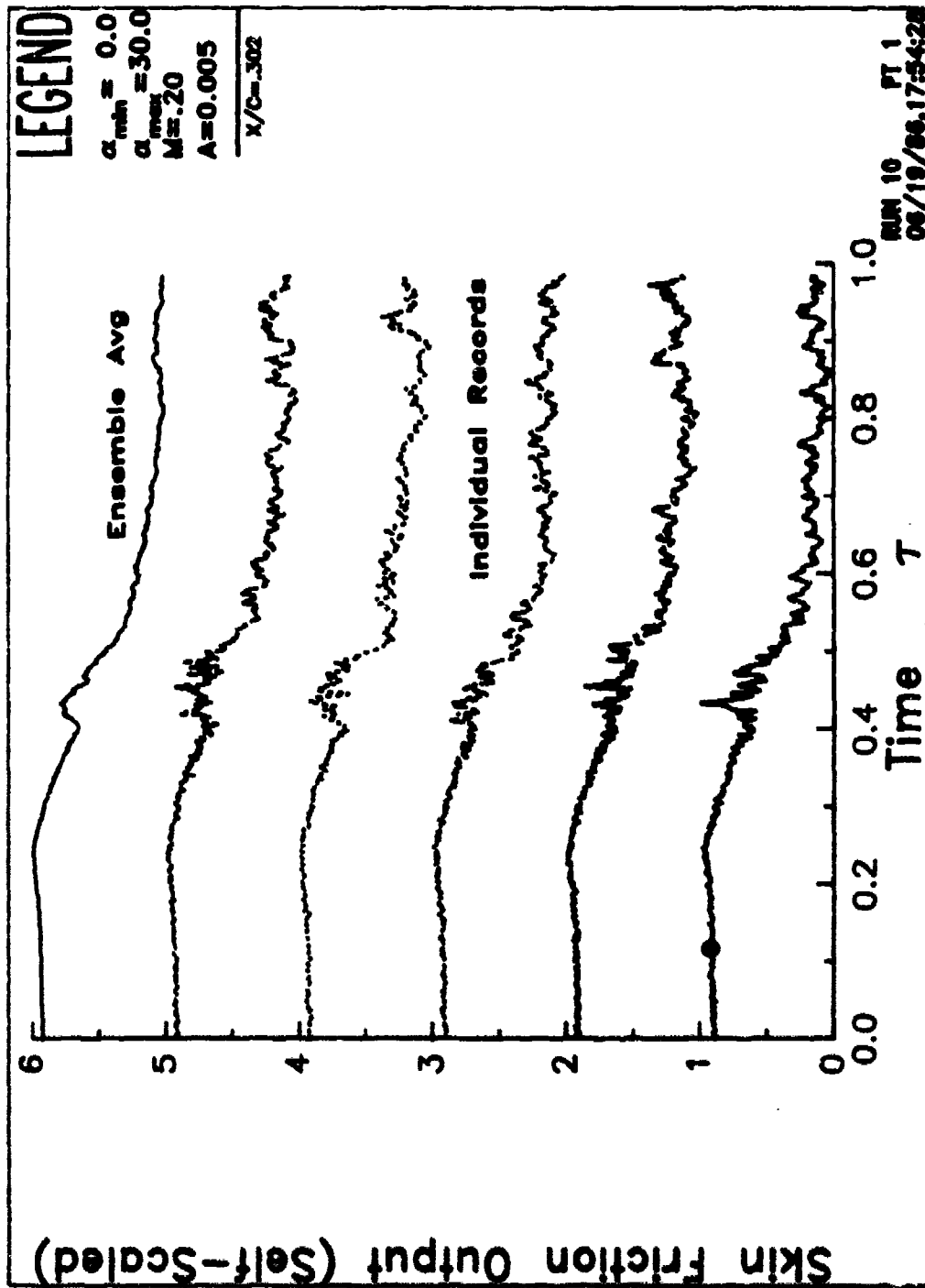


Figure 24. Individual hot film gage records. b)  $x/c = 0.302$ .

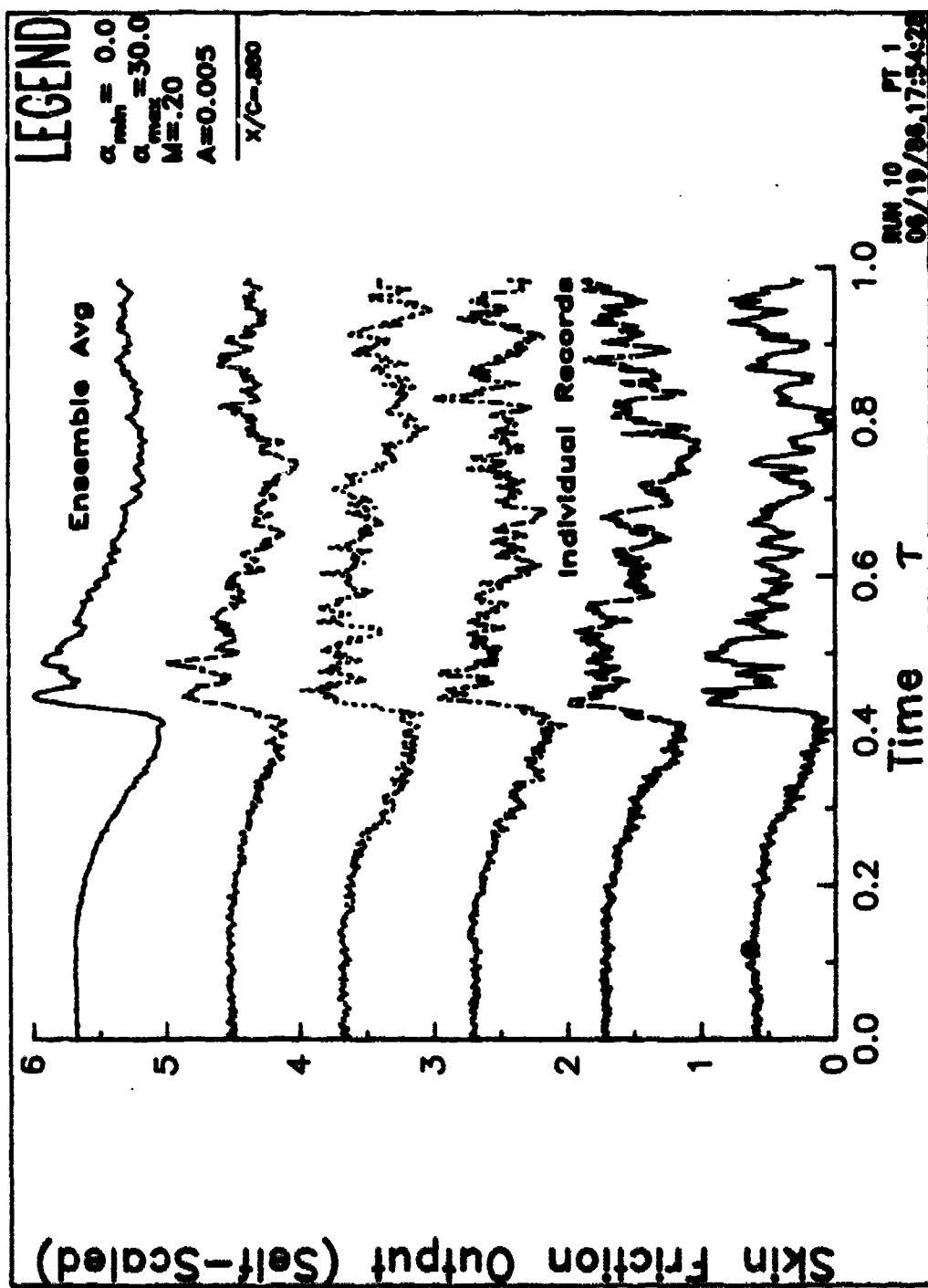


Figure 24. Individual hot film gage records. c)  $x/c = 0.880$

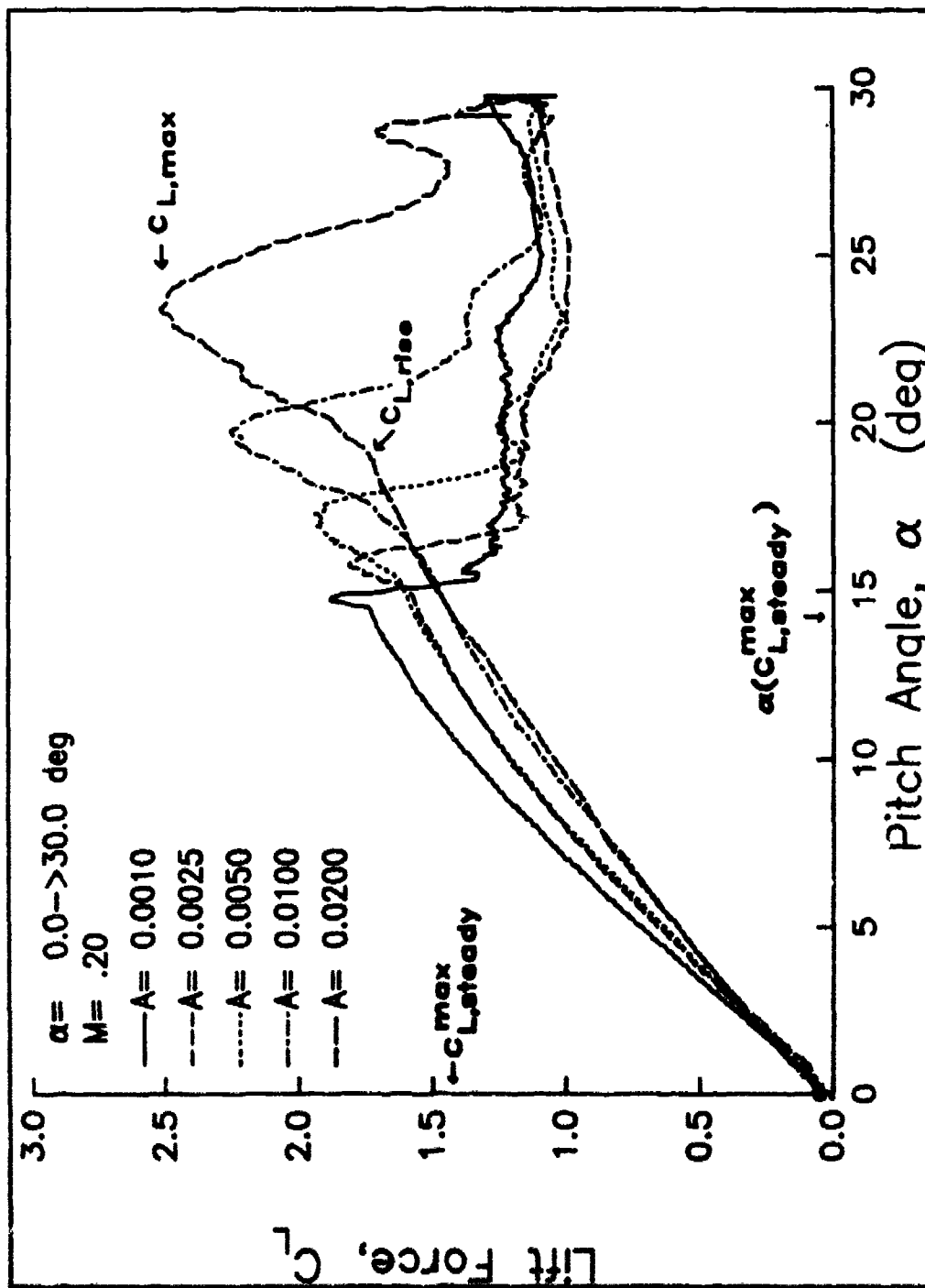


Figure 25. Airloads. a) Lift vs. pitch angle.

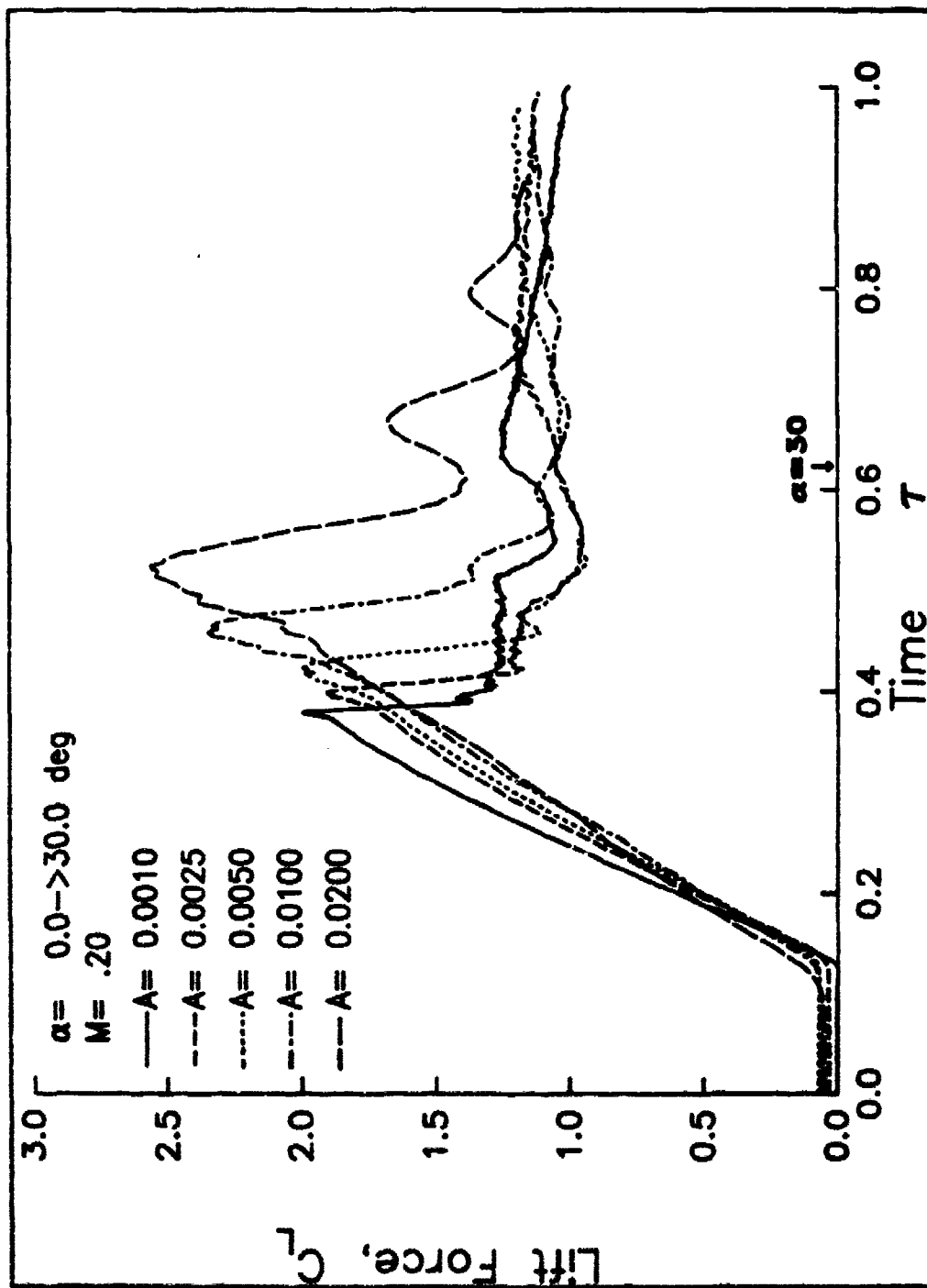


Figure 25. Airloads. b) Lift vs. time.

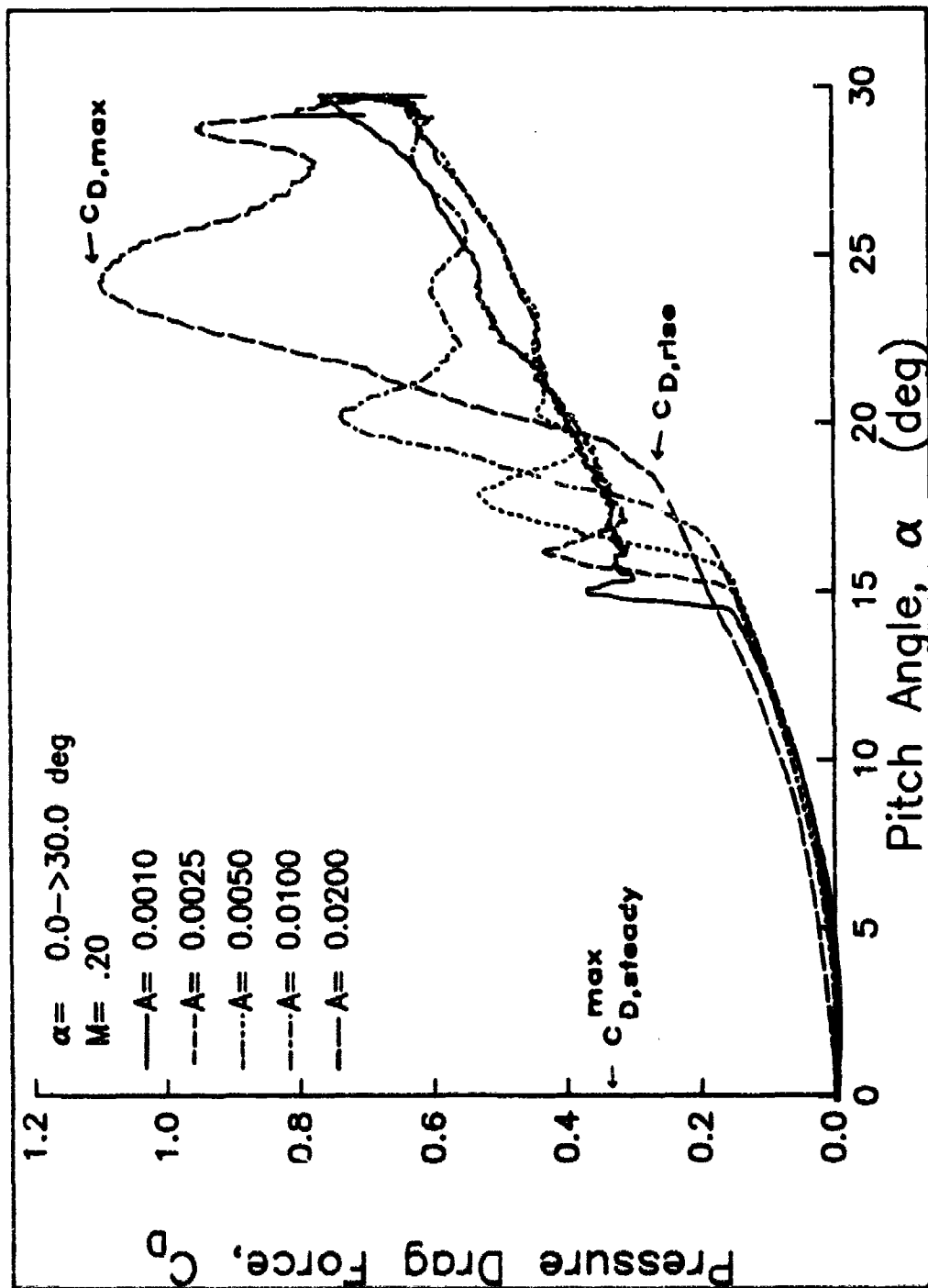


Figure 25. Airloads. c) Drag vs. pitch angle.

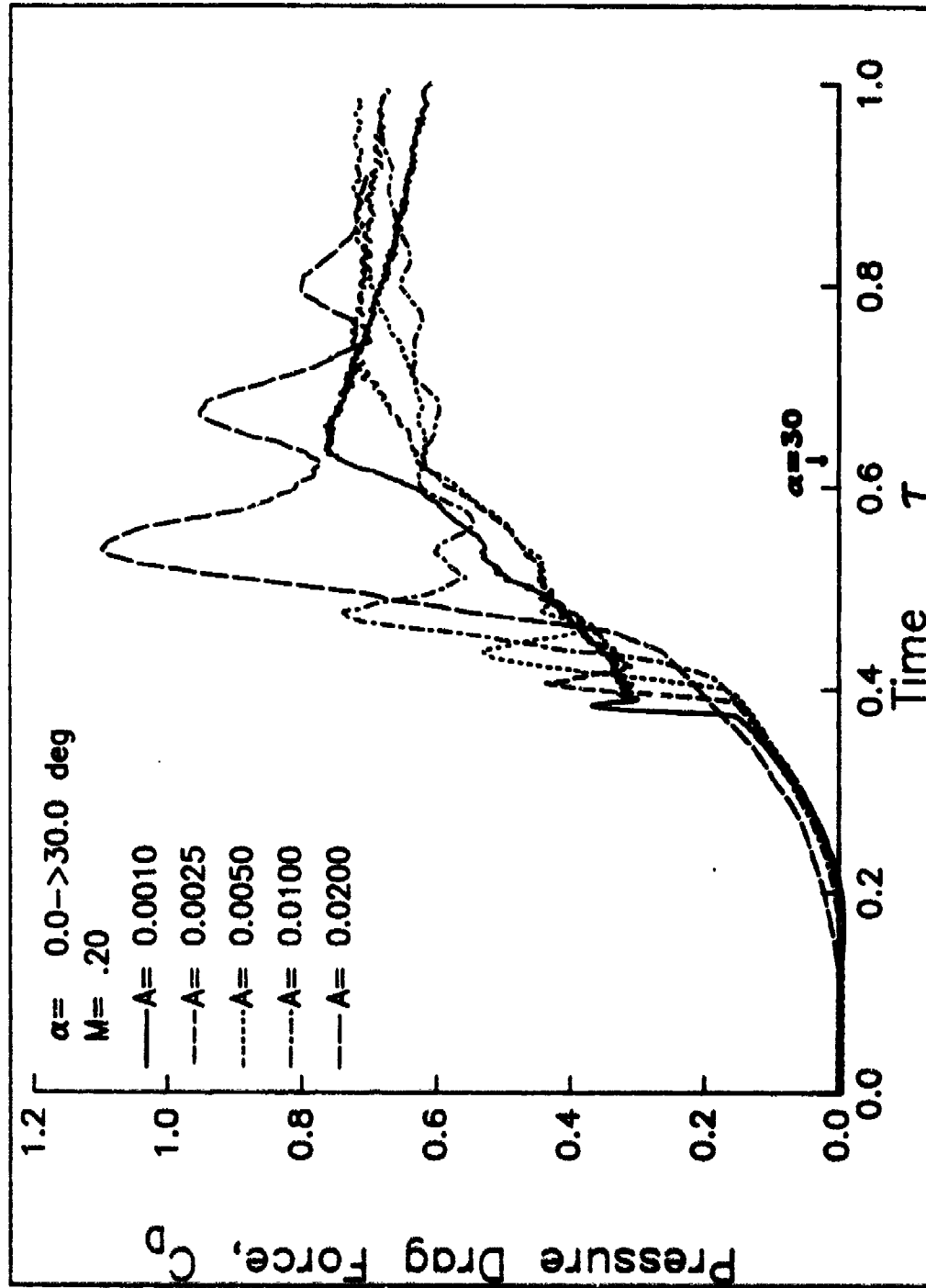


Figure 25. Airloads. d) Drag vs. time.

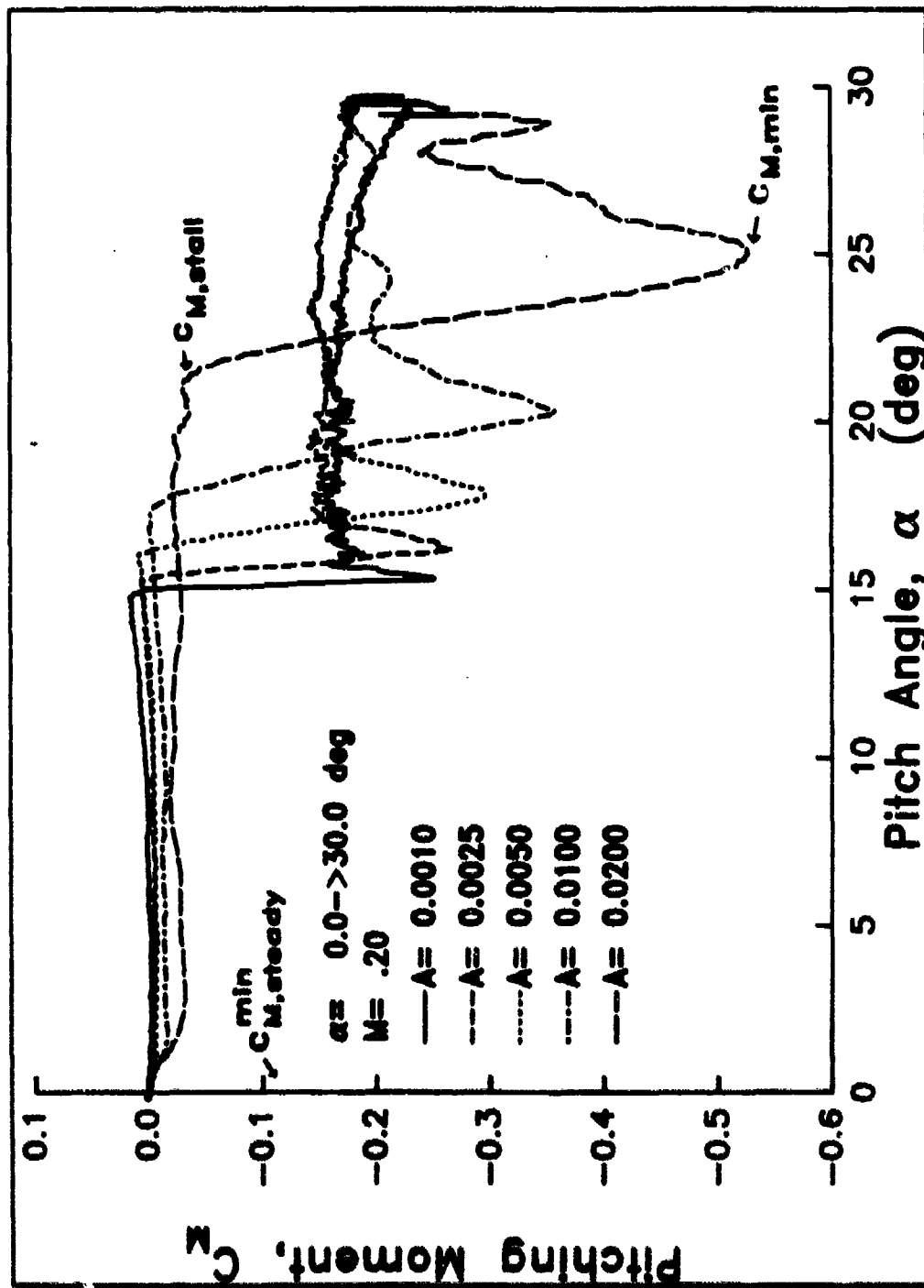


Figure 25. Airloads. e) Moment vs. pitch angle.

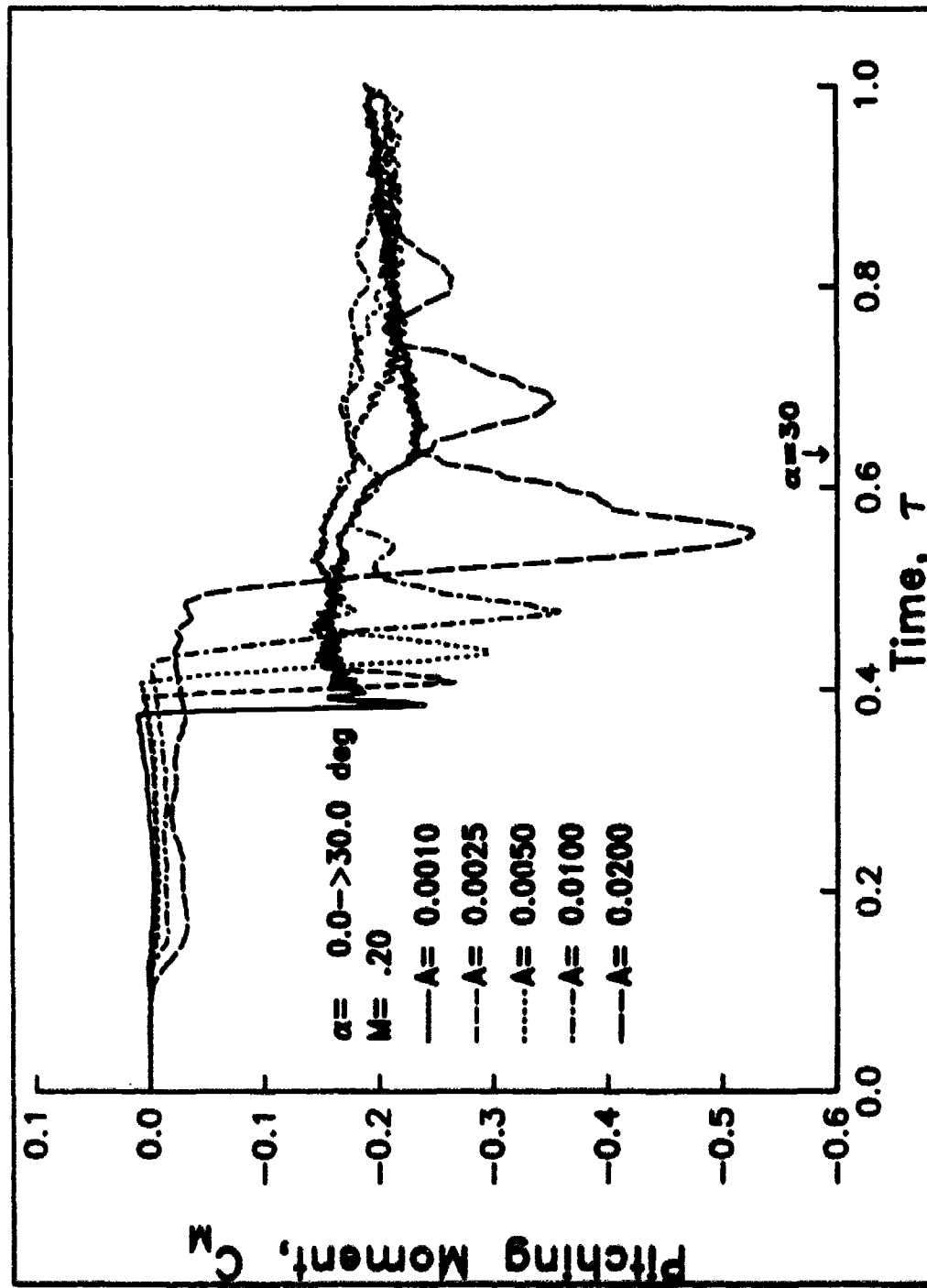


Figure 25. Airlods. f) Moment vs. time.



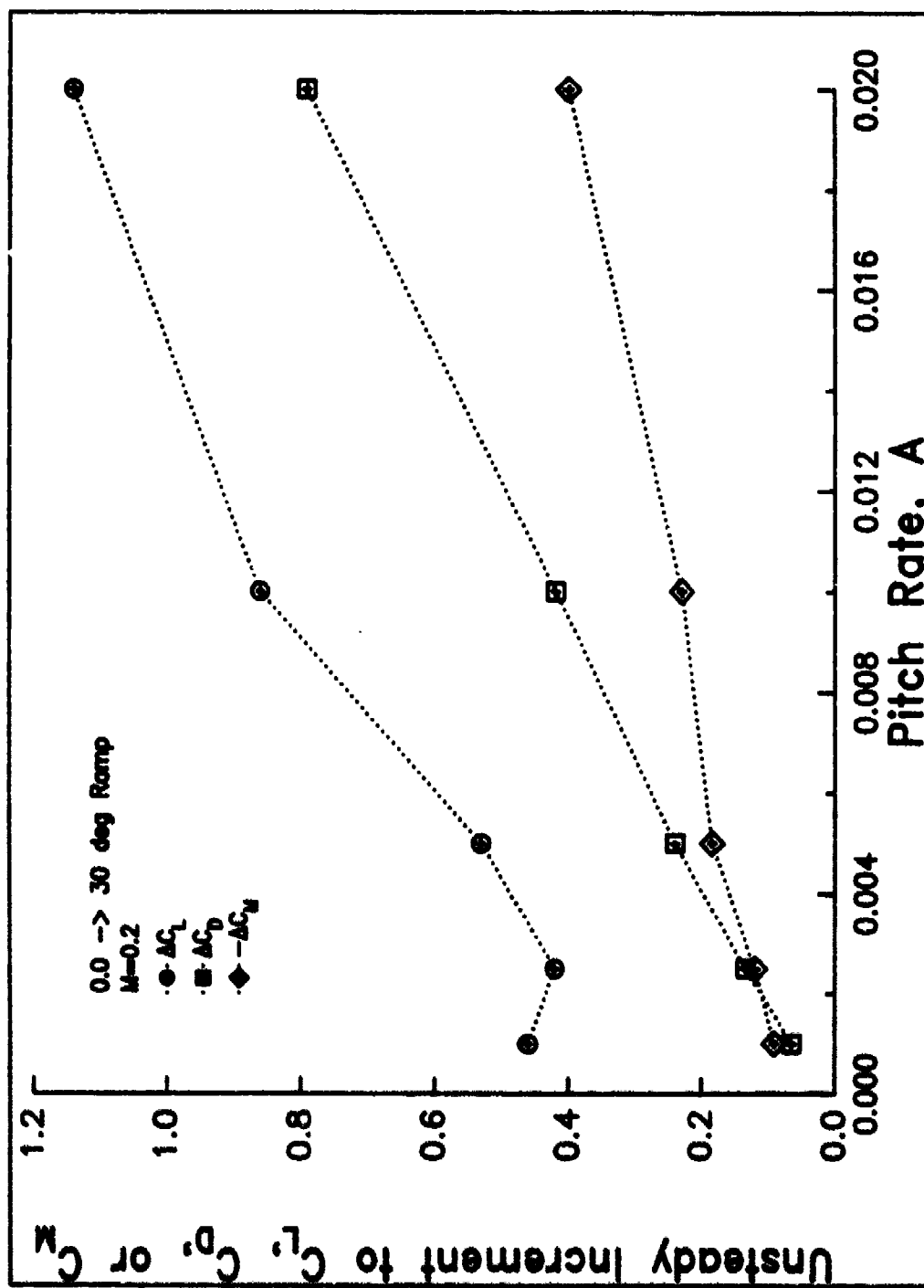


Figure 26. Unsteady increments to lift, drag, and moment.

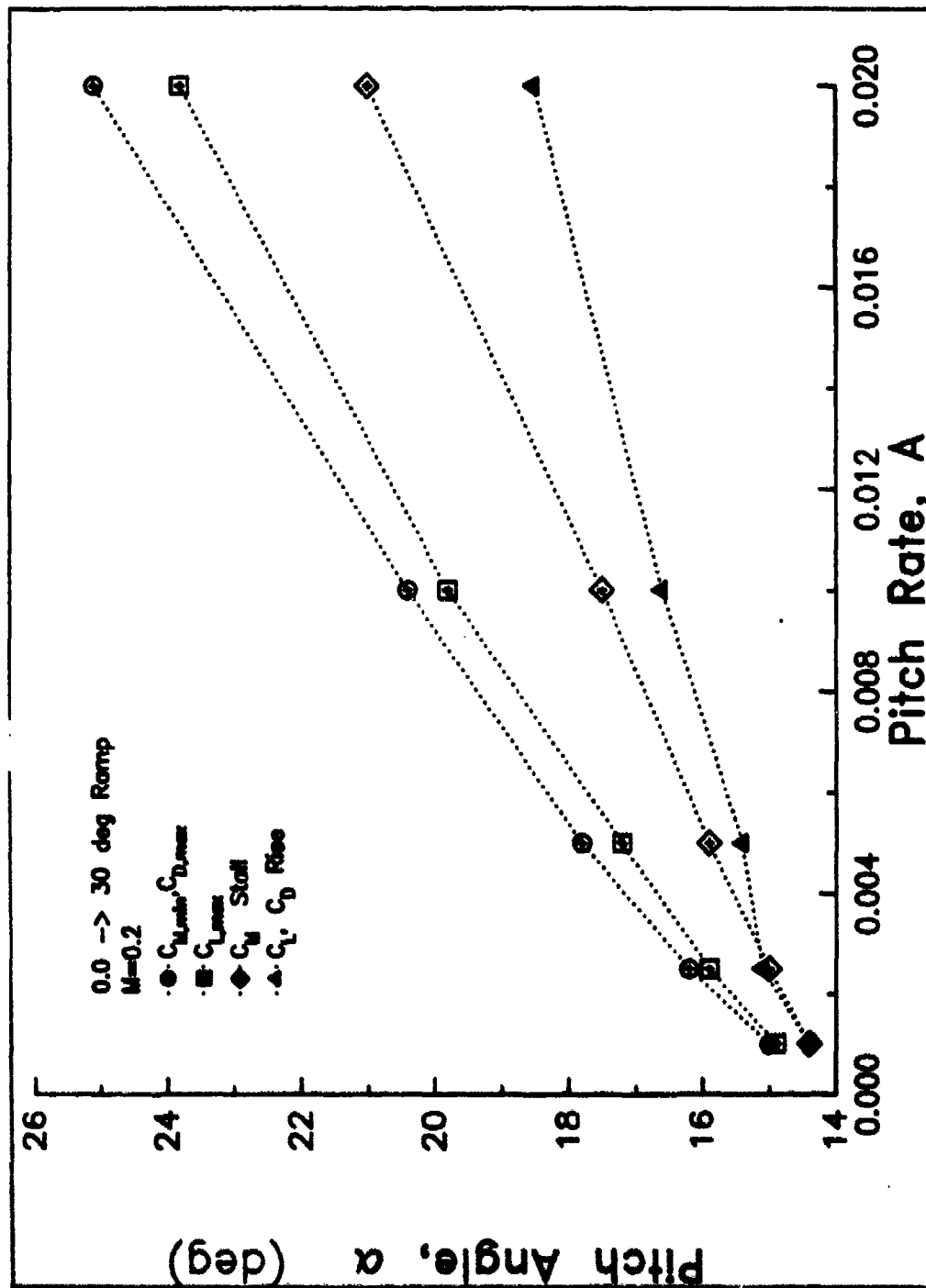


Figure 27. Sequence of stall events vs pitch rate.

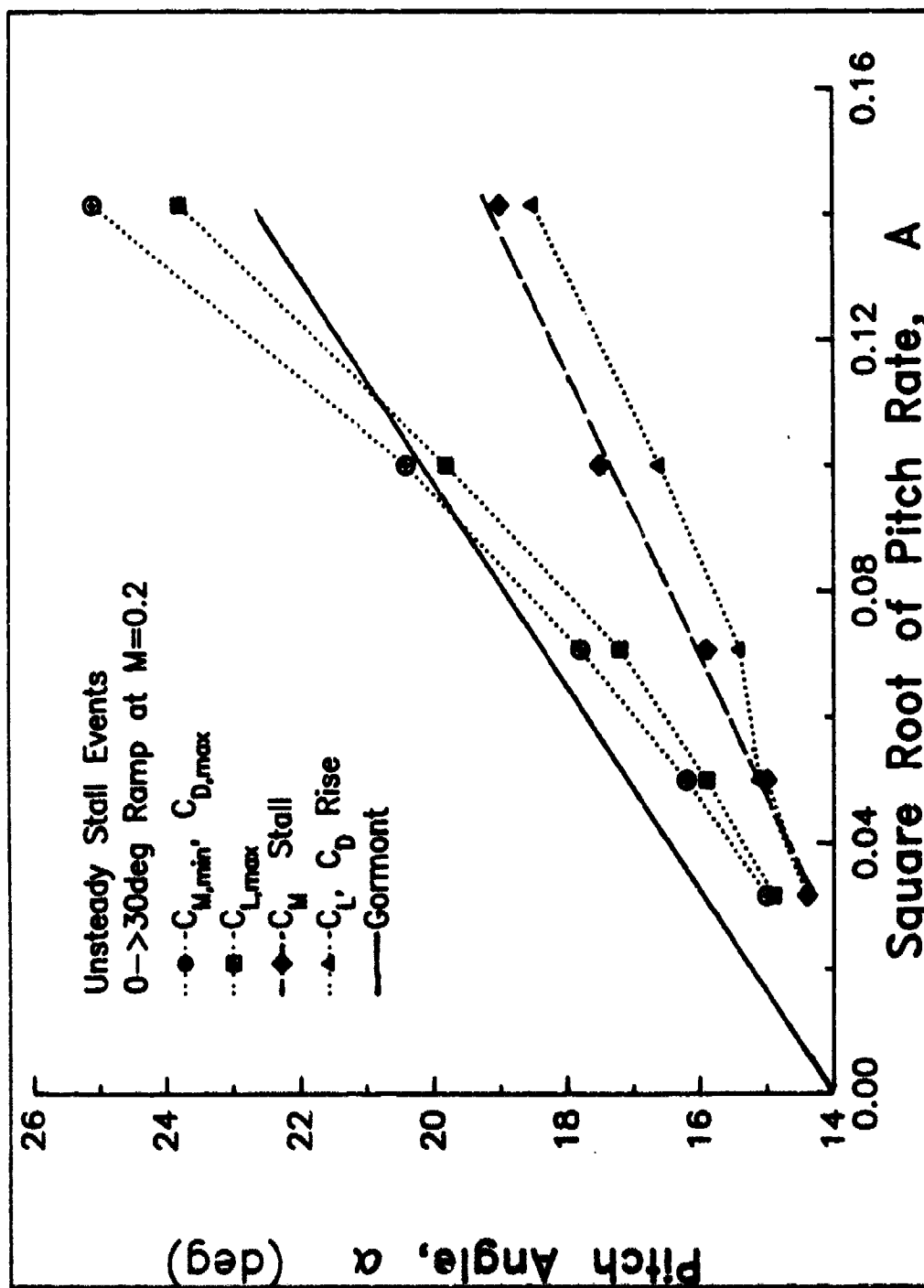


Figure 28. Sequence of stall events vs square root of pitch rate.

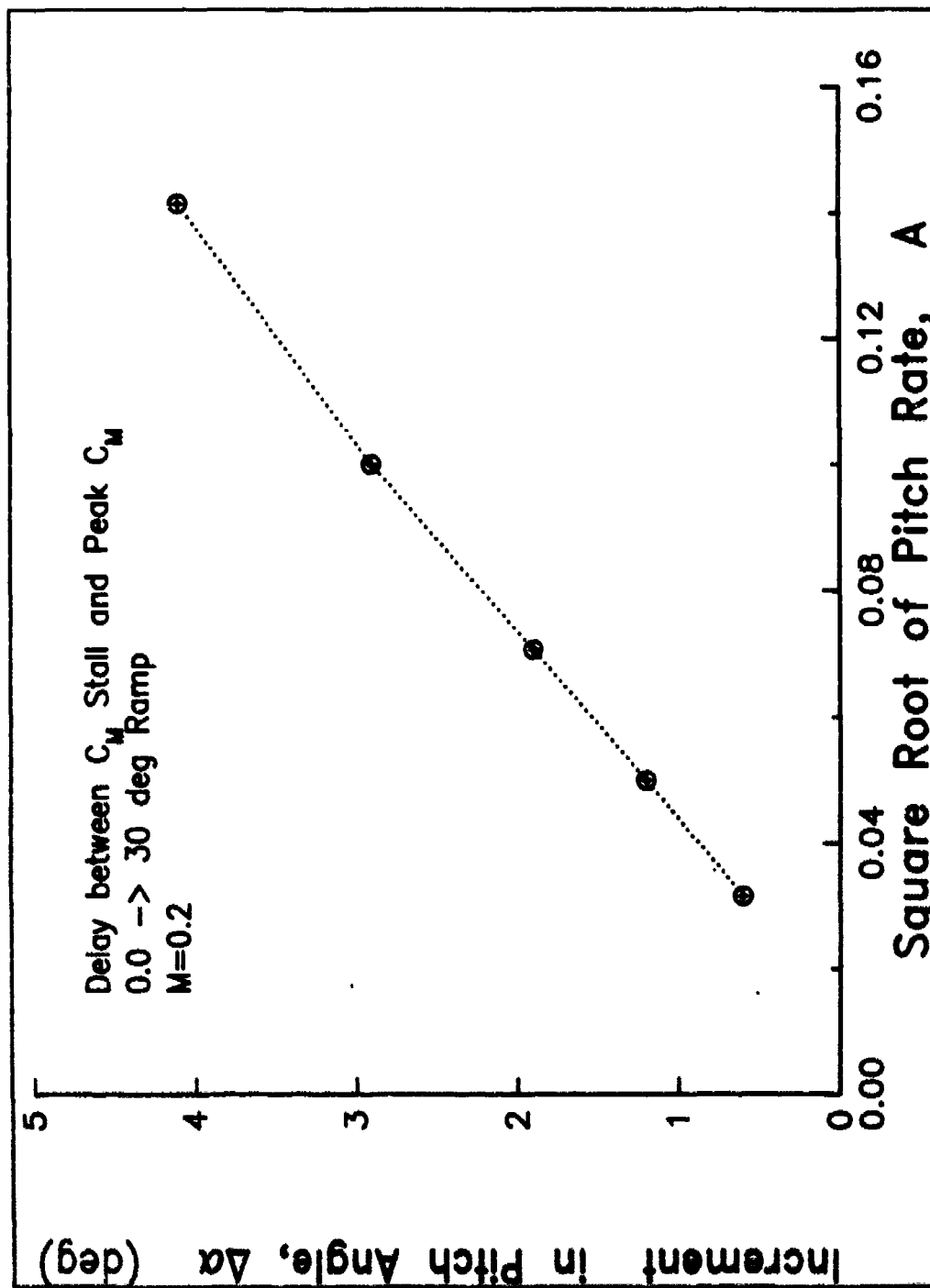


Figure 29. Delay between moment stall and past moment vs square root of pitch rate.

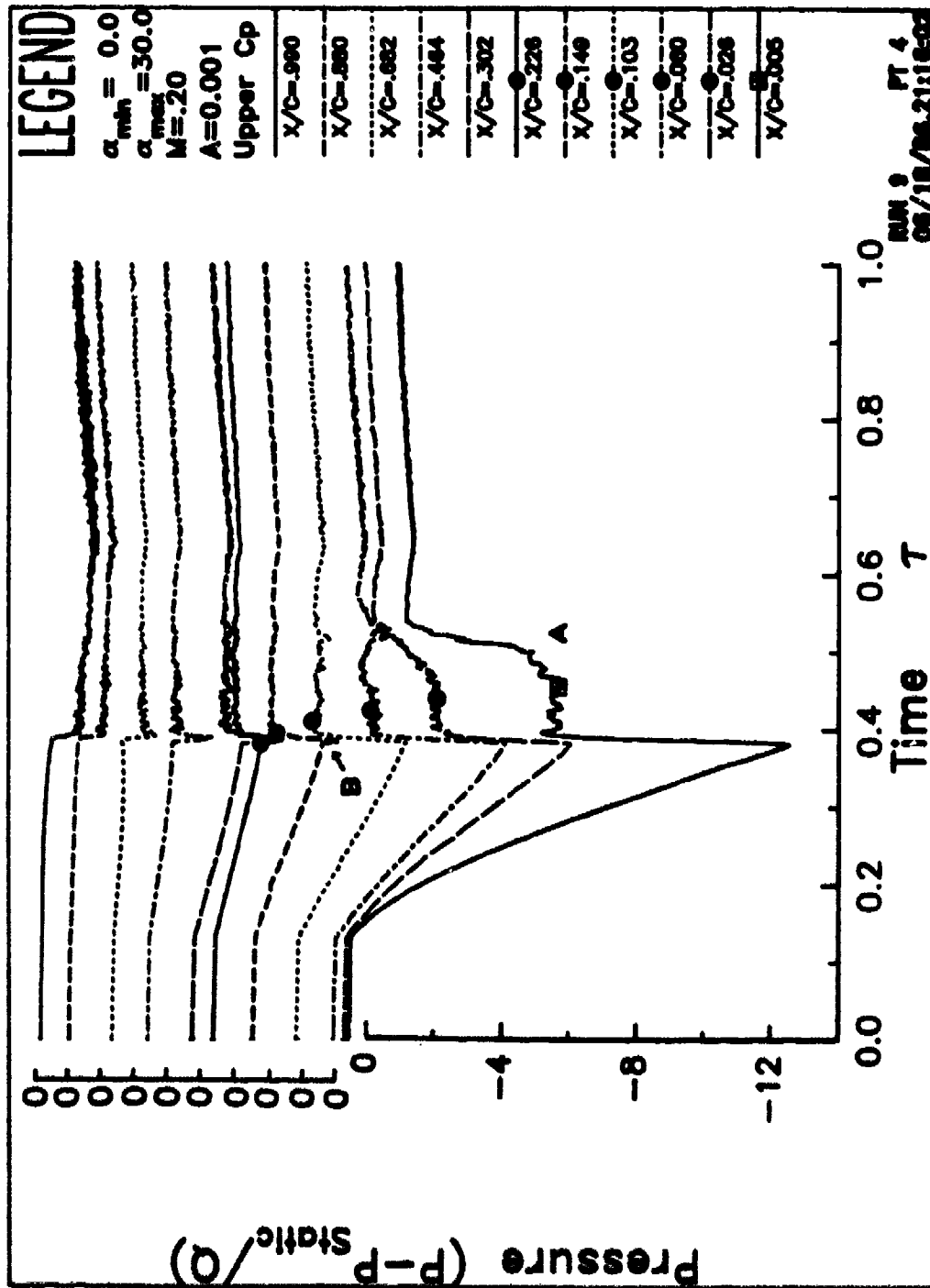


Figure 30. Upper surface pressure. a)  $A = 0.0010$ .

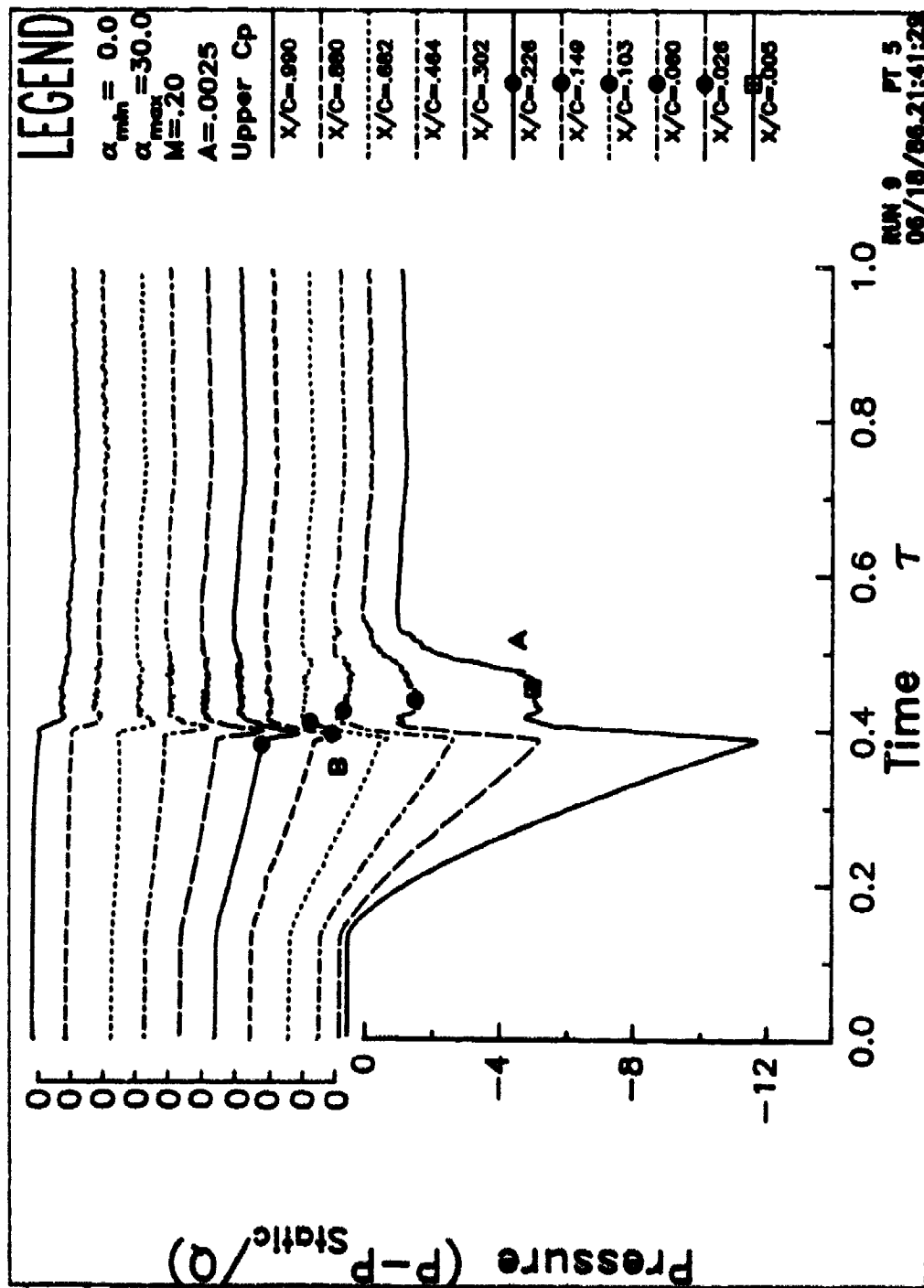


Figure 30. Upper surface pressure. b)  $A = 0.0025$ .

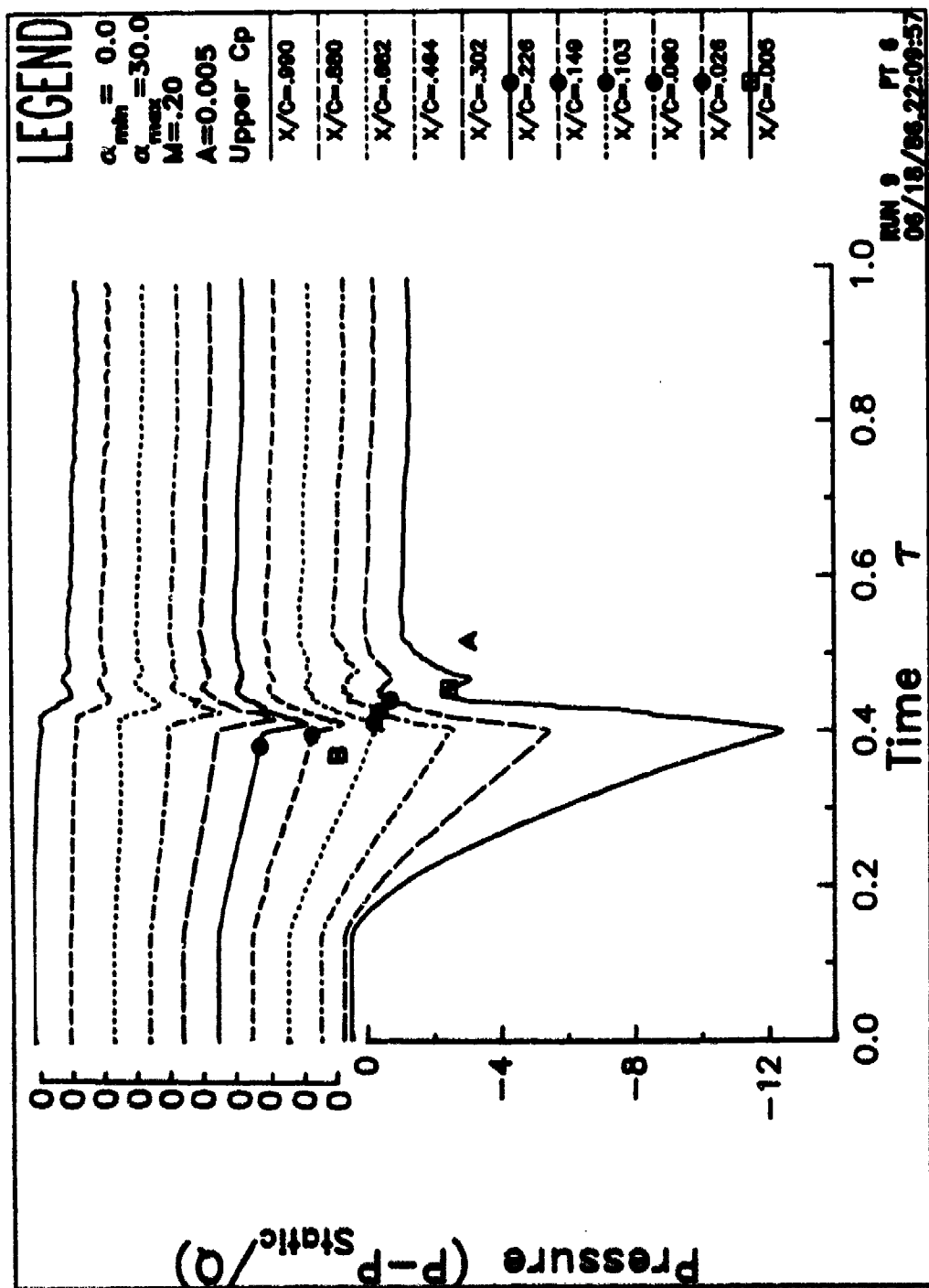


Figure 30. Upper surface pressure. c)  $A = 0.0050$ .

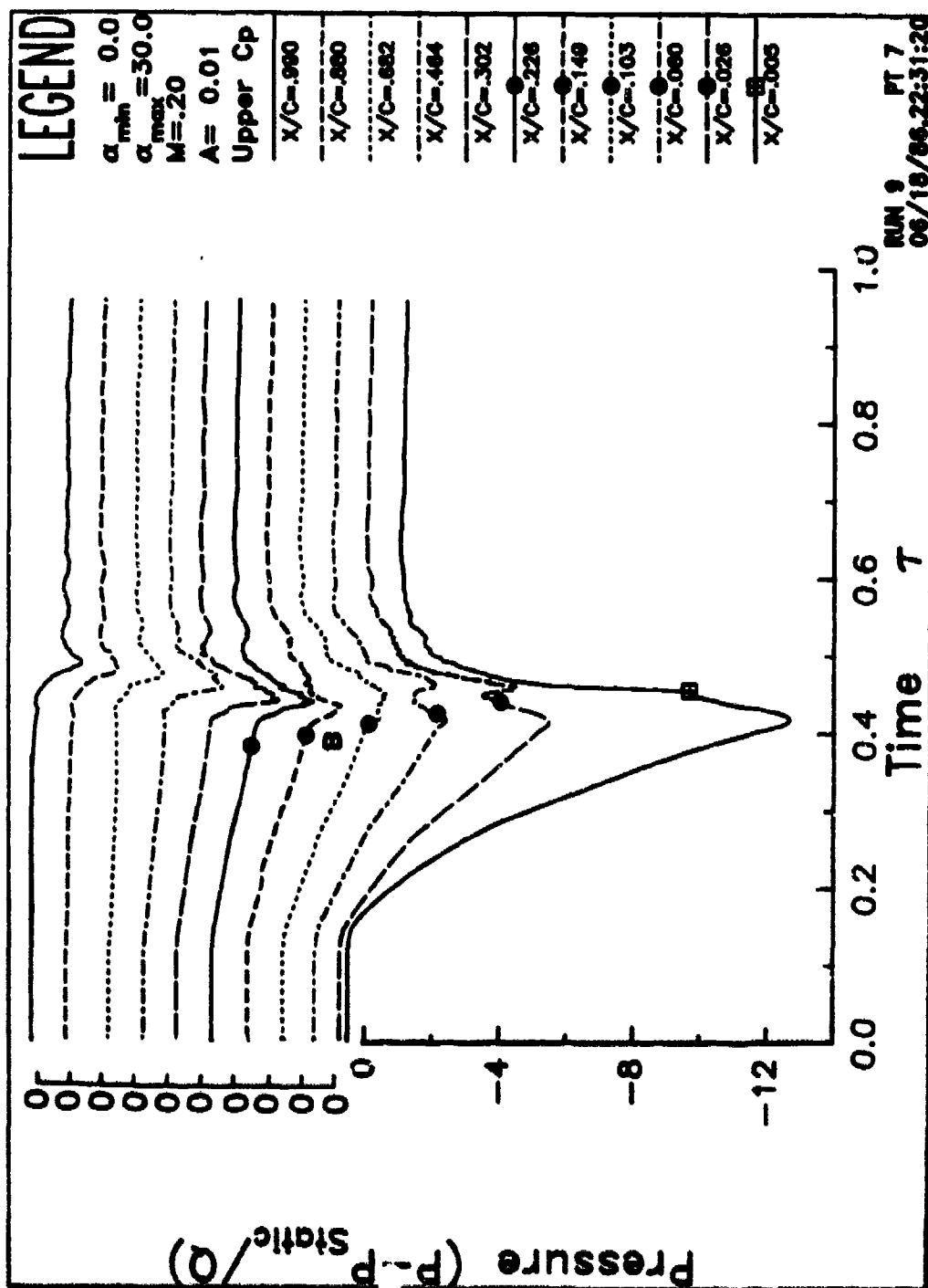


Figure 30. Upper surface pressure. d)  $A = 0.0100$ .



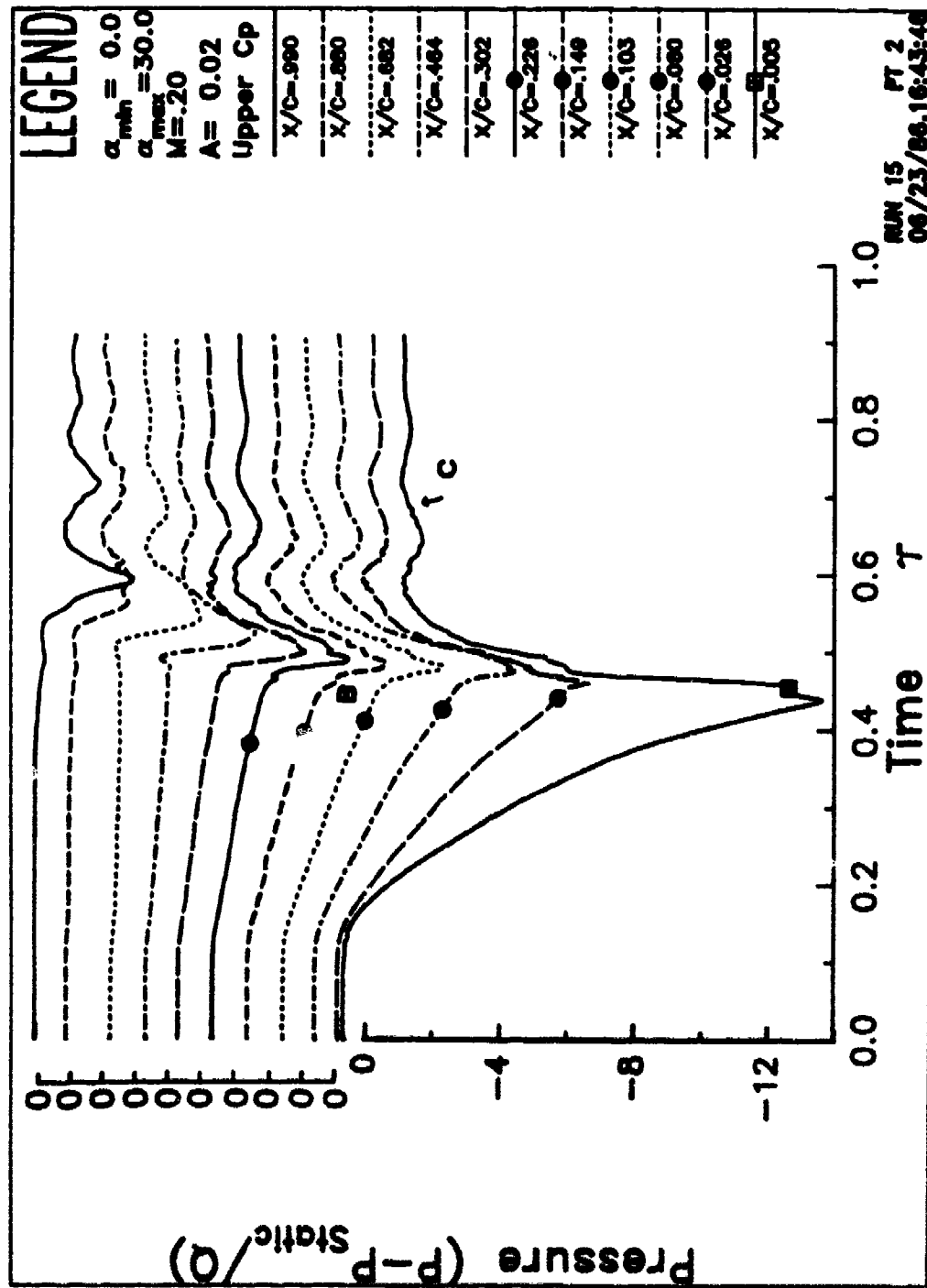


Figure 30. Upper surface pressure. e)  $A = 0.0200$ .

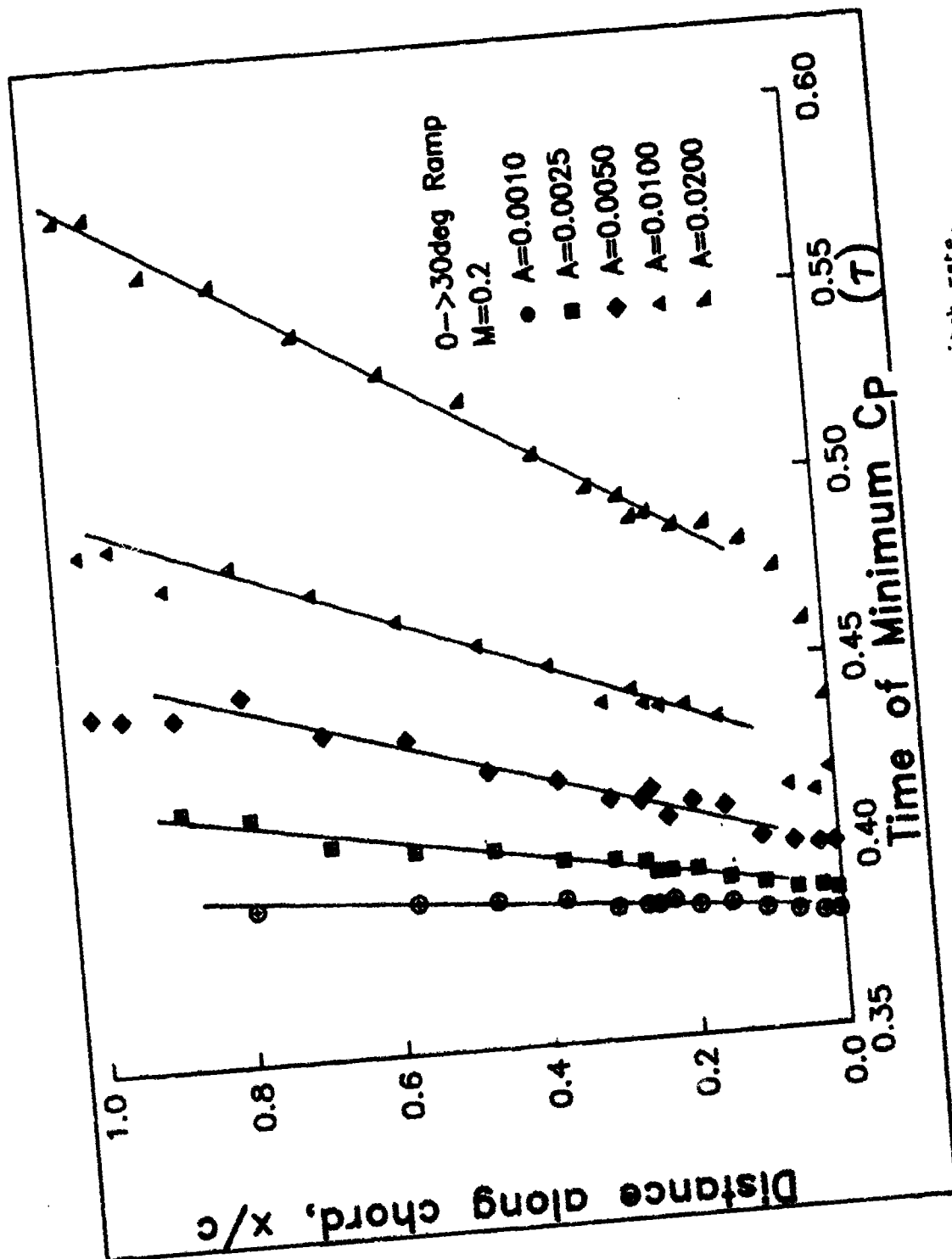


Figure 31. Times of minimum pressure at each pitch rate.

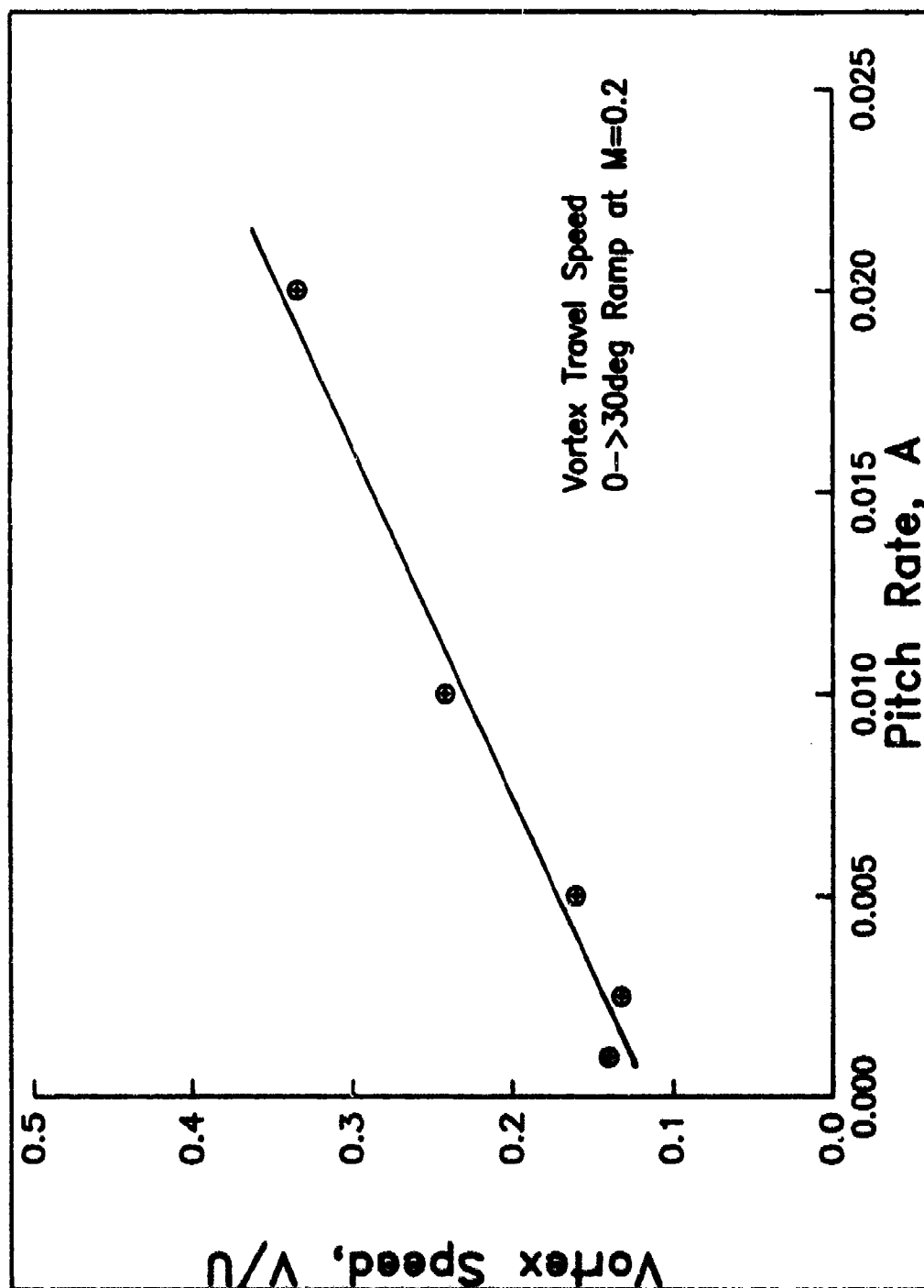


Figure 32. Vortex travel speed vs pitch rate.

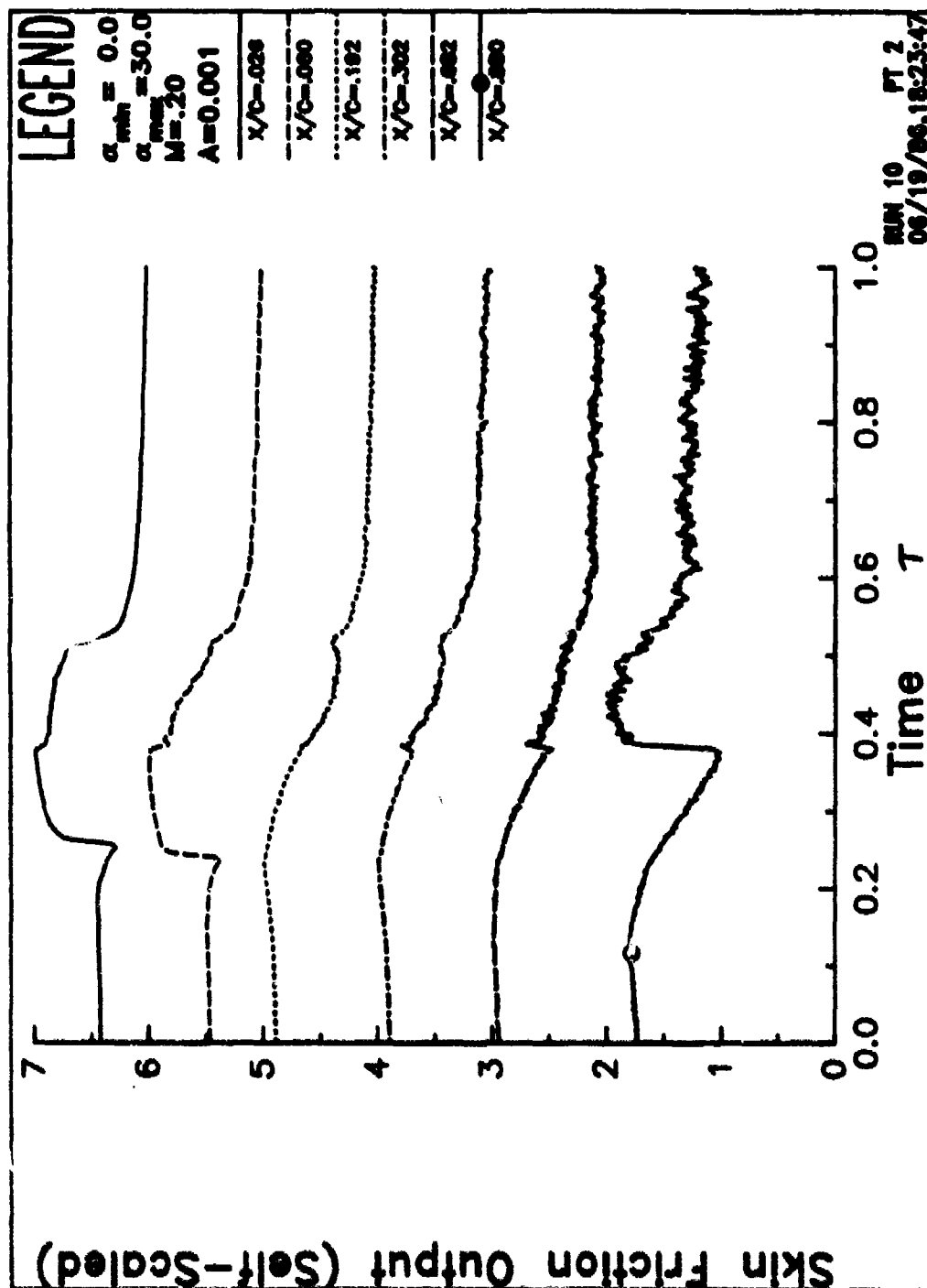


Figure 33. Hot film gage output. a)  $A = 0.0010$ .

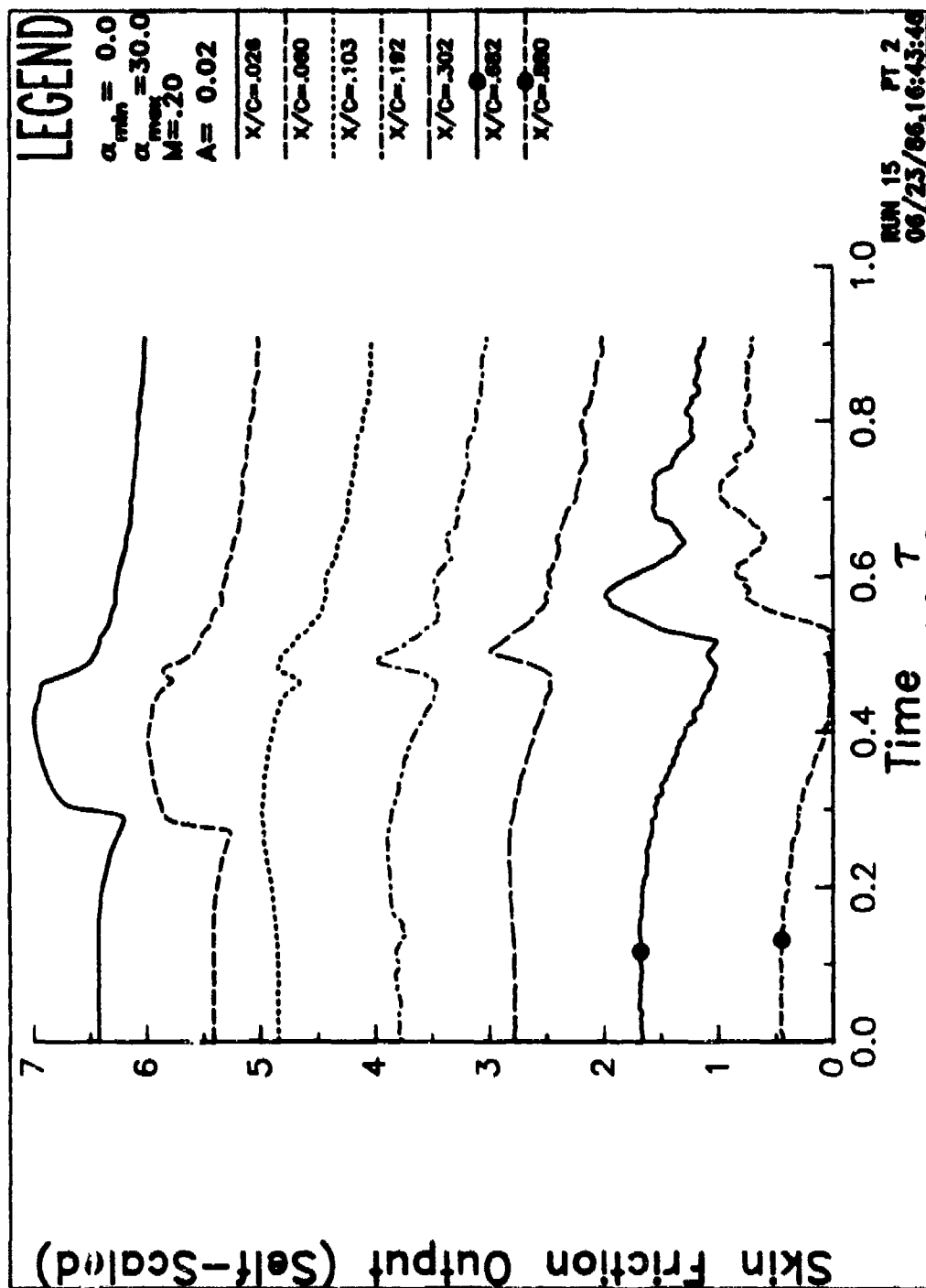


Figure 33. Hot film gage output. b)  $A = 0.020$ .

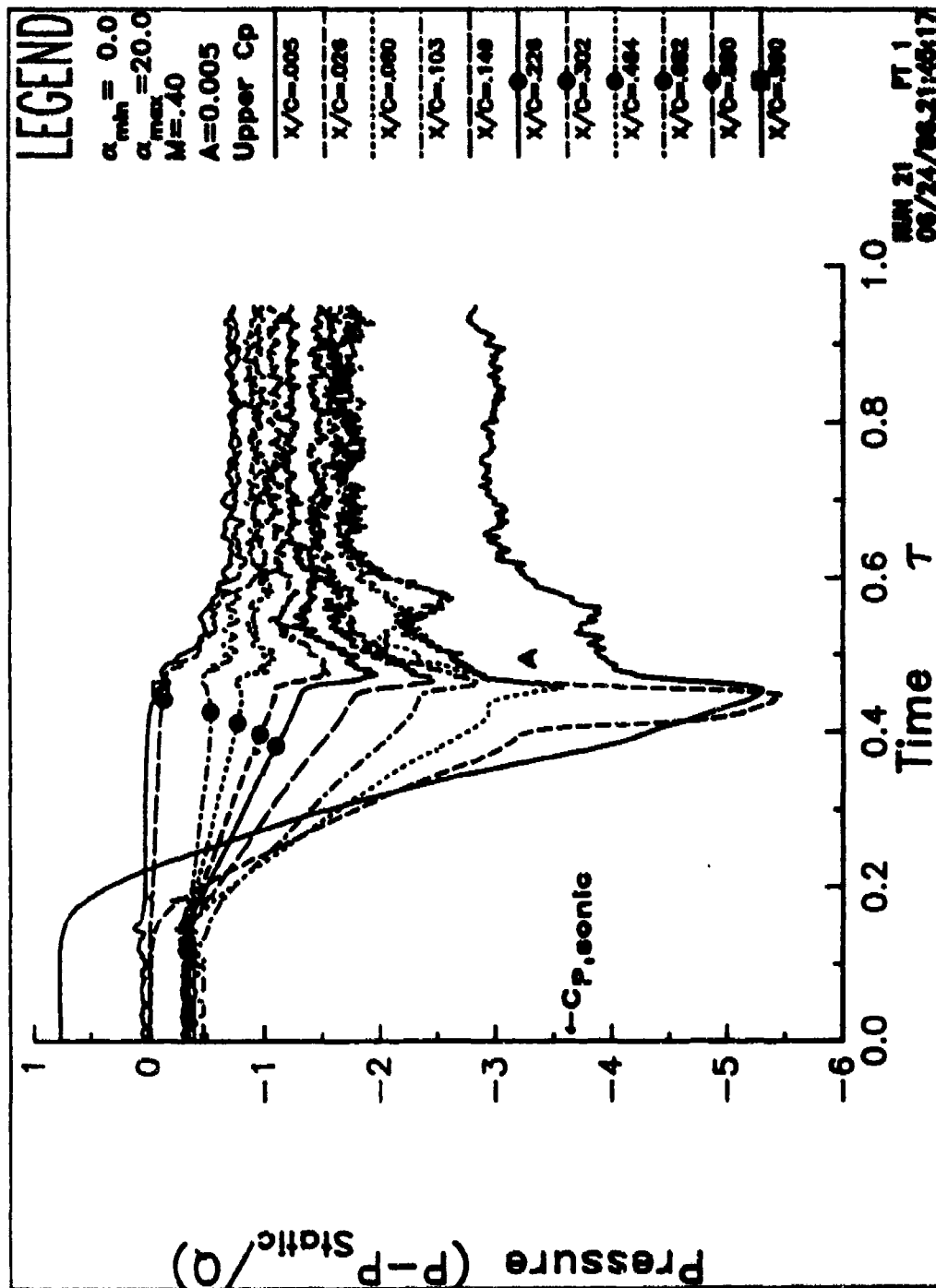


Figure 34. Upper surface pressures at  $A = 0.005$ .

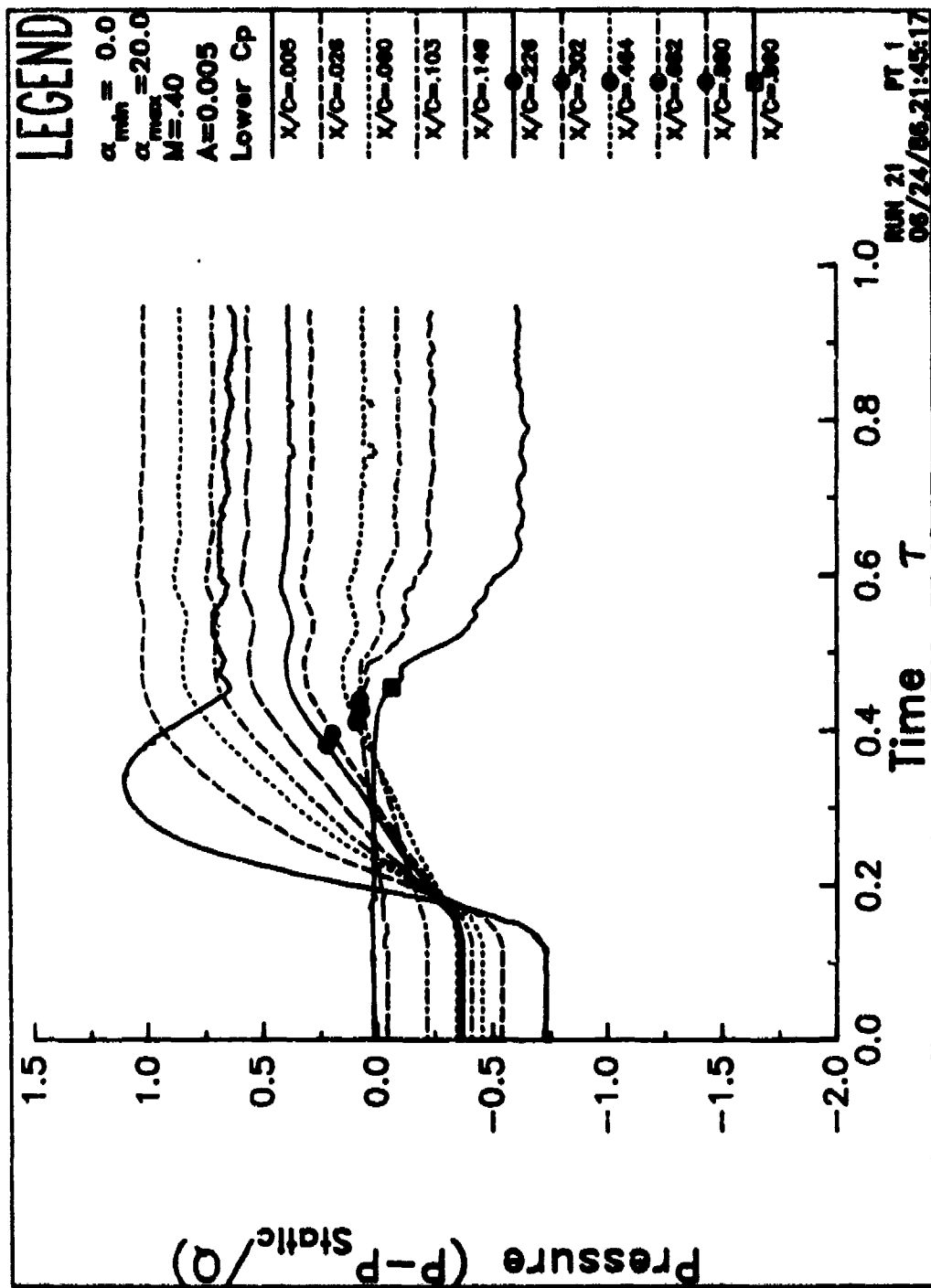


Figure 35. Lower surface. a) And difference

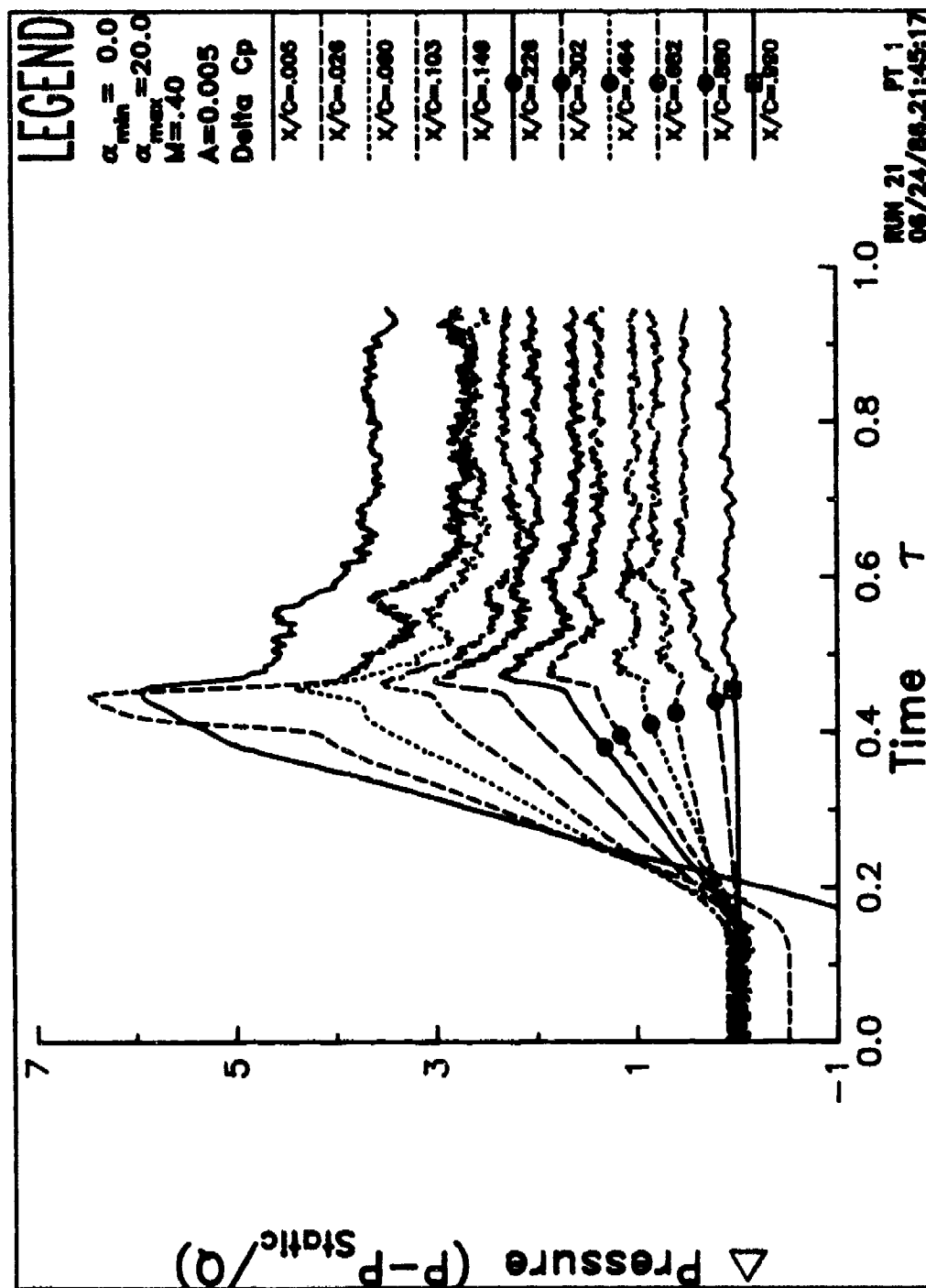


Figure 35. Lower surface. b) Pressures at  $A = 0.005$ .



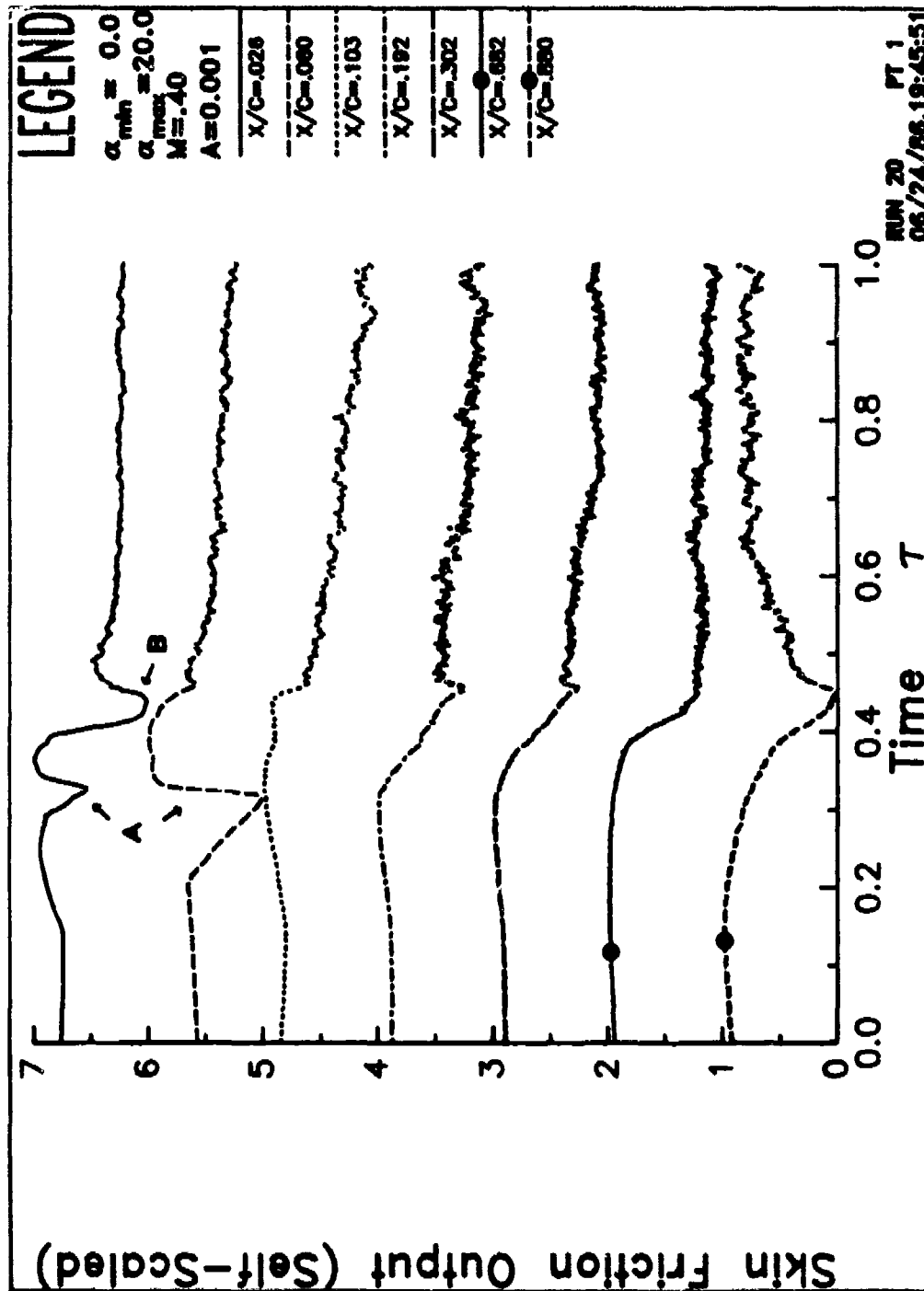


Figure 36. Hot film gage output at  $A = 0.0010$ . a) Ensemble average.

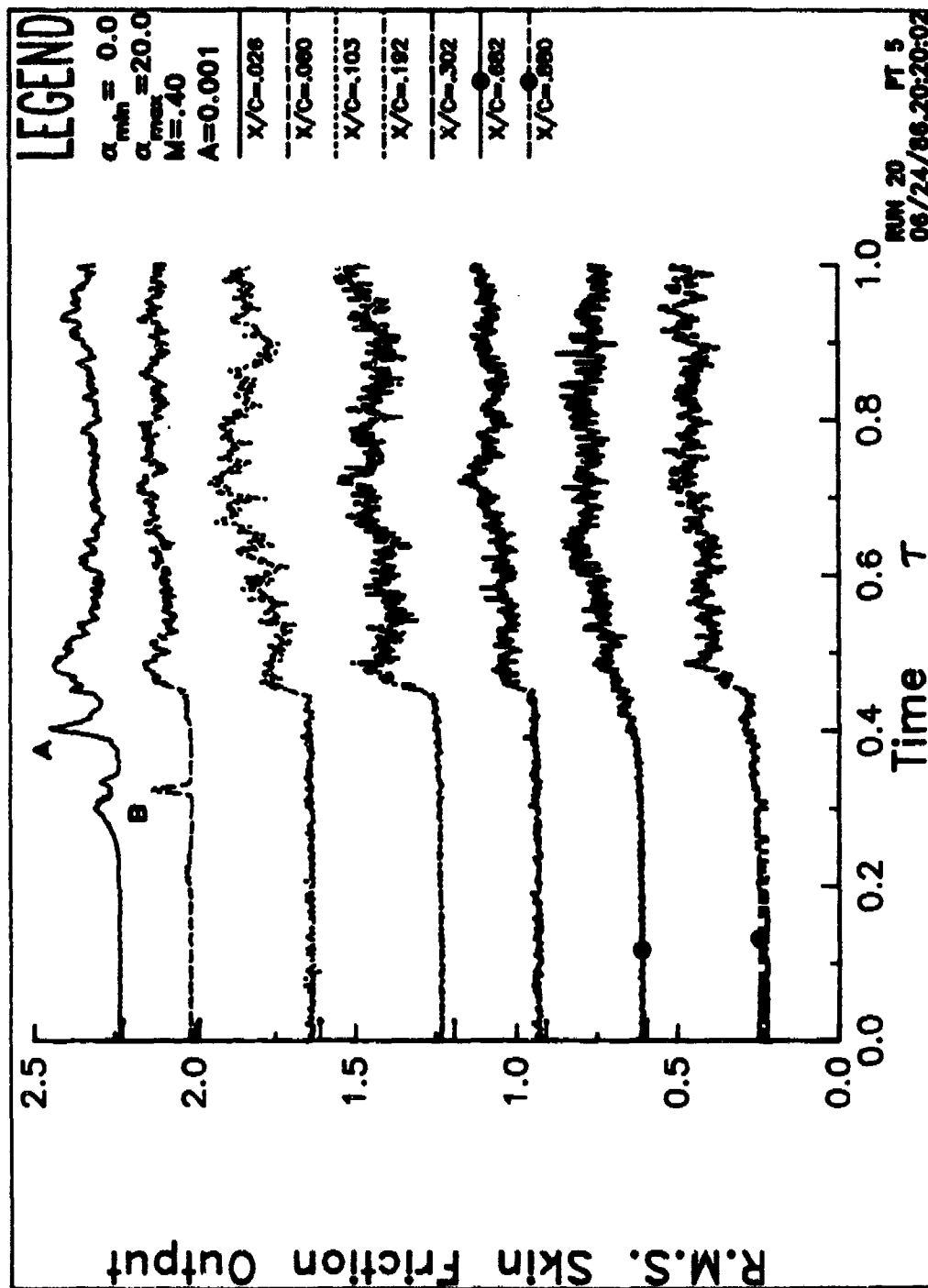


Figure 36. Hot film gage output at  $A = 0.0010$ . b) RMS

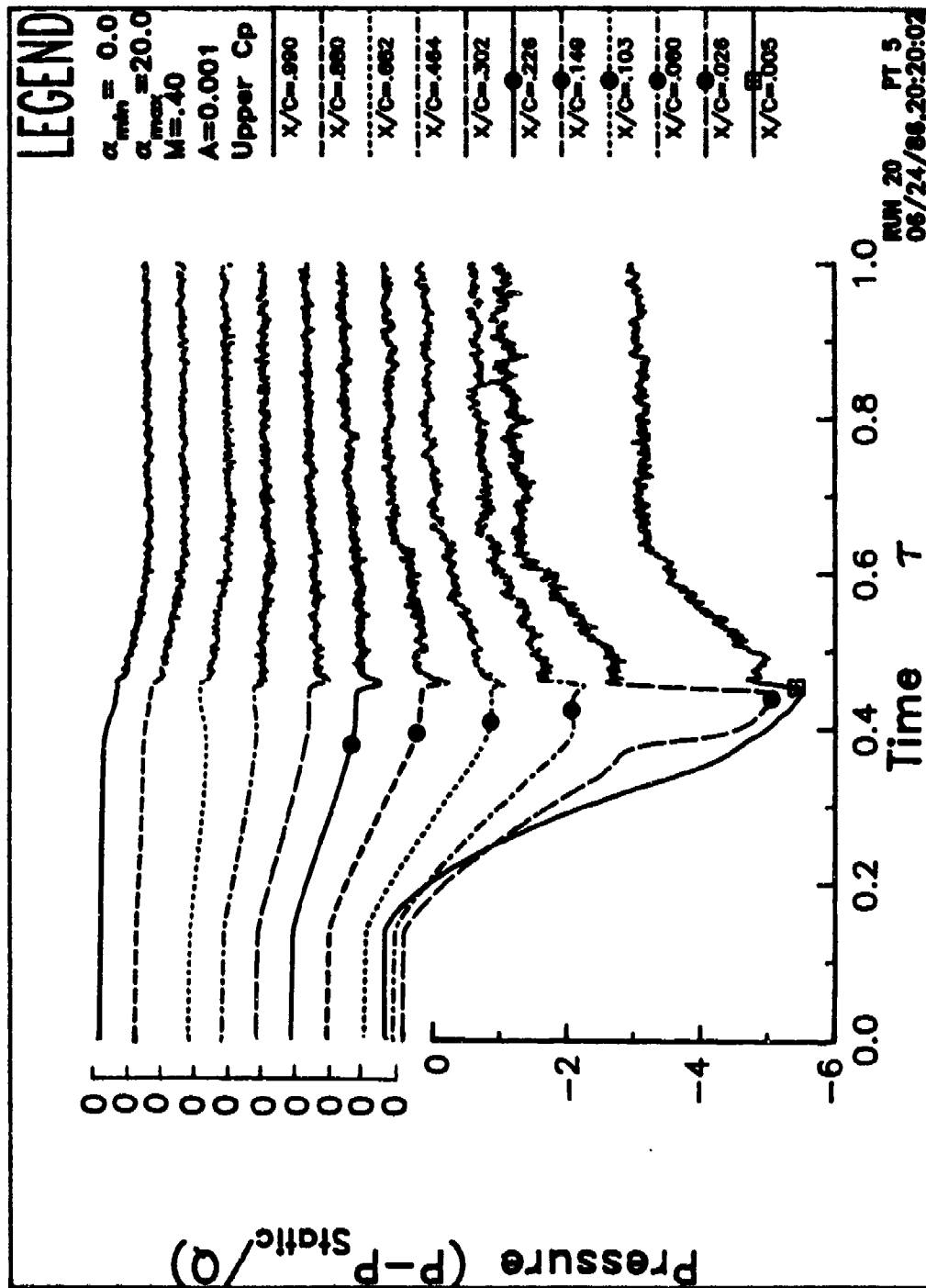


Figure 37. Upper surface pressures. a)  $A = 0.0010$ .



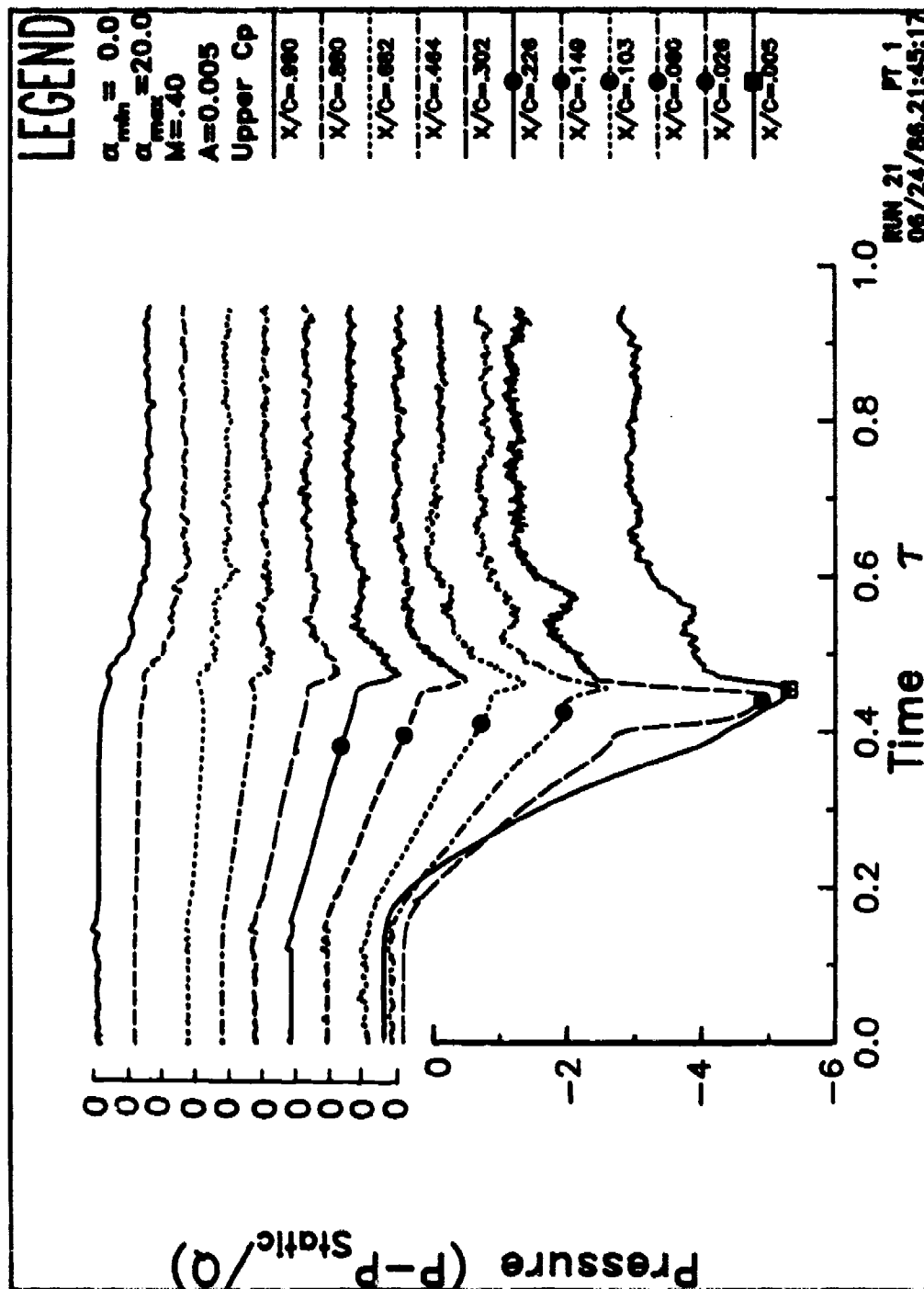


Figure 37. Upper surface pressures. c)  $A = 0.0050$ .

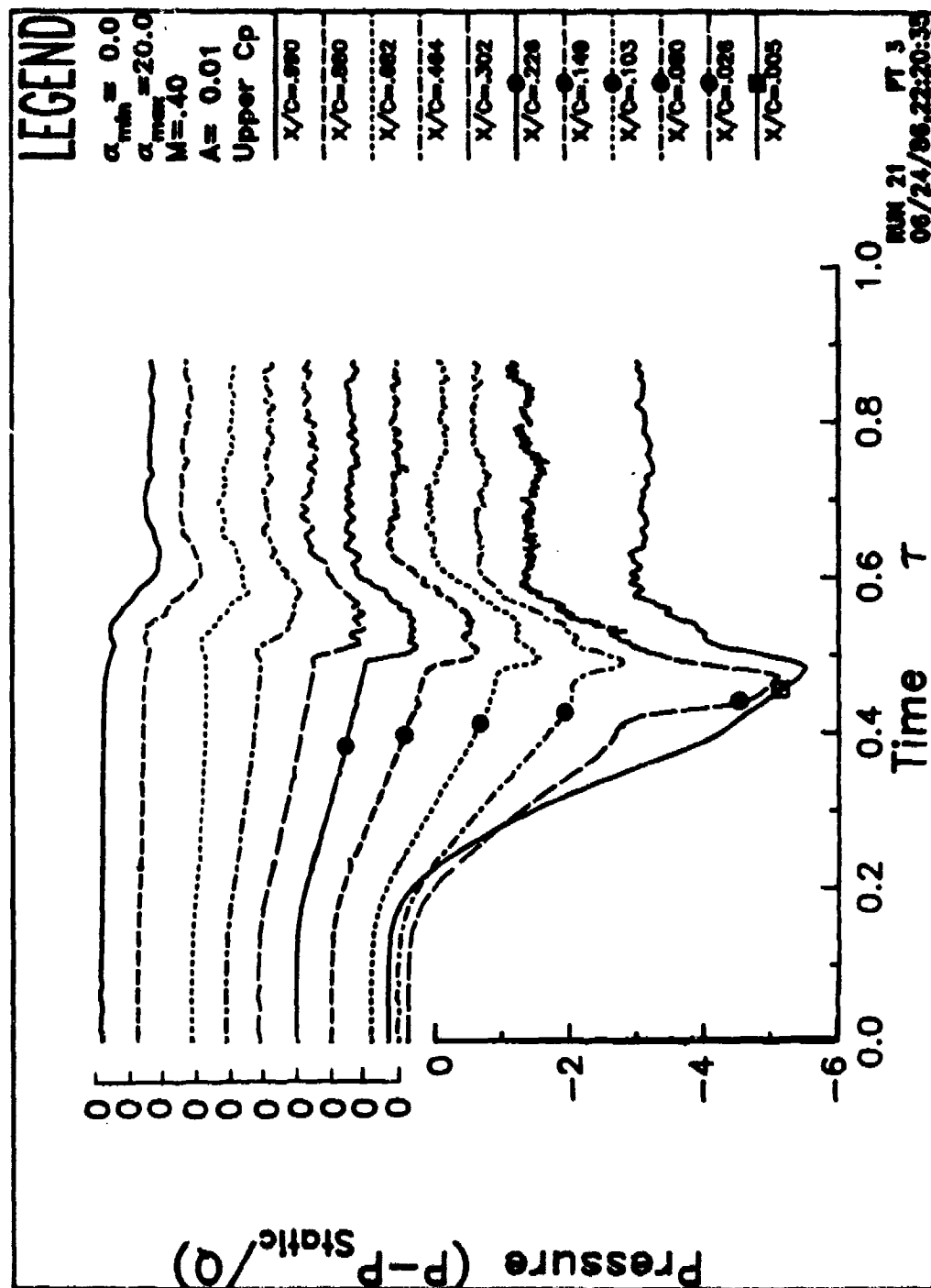


Figure 37. Upper surface pressures. d)  $A = 0.0100$ .

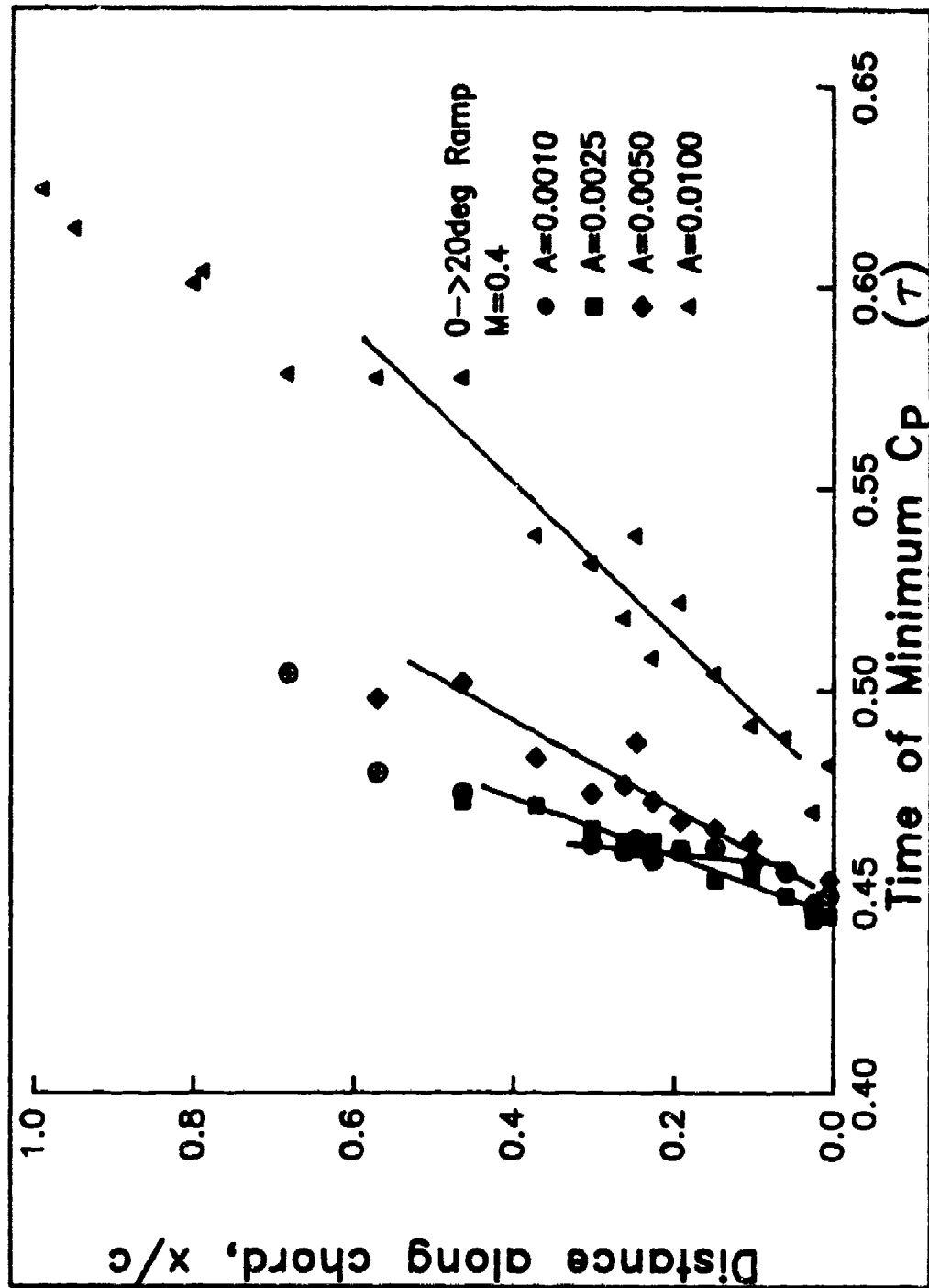


Figure 38. Times of minimum pressure at each pitch rate.

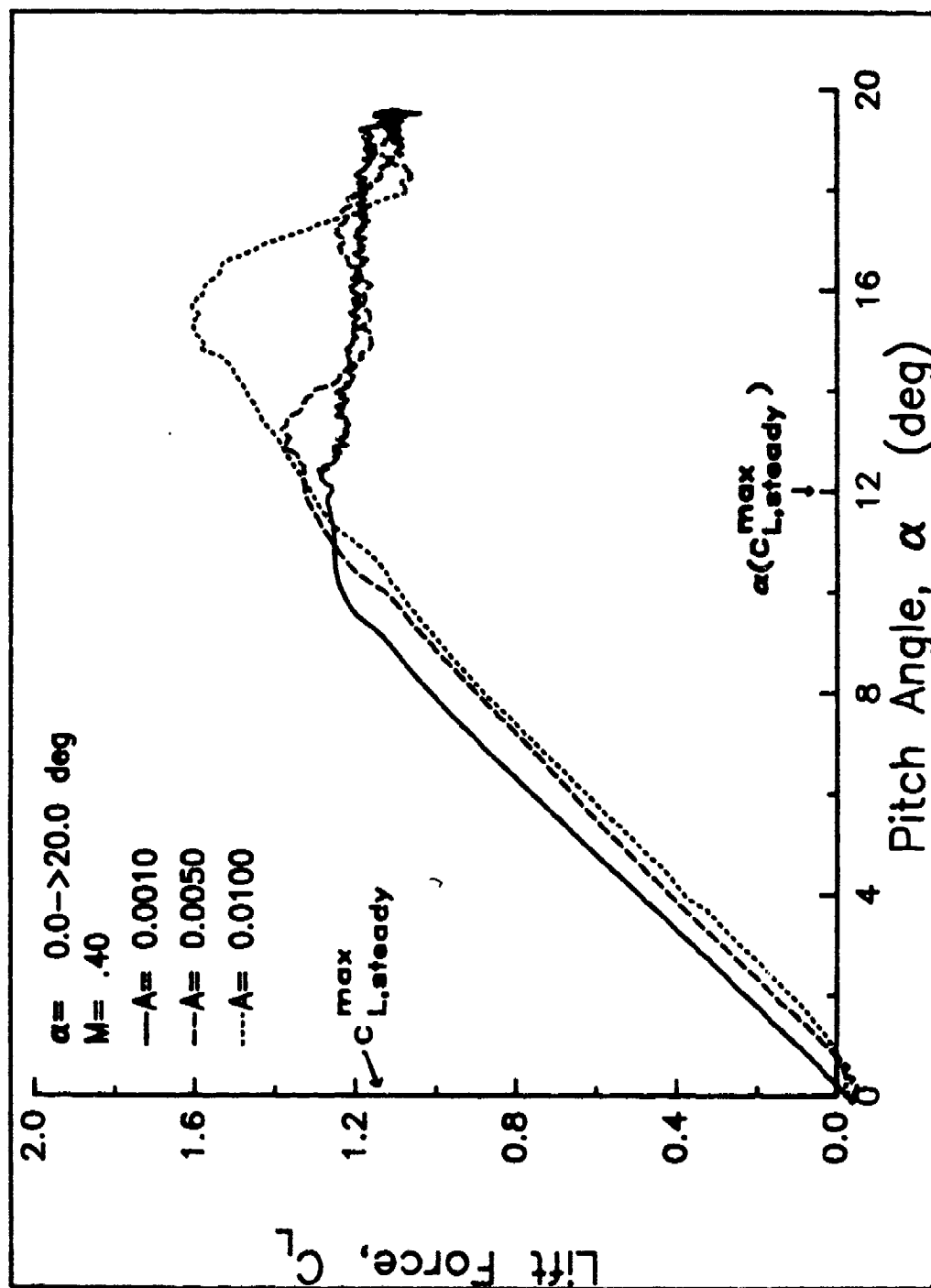


Figure 39. Airloads at  $A = 0.0010$ ,  $0.0050$ , and  $0.0100$ . a) Lift vs. pitch angle.



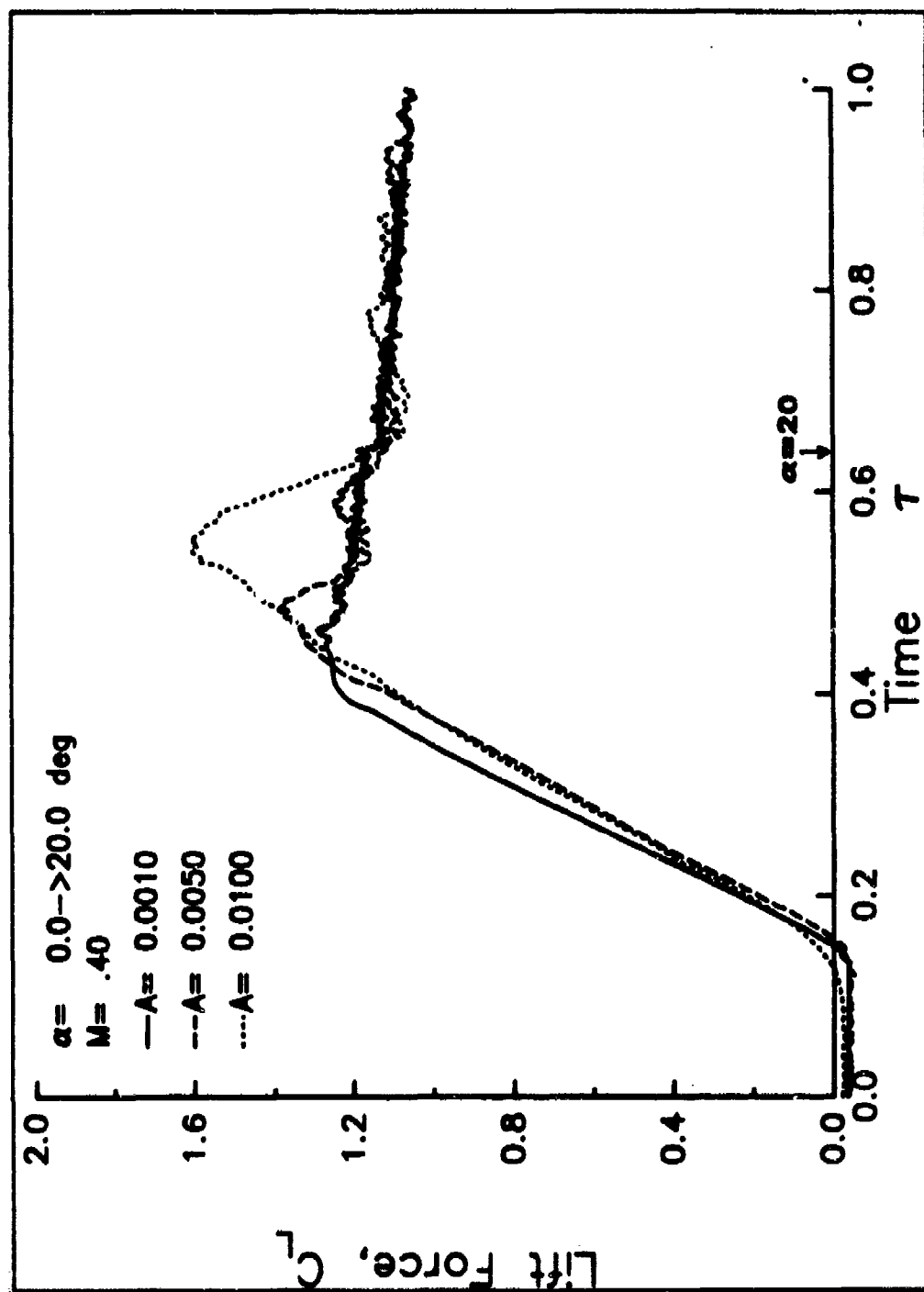


Figure 39. Airloads at  $A = 0.0010$ ,  $0.0050$ , and  $0.0100$ . b) Lift vs. time.

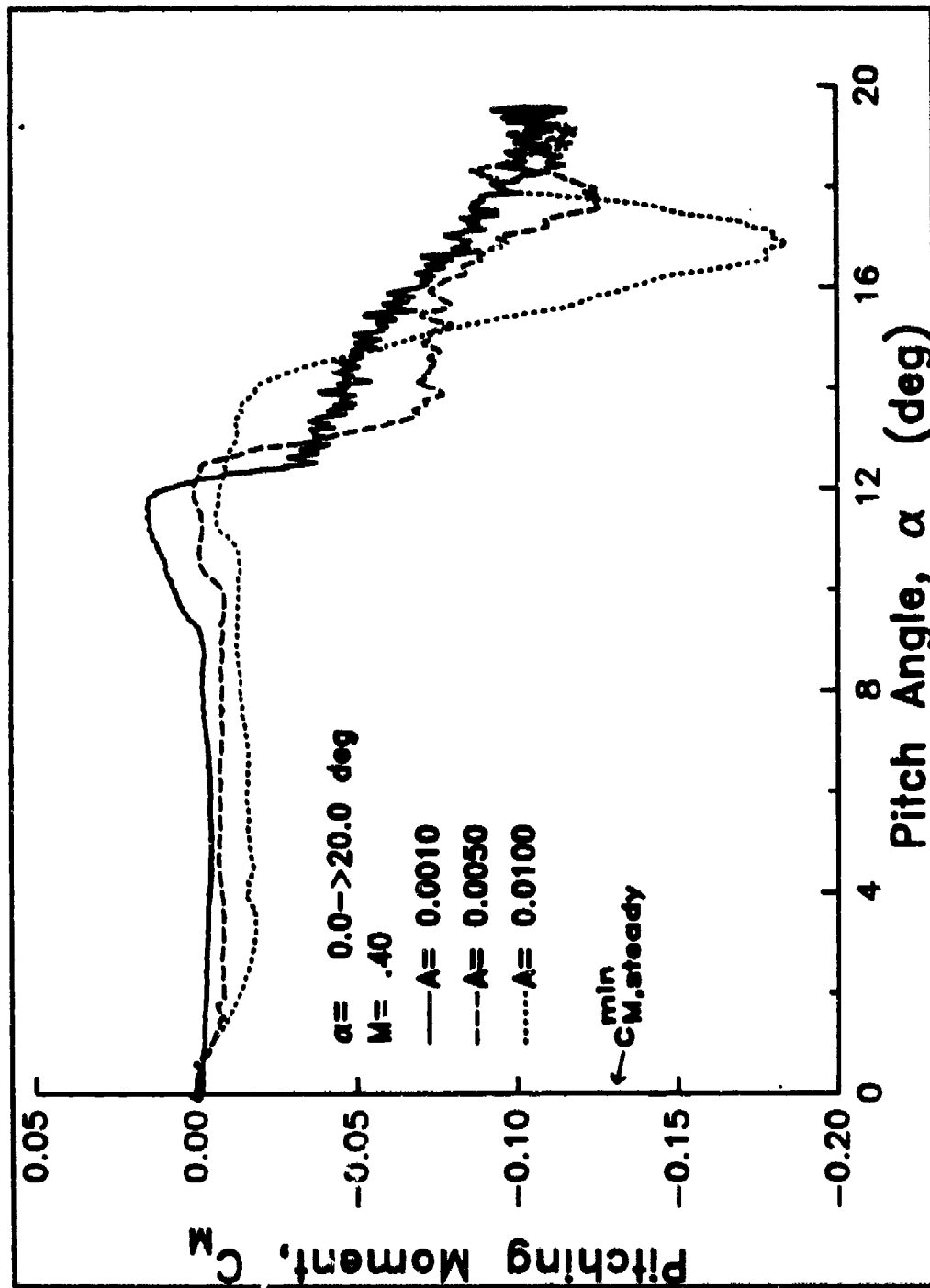


Figure 39. Airloads at  $A = 0.0010, 0.0050, 0.0100$ . c) Moment vs. pitch angle.

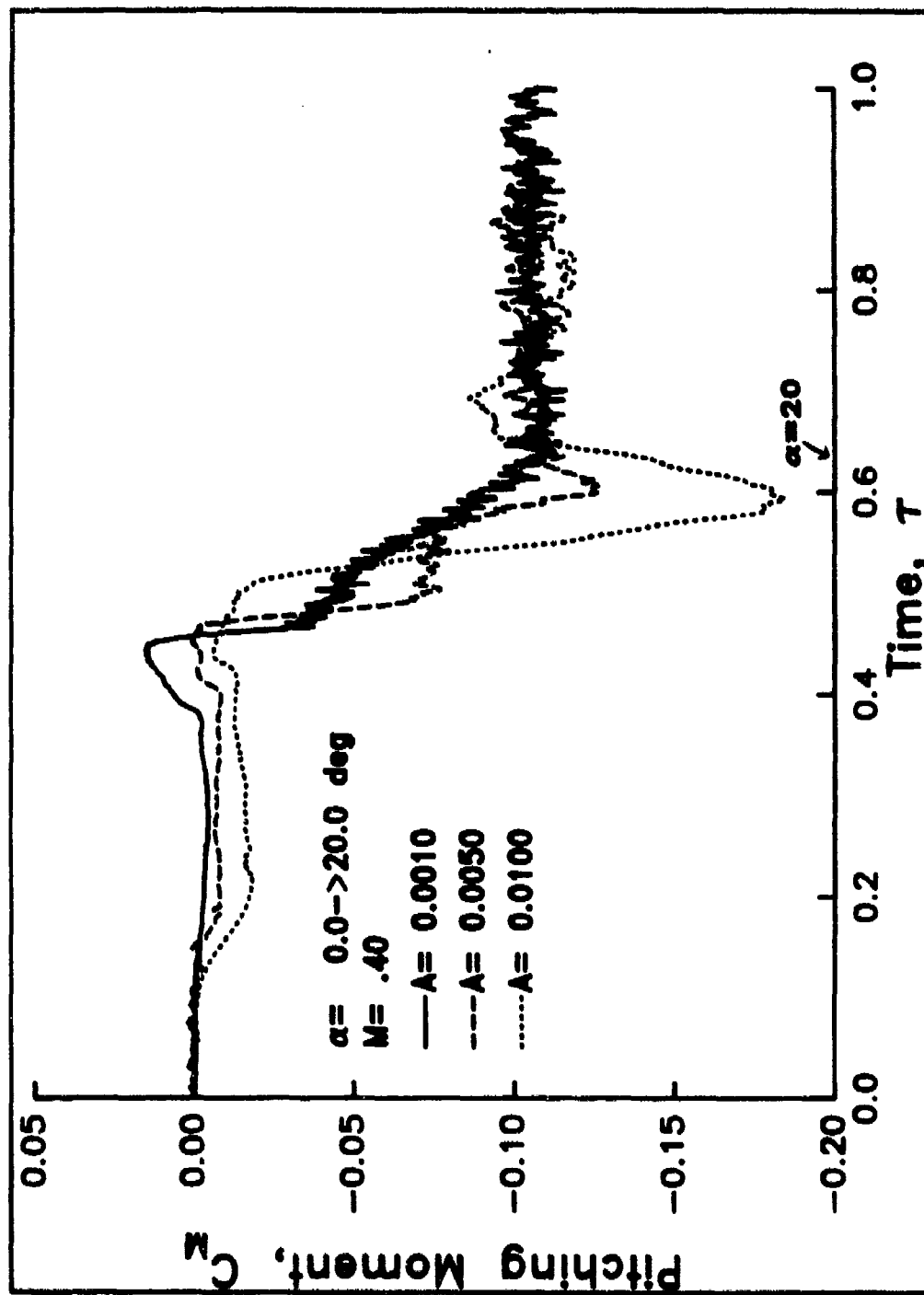


Figure 39. Airloads at  $A = 0.0010, 0.0050, 0.0100$ . d) Moment vs. time.

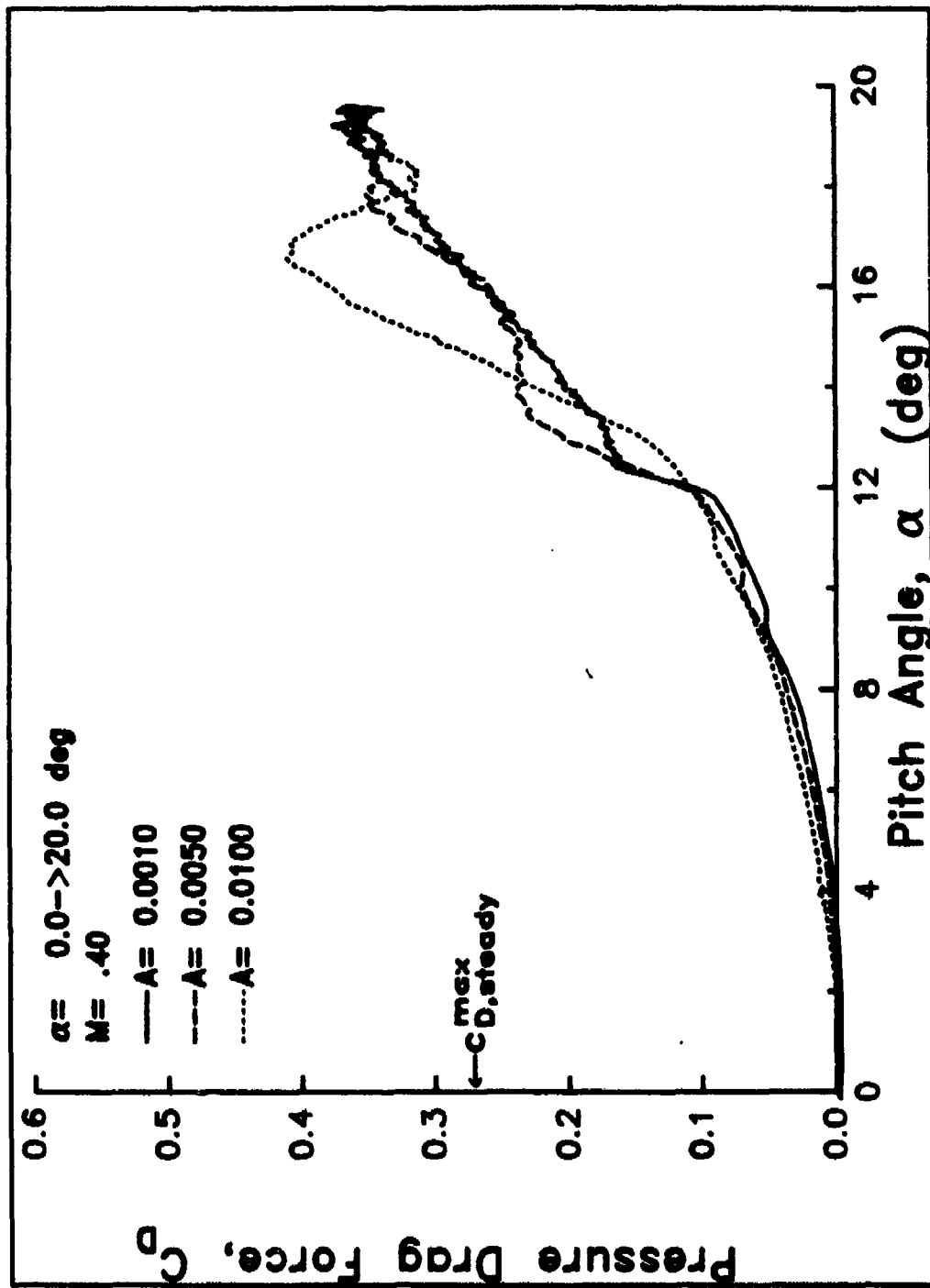


Figure 39. Airloads at  $A = 0.0010$ ,  $0.0050$ , and  $0.0100$ . e) Drag vs. pitch angle.

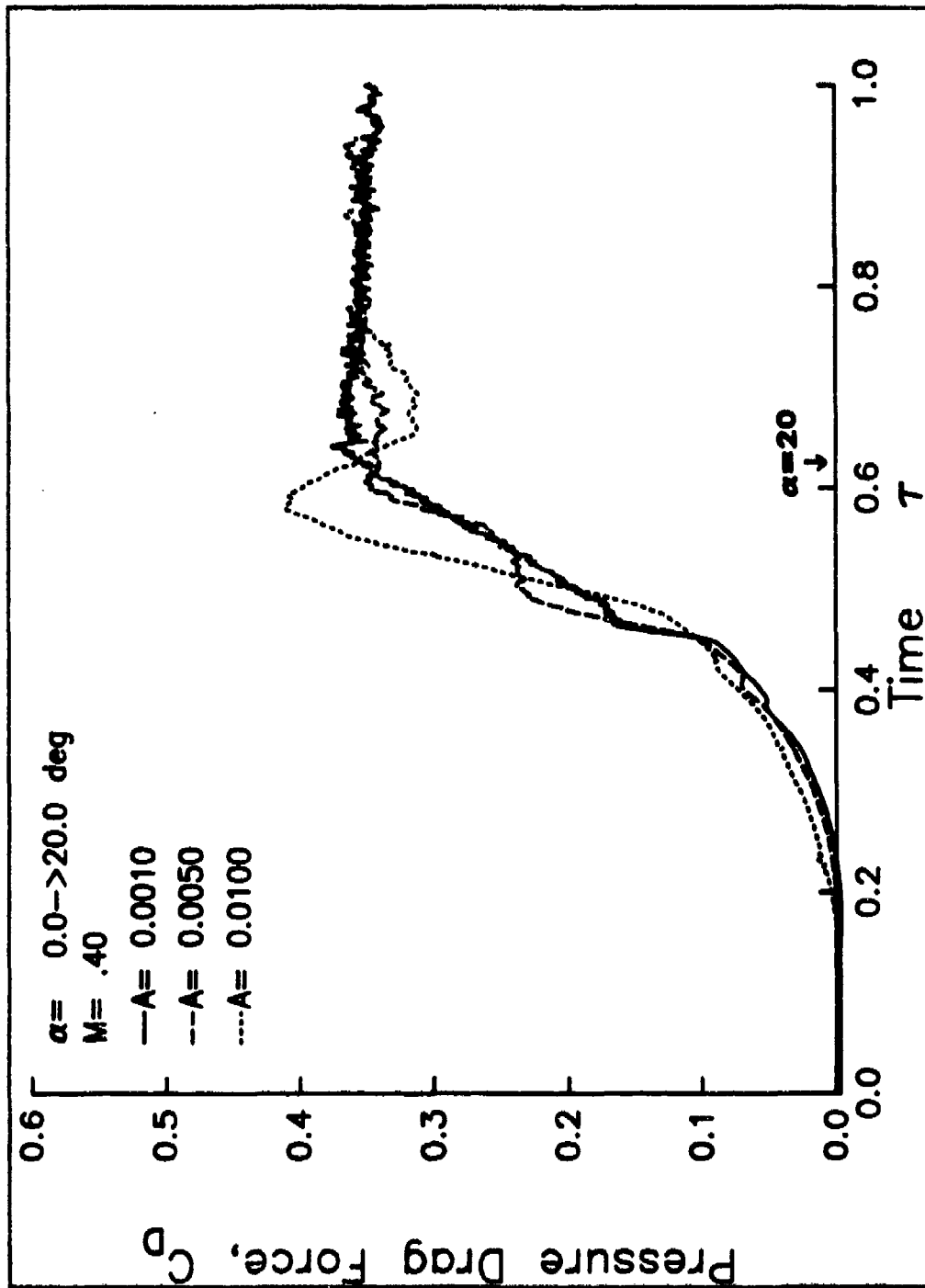


Figure 39. Airloads at  $A = 0.0010$ ,  $0.0050$ , and  $0.0100$ . f) Drag vs. time.

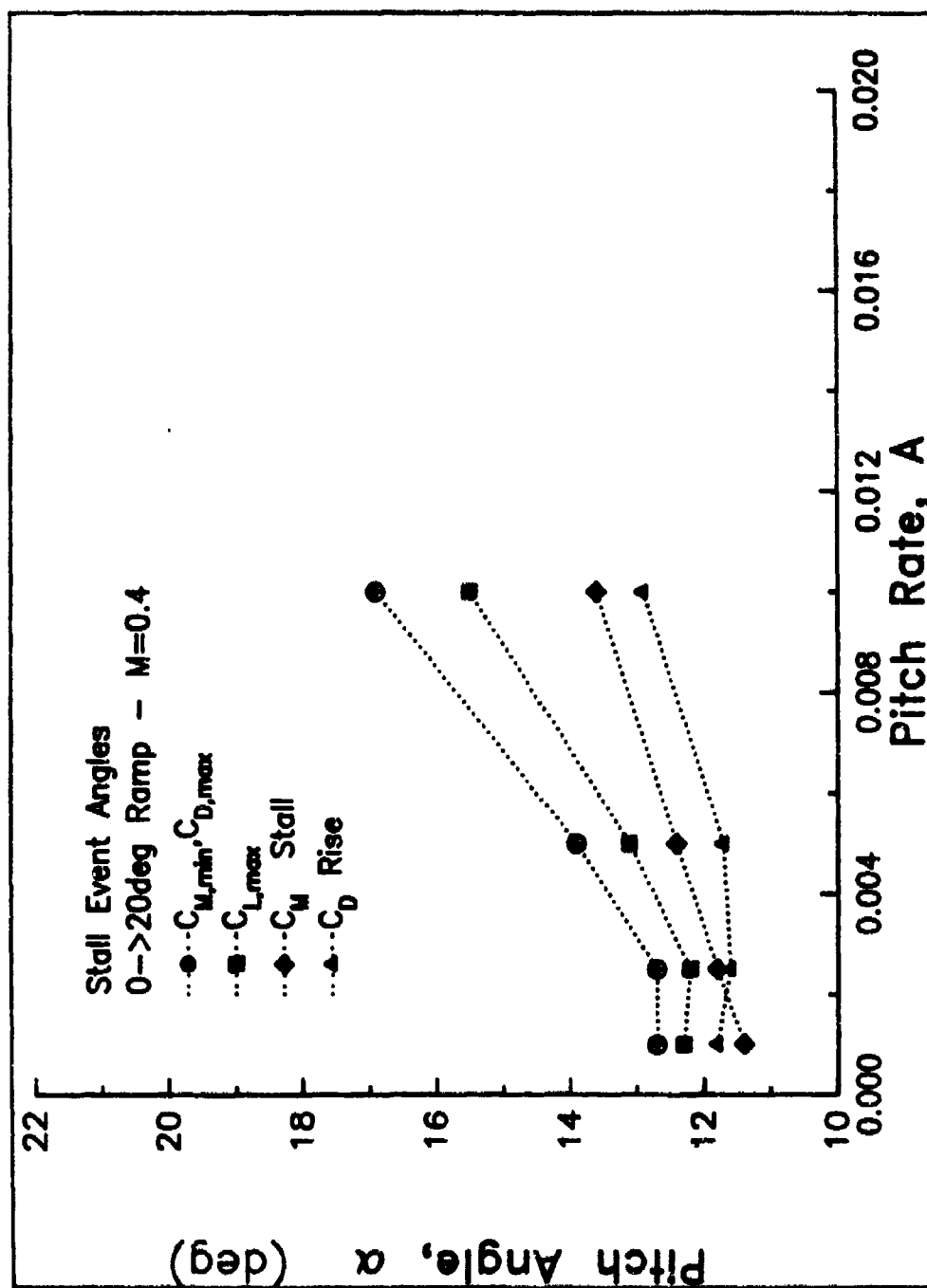


Figure 40. Sequence of stall events vs pitch rate.

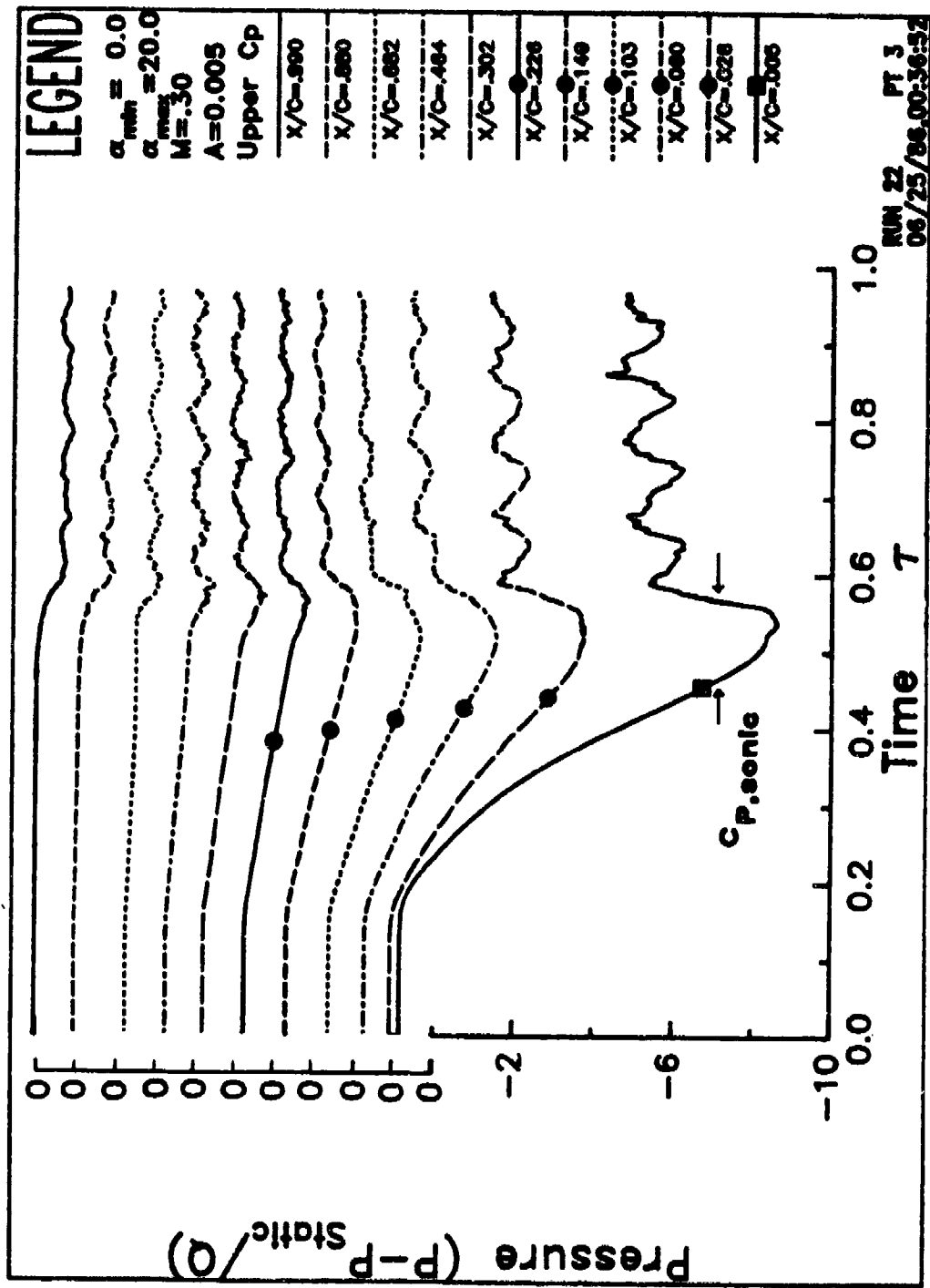


Figure 41. Upper surface pressures. a) 0 to 20 deg ramp at  $A = 0.0050$ .

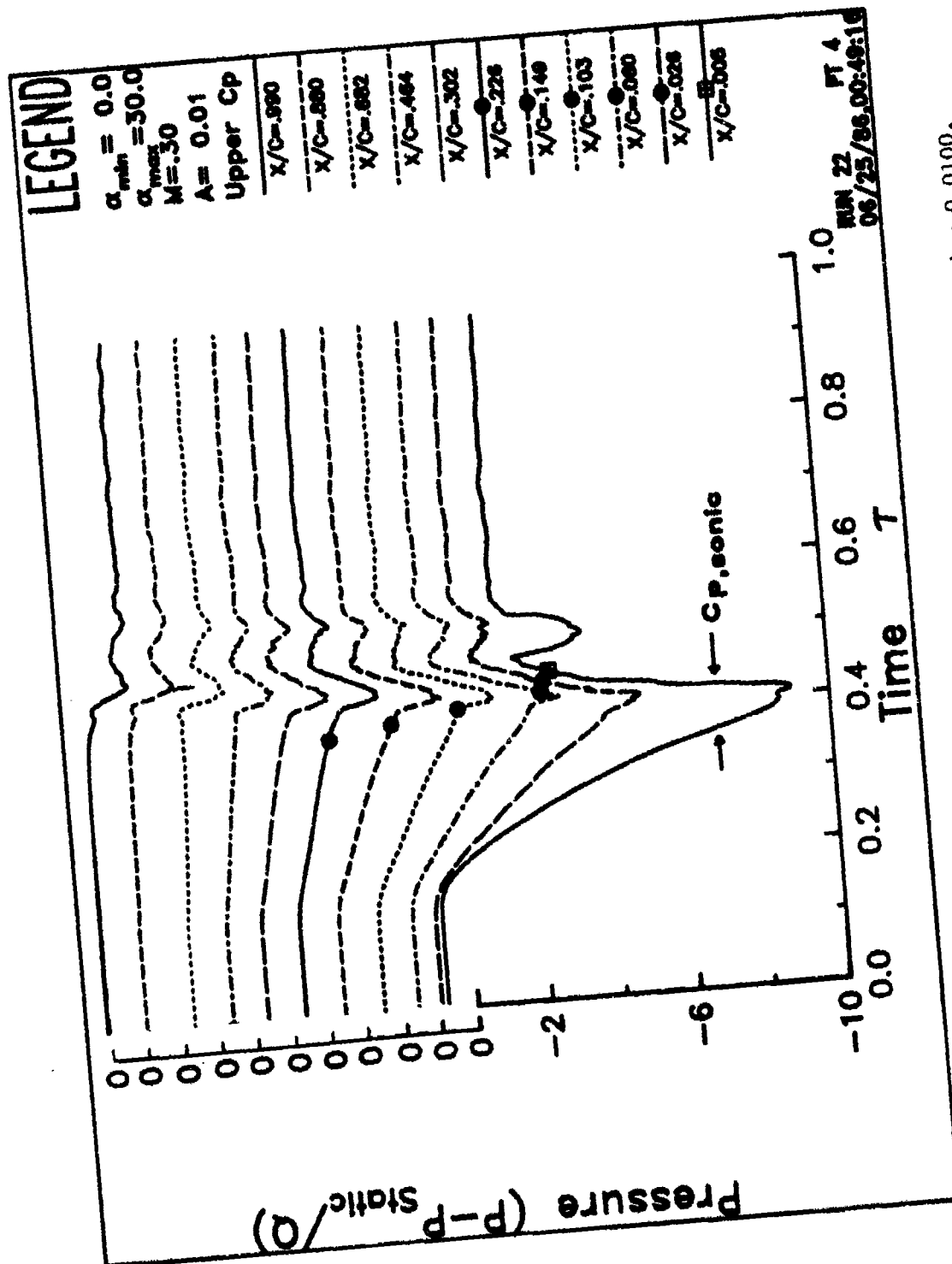


Figure 41. Upper surface pressures. b) 0 to 30 deg ramp at  $A = 0.0100$ .



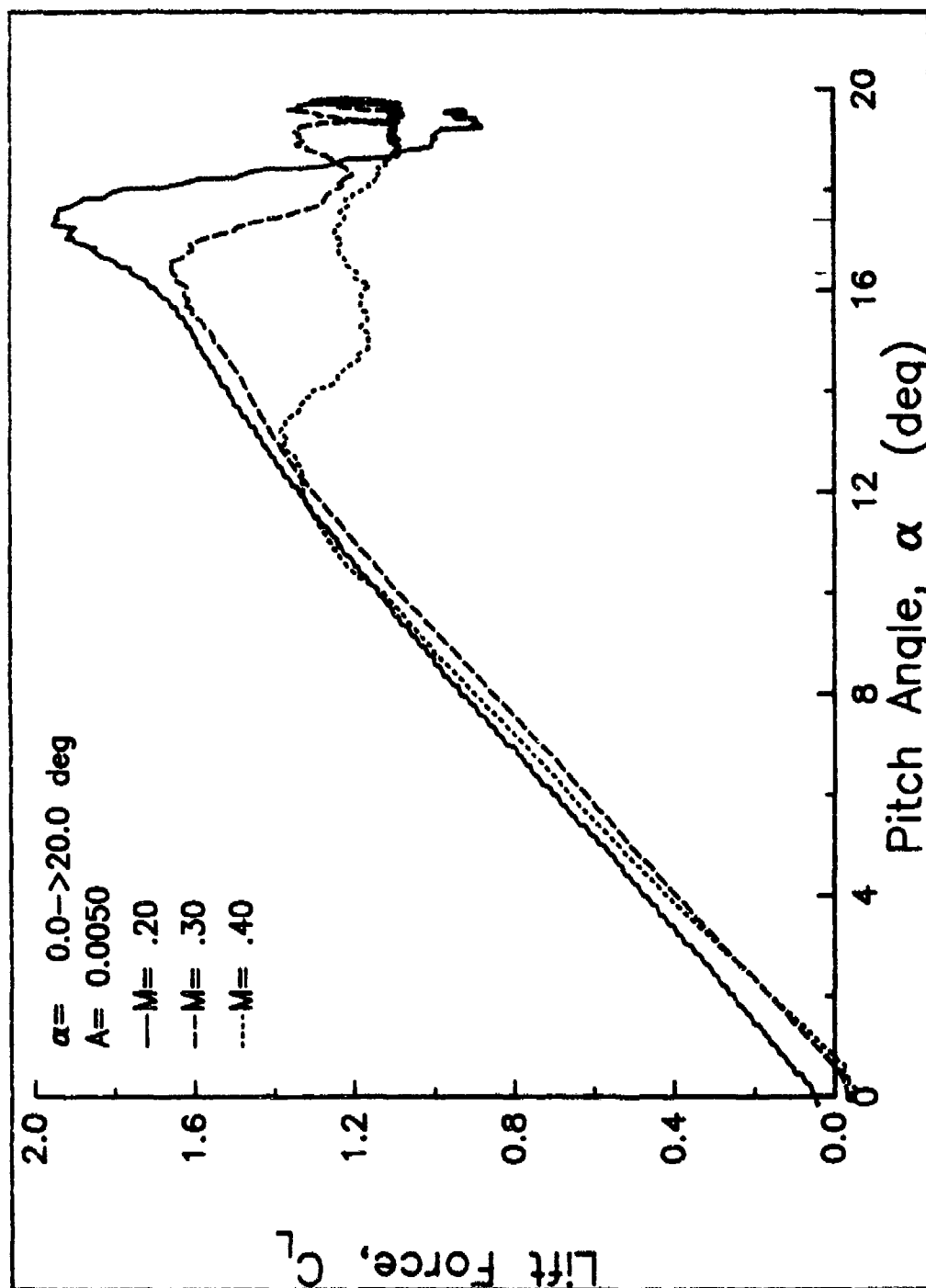


Figure 42. Airloads for a 0 to 20 deg ramp at  $A = 0.0050$  at  $M = 0.2, 0.3$ , and  $0.4$ .  
a) Lift.

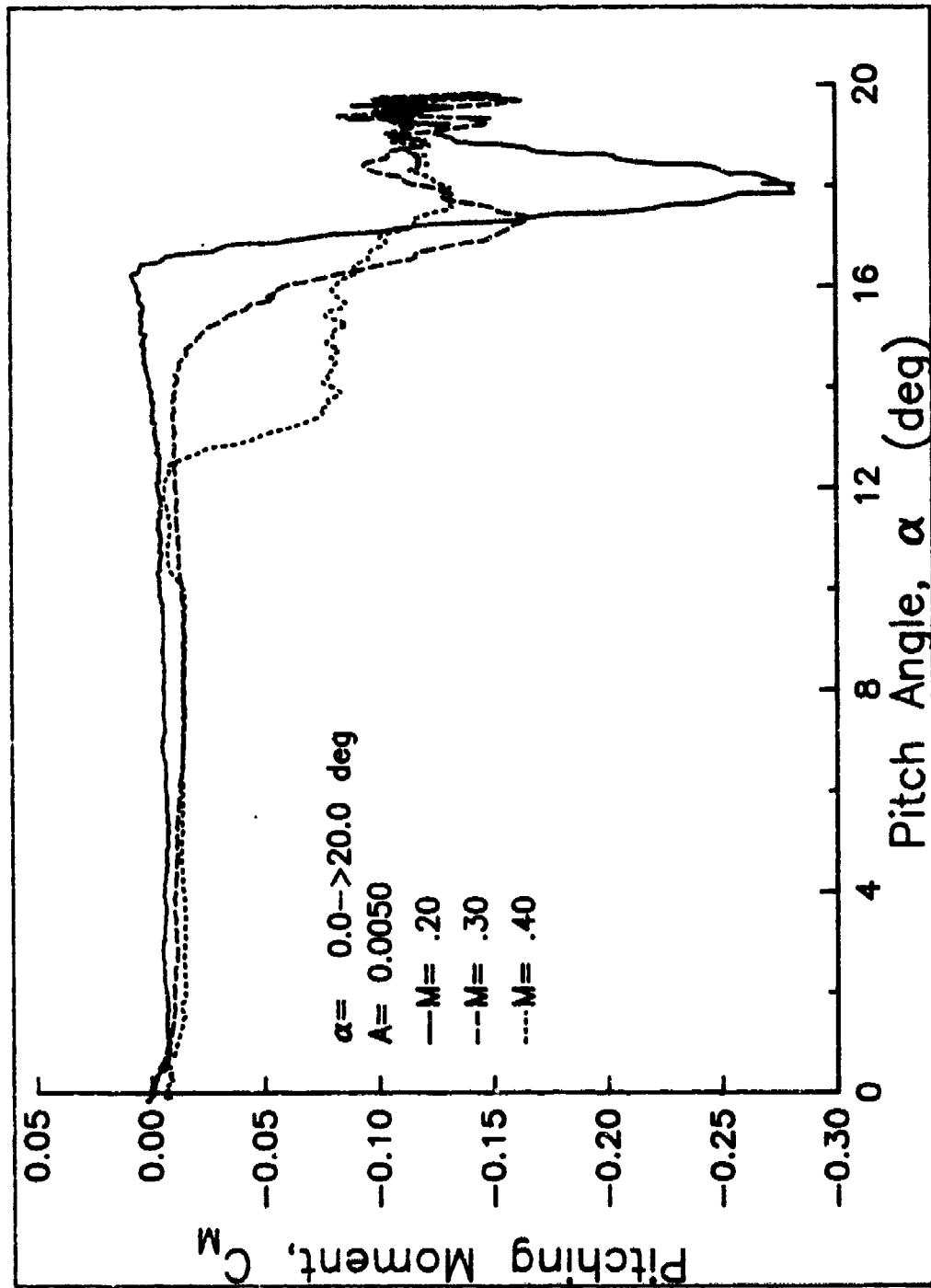


Figure 42. Airloads for a 0 to 20 deg ramp at  $A = 0.0050$  at  $M = 0.2, 0.3$ , and  $0.4$ .  
b) Moment.

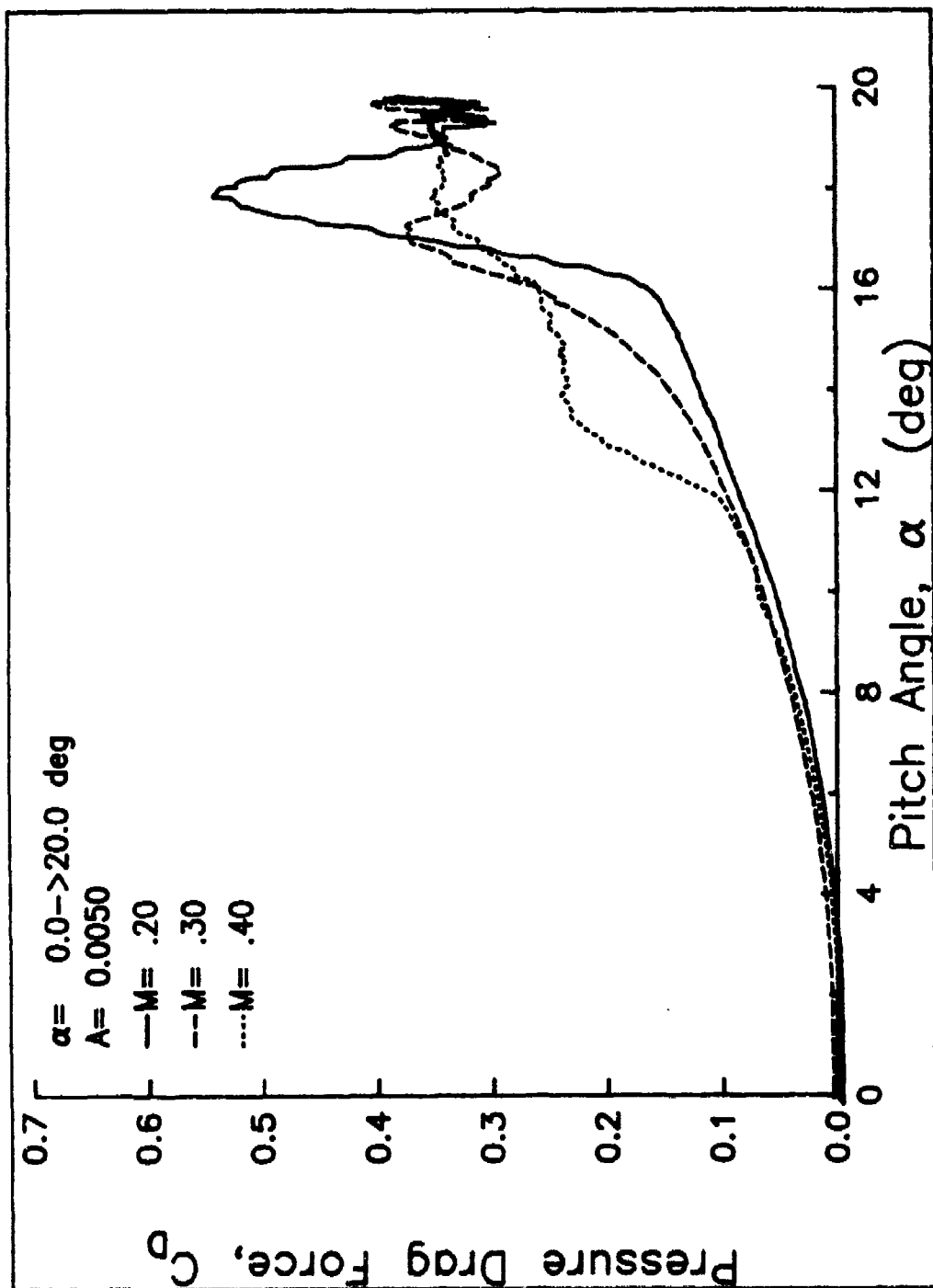


Figure 42. Airloads for a 0 to 20 deg ramp at  $A = 0.0050$  at  $M = 0.2$ ,  $0.3$ , and  $0.4$ .  
c) Drag.

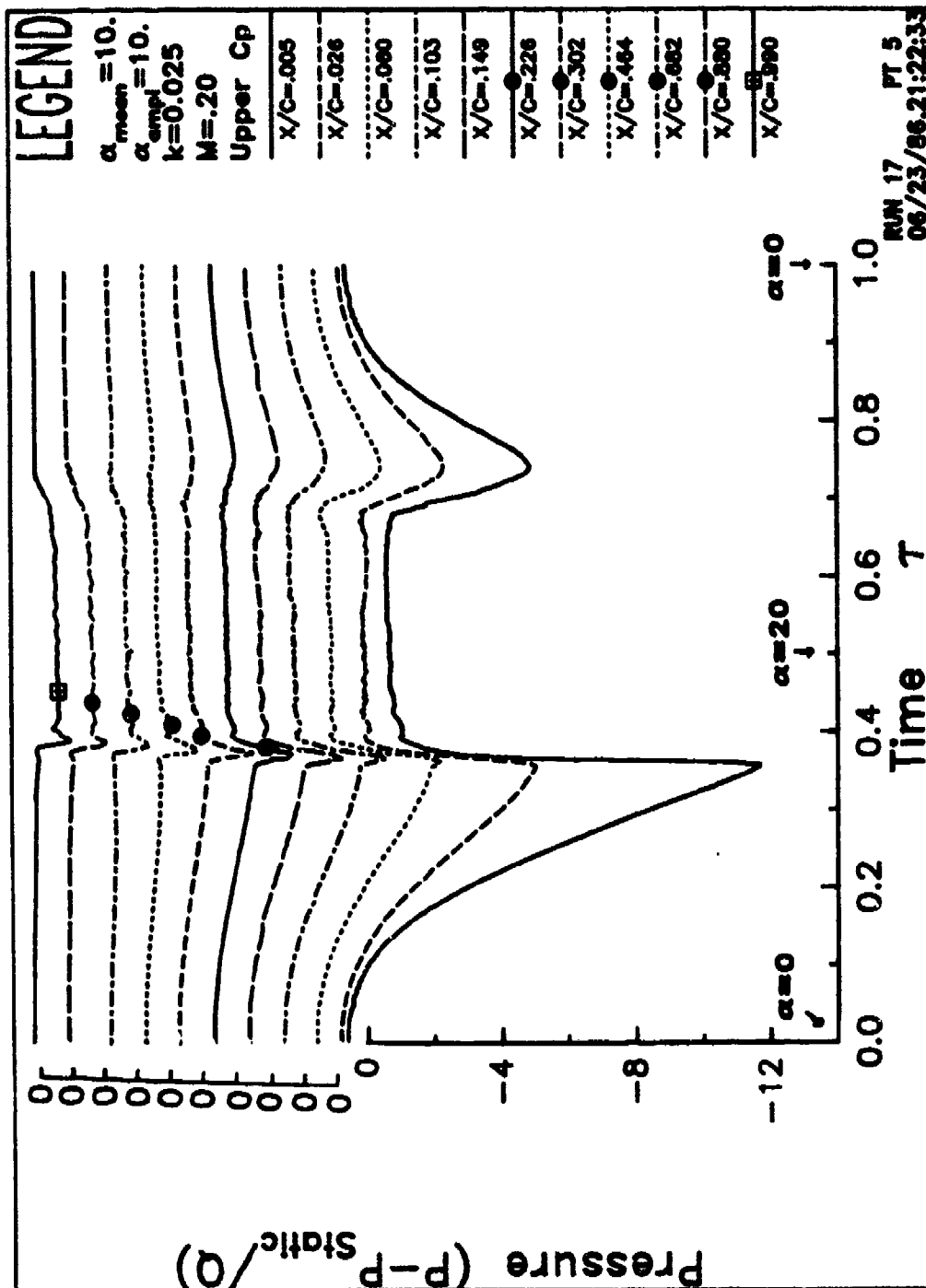


Figure 43. Upper surface pressures. a)  $k = 0.025$ ,  $\alpha = 10 - 10 \cos wt$

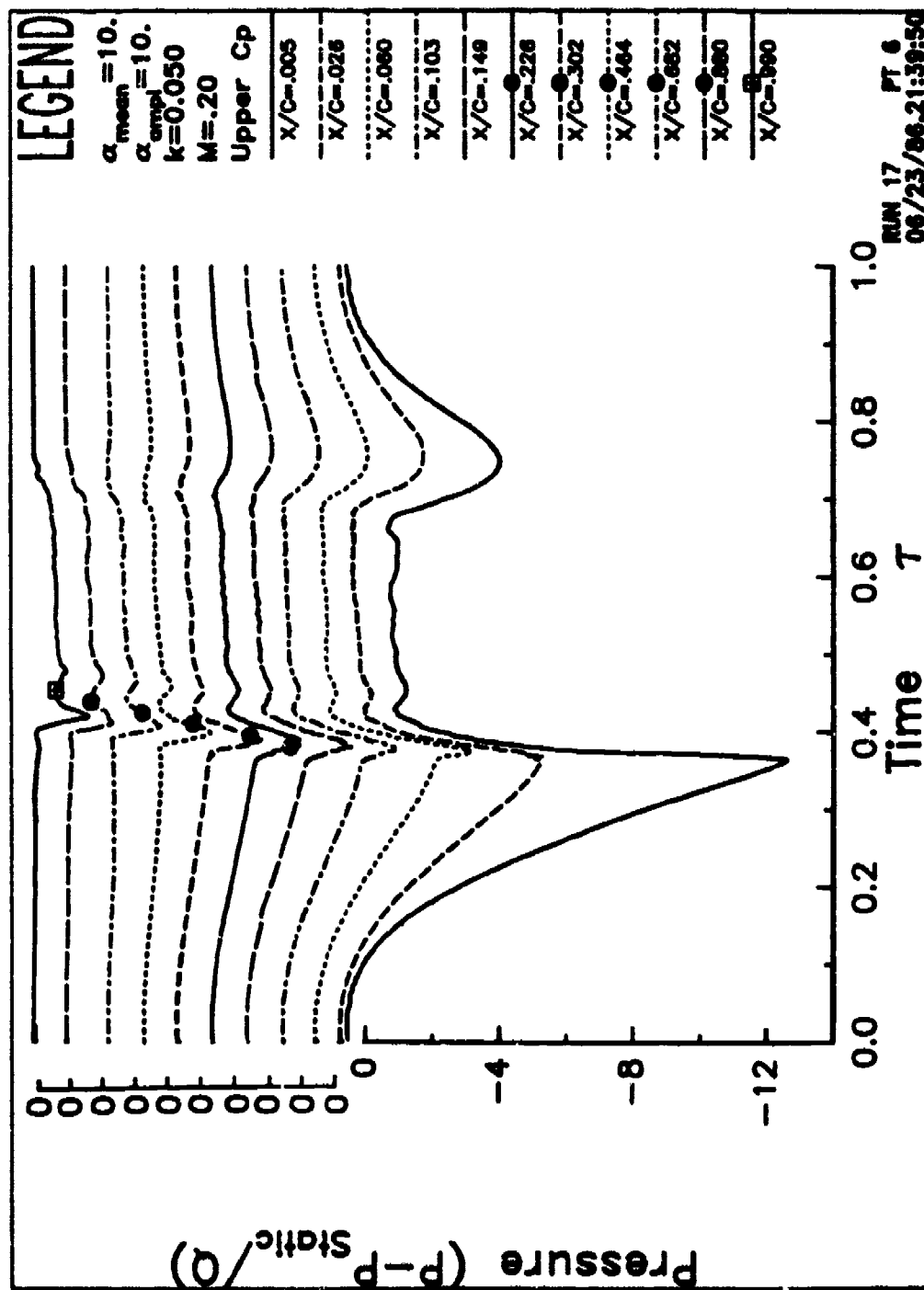


Figure 43. Upper surface pressures. b)  $k = 0.050$ ,  $\alpha = 10 - 10 \cos \omega t$

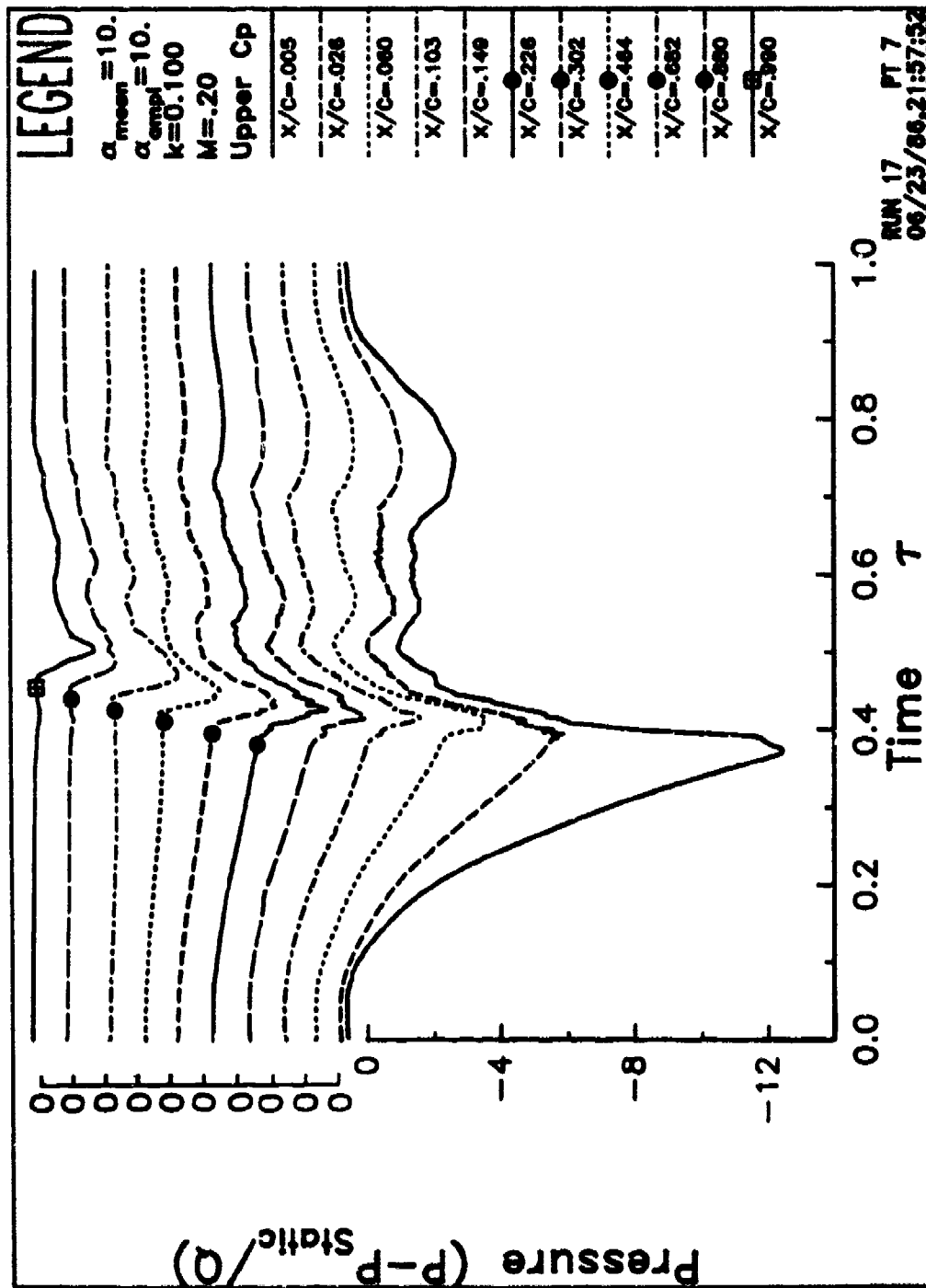


Figure 43. Upper surface pressures. c)  $k = 0.100$ ,  $\alpha = 10 - 10 \cos \omega t$

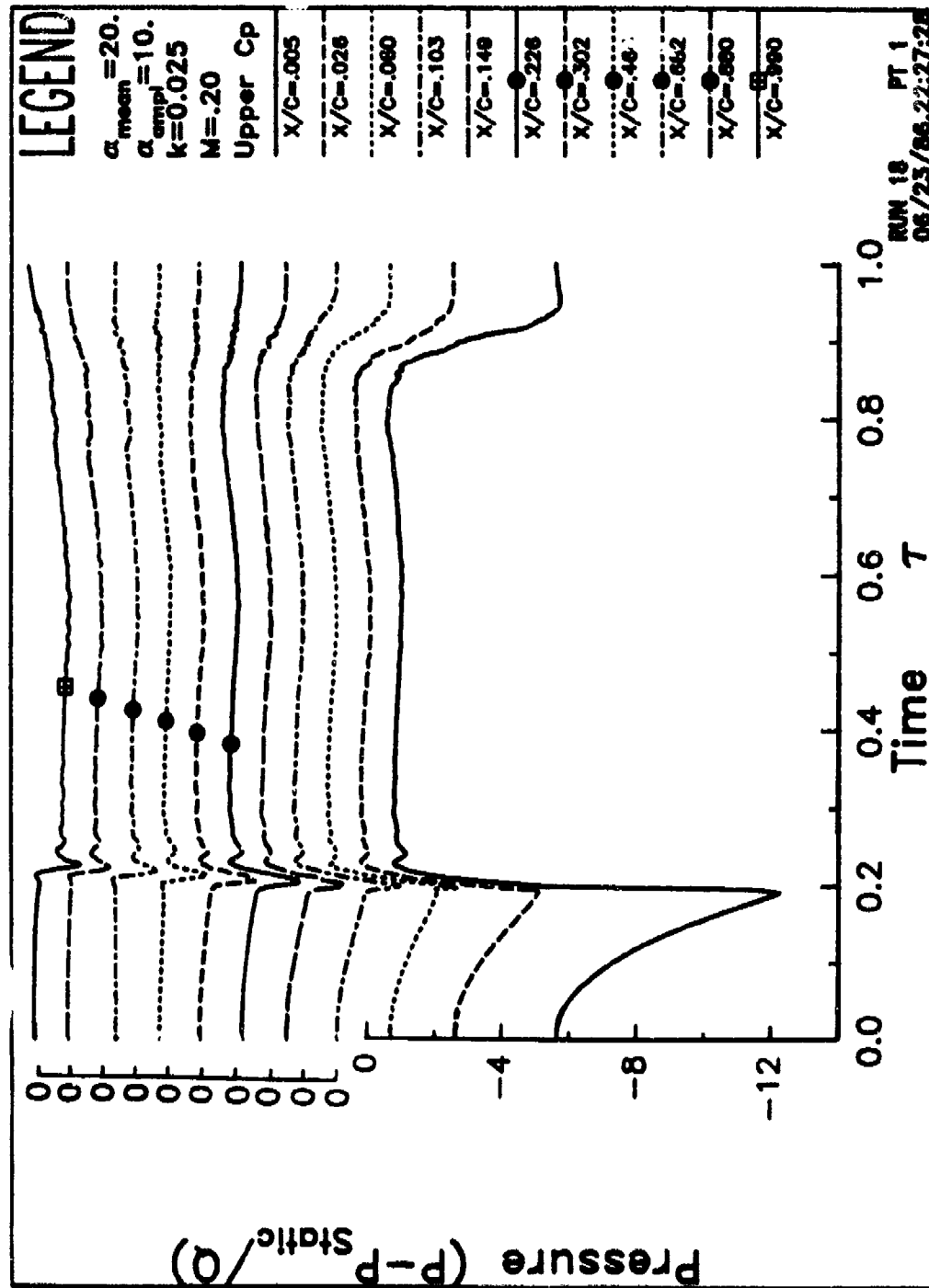


Figure 43. Upper surface pressures. d)  $k = 0.025$ ,  $\alpha = 20 - i0 \cos \omega t$

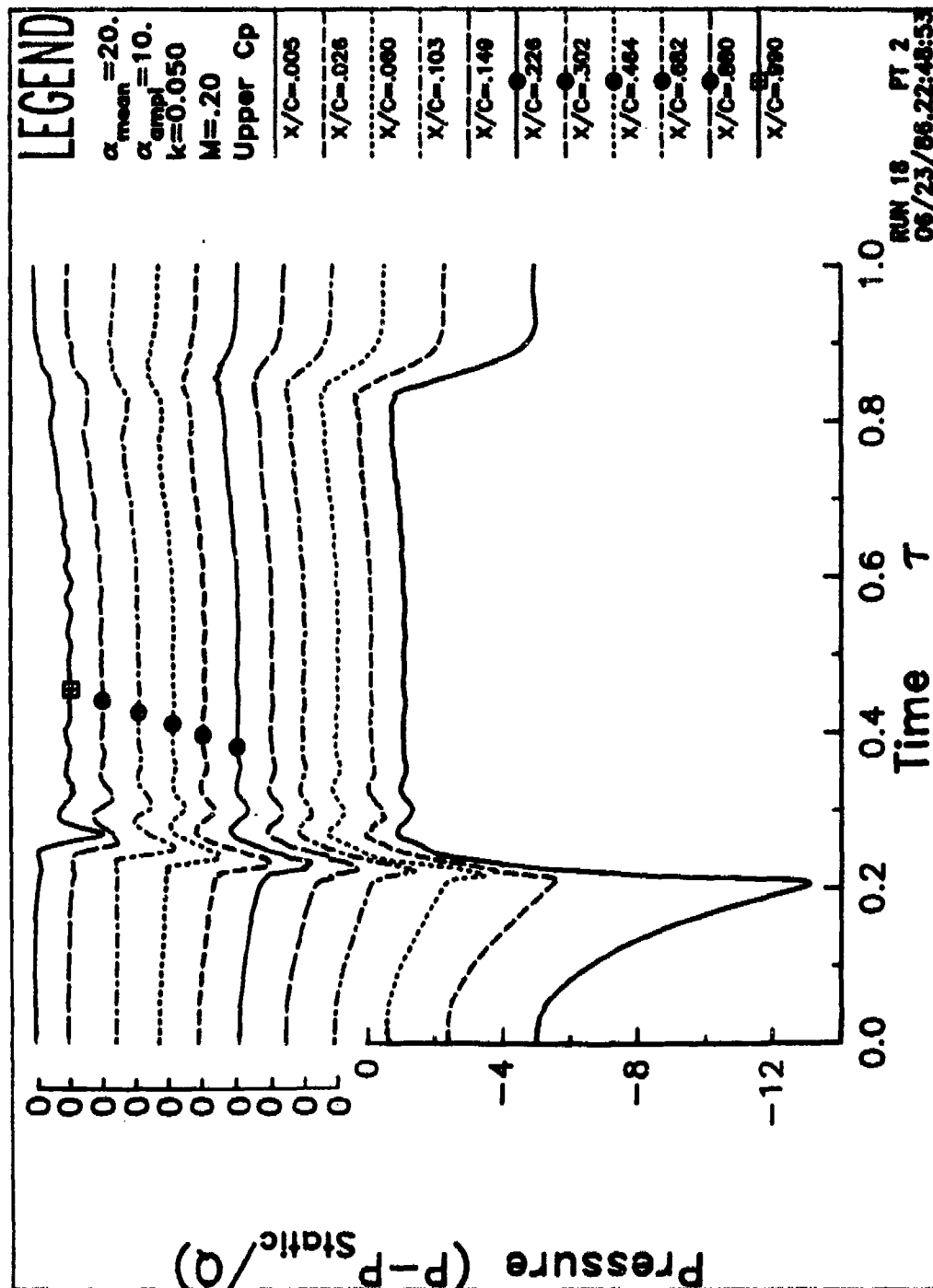


Figure 43. Upper surface pressures. e)  $k = 0.050$ ,  $\alpha = 20 - 10 \cos \omega t$



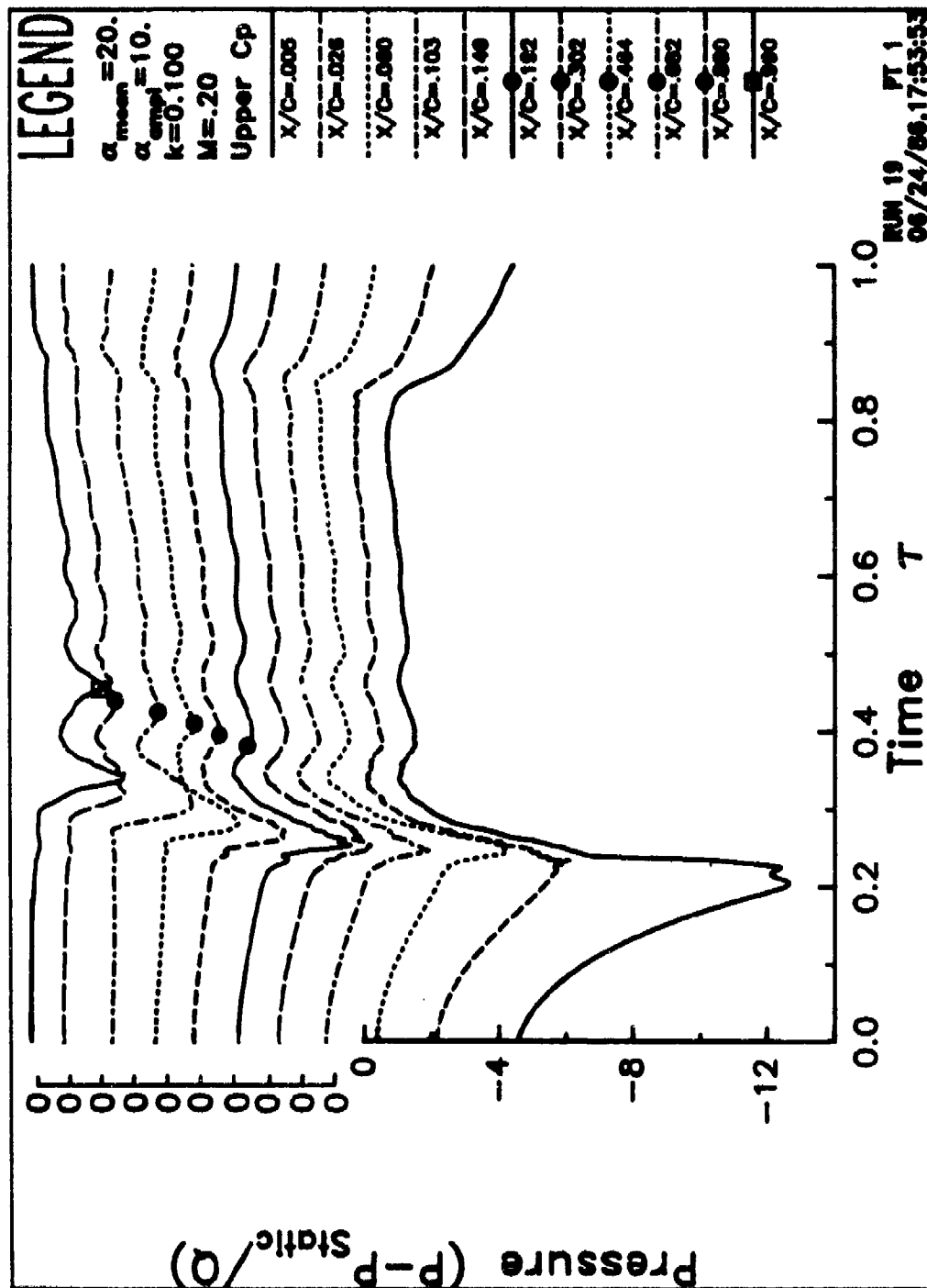


Figure 43. Upper surface pressures. f)  $k = 0.100$ ,  $\alpha = 20 - 10 \cos \omega t$

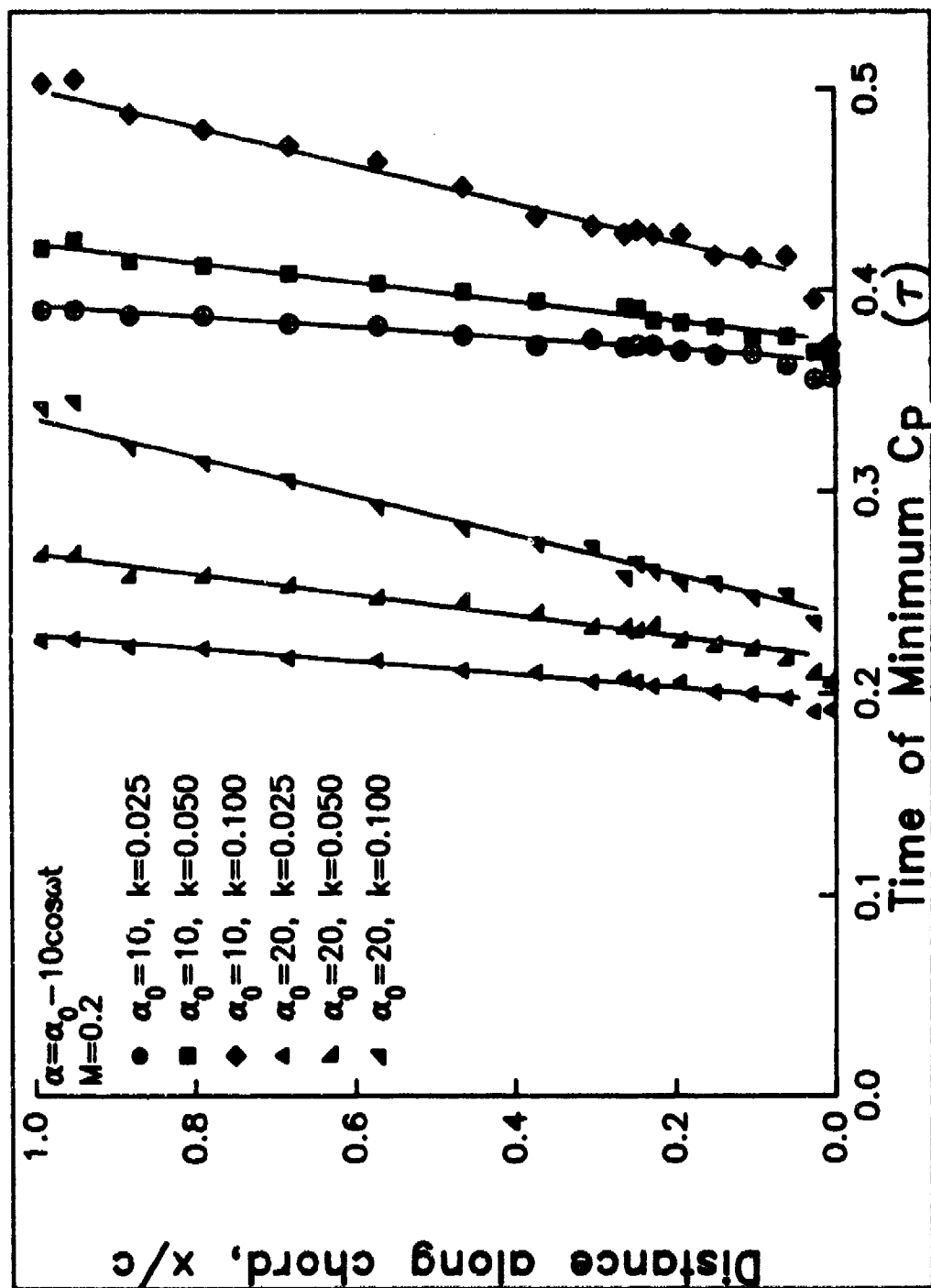


Figure 44. Times of minimum pressure for each sinusoid.

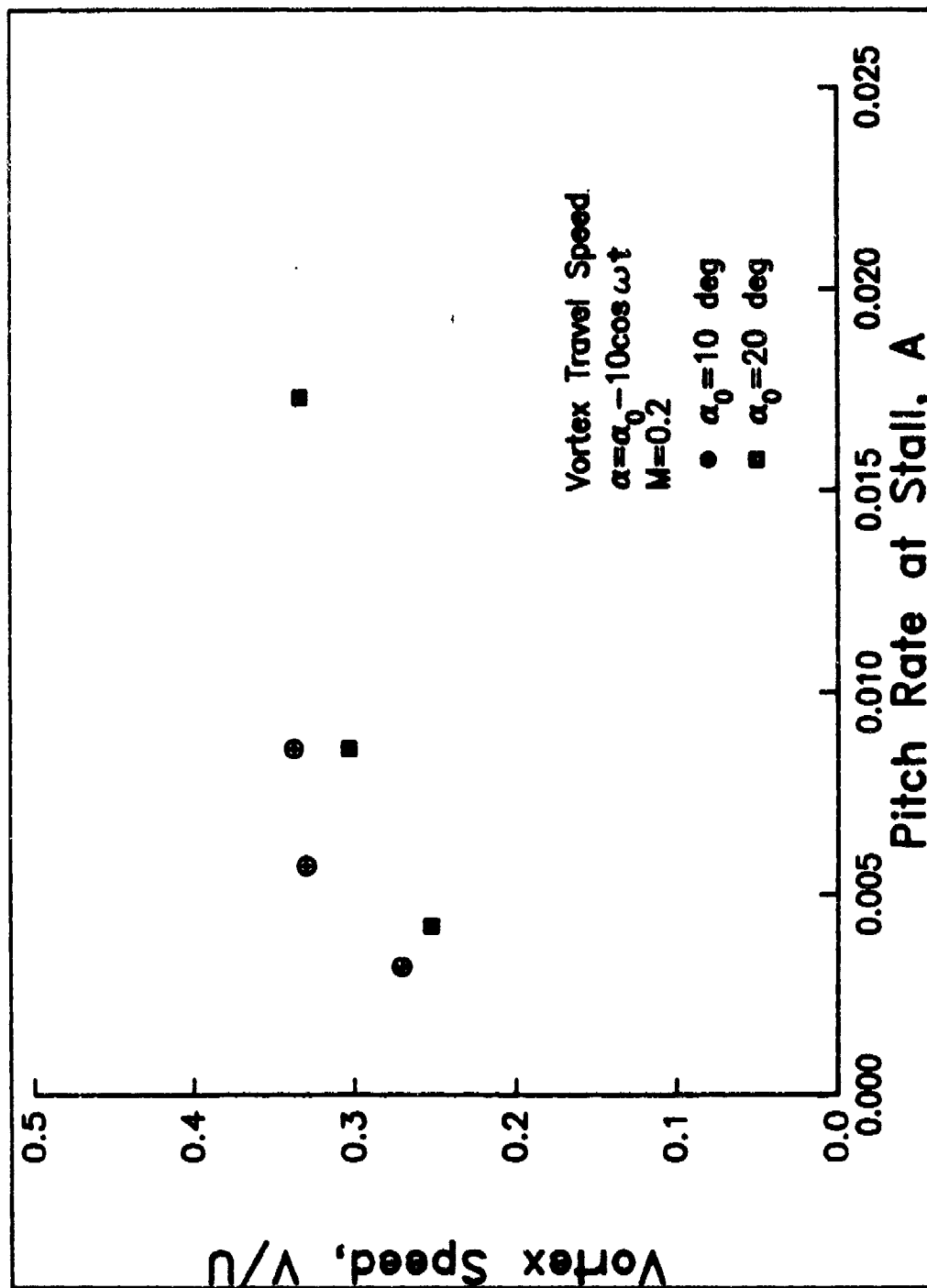


Figure 45. Vortex speed vs pitch rate at stall.

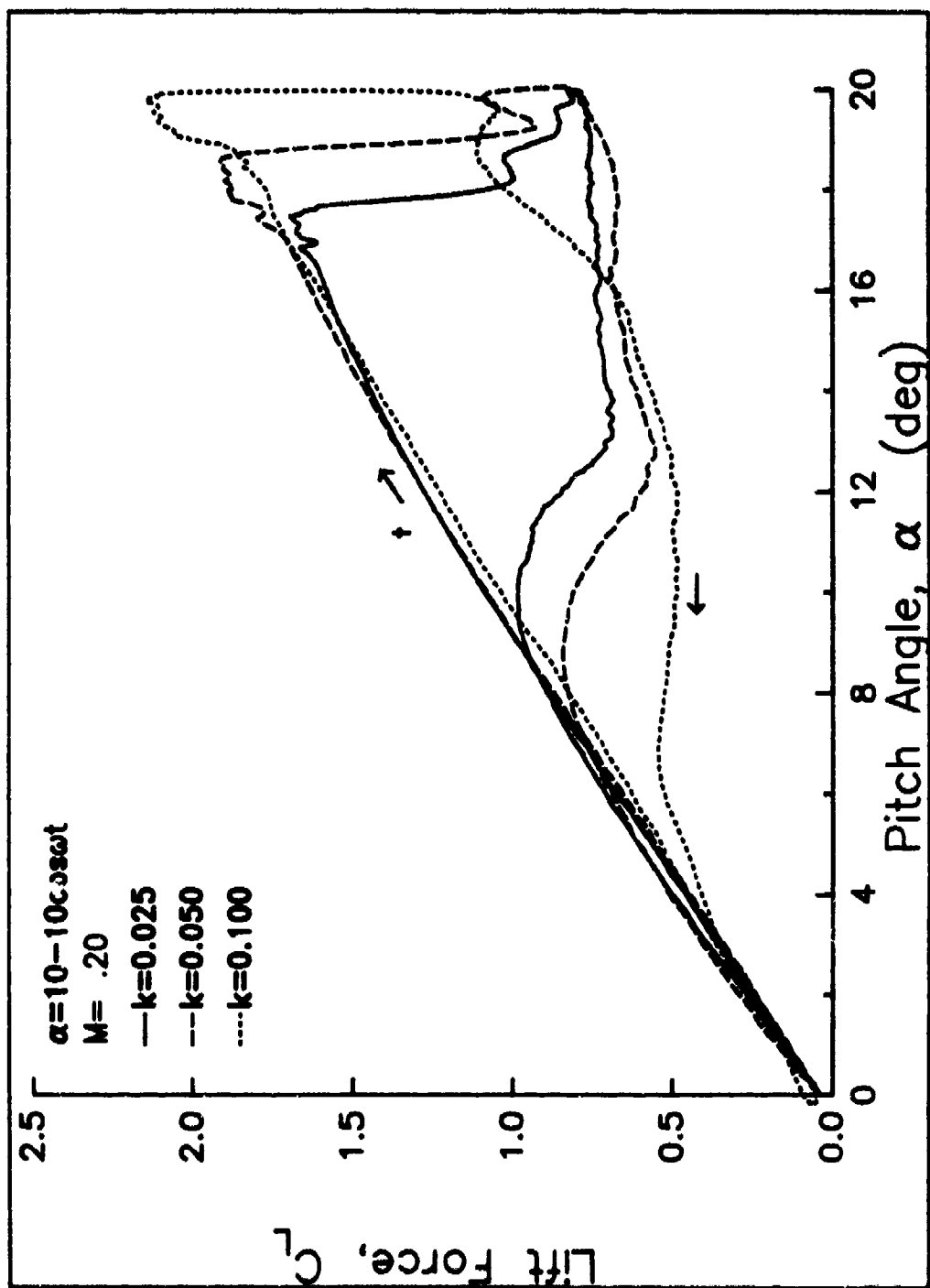


Figure 46. Loops of airloads vs. pitch angle. a) Lift,  $\alpha = 10 - 10 \cos wt$

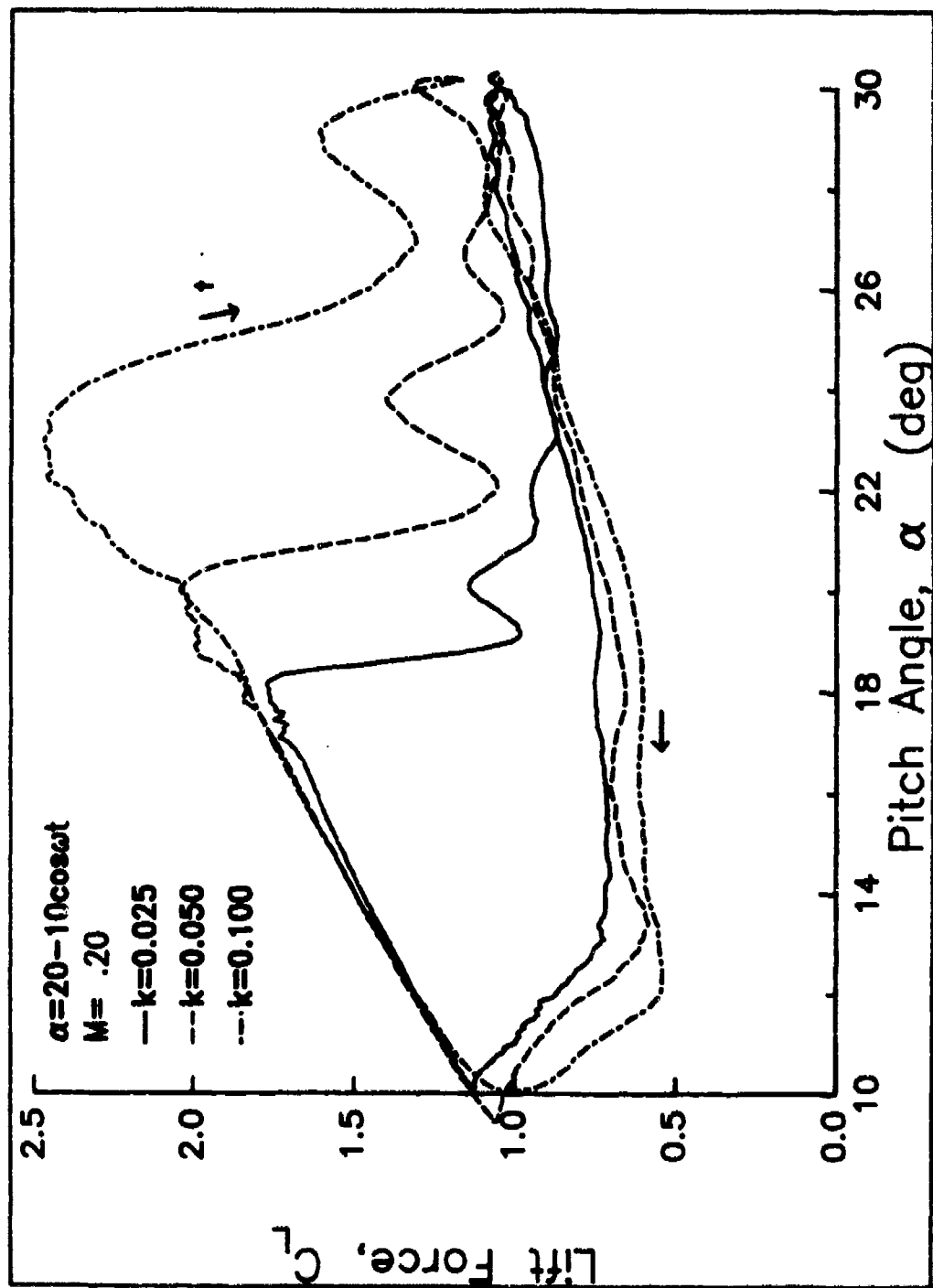


Figure 46. Loops of airloads vs. pitch angle. b) Lift,  $\alpha = 20 - 10 \cos wt$

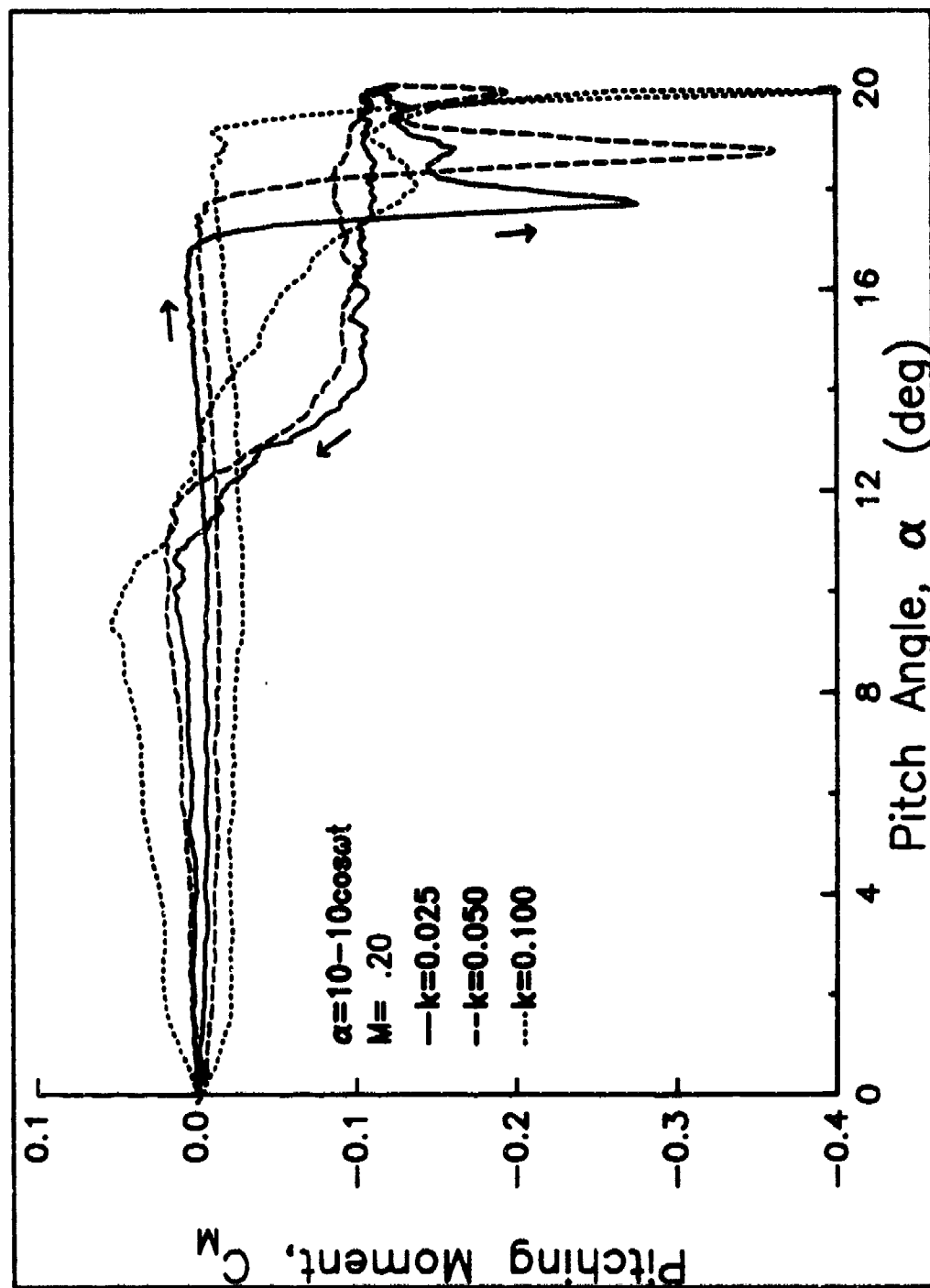


Figure 46. Loops of airloads vs. pitch angle. c) Drag,  $\alpha = 10 - 10 \cos wt$

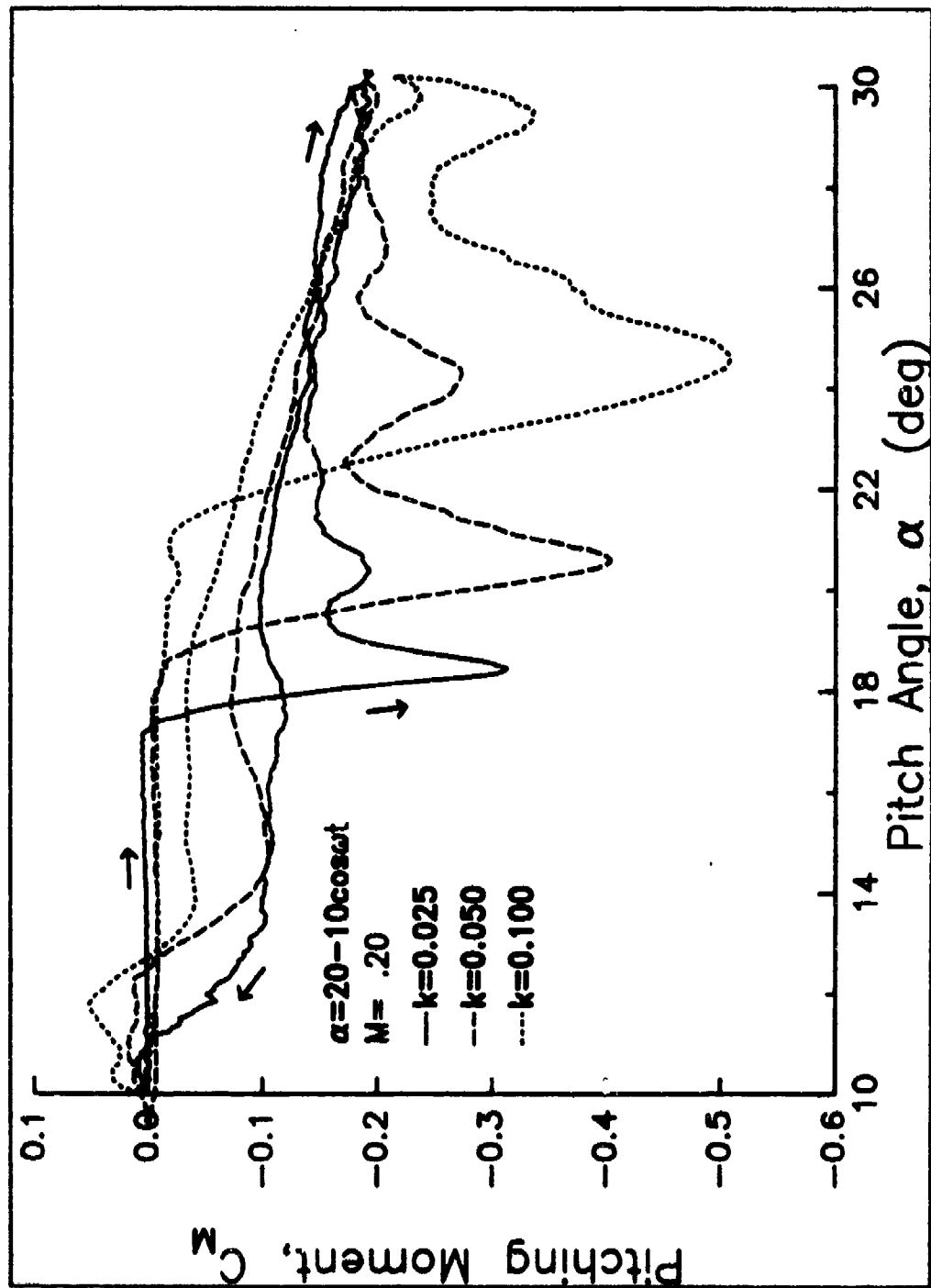


Figure 46. Loops of airloads vs. pitch angle. d) Drag,  $\alpha = 20 - 10 \cos \omega t$

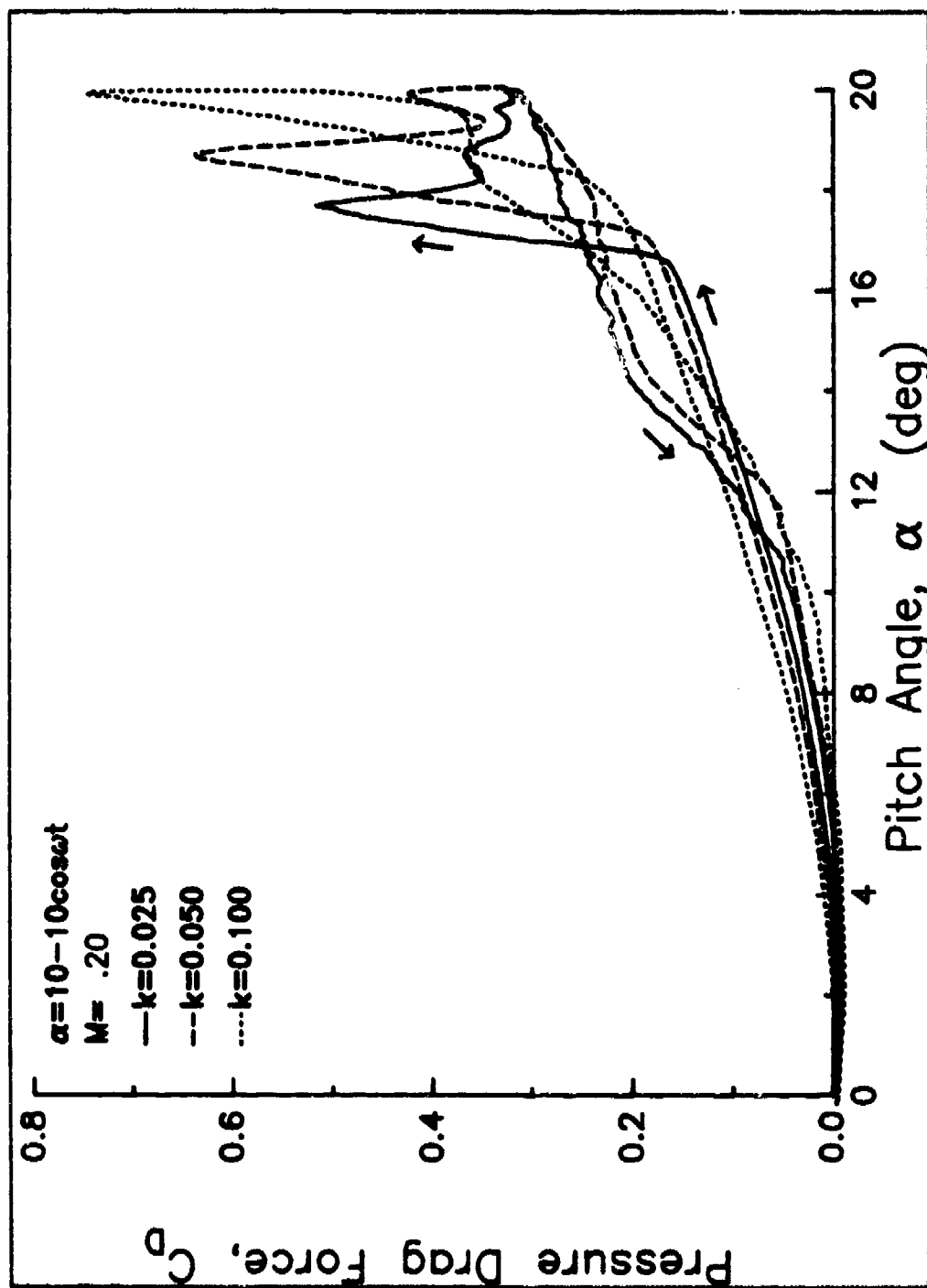


Figure 46. Loops of airloads vs. pitch angle. e) Moment,  $\alpha = 10 - 10 \cos \omega t$



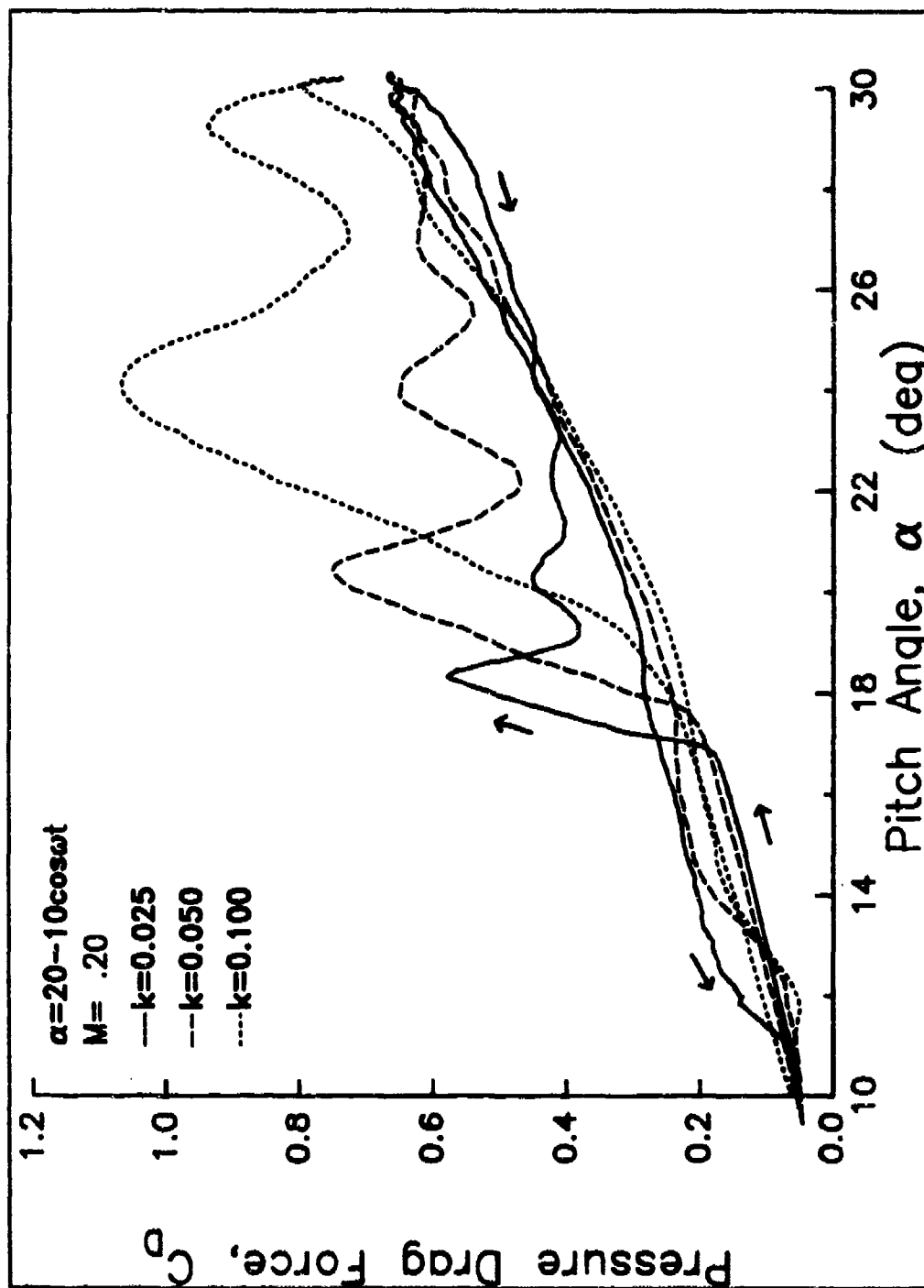


Figure 46. Loops of airloads vs. pitch angle. f) Moment,  $\alpha = 20 - 10 \cos \omega t$

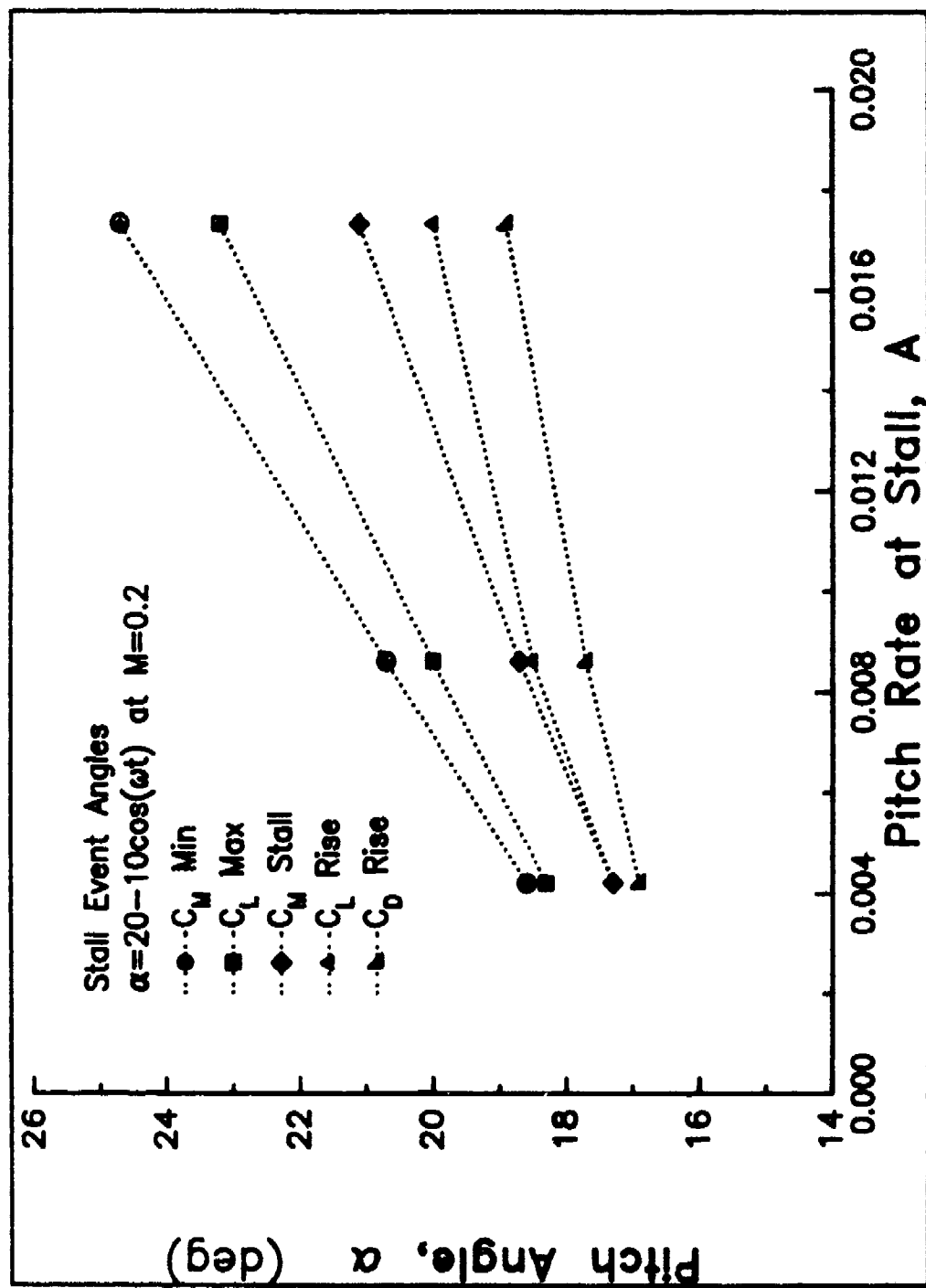


Figure 47. Sequence of stall events vs. pitch rate at stall.

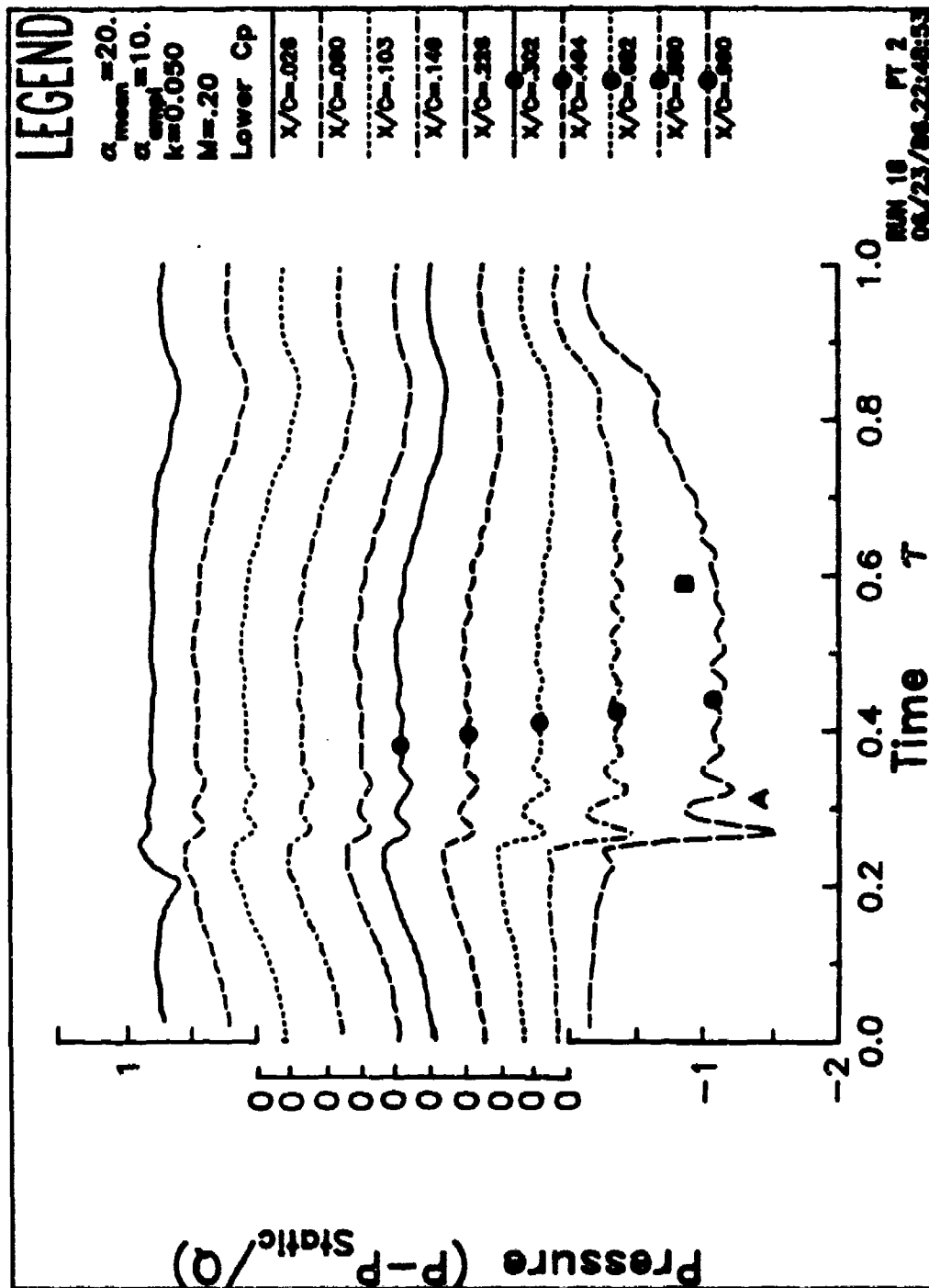


Figure 48. Lower surface pressures for  $\alpha = 20 - 10 \cos \omega t$  at  $k = 0.050$ .

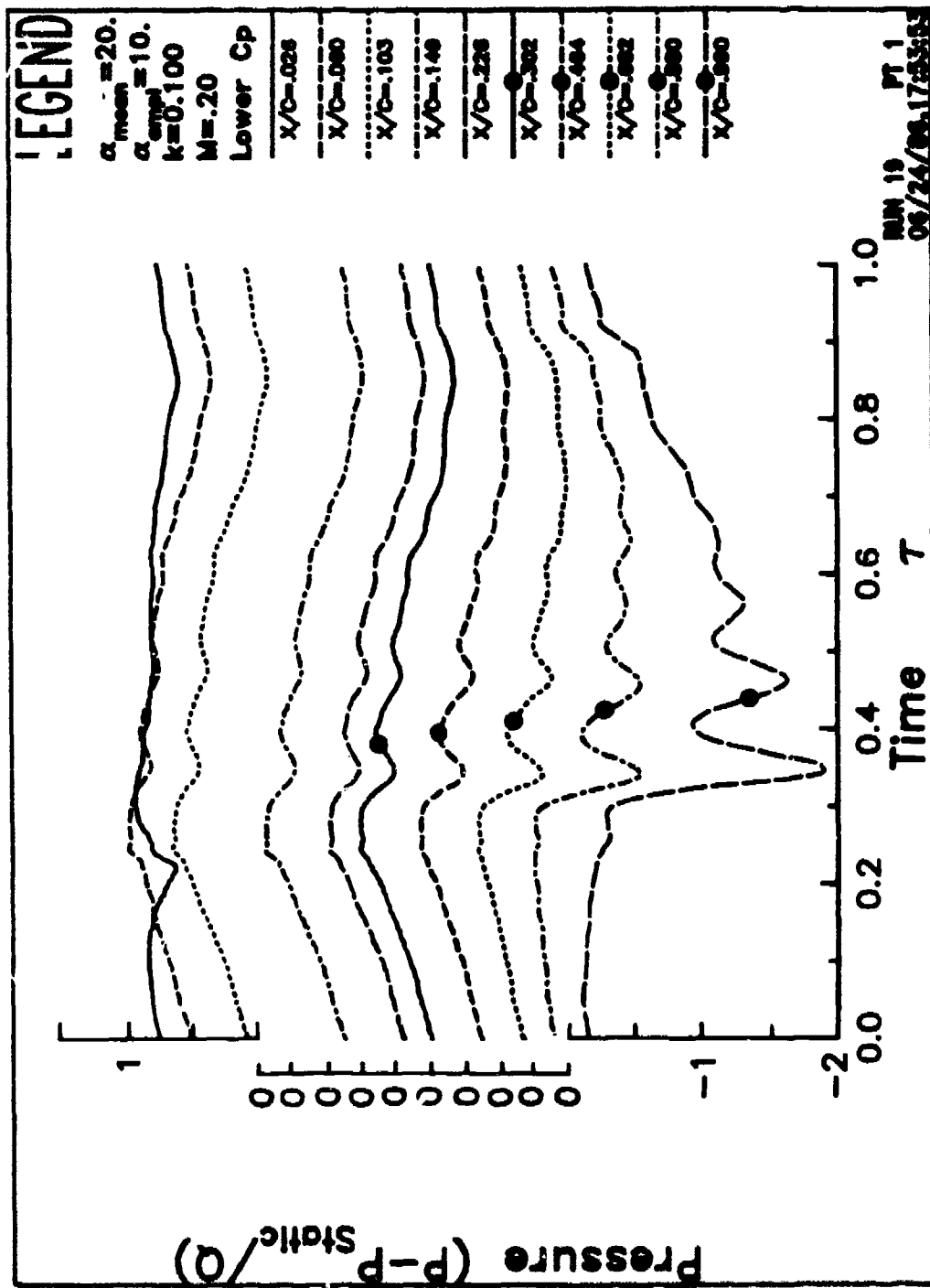


Figure 49. Lower surface pressures for  $\alpha = 20 - 10 \cos \omega t$  at  $k = 0.100$ .

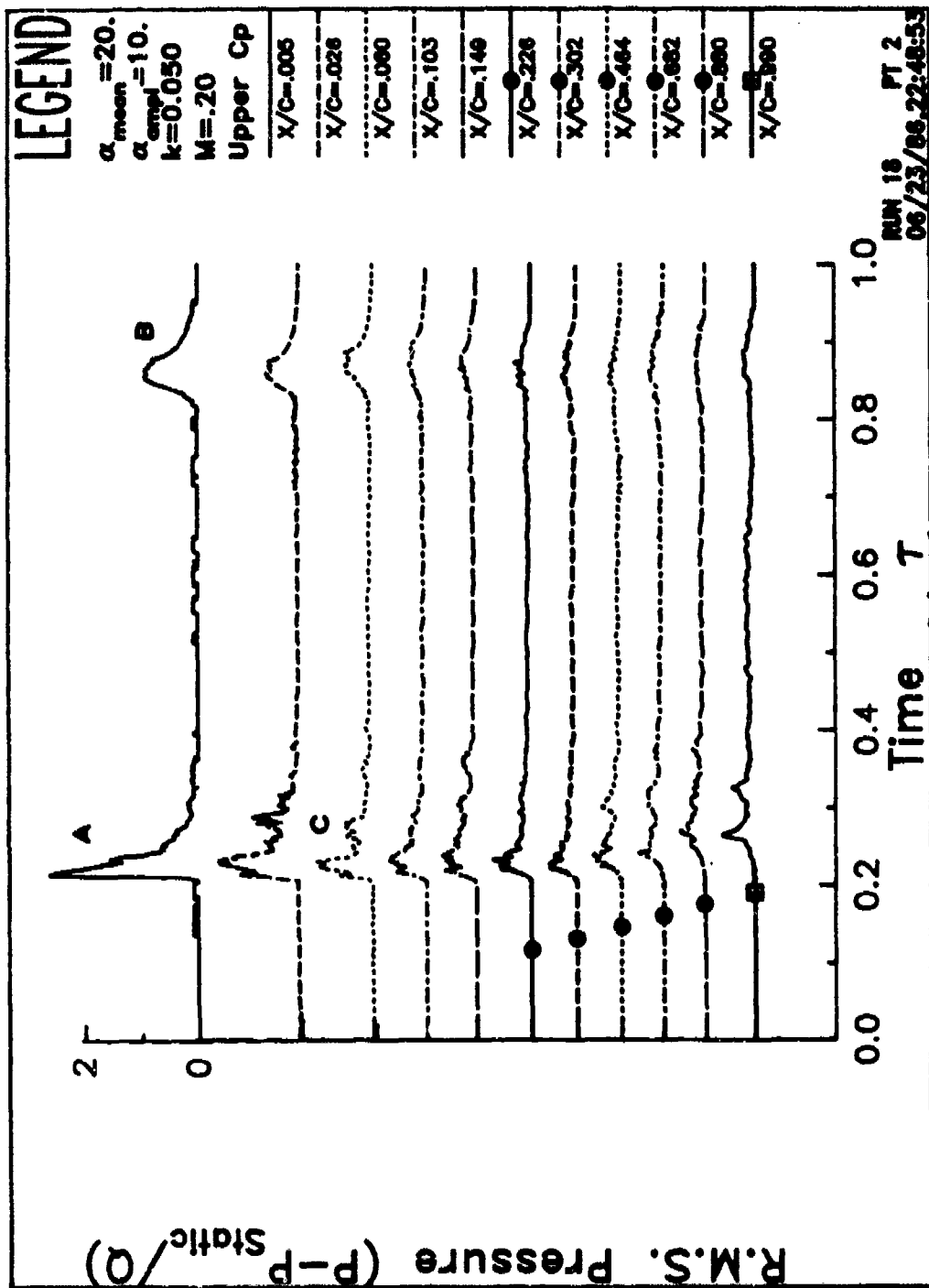


Figure 50. RMS pressures for  $\alpha = 20 - 10 \cos \omega t$  at  $k = 0.050$ . a) Upper surface.

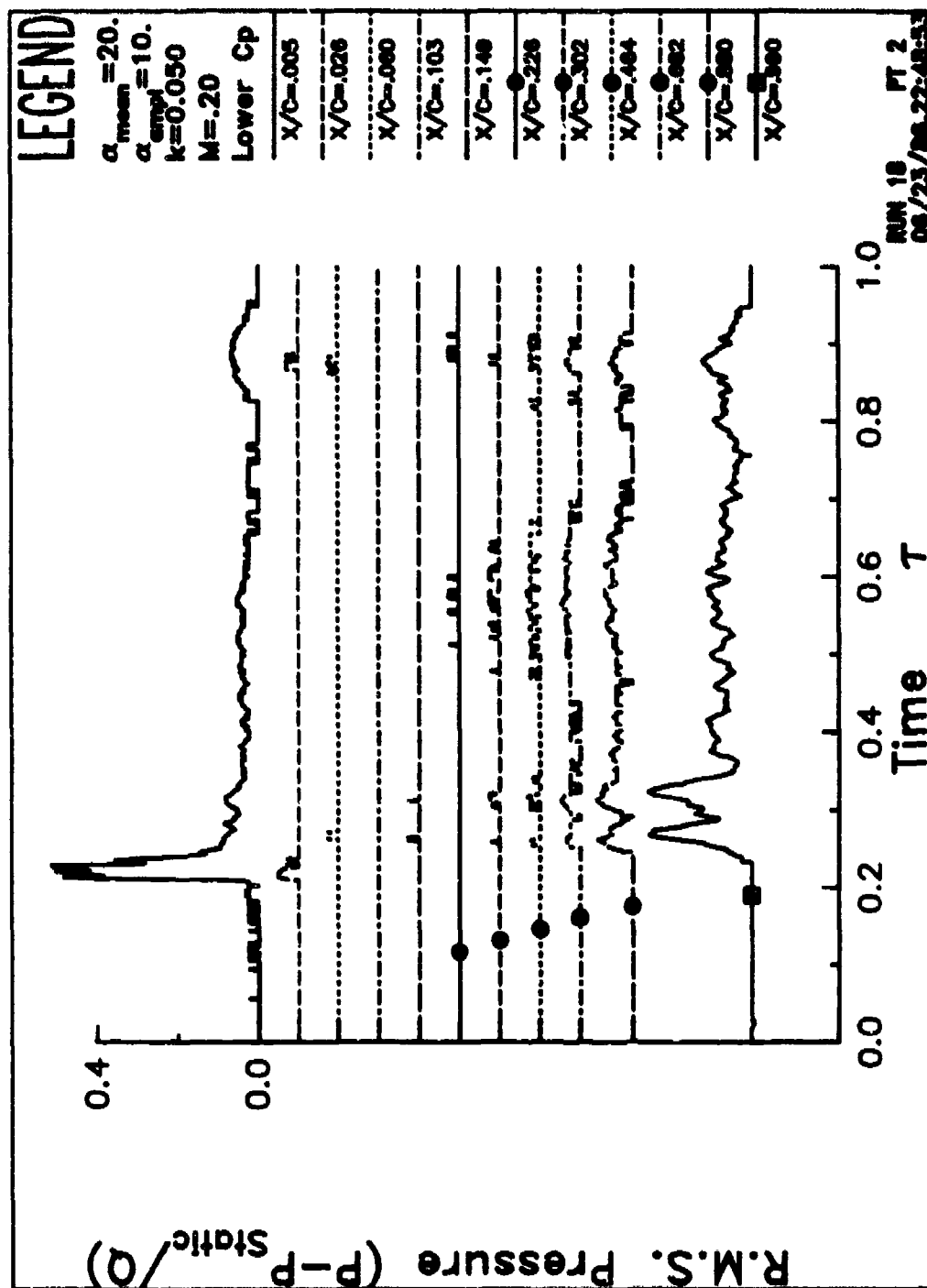


Figure 50. RMS pressures for  $\alpha = 20 - 10 \cos \omega t$  at  $k = 0.050$ . b) Lower surface.

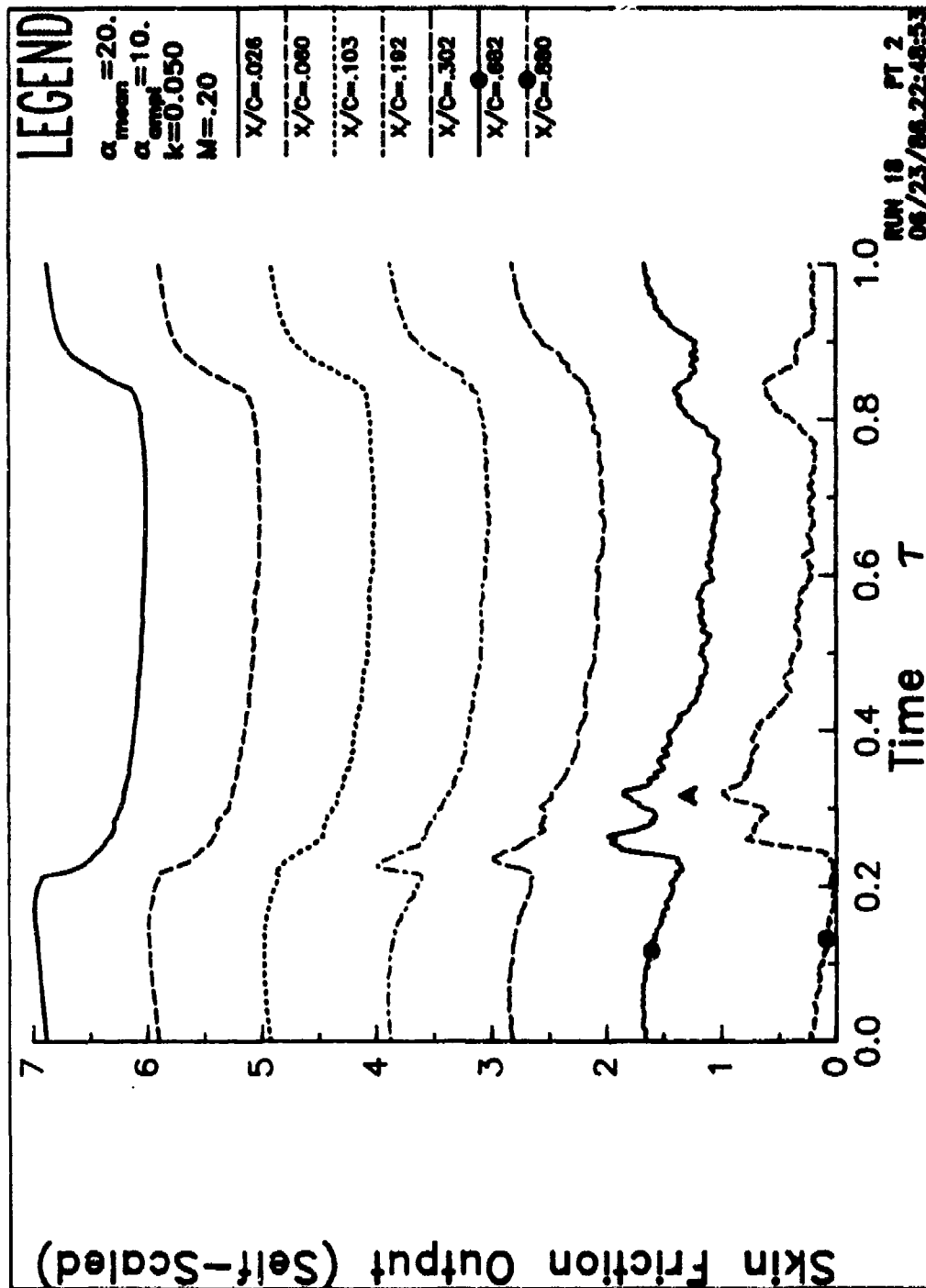


Figure 51. Hot film gage output for  $\alpha = 20 - 10 \cos \omega t$  at  $k = 0.050$ .  
a) Ensemble average.

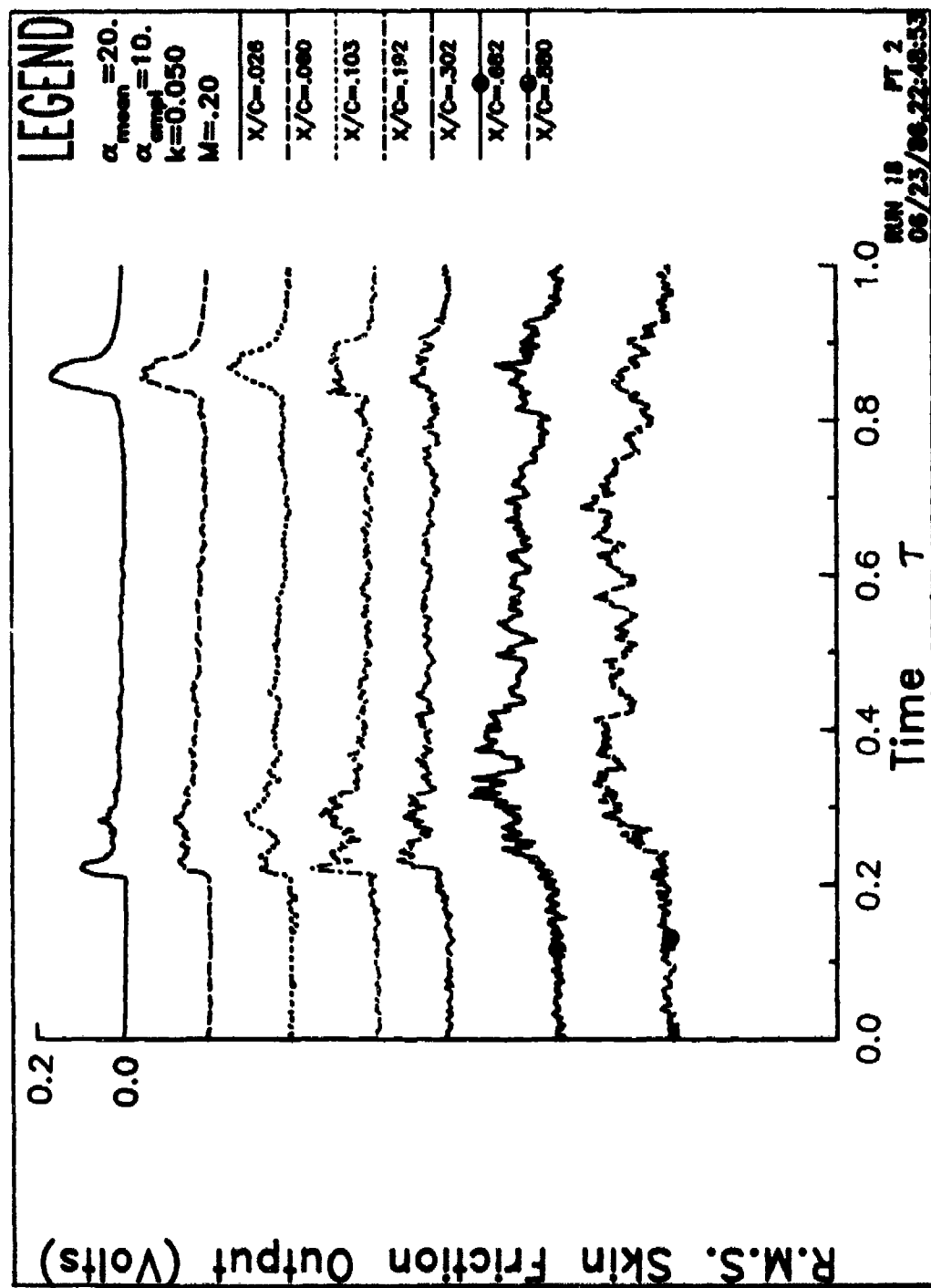


Figure 51. Hot film gage output for  $\alpha = 20 - 10 \cos \omega t$  at  $k = 0.050$ . b) RMS.



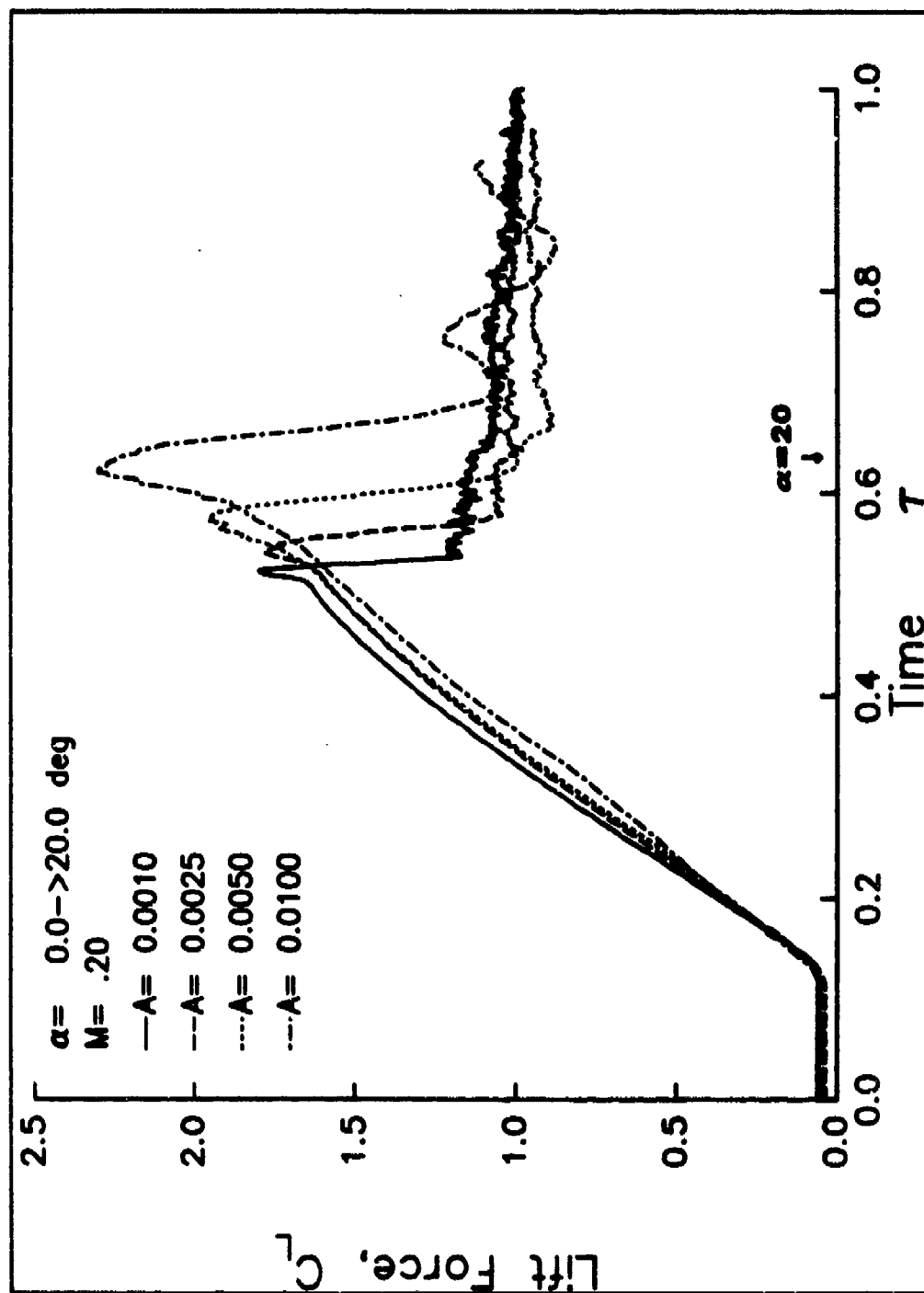


Figure 52. Airloads at  $A = 0.0010$ ,  $0.0025$ ,  $0.0050$ , and  $0.0100$ . a) Lift vs. time.

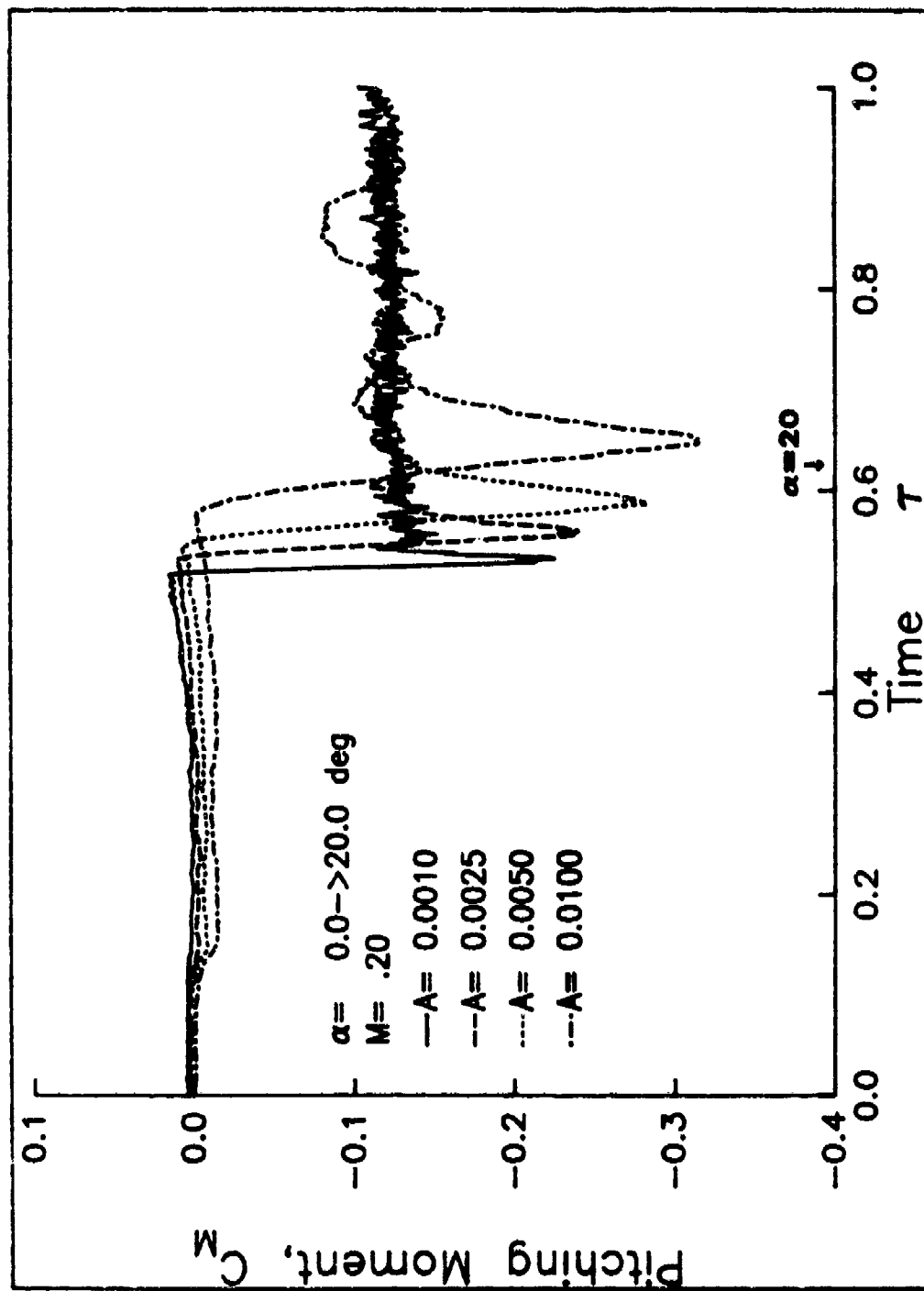


Figure 52. Airloads at  $A = 0.0010$ ,  $0.0025$ ,  $0.0050$ , and  $0.0100$ . b) Moment vs. time.

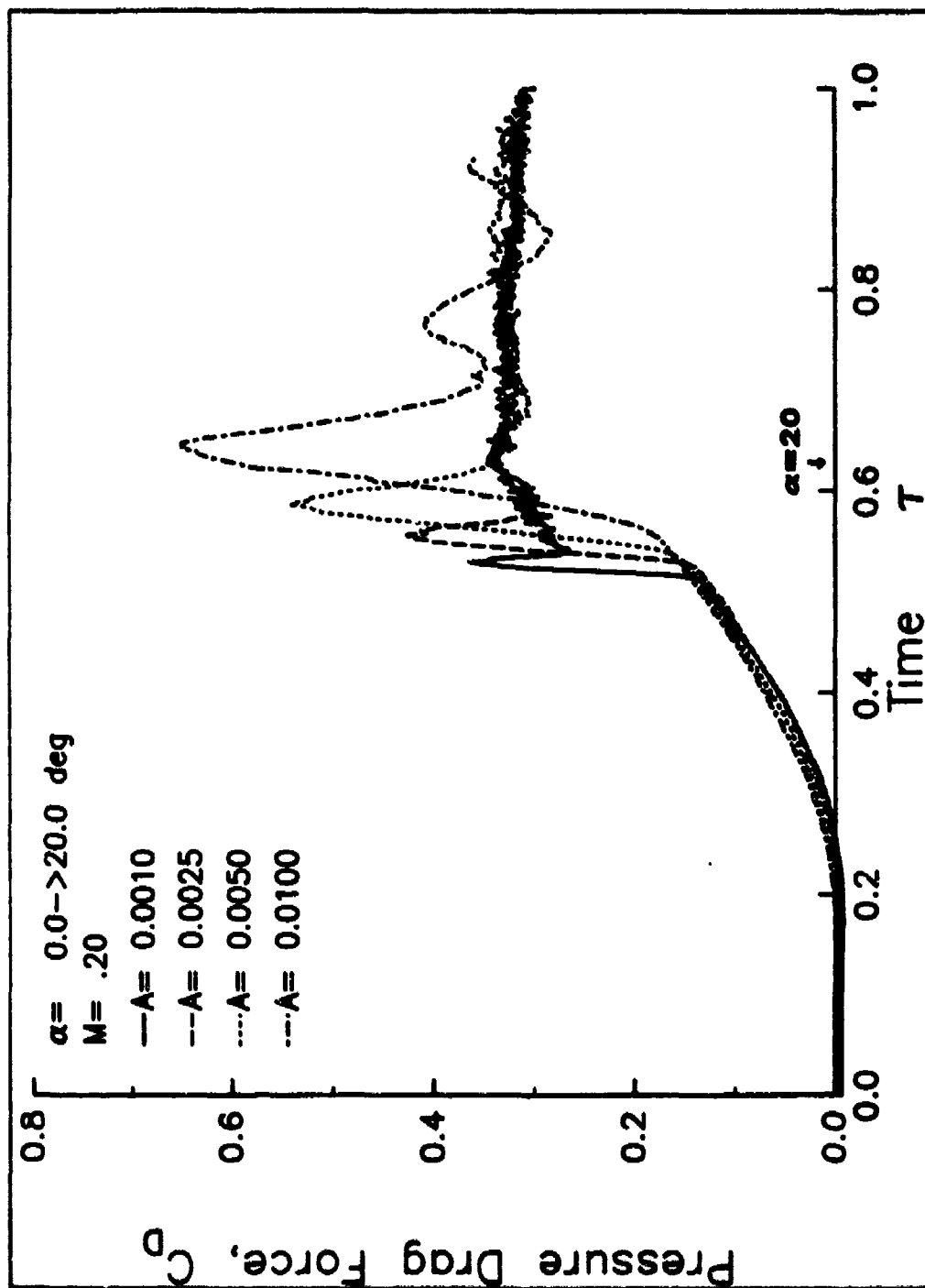


Figure 52. Airloads at  $A = 0.0010$ ,  $0.0025$ ,  $0.0050$ , and  $0.0100$ . c) Drag vs. time.

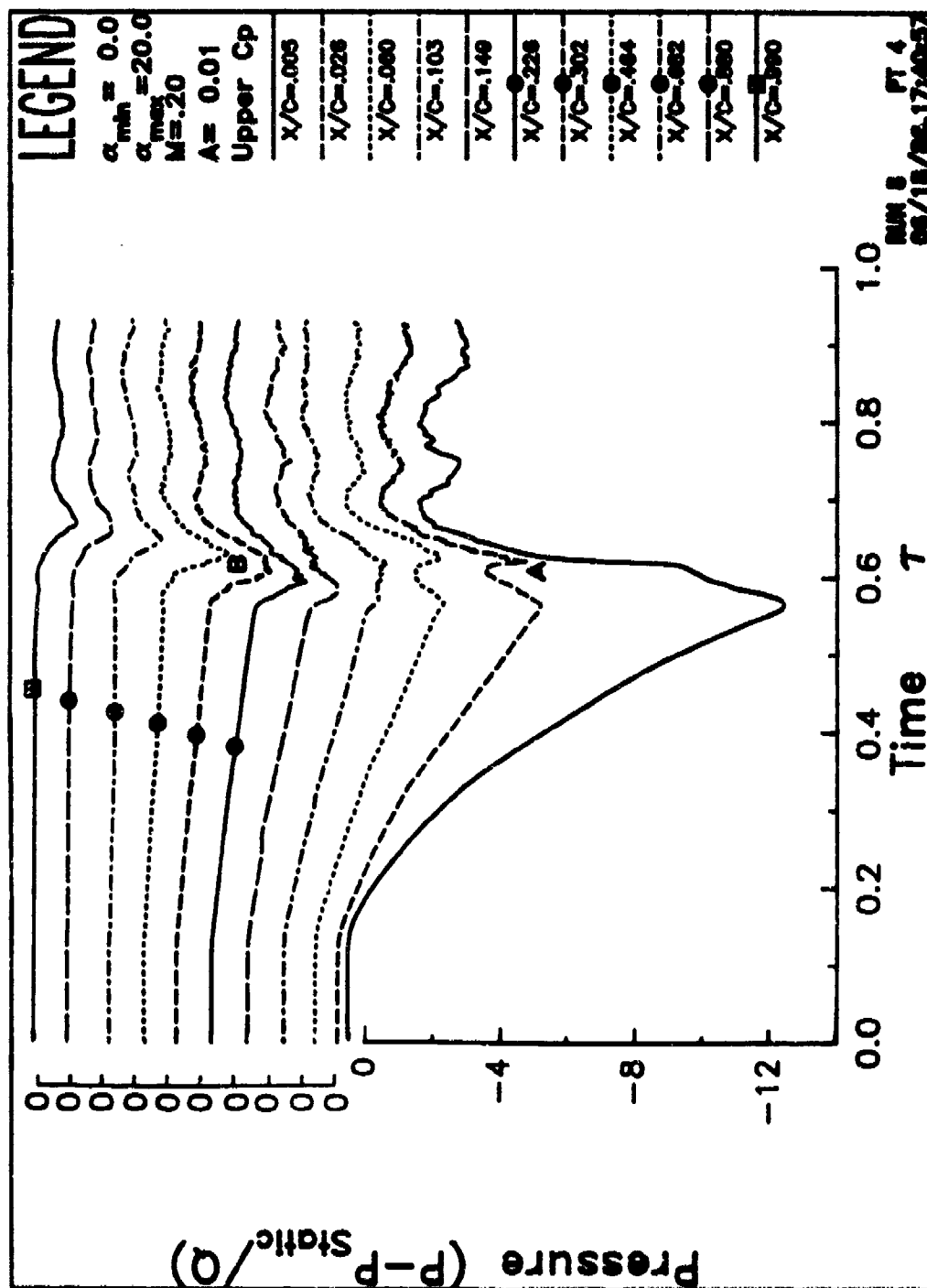


Figure 53. Upper surface pressures. a)  $A = 0.010$ .

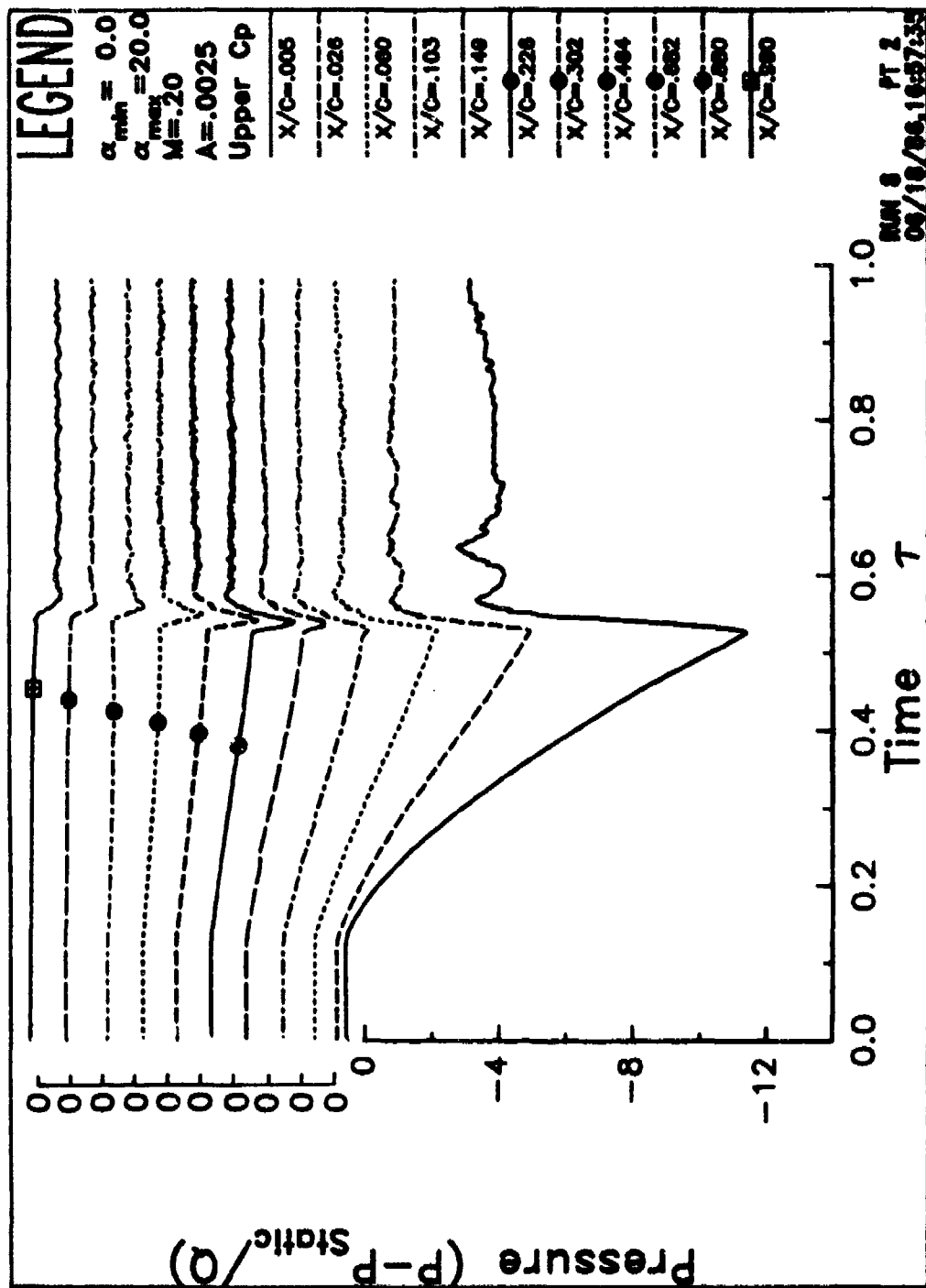


Figure 53. Upper surface pressures. b)  $A = 0.0025$ .

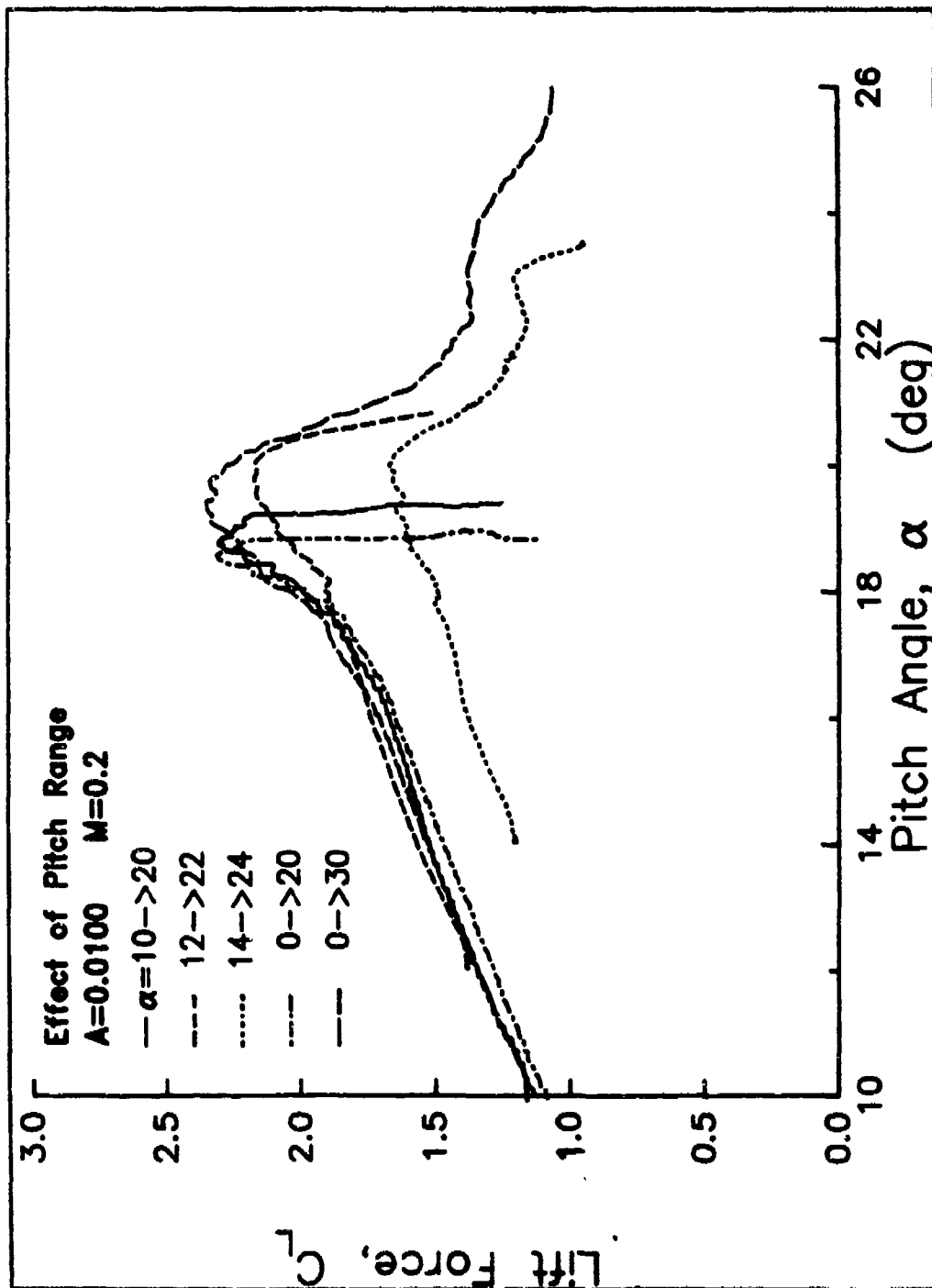


Figure 54. Airloads. a) Lift.

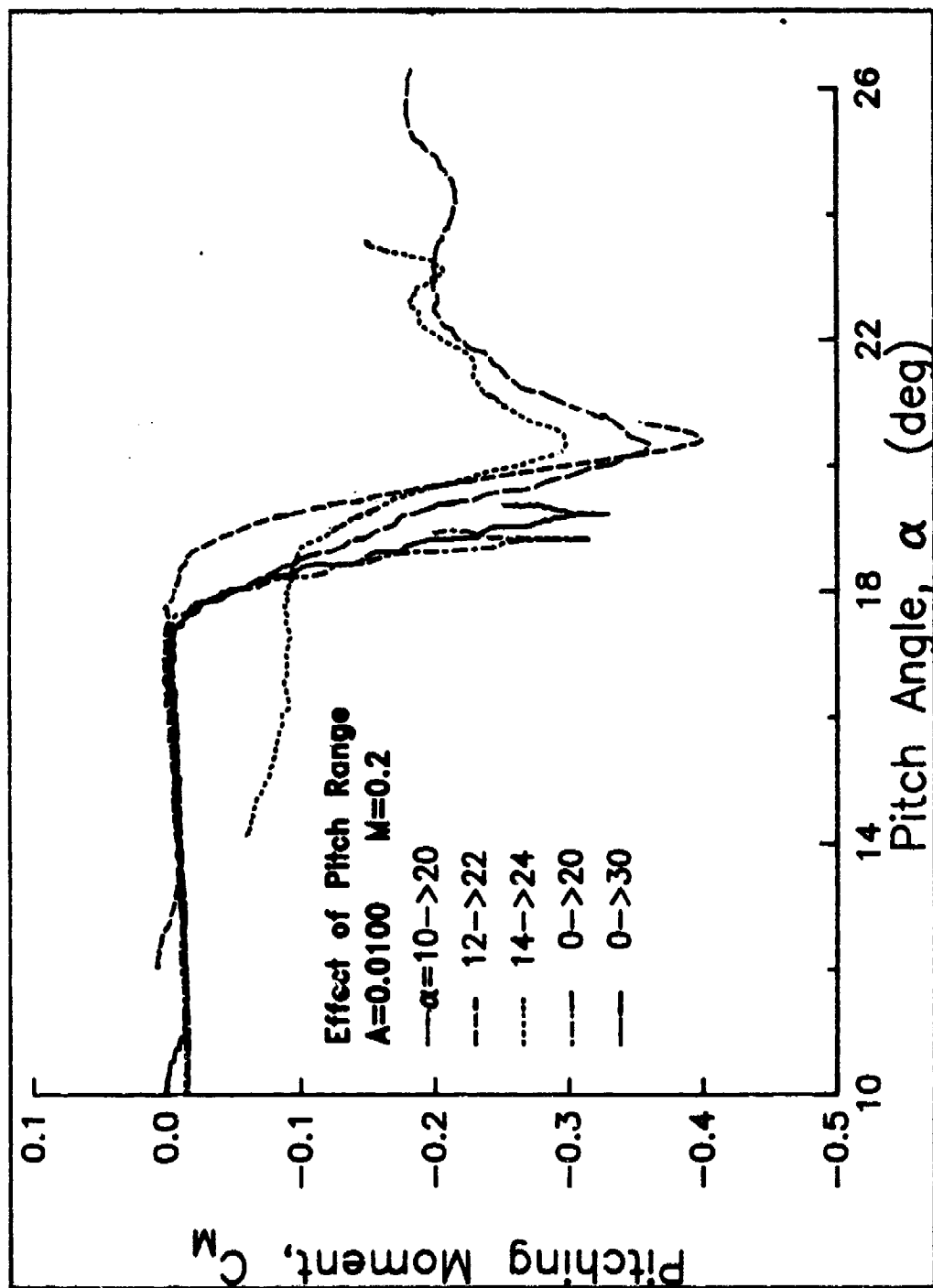


Figure 54. Airloads. b) Moment.

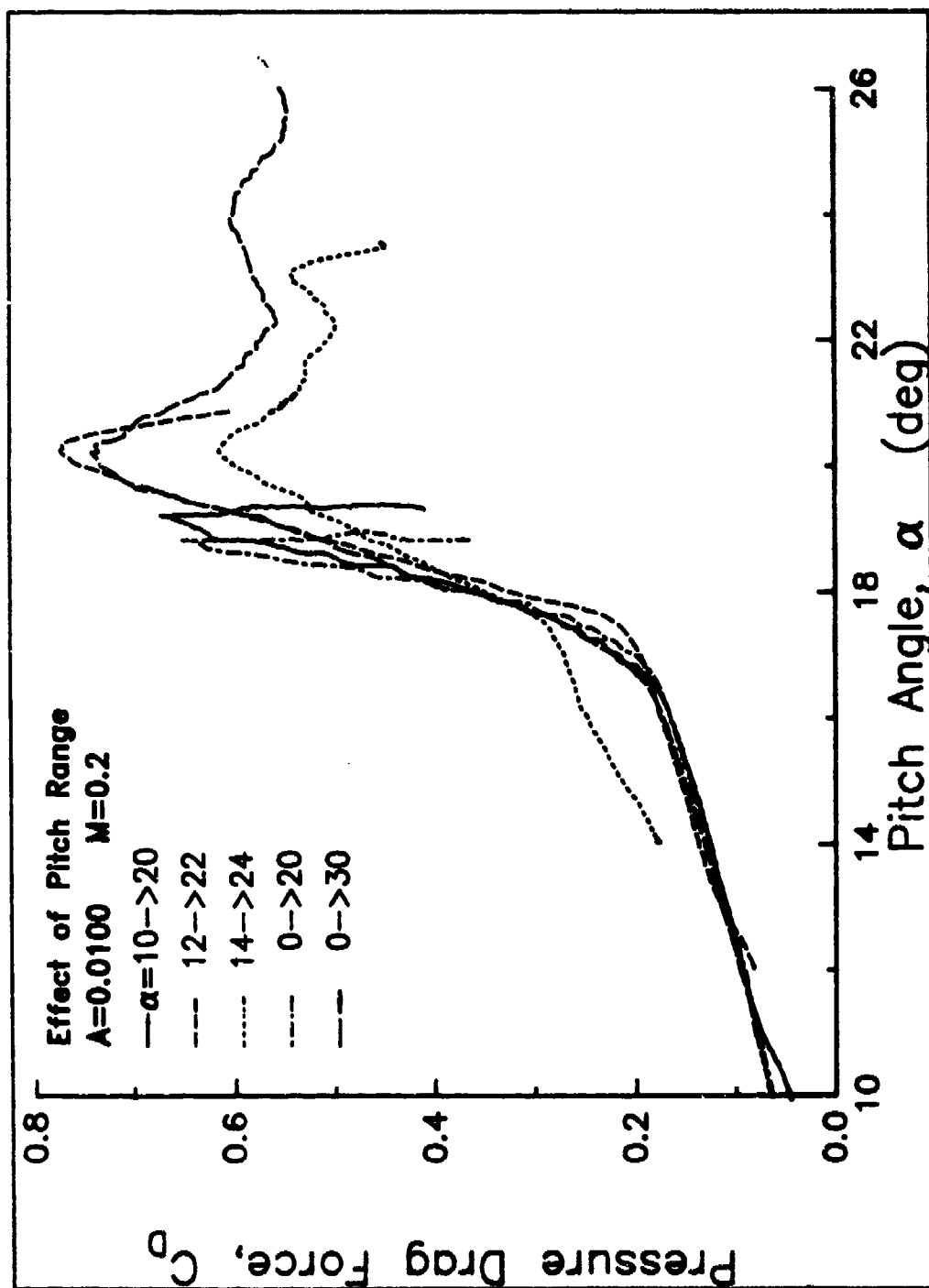


Figure 54. Airloads. c) Drag.



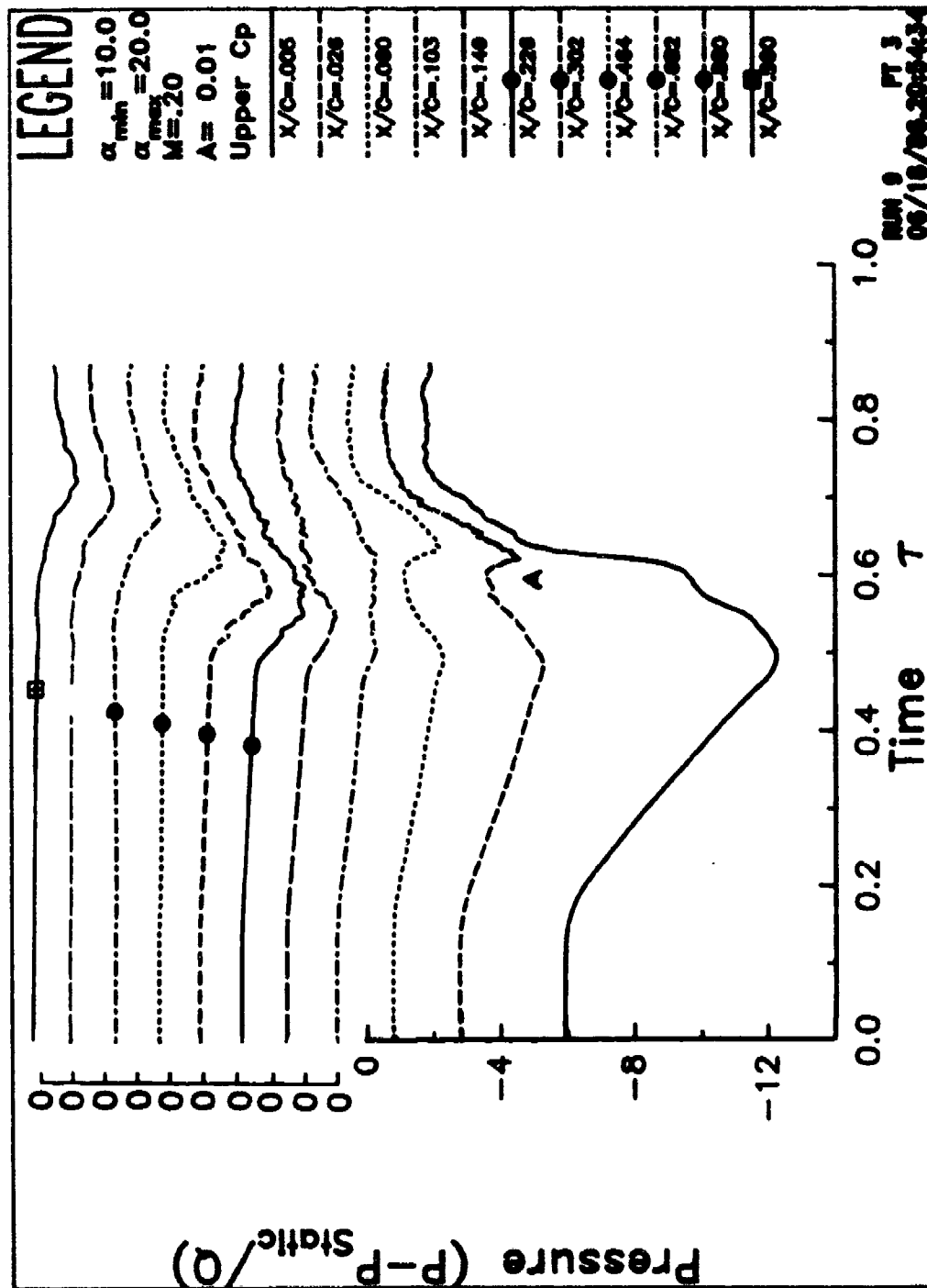


Figure 55. Upper surface pressures. a) 10 to 20 deg.

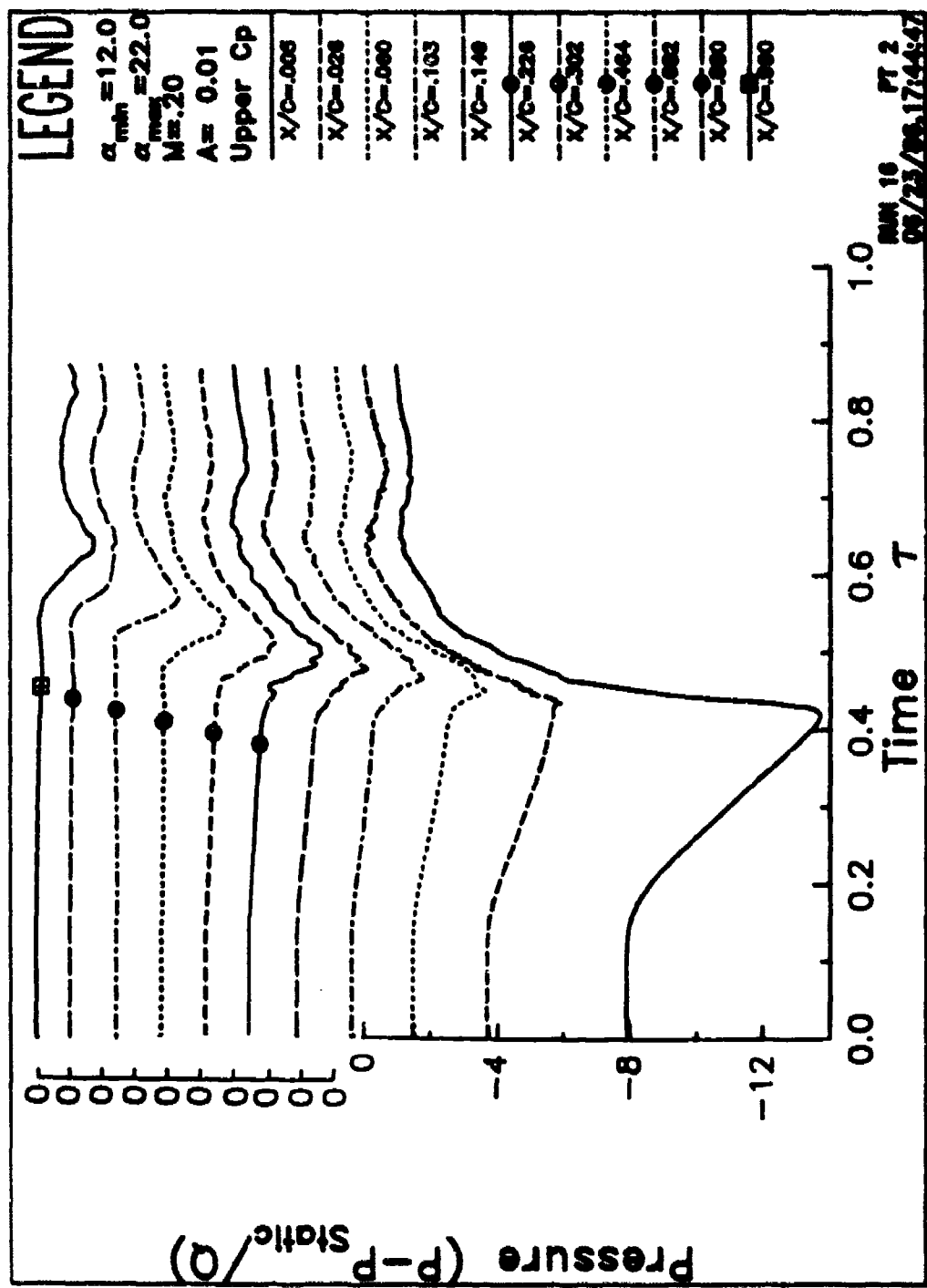


Figure 55. Upper surface pressures. b) 12 to 22 deg.

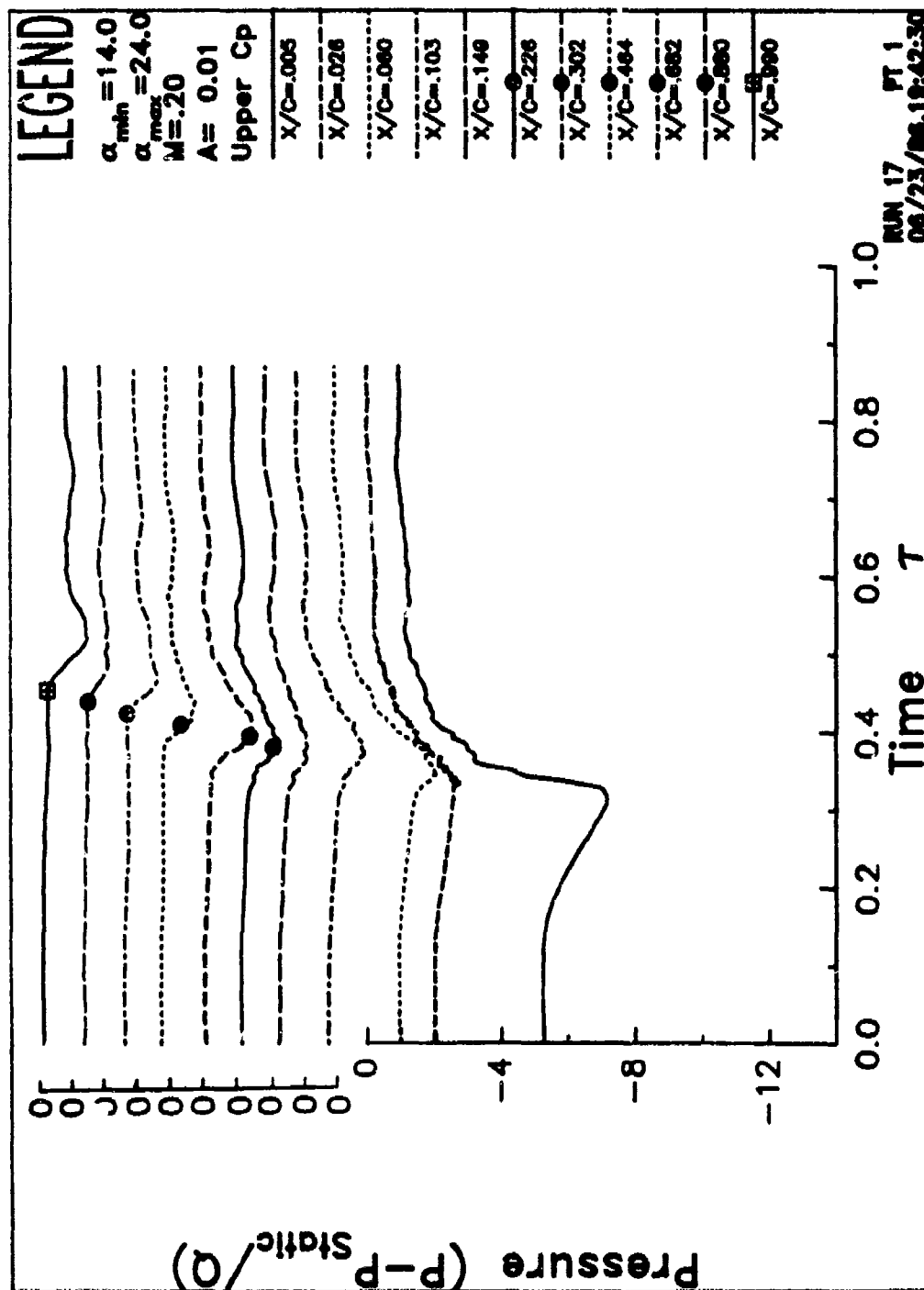


Figure 55. Upper surface pressures. c) 14 to 24 deg.

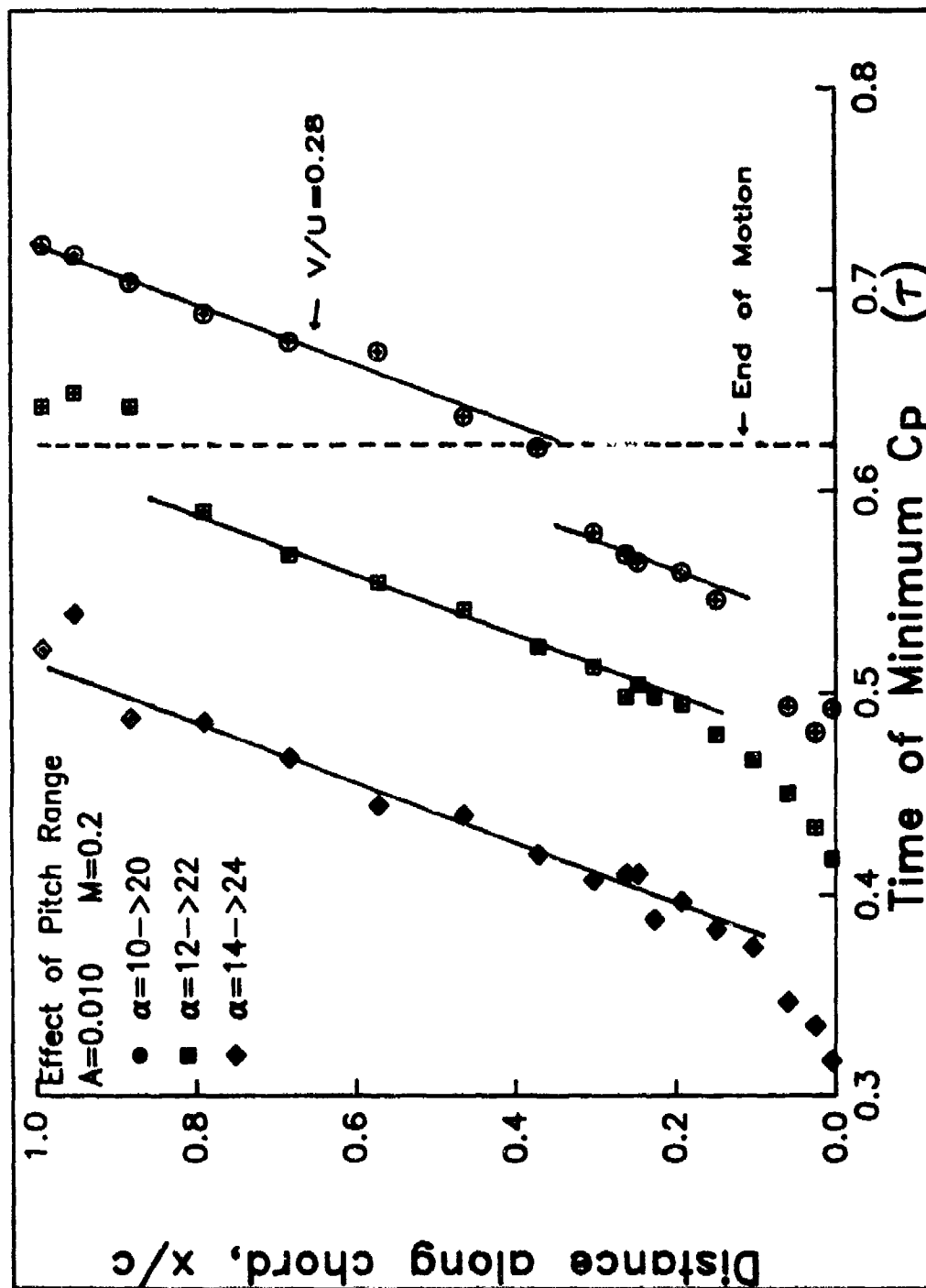


Figure 56. Times of minimum pressure for each range.



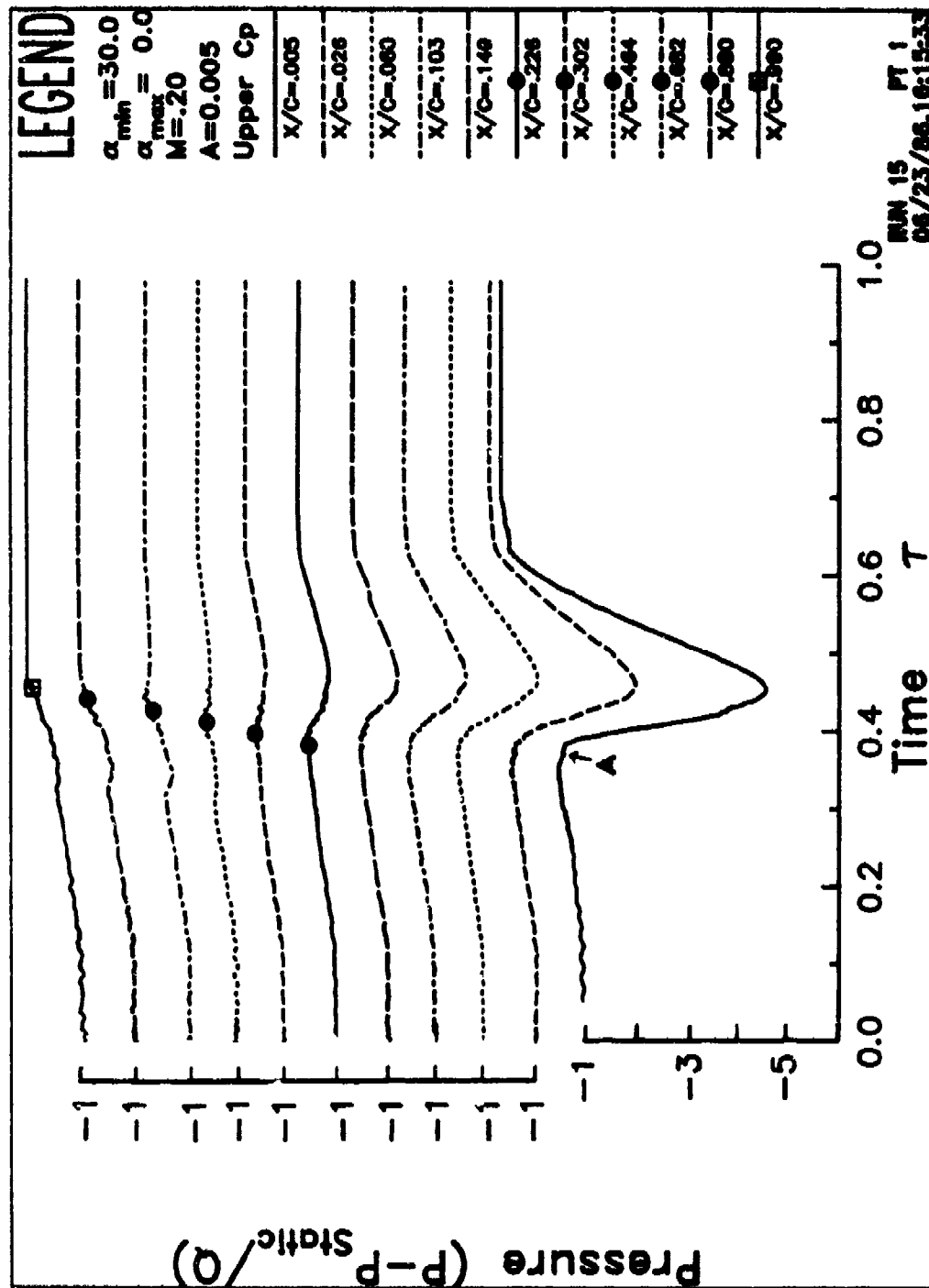


Figure 57. Upper surface pressures. b)  $A = 0.005$ .

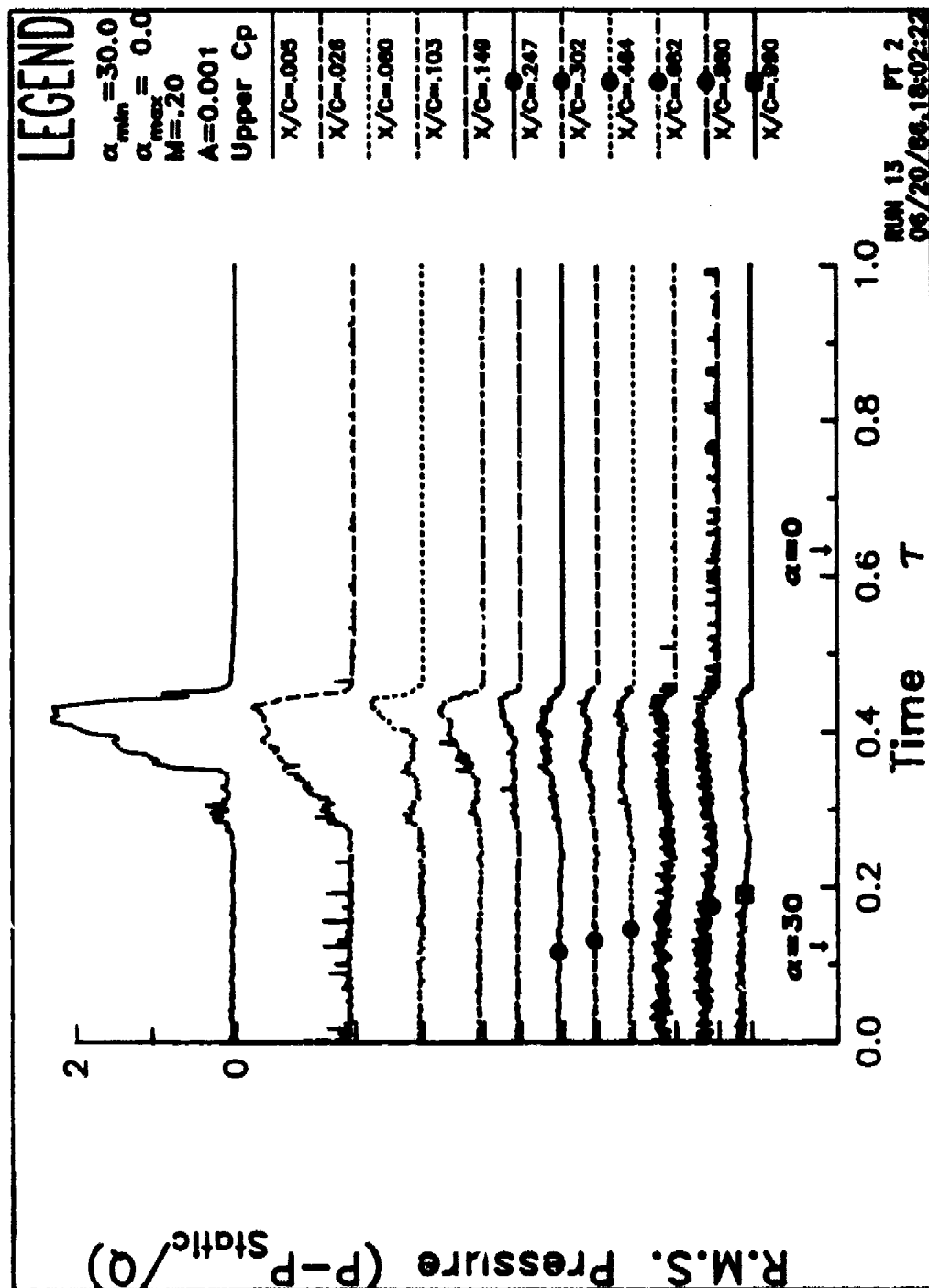


Figure 58. RMS upper surface pressures. a)  $A = 0.001$ .

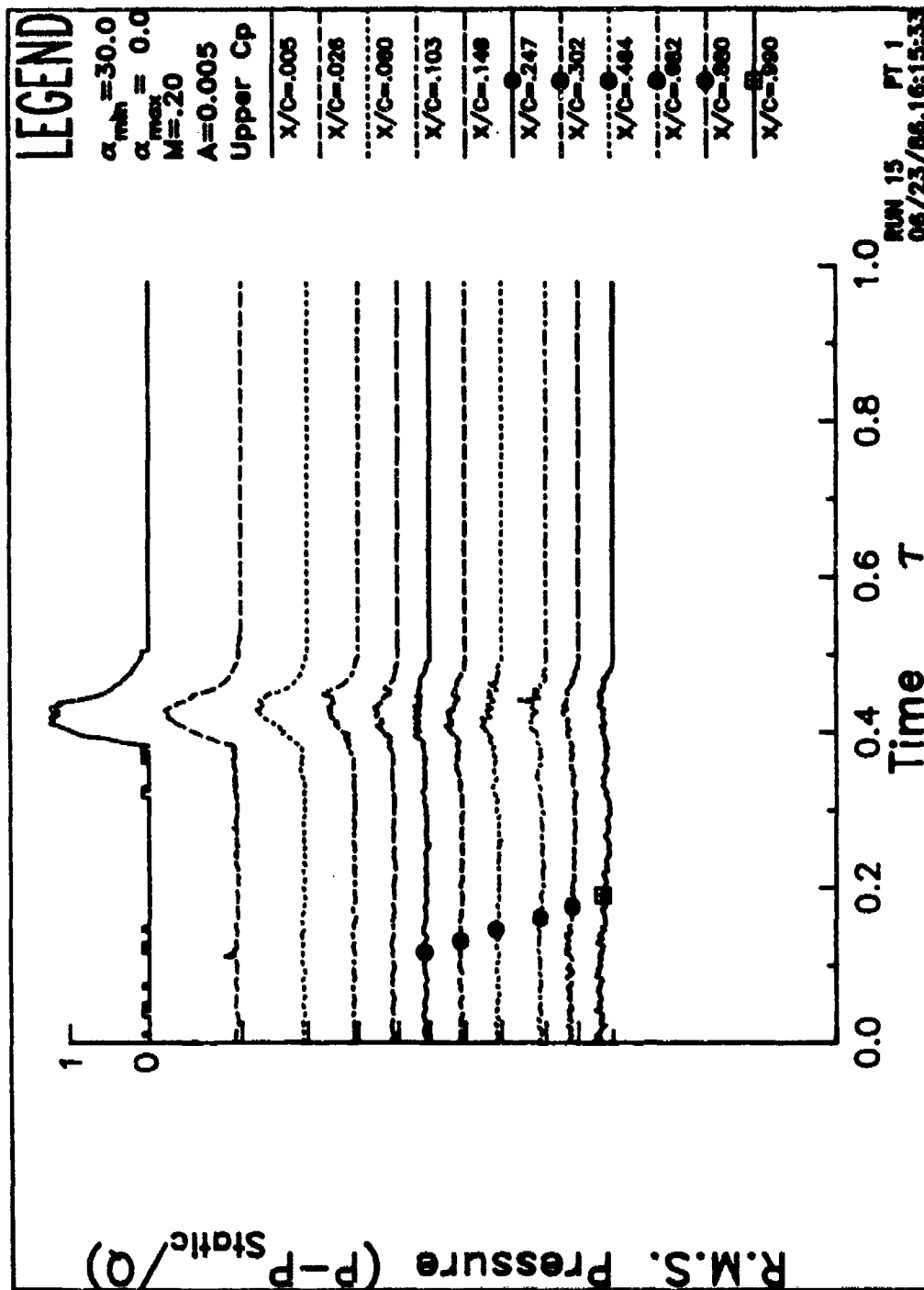


Figure 58. RMS upper surface pressures. b)  $A = 0.005$ .



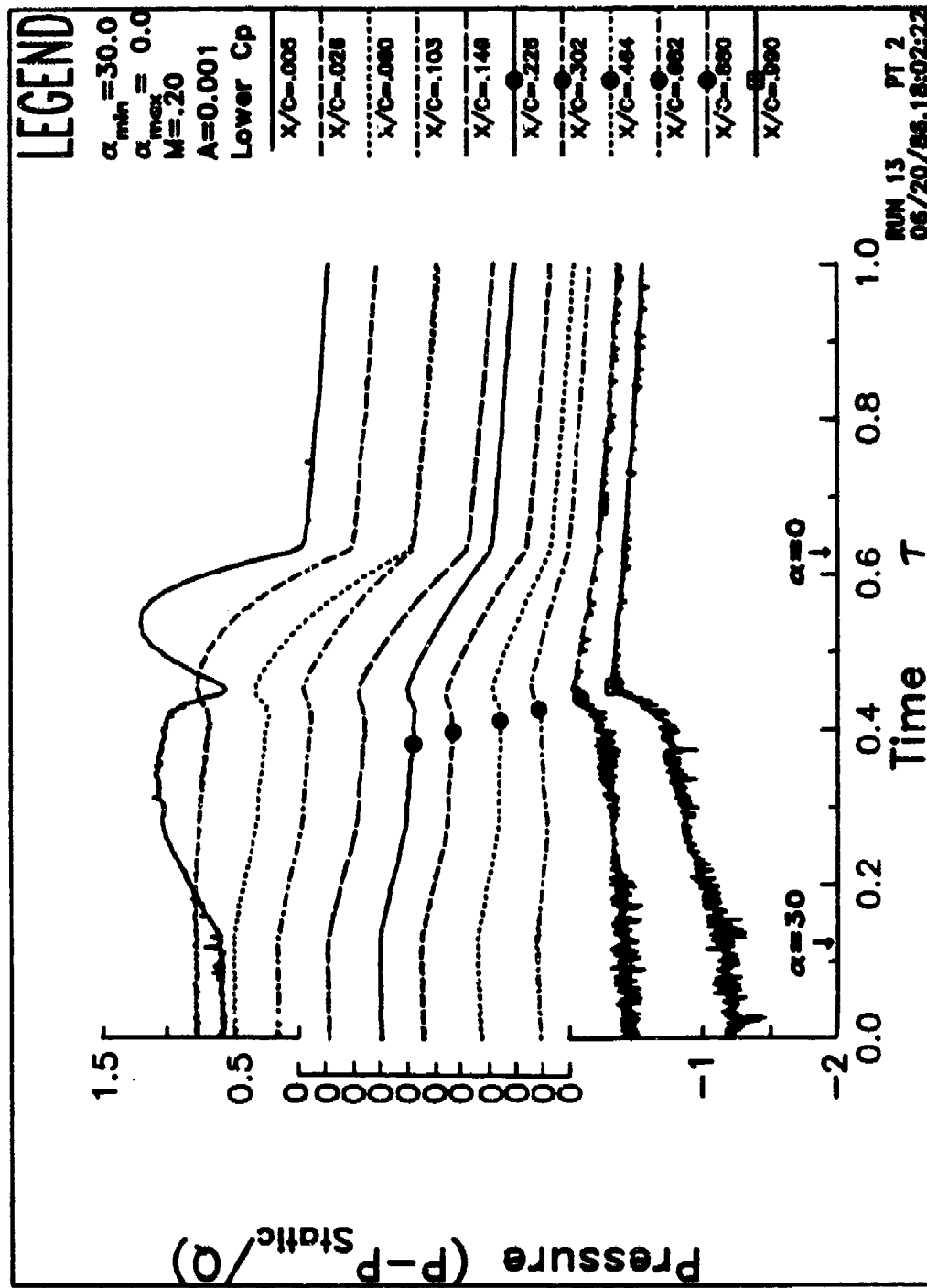


Figure 59. Lower surface pressures. a)  $A = 0.001$ .

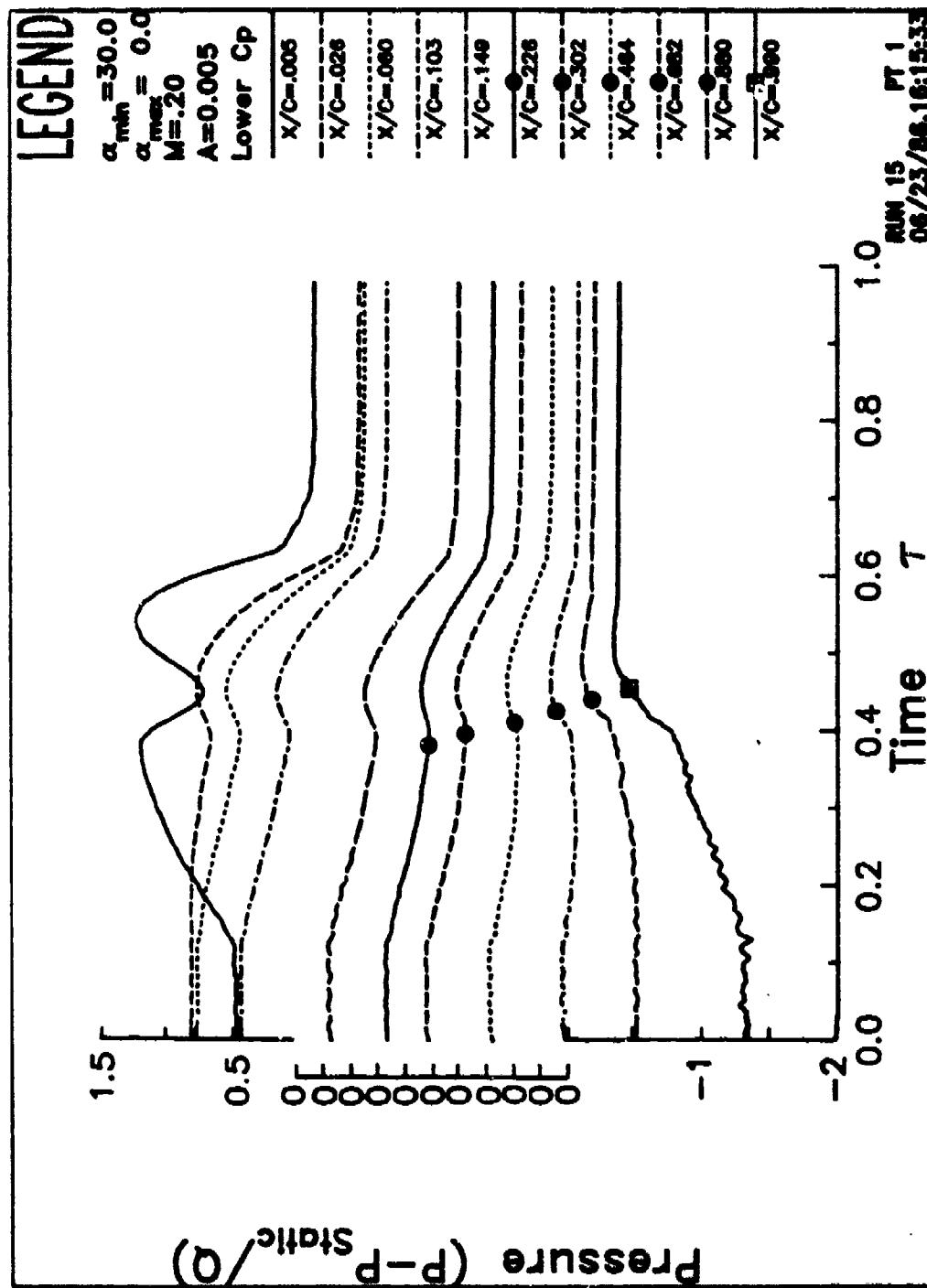


Figure 59. Lower surface pressures. b)  $A = 0.005$ .

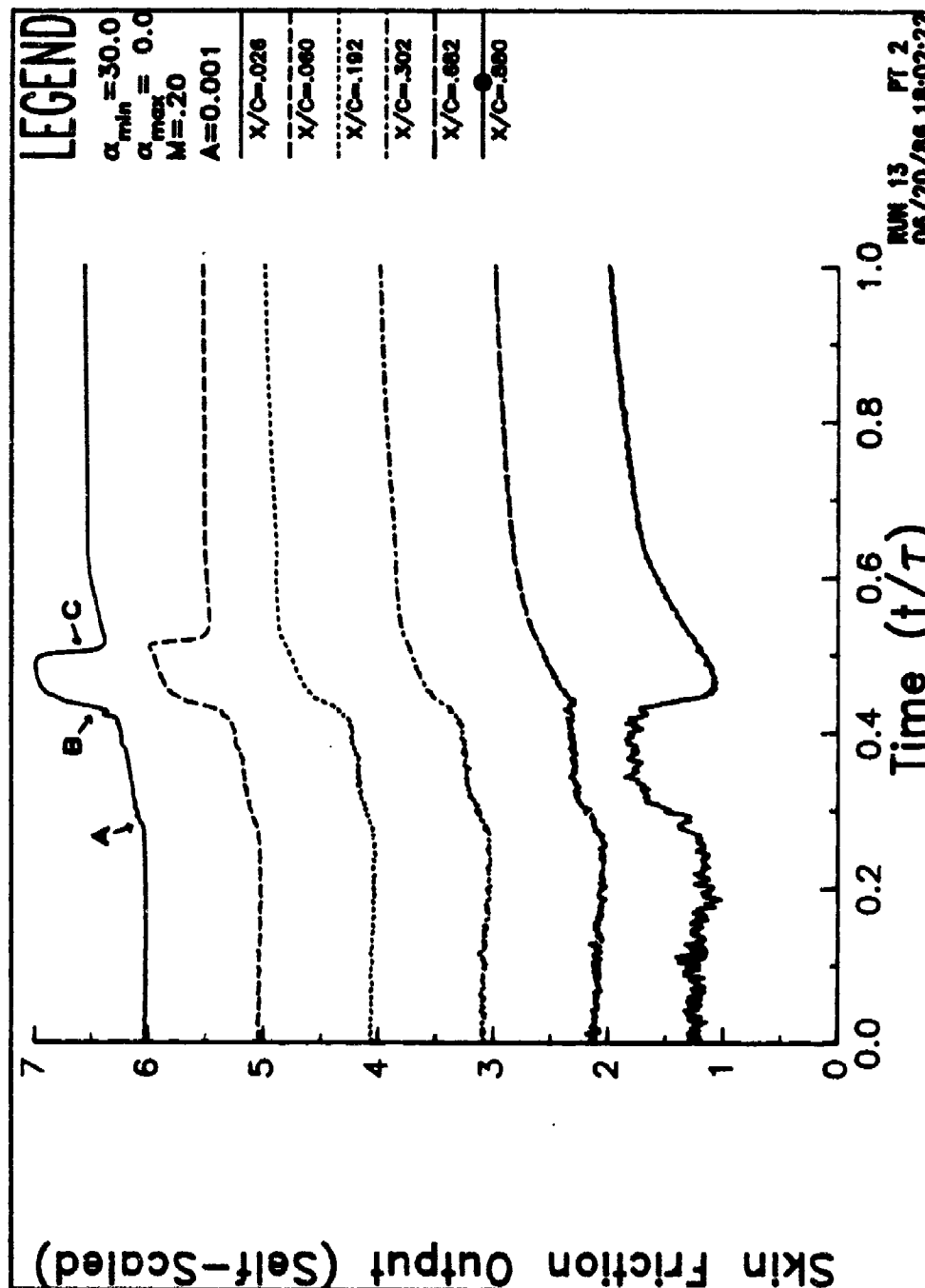


Figure 60. Hot film gage output at  $A = 0.001$ . a) ensemble

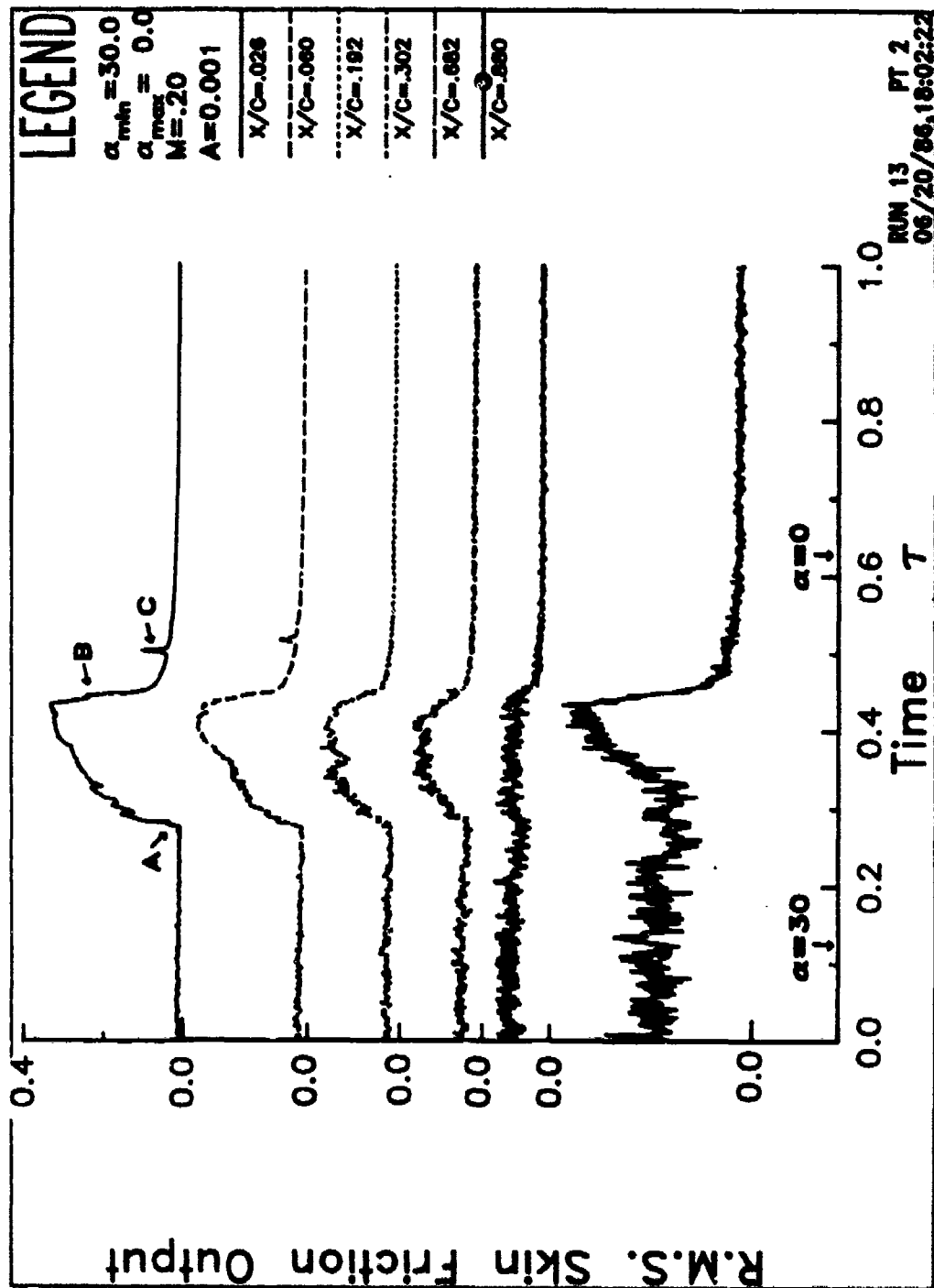


Figure 60. Hot film gage output at  $A = 0.001$ . b) RMS

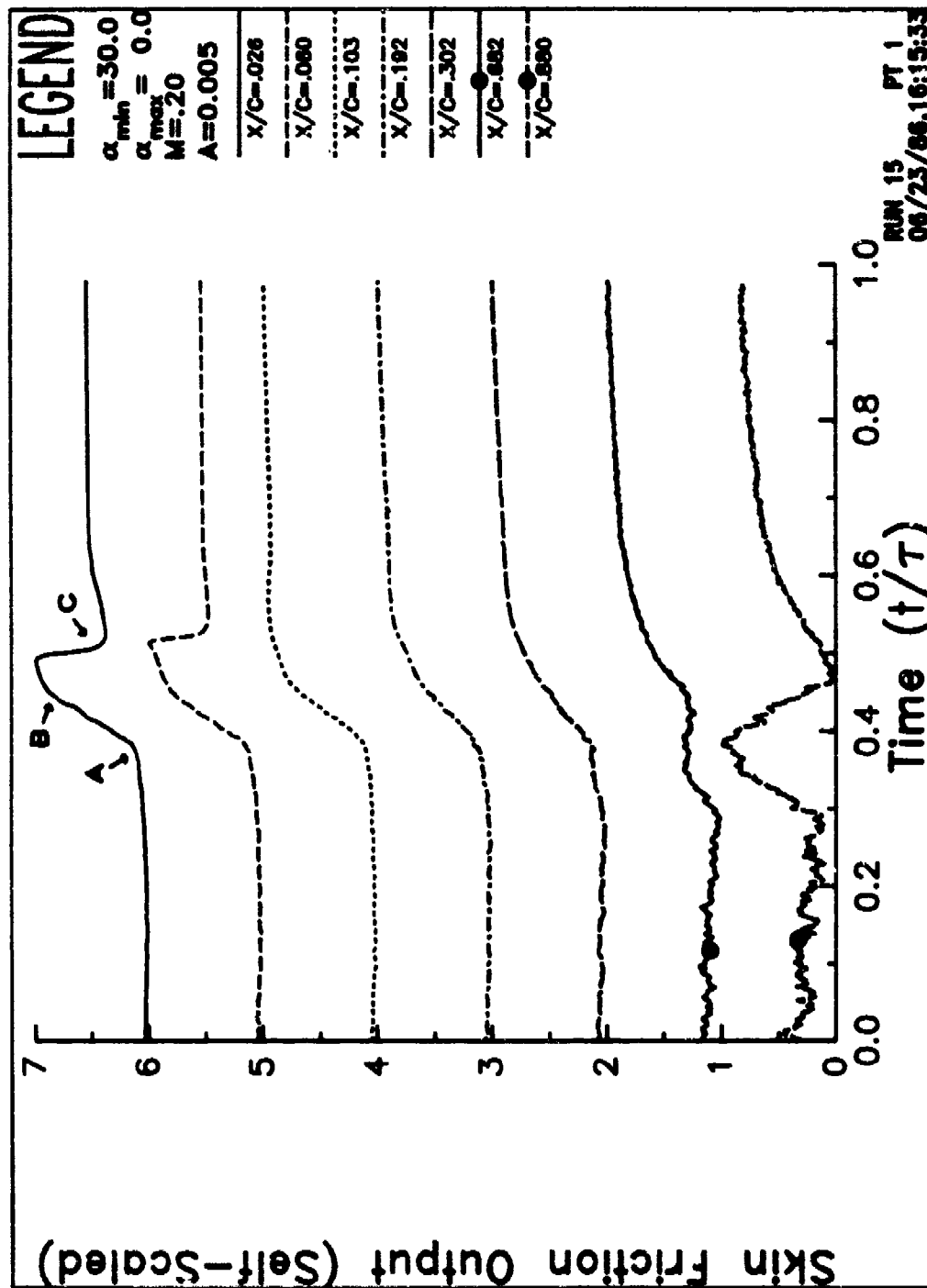


Figure 61. Hot film gage output at  $A = 0.005$ . a) Ensemble average.

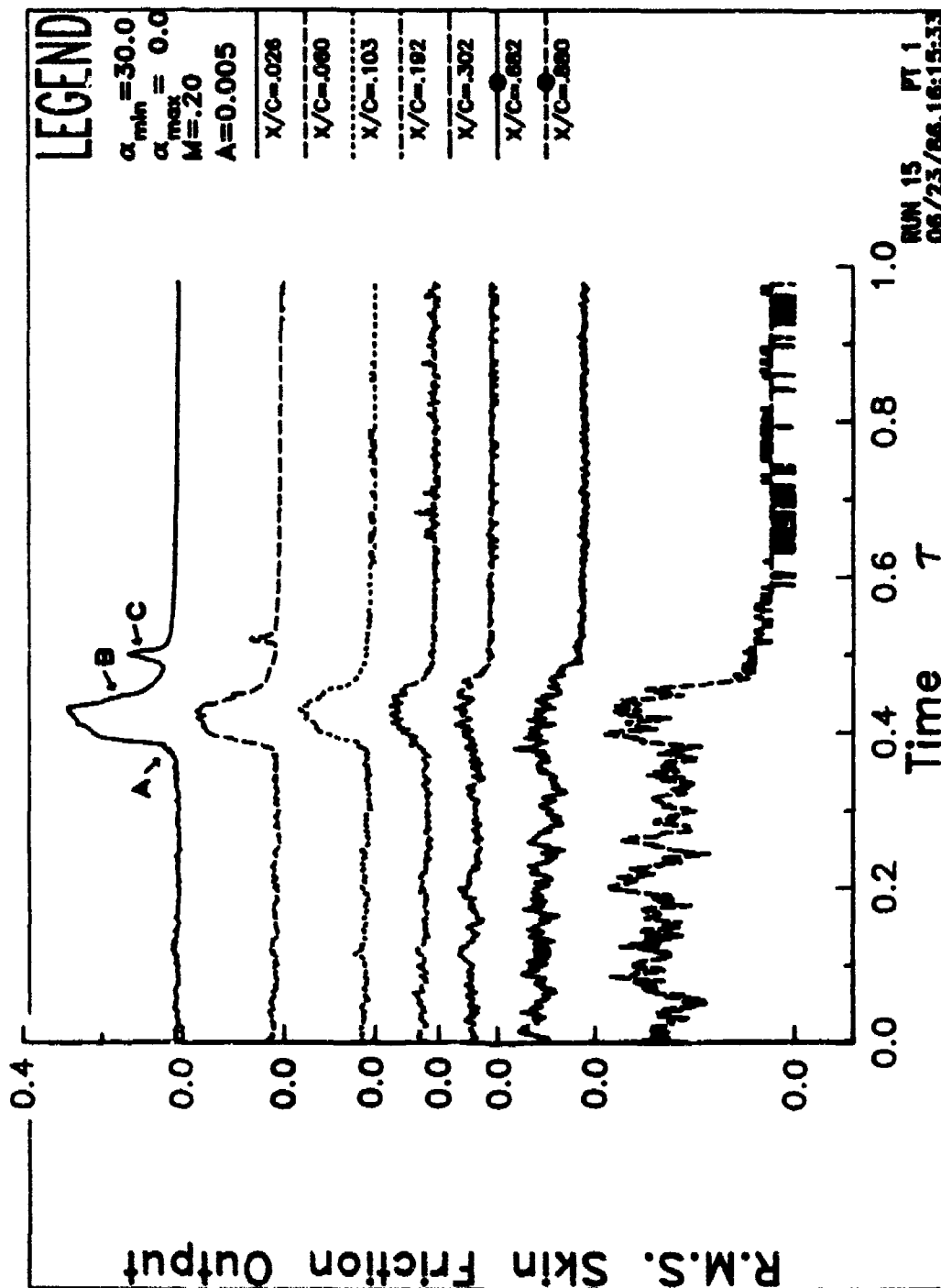


Figure 61. Hot film gage output at  $A = 0.005$ . b) RMS

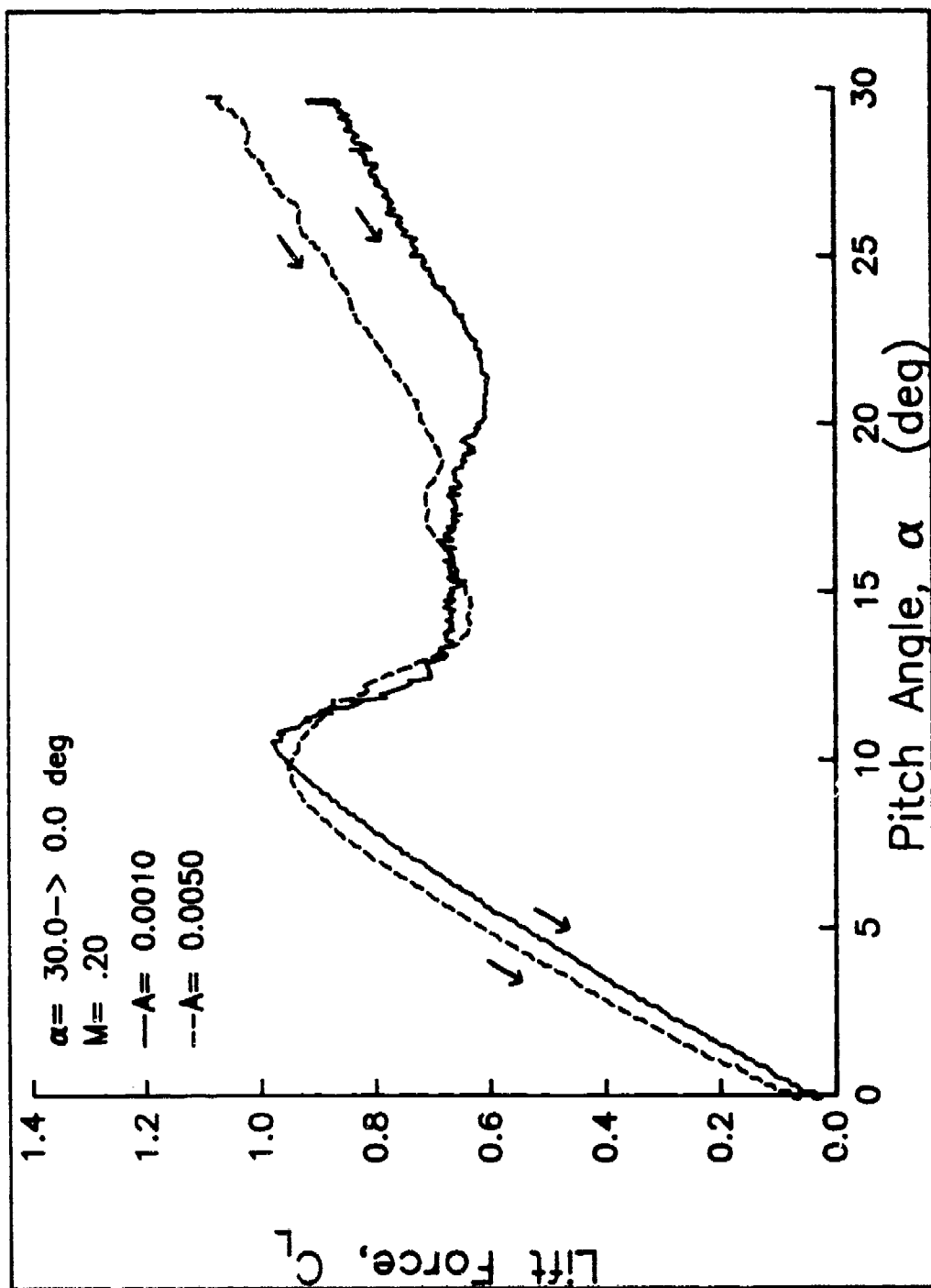


Figure 62. Airloads vs. time at  $A = 0.001$  and  $A = 0.005$ . a) Lift.

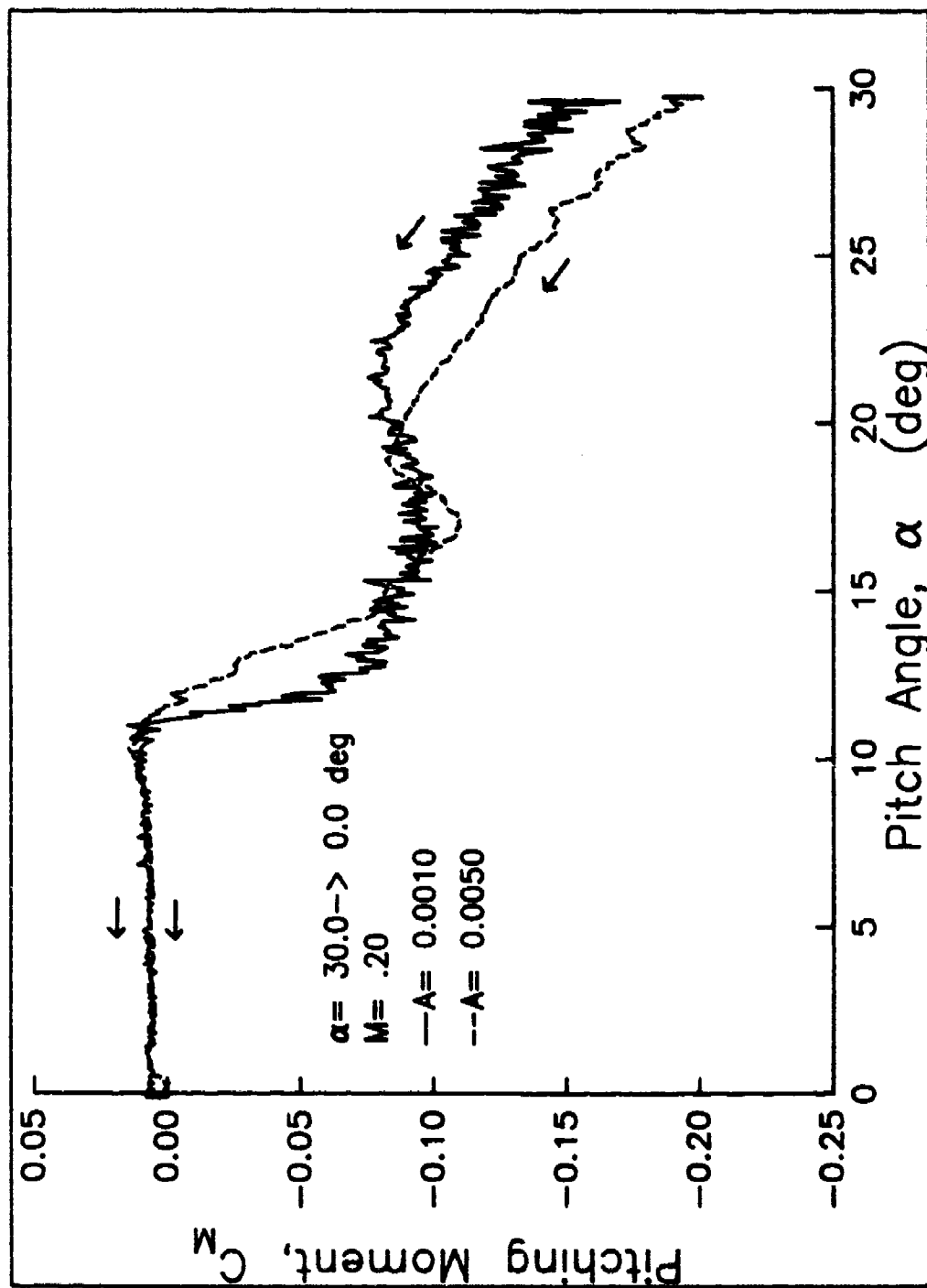


Figure 62. Airloads vs. time at  $A = 0.001$  and  $A = 0.005$ . b) Moment.



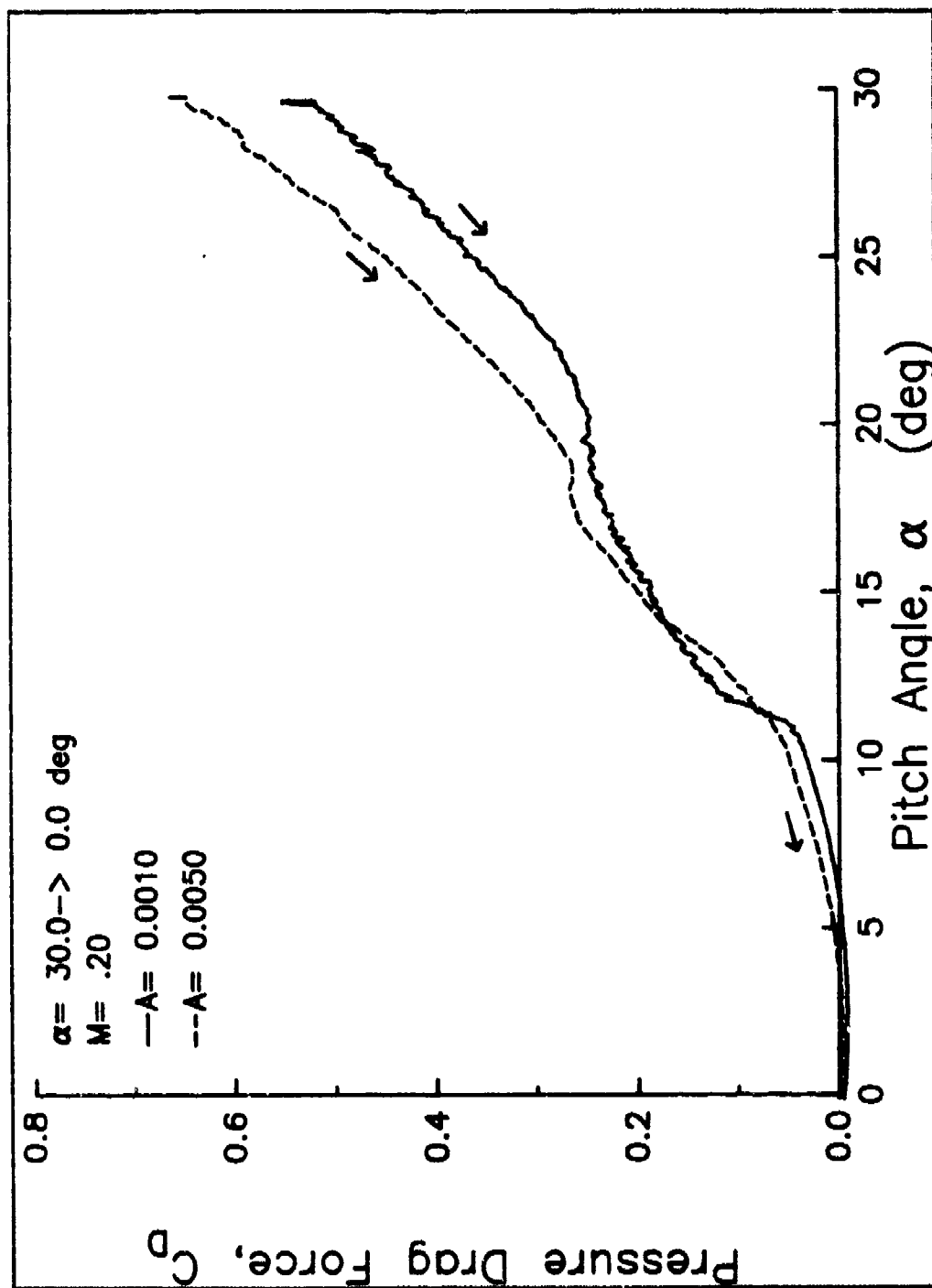


Figure 62. Airloads vs. time at  $A = 0.001$  and  $A = 0.005$ . c) Drag.

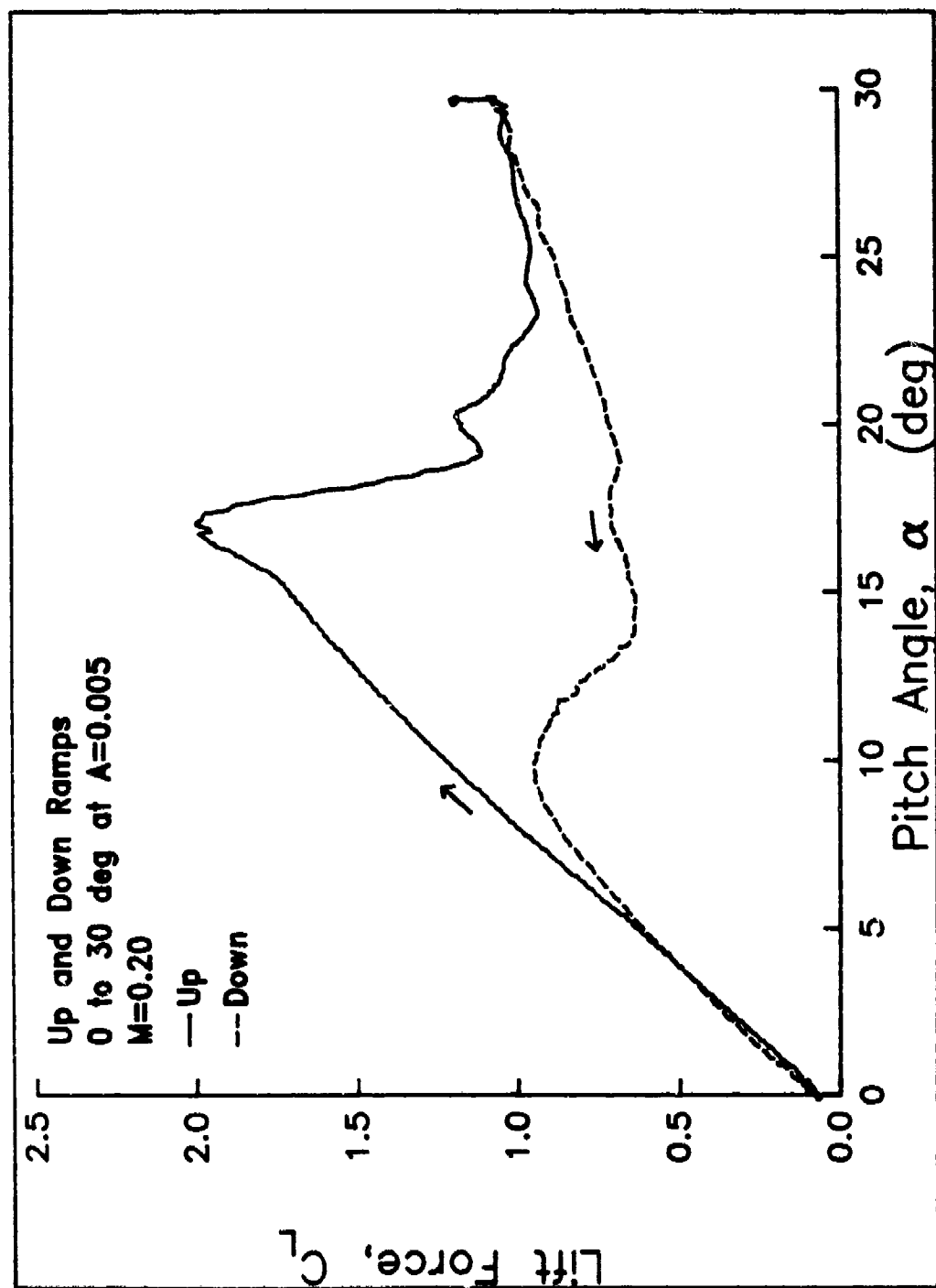


Figure 63. Up and down ramps plotted simultaneously at  $A = 0.005$ . a) Lift.

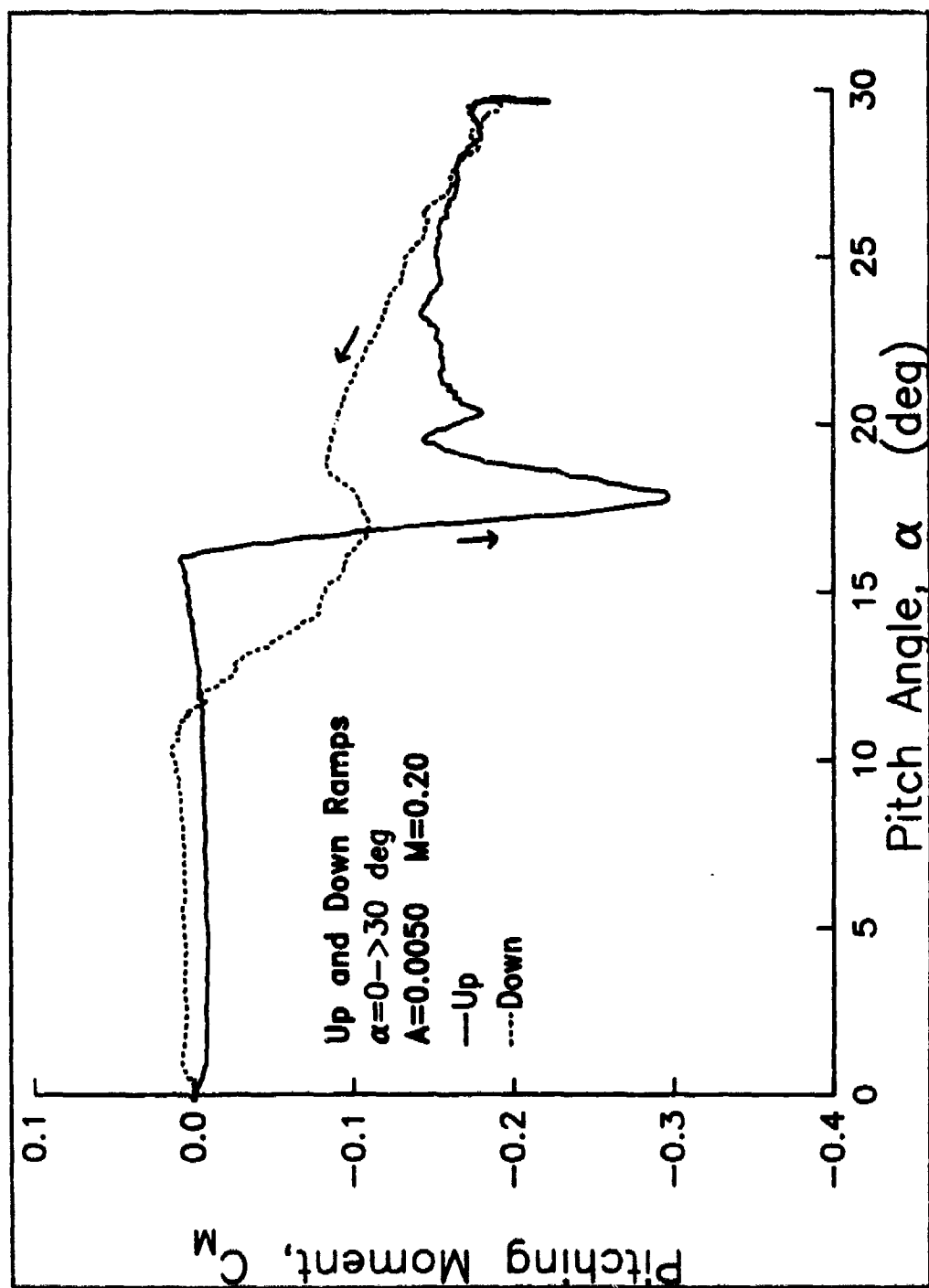


Figure 63. Up and down ramps plotted simultaneously at  $A = 0.005$ . b) Moment.

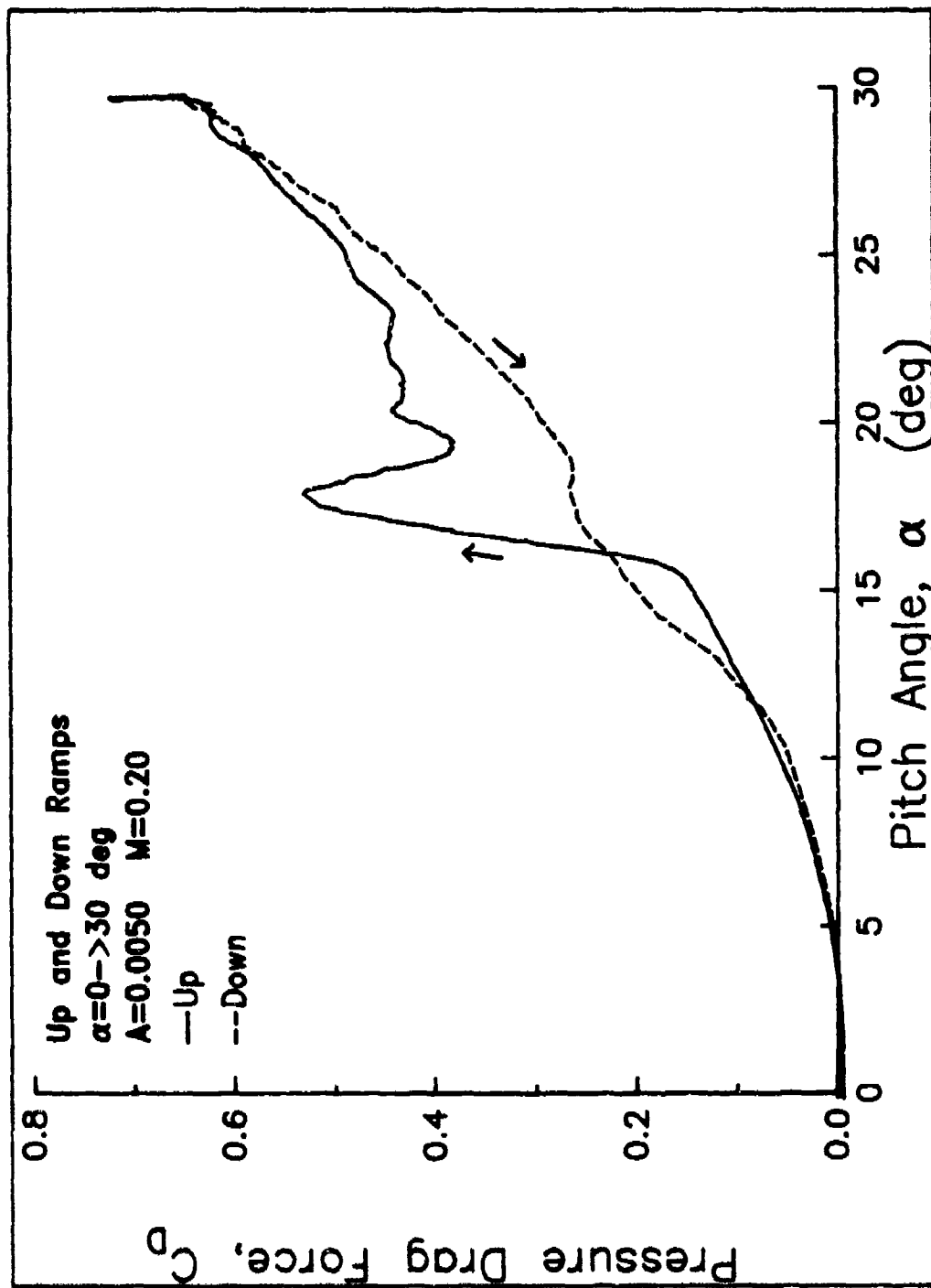


Figure 63. Up and down ramps plotted simultaneously at  $A = 0.005$ . c) Drag.

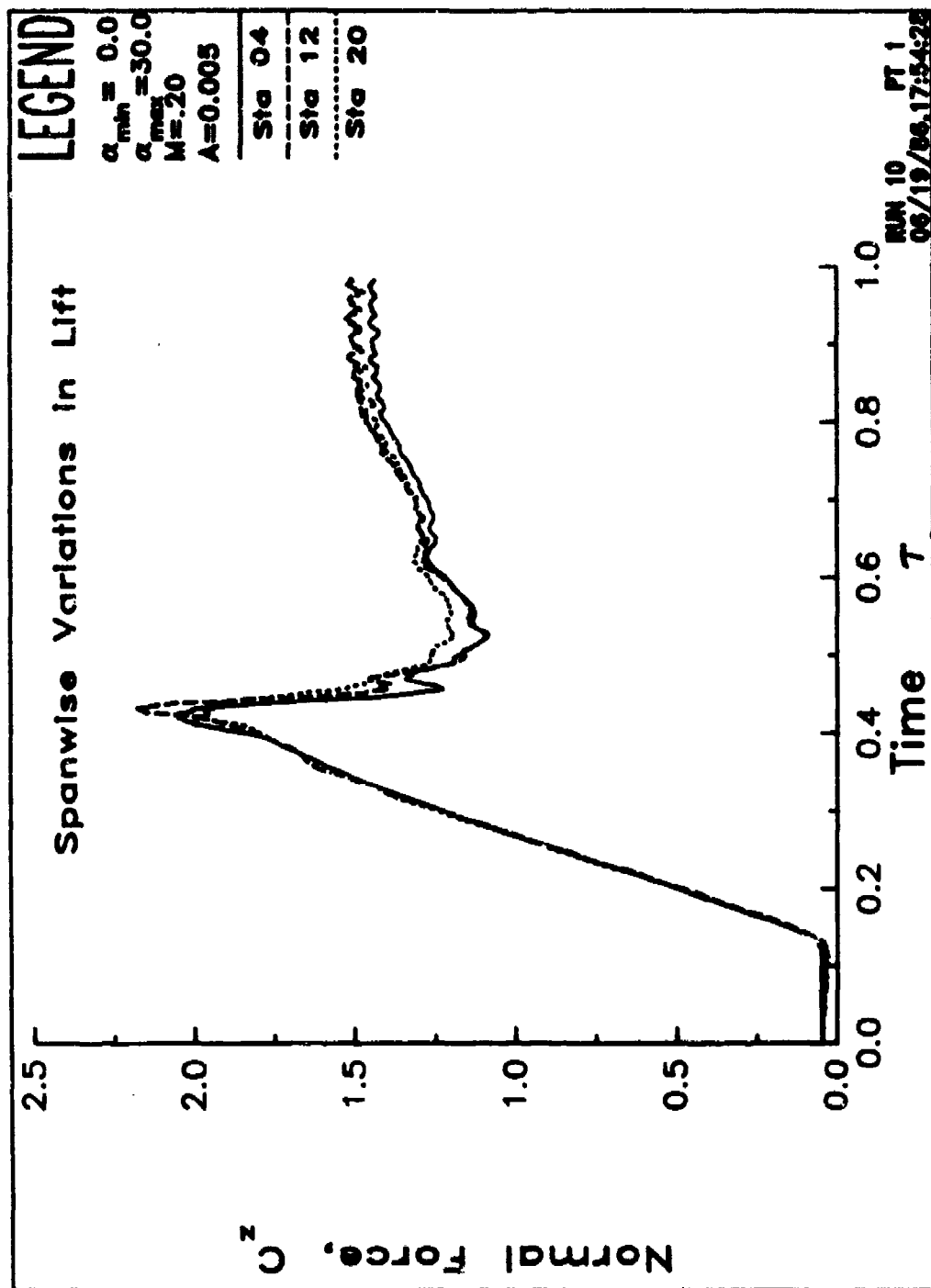


Figure 64. Spanwise variation of airloads. a) Normal force.

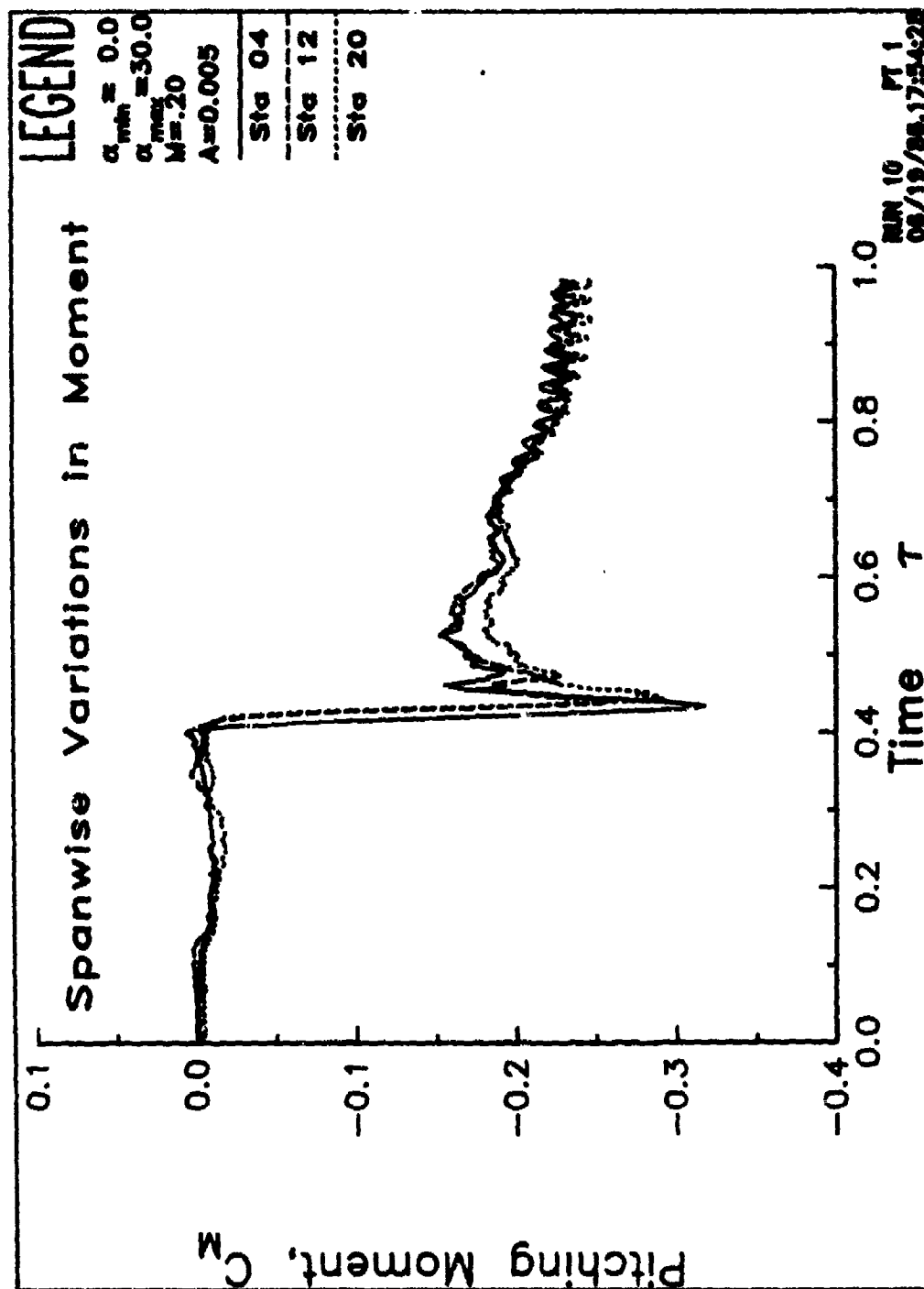


Figure 64. Spanwise variation of airloads. b) Moment.

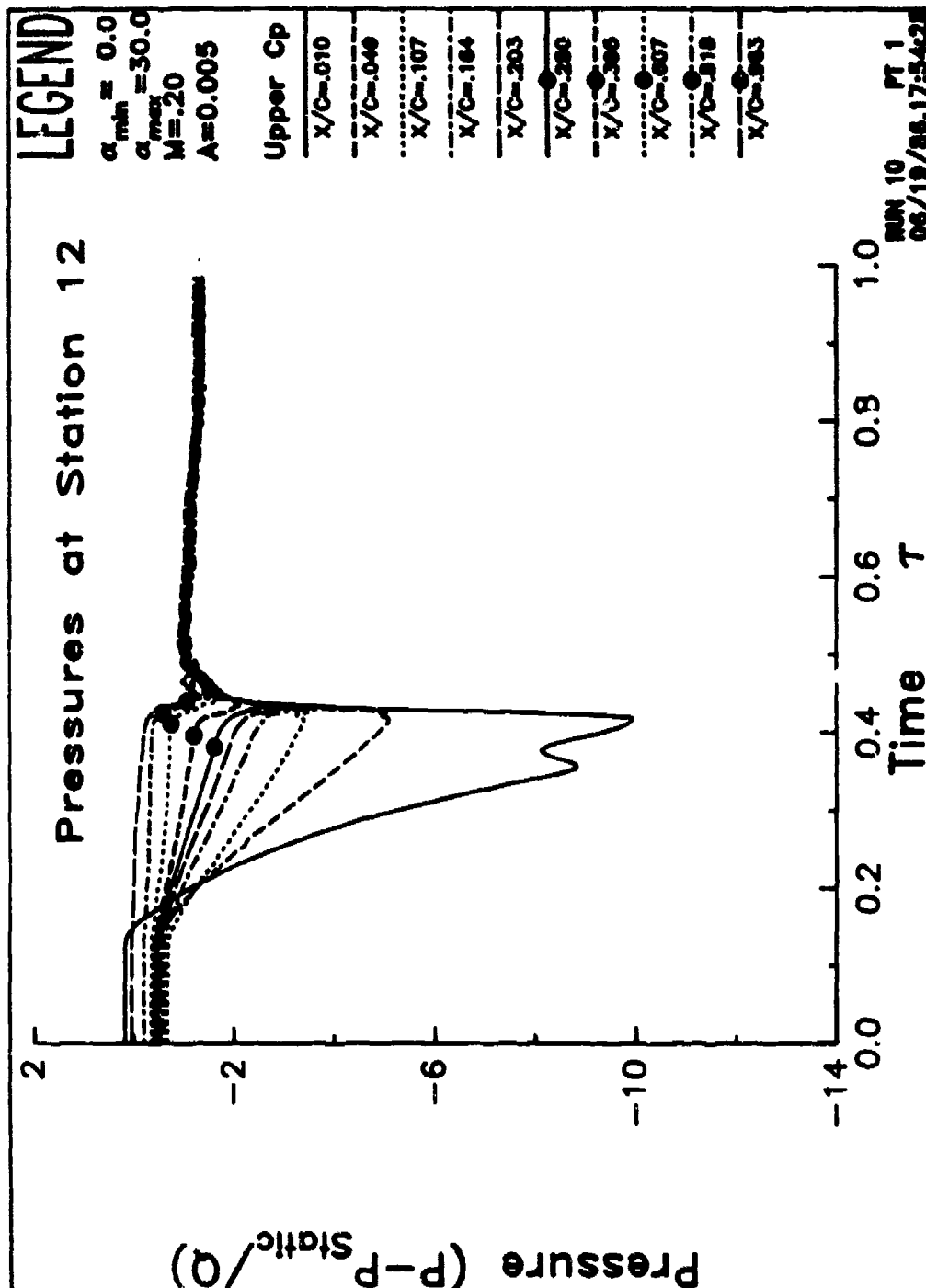


Figure 65. Upper surface pressures. a) spanwise station 12.

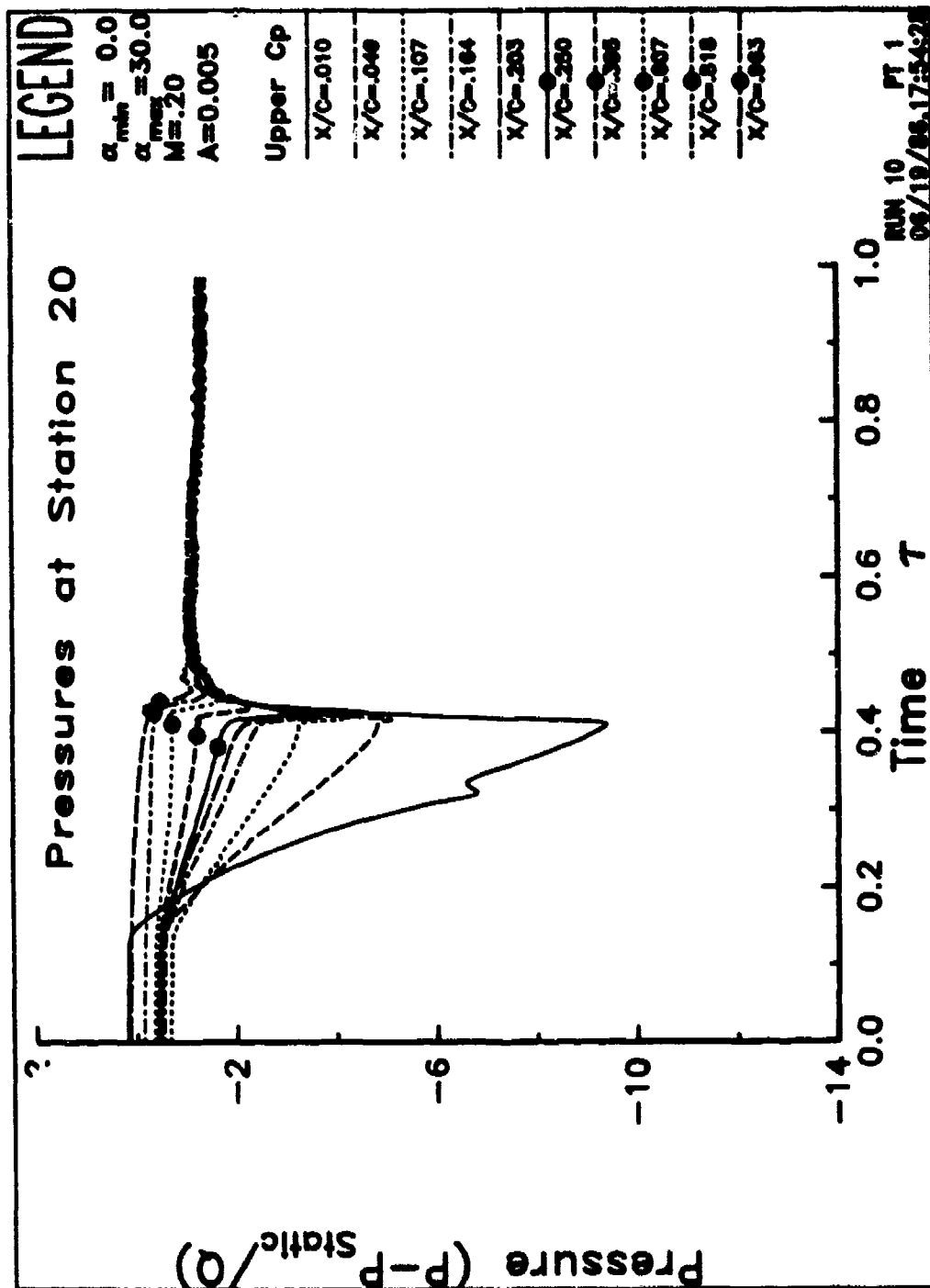


Figure 65. Upper surface pressures. b) Spanwise station 20.



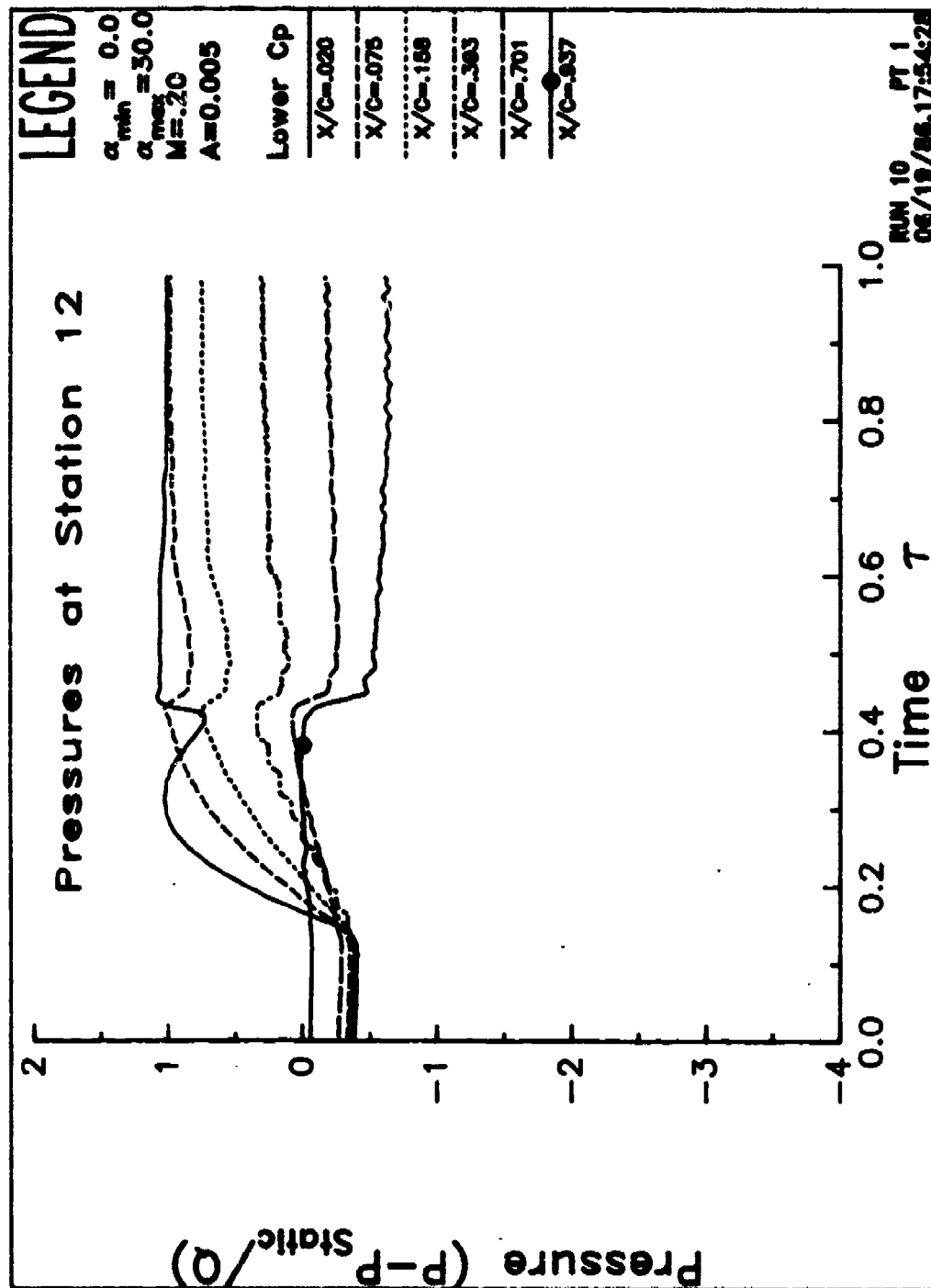


Figure 66. Lower surface pressures. a) spanwise station 12.

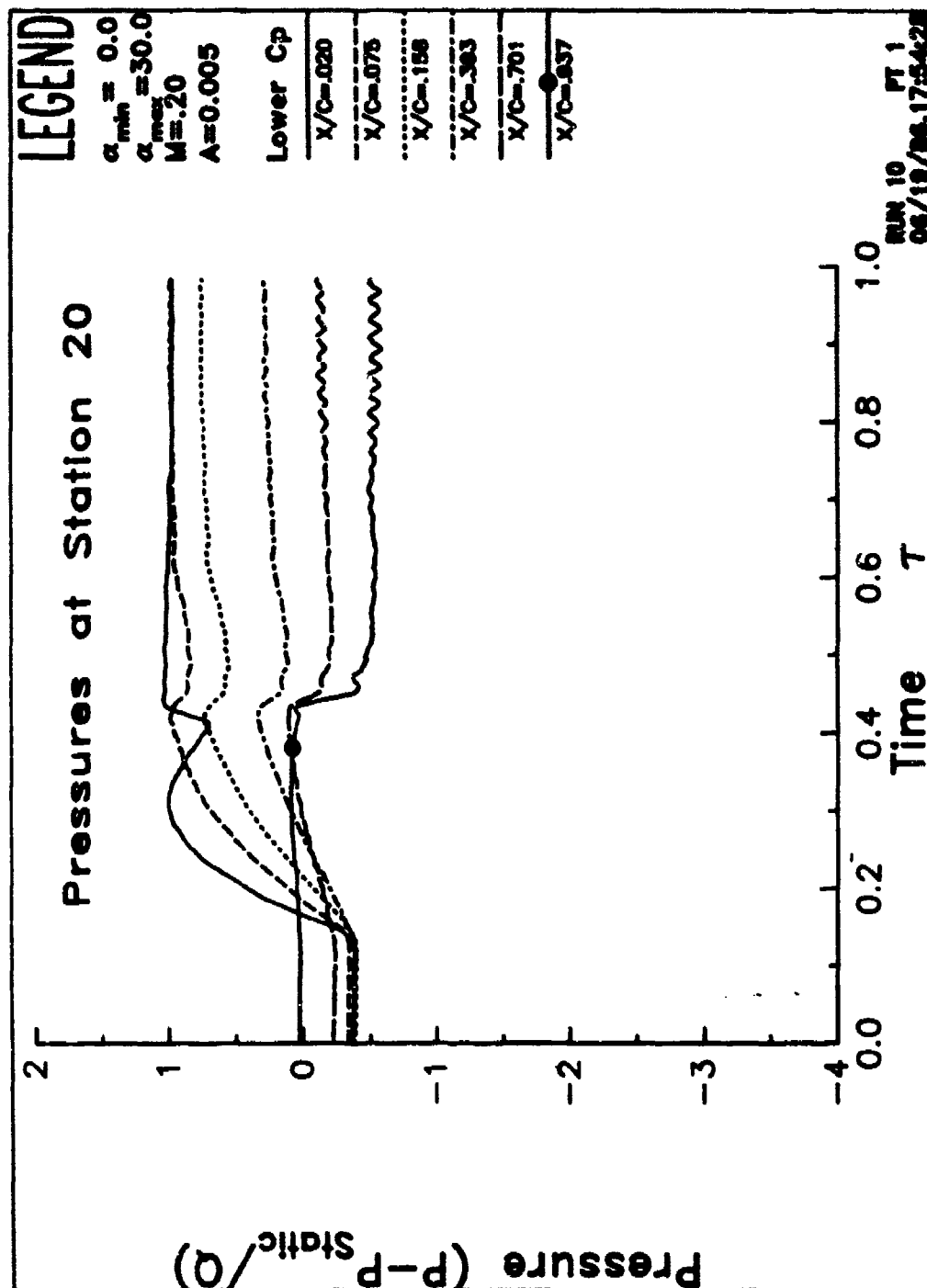


Figure 66. Lower surface pressures. b) Spanwise station 20.'

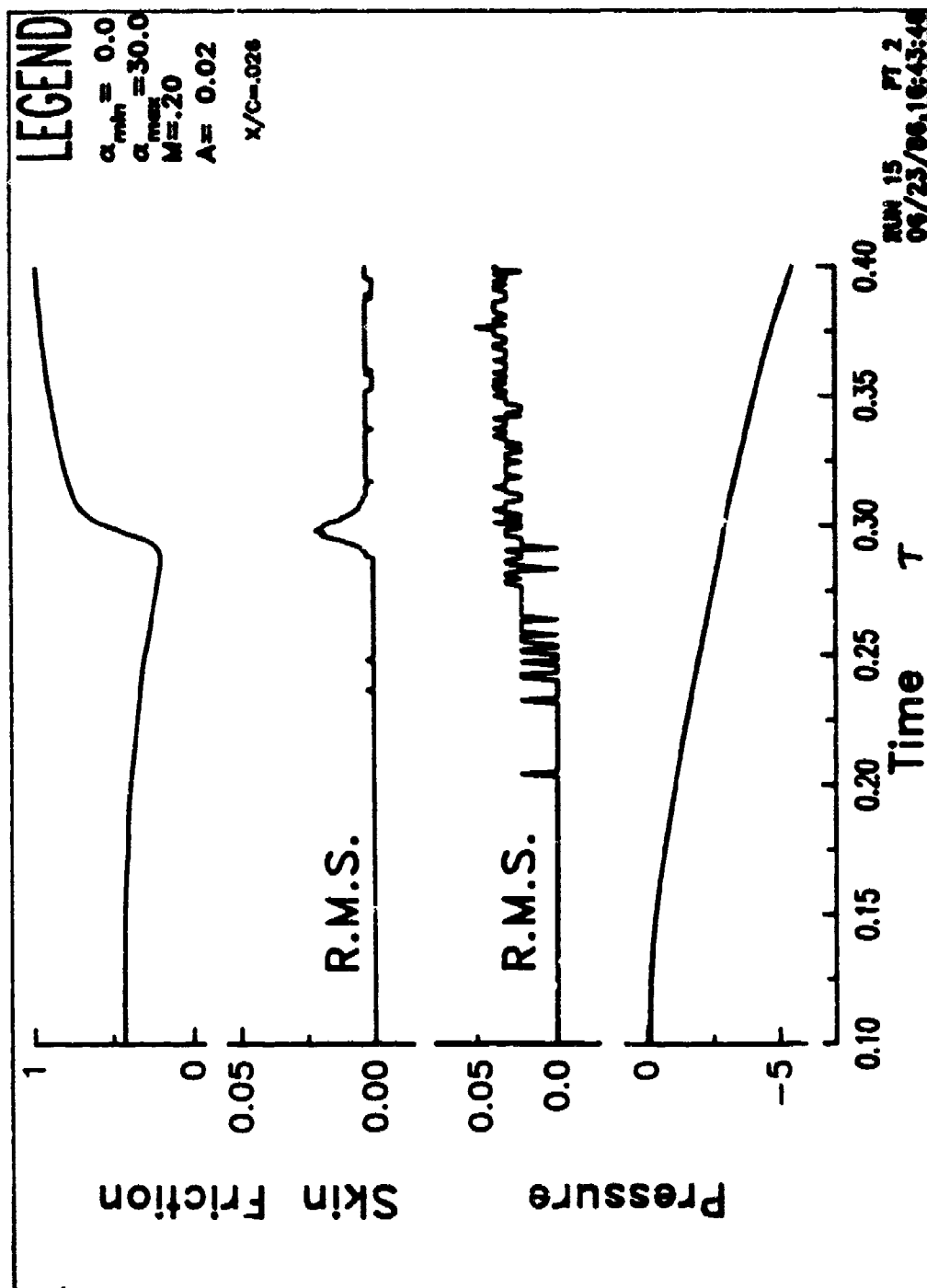


Figure 67. Pressure and skin friction time histories at  $x/c = 0.026$  near transition for a 0 to 30 deg ramp at  $M = 0.2$ . a)  $A = 0.020$ .

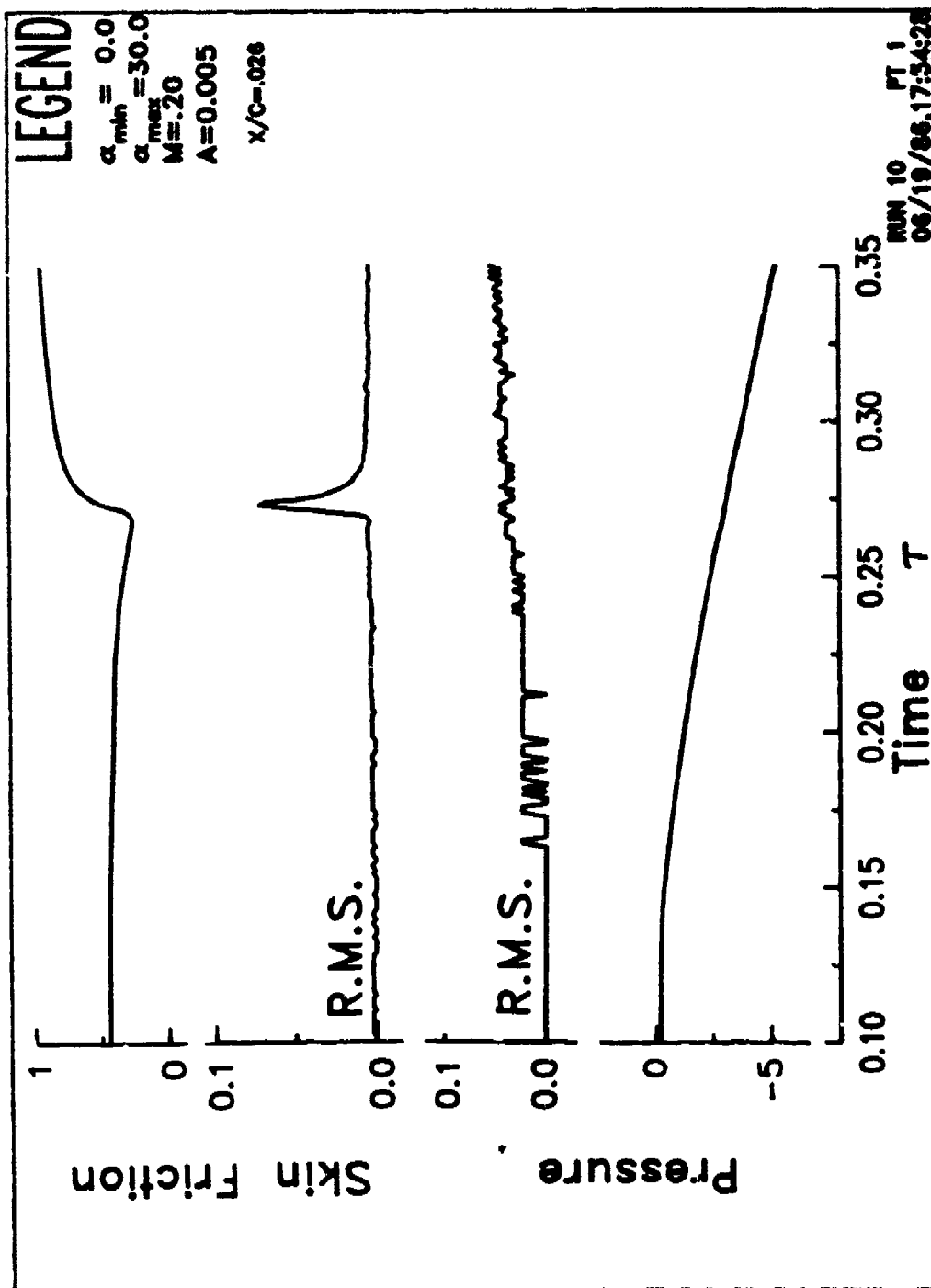


Figure 67. Pressure and skin friction time histories at  $x/c = 0.026$  near transition for a 0 to 30 deg ramp at  $M = 0.2$ . b)  $A = 0.065$ .